Suche nach assoziierter Chargino-Neutralino Produktion in Proton-Antiproton Kollisionen bei 1.96 TeV

DISSERTATION
zur
Erlangung der Doktorwürde
der Fakultät für Mathematik und Physik
der Albert-Ludwigs-Universität in Freiburg i.Br.

vorgelegt von
Ulla Blumenschein
geb. in Kaiserslautern

August 2005

Contents

My advice is to go for the messes
– that's where the action is.

Steven Weinberg

Introduction

The search for a fundamental theory of matter and forces in the universe has ever since attracted the interest of physicists. The large success of the gauge theories in the description of low-energy phenomena nourishes the hope that gauge symmetries are the clue to a unified description of all fundamental processes at high energy scales.

Particle collision experiments of the past decades have probed the structure of matter with increasing resolution. The phenomena observed in collision experiments at current energy scales are described with a large precision by the Standard Model of particle physics. Nevertheless, many open questions in the Standard Model suggest that it is an effective low-energy theory of a more fundamental theory: the numbers of free parameters of the model, the numbers of generations, the hierarchy between the electroweak scale and the Planck scale, the pending integration of gravity and the evolution of the strengths of the fundamental forces at large energy regimes. In addition, recent cosmological data suggest that the density of ordinary matter which is described by the Standard Model, corresponds only to a small fraction of the matter density in the universe.

Many of the above mentioned problems are addressed by an extension of the Standard Model that is based on an additional internal symmetry, the Supersymmetry (SUSY) of fermions and bosons. It predicts the existence of a partner for each known fundamental particle with the same quantum numbers but different spin. Supersymmetry must be broken at the energy regime of present collider experiments which leads to different masses of Standard Model particles and their super-partners.

Low-mass supersymmetric partners are expected to be produced at a sufficient rate at present or future collider experiments. In the analysis performed in this thesis, it is assumed that SUSY particles decay into their Standard Model partners and the stable lightest supersymmetric particle, which is only weakly interacting, carrying away energy and momentum and leading to detector signatures with large missing energy.

Supersymmetric particles have been searched for at the electron-positron collider LEP up to the kinematic limit. No evidence for these particles has been observed which results in lower limits on their masses. Additional constraints stem from precision measurements of quantities, which are sensitive to corrections from SUSY particles and from the search for dark matter in cosmological experiments.

The search for SUSY particles beyond the reach of LEP is continued at larger energy regimes at present and future hadron colliders. In its second phase of data taking (Run II), the center-of-mass energy of the proton-antiproton collider Tevatron at Fermilab has been raised and the luminosity has been increased considerably. The DØ experiment, one of the two Tevatron experiments, has been upgraded accordingly. The Tevatron collider allows to probe a substantial SUSY mass range beyond the LEP limits. The search will be continued at the Large Hadron Collider (LHC) which is presently being constructed at the European Research laboratory for particle physics CERN in Geneva.

At hadron colliders the supersymmetric partners of quarks and gluons are copiously

produced in strong interactions, provided they are light enough. Within most of the established SUSY models, these particles are too heavy to be produced at a sufficient rate at the Tevatron collider and the production of the lighter super-partners of the Higgs and gauge bosons, the charginos and neutralinos, becomes an important source of SUSY particles. Decays of these particles result in final states with leptons or hadrons and large missing energy. Leptonic final states can be separated more easily from the large background of hadronic Standard Model processes.

A search for the associated production of the lightest chargino and the second lightest neutralino has been performed in final states with two electrons, an additional lepton and large missing transverse energy using data collected with the DØ detector from April 2002 to July 2004. The results are interpreted stand-alone and in combination with other leptonic channels in the framework of constraint supersymmetric models.

1 Theoretical Framework

1.1 The Standard Model

The Standard Model (SM) of particle physics [1], a relativistic quantum field theory developed in the second half of the last century, describes a large part of the presently known fundamental particles and interactions in the framework of a spontaneously broken local $\mathrm{SU}(3) \times \mathrm{SU}(2)_\mathrm{L} \times \mathrm{U}(1)_\mathrm{Y}$ gauge theory. Fundamental constituents of matter are described as Dirac fermions (spin 1/2) and form representations of the gauge groups. Three of the fundamental forces (gravity is not included yet) are carried by gauge bosons which have to be introduced to preserve local gauge symmetry. The predictions of the SM have been successfully tested at a high degree of accuracy up to energy regimes of 100 GeV [2].

1.1.1 The Standard Model Lagrangian

Current theory describes a physical system by a Lagrangian density $\mathcal{L}$. In the case of the Standard Model it is a local function of a set of fields and their derivatives. Equations of motion follow from minimizing the action $S = \int d^4x\ \mathcal{L}$. The Lagrangian is ideally determined by a set of symmetry requirements, each symmetry corresponding to a transformation group, whose members leave the action invariant. From the symmetry follow conserved currents J_μ and conserved charges $Q = \int d^3x\ J_0$ which correspond to the generators of the group and form the Lie-algebra of the group. Irreducible representations are classified by a set of eigenvalues of commuting operators. The SM Lagrangian is invariant under global transformations of the Poincareé group (rotations and Lorenz boosts $M^{\mu\nu}$ and translations P^μ). The algebra of the Poincareé group is given by the Minkowski metric $g_{\mu\nu} = \mathrm{diag}(1, -1, -1, -1)$:

$$[M^{\mu\nu}, P^\sigma] = -i(P^\mu g^{\nu\sigma} - P^\nu g^{\mu\sigma}) \tag{1.1}$$

$$[M^{\mu\nu}, M^{\sigma\tau}] = i(M^{\mu\sigma} g^{\nu\tau} + M^{\nu\tau} g^{\mu\sigma} - M^{\mu\tau} g^{\nu\sigma} - M^{\nu\sigma} g^{\mu\tau}) \tag{1.2}$$

$$[P^\mu, P^\nu] = 0. \tag{1.3}$$

Irreducible representations of the Poincareé group (particles) are classified according to the eigenvalues of the two Casimir operators $P^2 = P_\mu P^\mu$ (Mass^2) and $W^2 = W_\sigma W^\sigma$ with $W_\sigma = \epsilon_{\mu\nu\tau\sigma} M^{\mu\nu} P^\tau$ (Spin^2). The dynamic state of a free particle can be classified in addition by the eigenvalues of three P^μ components (e.g. momentum) and one W_σ component (e.g. W_3-component).

Apart from that, the SM Lagrangian is determined by the following internal local symmetries:

- Local $\mathrm{U}(1)_\mathrm{Y}$ symmetry, generated by the weak Hypercharge Y (abelian).

- Local $SU(2)_L$ symmetry, generated by three weak Isospin operators T_i with the algebra: $[T_i, T_j] = i\epsilon_{ijk}T_k$. Representations (singlets and doublets) can be classified according to the eigenvalues of the weak Isopin $I^2 = \sum T_i T_i$.
- Local $SU(3)_C$ symmetry, generated by eight color-charge operators λ_C with the algebra $[\lambda_a, \lambda_b] = if_{abc}\lambda_c$, with the non-vanishing structure constants: $f_{123} = 1$, $f_{147} = f_{246} = f_{257} = f_{345} = f_{516} = f_{637} = \frac{1}{2}$, and $f_{458} = f_{678} = \frac{\sqrt{3}}{2}$.

The constituents of the Standard Model are summarized in Table 1.1. The three generations of fermions are classified into the only electroweakly interacting leptons and the quarks which in addition interact strongly and mix to the various mass eigenstates. The leptons are divided into charged leptons and neutrinos. The description of the fermions within the Dirac formalism includes two chirality states and a corresponding antiparticle.

Name		spin	fields	quantum numbers		
				Hypercharge Y	weak Isospin I	SU(3) repr.
Leptons	L	$\frac{1}{2}$	$\binom{\nu_{eL}}{e_L}$, $\binom{\nu_{\mu L}}{\mu_L}$, $\binom{\nu_{\tau L}}{\tau_L}$	-1/2	1/2	singlet
	e		(e_R), (μ_R), (τ_R)	-1	0	singlet
Quarks	Q	$\frac{1}{2}$	$\binom{u_L}{d'_L}$, $\binom{c_L}{s'_L}$, $\binom{t_L}{b'_L}$	1/6	1/2	triplet
	u		(u_R), (c_R), (t_R)	4/6	0	triplet
	d		(d'_R), (s'_R), (b'_R)	-2/6	0	triplet
Higgs field		0	$\binom{\phi_1}{\phi_2}$	1/2	1/2	singlet
U(1) gauge field		1	B	0	0	singlet
SU(2) gauge fields		1	W^1, W^2, W^3	0	1	singlet
SU(3) gauge fields		1	g^1, g^2, $\ldots g^8$	0	0	octet

Table 1.1: The constituents of the Standard Model. The quark fields and the gauge fields mix to form mass eigenstates.

Since a Lagrangian for a single fermion is in general not invariant under a local symmetry transformation, a massless gauge field has to be introduced for each generator. It transforms such, that the combined Lagrangian is invariant after replacing the derivative with the corresponding covariant derivative. A scalar field is added in order to generate mass terms for the gauge bosons. In order to accommodate the experimental evidence for non-zero masses for the left-handed neutrinos [3], right-handed, heavy neutrinos have to be included into future versions of the Standard Model [4].

The dynamics of the system is determined by the time-evolution operator $U = \exp(-Ht)$ with the Hamiltonian $H = \int T_0^0 d^3x$. Dynamic calculations in a set of interacting fields which are no longer eigenstates of the total Hamiltonian are performed by a perturbation expansion of U. A measurement of the parameters (e.g. masses, couplings) of the Lagrangian at a certain energy scale yields effective values which are a result of higher-order perturbation effects. With increasing energy the effective values evolve towards their *bare*

values (*running masses, running couplings*). Adjusting the effective parameters in all orders of a perturbation calculation is called *renormalization*. A theory whose perturbation expansion keeps finite after this adjustment is called *renormalizable*. The Standard Model Lagrangian is determined by the above listed symmetry requirements and the requirement of renormalizability.

Construction of the Lagrangian

A Lagrangian for massless fermion fields can be written as:

$$\mathcal{L}_{SM} = i\bar{\Psi}_i \gamma^\mu \partial_\mu \Psi_i \tag{1.4}$$

where the sum goes over all fermion fields Ψ_i.

In order to ensure invariance under a local $\mathrm{SU(3)} \times \mathrm{SU(2)_L} \times \mathrm{U(1)_Y}$ transformation, the massless vector gauge fields B_μ, $W^1_\mu \dots W^3_\mu$, $g^1_\mu \dots g^8_\mu$ with the couplings $\mathrm{g_1}$, $\mathrm{g_2}$ and $\mathrm{g_3}$ have to be introduced for the transformation groups $\mathrm{U(1)_Y}$, $\mathrm{SU(2)_L}$ and $\mathrm{SU(3)_C}$ respectively. The simple derivative in Eqn. 1.4 is replaced by the covariant derivative:

$$\mathbf{D}_\mu = \partial_\mu + \mathrm{i g_k} \mathbf{V}^{\mathrm{k}}_\mu \tag{1.5}$$

where $\mathbf{V}_\mu = V^\alpha_\mu \mathbf{T}_\alpha$ with the generators $\mathbf{T}_\alpha$ and the vector gauge fields V^α_μ of the corresponding gauge group. The Lagrangian becomes then:

$$\mathcal{L}_{SM} = i\bar{\Psi}_i \gamma^\mu \mathbf{D}_\mu \Psi_i \tag{1.6}$$

where the sum goes over all fermion fields and gauge fields in Table 1.1 and the fermion fields Ψ_i enter the equations as representations of the corresponding gauge groups (SU(2) doublets and singlets, color triplets and singlets etc.). The gauge fields in the covariant derivative couple only to fermions of the same representation of the gauge group. This prohibits e.g. neutral $\mathrm{U(1)} \times \mathrm{SU(2)}$ interactions which change the flavor (*flavor changing neutral currents FCNC*).

Kinetic terms for the gauge fields V^j_μ are expressed as

$$\frac{1}{4} V^\alpha_{\mu\nu} V^{\mu\nu}_\alpha \tag{1.7}$$

with the field strength tensors $V^\alpha_{\mu\nu} = \partial_\mu V^\alpha_\nu - \partial_\nu V^\alpha_\mu + g f^{\alpha \mathrm{bc}} V^{\mathrm{b}}_\mu V^{\mathrm{c}}_\nu$, where $f^{\alpha\mathrm{bc}}$ is the structure constant of the corresponding gauge group. The last term does not vanish for the non-abelian groups SU(2) and SU(3). As a consequence, Eqn. 1.7 contains also cubic and quartic self-interactions of the corresponding gauge bosons. In contrast to the electroweak gauge bosons which acquire masses (see below), the gluons remain massless, such that the gluon self-interaction leads to an effective (renormalized) coupling which becomes stronger at large distances (low energies). This results in the *confinement* of colored particles within color singlet bound states. For low distances (high energies) a small effective coupling leads to *asymptotic freedom* of the colored particles and enables perturbative calculation.

Whereas mass terms for the fermions can be introduced explicitly, similar terms for the gauge bosons are not gauge invariant. The experimental evidence for massive gauge bosons

of the weak force is accommodated in a gauge invariant and renormalizable way by the *Higgs mechanism*: A scalar SU(2) doublet, the Higgs field Φ, is introduced into the Lagrangian as a potential:

$$\mathrm{V}(\Phi^*\Phi) = -\mu^2(\Phi^*\Phi) + \lambda(\Phi^*\Phi)^2, \quad \mu^2 > 0. \tag{1.8}$$

The tachyonic mass term $-\mu^2(\Phi^*\Phi)$ in the Higgs potential leads to a degenerate vacuum state with $<\Phi>^2 = \frac{\mu^2}{2\lambda} = \nu^2$. After breaking the $\mathrm{U(1)_Y \times SU(2)_L}$ symmetry of the vacuum state by choosing e.g. $\Phi_{vacuum} = \binom{0}{\nu}$ and expanding around this state, the covariant derivative of the Higgs field results in mass terms for three linear combinations of the electroweak gauge fields, the charged W-bosons and the neutral Z-boson:

$$\mathrm{Z}_\mu = \mathrm{W}^3_\mu \cdot \cos\theta_\mathrm{W} - \mathrm{B}_\mu \cdot \sin\theta_\mathrm{W} \tag{1.9}$$

$$\mathrm{W}^+_\mu = \sqrt{2}(\mathrm{W}^1_\mu - \mathrm{i}\mathrm{W}^2_\mu) \tag{1.10}$$

$$\mathrm{W}^-_\mu = \sqrt{2}(\mathrm{W}^1_\mu + \mathrm{i}\mathrm{W}^2_\mu) \tag{1.11}$$

with the *Weinberg angle* θ_W which is a function of the electroweak couplings: $\cos\theta_\mathrm{W} = \frac{\mathrm{g_2}}{\sqrt{\mathrm{g_1^2}+\mathrm{g_2^2}}}$ and $\sin\theta_\mathrm{W} = \frac{\mathrm{g_1}}{\sqrt{\mathrm{g_1^2}+\mathrm{g_2^2}}}$,

The orthogonal combination to the Z boson, the photon A, remains massless:

$$\mathrm{A}_\mu = \mathrm{W}^3_\mu \cdot \sin\theta_\mathrm{W} + \mathrm{B}_\mu \cdot \cos\theta_\mathrm{W}. \tag{1.12}$$

This mechanism is called *electroweak symmetry breaking, EWSB*. The generation of the mass terms for three gauge bosons, which is connected with an additional polarization degree of freedom, uses three of the four degrees of freedom of the complex scalar Higgs doublet. The remaining degree of freedom results in a scalar Higgs boson which acquires a mass term from the Higgs potential after EWSB. Direct searches for the Higgs boson at LEP result in a lower bound on the mass of the SM Higgs boson of 114.4 GeV [5]. Precision measurements of electroweak observables [6] yield an upper bound on its mass of 208 GeV at 95% confidence level with the current world average for the top mass of $m_\mathrm{top} = 174.3 \pm 3.4\,\mathrm{GeV}$ [7].

Mass terms for the fermions are generated by trilinear Yukawa couplings of the Higgs fields:

$$\mathcal{L}_\mathrm{Yukawa} = \bar{\mathrm{Q}}\mathbf{h_u}\Phi^\mathrm{C}\mathrm{u} + \bar{\mathrm{Q}}\mathbf{h_d}\Phi\mathrm{d}' + \bar{\mathrm{L}}\mathbf{h_e}\Phi\mathrm{e} + \mathrm{h.c.} \tag{1.13}$$

with the charge-conjugated Higgs field Φ^C and the Yukawa matrices $\mathbf{h_u} = \mathrm{h_u}\mathbf{1}$, $\mathbf{h_e} = \mathrm{h_e}\mathbf{1}$ and $\mathbf{h_d} = \mathbf{V}\mathrm{h_d}\mathbf{V}^*$. The last term contains the 3×3 CKM matrix $\mathbf{V}$ in quark generation space [8]. The CKM matrix can not be made real by redefinition of the quark fields, such that the Standard Model Lagrangian is not invariant under a combined transformation of charge conjugation and parity (*CP-violation*) [8].

Summarizing all of the above terms, the complete SM Lagrangian can be written as:

$$\mathcal{L}_{SM} = i\Psi_i\gamma^\mu\mathbf{D}_\mu\Psi_i - \frac{1}{4}V^j_{\mu\nu}V^{\mu\nu}_j + [\mathbf{D}_\mu\Phi]^2 - V(\Phi^*\Phi) - \mathcal{L}_{Yukawa}. \tag{1.14}$$

The sum goes over all fields from Table 1.1.

Mass terms for the gauge bosons are also possible in non-minimal models with two Higgs doublets Φ_1 and Φ_2 ($\mathrm{Y} = \pm\frac{1}{2}$). Symmetry breaking in the vacuum states of the two Higgs doublets results then in mass terms for two scalar (h, H) and one pseudoscalar Higgs boson (A) and for two charged Higgs bosons ($\mathrm{H}^+, \mathrm{H}^-$).

1.1.2 Problems of the Standard Model

The Standard Model in its present form provides an excellent description of many fundamental constituents of the universe and their interactions at energy scales up to the order of 100 GeV. All predicted constituents have been observed except for the Higgs Boson which is crucial for the verification of the EWSB mechanism.

Nevertheless the Standard Model has to be considered as a work in progress which will have to be extended in order to include at least all present results from particle physics and cosmology and in order to describe physics at arbitrarily high energy scales. The following part provides an overview of the problems of the current version of the Standard Model:

- The large number of free parameters of the Standard Model (the fermion masses, the neutrino and quark mixing parameters, the strength of the gauge couplings, the Higgs vacuum expectation value and the mass of the Higgs boson) reduce its predictive power. It has to be considered as an effective low-energy approximation of a more fundamental theory.
- Since it is not possible to integrate gravity in a renormalizable way into the present Standard Model, this force is still described by the Einstein formalism outside the framework of gauge theories. Besides there are problems to derive quantum gravity as a consequence of local gauge invariance alone without imposing the equivalence principle [9]. Due to the weakness of the gravitational force the current approximation of neglecting the gravitation in particle physics works well at low energy scales but is expected to fail at the latest at the order of the Planck Scale $\mathrm{M_P} = \sqrt{\frac{\hbar \mathrm{c}}{\mathrm{G_N}}} \approx 1.2 \times 10^{19}\,\mathrm{GeV}$.
- A more fundamental and predictive theory can be obtained by embedding the SM into a higher symmetry group (for example SO(10)), which is broken into the symmetry groups of the Standard Model at low energy scales (Grand Unified Theories, GUT). One of the implications of GUTs consists in the unification of the electroweak and strong couplings $\alpha_1 = \frac{5}{3}\frac{g_1^2}{4\pi}$, $\alpha_2 = \frac{g_2^2}{4\pi}$, $\alpha_3 = \frac{g_3^2}{4\pi}$ at higher energies (GUT scale, M_{GUT}). However, when the current measurements of the coupling strengths are extrapolated towards higher energies, the couplings do approach each other but they do not not unify at the same energy scale [10] (see Fig. 1.1a).
- Recent measurements of anisotropies of the Cosmic Microwave Background (CMB) [11] confirm the Cosmological Standard Model (ΛCDM model) and measure its parameters with high precision. According to the best fit of the parameters of this model, only 4% of the matter in the universe consists of ordinary baryonic matter, whose ingredients are described by the Standard Model of particle physics. The fraction of cold dark matter (CDM), for which the Standard Model provides no explanation, is measured to be 23 %. The dominant component, the dark energy corresponding to the cosmological constant Λ, is more than 50 orders of magnitude below its natural value if attributed to SM quantum fluctuations alone [12].
- The value of the Higgs boson mass expected from electroweak precision measurements is approximately of the order of 100 GeV (see Section 1.1.1). It is like the

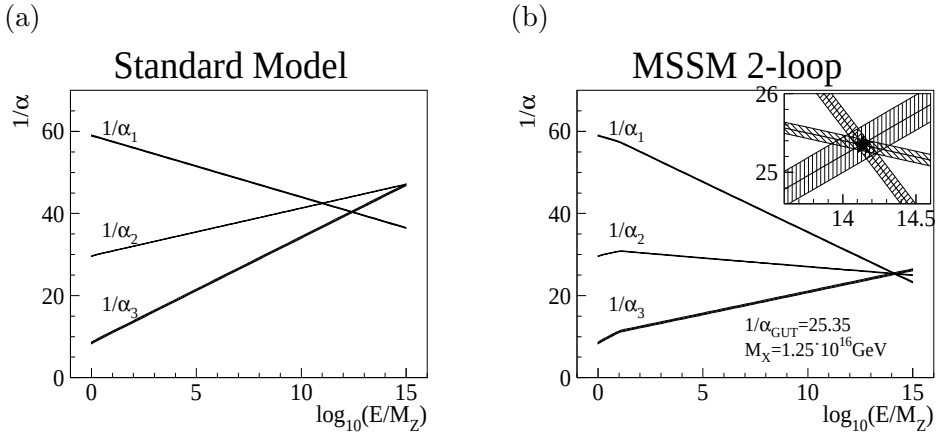

Figure 1.1: Scale dependence of the couplings (a) in the SM and (b) in a SUSY scenario.

other masses at the electroweak scale an effective value resulting from a *bare* Higgs mass and radiative corrections. Assuming the Standard Model to be a valid approximation up to a large energy scale (e.g. up to the Planck scale) the squared Higgs boson mass receives quadratically divergent radiative corrections (see Figure 1.2) at the order of M_P^2 from Standard Model particles and from new particles at larger energy scales which would have to be canceled by fine tuning the squared bare Higgs mass at the order of M_P to an accuracy of 10^{-34} (*fine tuning problem, hierarchy problem* [13, 14]).

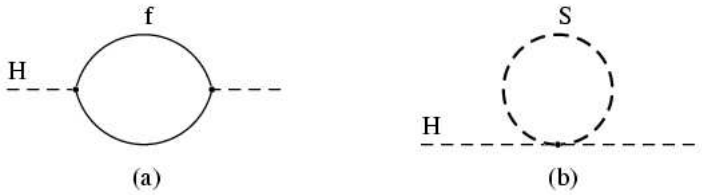

Figure 1.2: Radiative corrections to the Higgs Boson mass (a) from fermions f and (b) from scalars S.

1.2 Supersymmetry

Various extensions of the Standard Model towards higher energies are presently discussed. Supersymmetry (SUSY) [15] is one of the most popular models, providing possible solutions to various topics like the hierarchy problem, the unification of the gauge couplings, quantum gravity and the origin of cold dark matter.

This section starts with a brief introduction and motivation for supersymmetry. The following part presents the theoretical foundations for supersymmetric models. The phenomenological consequences are discussed in case of a minimal extension of the Standard

Model, the Minimal Supersymmetric Standard Model *MSSM*, on which the analysis in this thesis is based. The section finishes with a discussion of the various theoretical and experimental constraints on the parameter space of this model.

1.2.1 Introduction into supersymmetry

Supersymmetry (SUSY) is a symmetry between fermions and bosons. The theory requires the invariance of the Lagrangian under a global supersymmetry transformation.

Since there is no candidate pairs of Standard Model particles with equal quantum numbers except for the Spin, SUSY requires a new partner for each Standard Model field:

- scalar *sfermions* as partners of the SM fermions
- fermionic *higgsinos* as partners for the Higgs bosons
- fermionic *gauginos* for the gauge bosons.

Since the partners have not been found yet, supersymmetry has to be broken and the SUSY particles must be heavier than their SM partners. Provided their masses are in the range $\mathcal{O}$(100 GeV – 1 TeV) and SUSY is broken softly (see Section 1.2.2), the following problems of the SM presented in the last section are addressed by SUSY:

- The quadratic divergent radiative corrections on the mass of the scalar Higgs bosons cancel in a sufficient way because of equal coupling strengths but different signs for fermion and boson correction terms. This stabilizes the Higgs mass at the electroweak scale [13, 14].
- The evolution of the coupling constants is also affected by SUSY contributions and allows the couplings to unify at a common scale of 10^{16} GeV (see Fig.1.1b), which encourages the integration of SUSY in GUT theories [9].
- Local supersymmetry (see Section 1.2.5) leads naturally to the introduction of a graviton field and provides thus the framework for a unified description of gravity and the other fundamental forces. Nevertheless without an extension of the theory (e.g. integration into *string theory* [16]) the theory is not renormalizable.
- SUSY models which preserve R-parity (see Section 1.2.2) lead to a stable Lightest Supersymmetric Particle (LSP) which is a good candidate for CDM.

1.2.2 Theoretical foundations

Minimal supersymmetry is based on an extension of the Poincareé algebra (see Section 1.1.1) by an anti-commuting fermionic generator $\mathrm{Q_a}$, a=1,2 and its conjugate $\bar{Q}_a$, expressed in the following as Weyl spinor. The additional relations are:

$$\{\mathrm{Q_a}, \bar{\mathrm{Q}}_\mathrm{b}\} = 2\sigma^\mu_{\mathrm{ab}}\mathrm{P}_\mu \tag{1.15}$$

$$\left[\mathrm{P}_\mu, \bar{\mathrm{Q}}_\mathrm{a}\right] = 0 \tag{1.16}$$

$$[\mathrm{M}_{\mu\nu}, \mathrm{Q_a}] = -\mathrm{i}\sigma_{\mu\nu}{}^\mathrm{b}_\mathrm{a}\mathrm{Q_b}. \tag{1.17}$$

From the second equation follows, that Q and P^2 commute: SUSY transformations do not change the mass.

A general representation of the SUSY algebra, a *superfield*, can be expressed as a function of the 8-dimensional *superspace* corresponding to space-time extended by two fermionic anti-commuting *Grassman variables* Θ and $\bar{\Theta}$: $\Phi(x, \Theta\bar{\Theta})$. A general infinitesimal SUSY-transformation of a superfield can be written as [14]

$$\delta_{\mathrm{S}}(0, \alpha, \bar{\alpha})\phi(\mathrm{x}, \Theta, \bar{\Theta}) = \left[\alpha\frac{\partial}{\partial\Theta} + \bar{\alpha}\frac{\partial}{\partial\bar{\Theta}} - \mathrm{i}(\alpha\sigma_\mu\bar{\Theta} - \Theta\sigma_\mu\bar{\alpha})\right]\phi(\mathrm{x}, \Theta, \bar{\Theta}) \tag{1.18}$$

with the Grassman variables α, $\bar{\alpha}$, corresponding to the generators

$$\mathrm{Q} = \frac{\partial}{\partial\Theta} - \mathrm{i}\sigma^\mu\bar{\Theta}\partial_\mu \tag{1.19}$$

$$\bar{\mathrm{Q}} = -\frac{\partial}{\partial\bar{\Theta}} + \mathrm{i}\Theta\sigma^\mu\partial_\mu \tag{1.20}$$

with two irreducible representations:

- Vector superfield $\mathbf{V}$
  $\mathbf{V}(\mathrm{x}, \Theta, \bar{\Theta}) = -\Theta\sigma_\mu\bar{\Theta}\mathrm{A}^\mu(\mathrm{x}) + \mathrm{i}\Theta^2\bar{\Theta}\bar{\lambda}(\mathrm{x}) - \mathrm{i}\bar{\Theta}^2\Theta\lambda(\mathrm{x}) + \frac{1}{2}\Theta^2\bar{\Theta}^2\mathrm{D}(\mathrm{x})$
  with the Vector field A_μ (gauge field), the Weyl-Spinor λ (gaugino) and the real scalar D (auxiliary field which does not acquire kinetic terms).
- Chiral superfields $\mathbf{\Phi}_\mathrm{L}$ and $\mathbf{\Phi}_\mathrm{R}$, with
  $\mathbf{\Phi}_\mathrm{L}(\mathrm{x}, \Theta\bar{\Theta}) = \Phi(\mathrm{x}) + \sqrt{2}\Theta\Psi + \Theta^2\mathrm{F} + \mathrm{i}\Theta\sigma^\mu\bar{\Theta}\partial_\mu\Psi - \frac{\mathrm{i}}{\sqrt{2}}\Theta^2\partial_\mu\Psi\sigma^\mu\bar{\Theta} + \frac{1}{4}\Theta^2\bar{\Theta}^2\partial^2\Phi$
  where Φ and Ψ refer to a Higgs boson an the corresponding higgsino or to a sfermion and its partner fermion. $\mathbf{\Phi}_\mathrm{R}$ is the hermitian conjugate of $\mathbf{\Phi}_\mathrm{L}$.

In terms of the scalar and chiral component fields the infinitesimal SUSY transformation $\delta_\mathrm{s}(\alpha, \bar{\alpha})$ can be written as

$$\delta_\mathrm{S}\Phi = \sqrt{2}\alpha\Psi \tag{1.21}$$

$$\delta_\mathrm{S}\Psi = \sqrt{2}\alpha\mathrm{F} + \mathrm{i}\sqrt{2}\sigma^\mu\bar{\alpha}\partial_\mu\Phi \tag{1.22}$$

$$\delta_\mathrm{S}\mathrm{F} = -\mathrm{i}\sqrt{2}\partial_\mu\Psi\partial^\mu\bar{\alpha} \tag{1.23}$$

$$\delta_\mathrm{S}\mathrm{D} = -\alpha\sigma^\mu\partial_\mu\bar{\lambda} + \bar{\alpha}\sigma^\mu\partial_\mu\lambda \tag{1.24}$$

from which follows that SUSY operations indeed transform bosons into fermions and vice versa.

A supersymmetric Lagrangian

A SUSY Lagrangian of free chiral superfields can be written as:

$$\mathcal{L}_{chiral} = \mathcal{L}_{kin} + \mathcal{L}_W = \int d^2\Theta d^2\bar{\Theta}\mathbf{\Phi}_i\mathbf{\Phi}_i^\dagger + \left[\int d^2\Theta W(\mathbf{\Phi}_i) + h.c\right] \tag{1.25}$$

with the superpotential $W(\mathbf{\Phi}) = k_i\mathbf{\Phi}_i + m_{ij}\mathbf{\Phi}_i\mathbf{\Phi}_j + g_{ijk}\mathbf{\Phi}_i\mathbf{\Phi}_j\mathbf{\Phi}_k$, where k, m and g are constants with appropriate mass dimension and the expressions sum over all chiral fields

$\mathbf{\Phi}$. After the expansion of the chiral superfields, $\mathcal{L}_{\rm kin}$ results in the usual kinematic terms for scalar and fermion fields whereas $\mathcal{L}_{\rm W}$ results in Yukawa couplings, scalar interactions and mass terms for fermions and scalars:

$$\mathcal{L}_W = |F|^2 + |\partial_\mu \Phi|^2 - i\bar{\Psi}\sigma_\mu \partial^\mu \Psi - \left[\frac{\partial^2 W}{\partial\Phi_j \partial\Phi_k}\Psi_j \Psi_k + \text{h.c.}\right] - \sum_j \frac{\partial W}{\partial \Phi_j}. \tag{1.26}$$

Gauge interactions are introduced by replacing $\mathcal{L}_{\rm kin}$ by

$$\begin{aligned} \mathcal{L}_{kin} &= \int d^2\Theta d^2\bar{\Theta}\mathbf{\Phi}^\dagger e^{2gV}\mathbf{\Phi} \\ &= |D_\mu \Phi|^2 - i\bar{\Psi}\sigma_\mu D^\mu \Psi + g\Phi^* D\Phi + ig\sqrt{2}(\Phi^*\lambda\Psi - \bar{\lambda}\bar{\Psi}\Phi) + |F|^2 \end{aligned} \tag{1.27}$$

with the covariant derivative $D_\mu = \partial_\mu + igA^\alpha_\mu T_\alpha$. In addition to the usual interactions of matter fields with gauge fields, this procedure yields gauge strength Yukawa interactions between matter fermions, sfermions and gauginos and between higgsinos, Higgs bosons and gauginos ($\Phi\lambda\Psi$ terms).

$\mathcal{L}_{\rm kin}$ has to be extended by the kinetic term for the gauge fields, constructed with $W_\alpha = \frac{1}{4g}\bar{D}^2 e^{-gV} D_\alpha e^{gV}$, an analogue of the field strength tensor:

$$\begin{aligned} \mathcal{L}_{gauge} &= \frac{1}{2} W_\alpha W^\alpha \\ &= -\frac{1}{4} V^\alpha_{\mu\nu} V^{\mu\nu}_\alpha + \frac{1}{2} D_\alpha D^\alpha + \left[\frac{1}{2} g f^{abc} \lambda_\alpha \sigma_\mu A^\mu_b \bar{\lambda}_c - \frac{i}{2}\lambda^\alpha \sigma_\mu \sigma^\mu \bar{\lambda}_\alpha + \text{h.c.}\right] \end{aligned} \tag{1.28}$$

with the corresponding group structure constants f^{abc} which renders in addition to the kinetic energy of the gauge fields the kinetic terms for the gauginos and the canonical coupling of the gauginos to the gauge fields. The contribution of the auxiliary field D can be integrated out and yields additional scalar interactions: $-V_D = -\frac{1}{2}\sum_\alpha |g\Phi_i^* T^\alpha_{ij}\Phi_j|^2$ The complete supersymmetric Lagrangian is then:

$$\begin{aligned} \mathcal{L}_{SUSY} &= \mathcal{L}_{kin} + \mathcal{L}_W \\ &= |D_\mu \Phi|^2 - i\bar{\Psi}\alpha_\mu D^\mu \Psi + ig\sqrt{2}(\Phi^*\lambda\Psi - \bar{\lambda}\bar{\Psi}\Phi + |F|^2 - \frac{1}{4} V^\alpha_{\mu\nu} V^{\mu\nu}_\alpha \\ &\quad + \left[\frac{1}{2} g f^{abc} \lambda_\alpha \sigma_\mu A^\mu_b \bar{\lambda}_c - \frac{i}{2}\lambda^\alpha \sigma_\mu \sigma^\mu \bar{\lambda}_\alpha + \text{h.c.}\right] \\ &\quad - \frac{1}{2}\sum_\alpha |g\Phi_i^* T^\alpha_{ij}\Phi_j|^2 - \left[\frac{\partial^2 W}{\partial\Phi_j \partial\Phi_k}\Psi_j \Psi_k + \text{h.c.}\right] - \sum \frac{\partial W}{\partial \Phi_j}. \end{aligned} \tag{1.29}$$

R-parity

$\mathcal{L}_W$ contains also Baryon and Lepton number violating terms. In minimal models they are expelled by imposing an additional Symmetry requirement on the Lagrangian, the R-parity:

$$R = (-1)^{3(B-L)+2S}. \tag{1.30}$$

SM particles and SUSY particles are eigenstates of R with eigenvalues +1 and -1 respectively. Imposing R-parity conservation yields the following features:

- SUSY particles are created in pairs
- A SUSY particle decays into an uneven number of SUSY particles
- The lightest SUSY particle is stable and provides a candidate for dark matter.

R-parity violation is not ruled out experimentally and searches are performed also for topologies predicted by R-parity violating SUSY [17]. This analysis, though, focuses on R-parity conserving (RPC) scenarios.

SUSY breaking

Since SUSY particles with the masses of their Standard Model partners have not been found, SUSY must be broken at the electroweak scale. There are several theoretical models that describe the mechanism of SUSY breaking [9] with varying degrees of predictability. The most general approach is to parameterize the effect of SUSY breaking by inserting all possible *soft breaking terms* into the Lagrangian, which do not destroy the cancellation of quadratic divergences in the corrections to the Higgs boson mass, one of the main motivations for supersymmetry (see Section 1.2.1), and which do not disturb the renormalizability of the theory [9]. They consist of:

- scalar mass terms $-m^2_{\Phi_i}|\Phi_i|^2$
- trilinear scalar interactions $-(A_{ijk}\Phi_i\Phi_j\Phi_k + \text{h.c.})$
- gaugino mass terms $-\frac{1}{2}M_k\bar{\lambda}_k\lambda_k$
- bilinear terms $-(B_{ij}\Phi_i\Phi_j + \text{h.c.})$
- linear terms $-C_i\Phi_i$.

The total effective Lagrangian at the electroweak scale becomes then: $\mathcal{L} = \mathcal{L}_{SUSY} + \mathcal{L}_{soft}$.

1.2.3 The MSSM

The results of the previous section are derived for a general supersymmetric model. The following sections are based on an extension of the Standard Model with minimal particle content, the Minimal Supersymmetric Standard Model (MSSM). In what follows, only models are considered, which preserve R-parity (RPC Supersymmetry).

The minimal R-parity conserving supersymmetric Lagrangian $\mathcal{L}_{SUSY}$ is completely determined by the parameters of a Standard Model with two Higgs doublets. All additional parameters are introduced in the parameterization of the SUSY breaking due to our lack of knowledge of the exact mechanism and the starting conditions in $\mathcal{L}_{soft}$. The aim of the following section is to derive an effective low-energy theory which results in phenomenological predictions.

Table 1.2 gives an overview over the MSSM superfields and their physical field content.

Chiral superfields $\mathbf{\Phi}$		Spin $\frac{1}{2}(\Psi)$		Spin $0\,(\Phi)$	
Lepton	L	(ν_e, e_L)		$(\tilde{\nu}_e, \tilde{\mathrm{e}}_\mathrm{L})$	sneutrino, left-handed slepton
	E	$(e_R^\dagger)$		$(\tilde{\mathrm{e}}_\mathrm{R}^*)$	right-handed slepton
Quark	Q	(u_L, d_L)		$(\tilde{u}_L, \tilde{d}_L)$	left-handed squark
	U	$u_R^\dagger$		$\tilde{u}_R^*$	right-handed squark
	D	$d_R^\dagger$		$\tilde{d}_R^*$	right-handed squark
Higgs	H_1	$(\tilde{H}_1^0, \tilde{H}_1^-)$	higgsino	(H_1^0, H_1^-)	
	H_2	$(\tilde{H}_2^+, \tilde{H}_2^0)$	higgsino	(H_2^+, H_2^0)	
Vector superfields $\mathbf{V}$		Spin 1 (V)		Spin $\frac{1}{2}$ (λ)	
U(1)	$\hat{B}$	B		$\tilde{B}$	bino
SU(2)	$\hat{W}$	W_1, W_2, W_3		$\tilde{W}_1, \tilde{W}_2, \tilde{W}_3,$	wino
SU(3)	$\hat{G}$	$g_1 \ldots g_8$		$\tilde{g_1} \ldots \tilde{g_8}$	gluino

Table 1.2: The superfields in the MSSM. Only one generation of the chiral lepton and quark fields is presented.

The most general R-parity conserving potential with these fields can be written as:

$$W_{RPC} = \epsilon_{kl}\left[U\mathbf{y}_u Q^k H_2^l - D\mathbf{y}_d Q^k H_1^l - E\mathbf{y}_e L^k H_1^l + \mu H_1^k H_2^l\right] \tag{1.31}$$

with the indices k and l of the SU(2)-doublets, the Higgs(ino) mass parameter μ and the 3×3 Yukawa matrices in generation space. The supersymmetric Lagrangian $\mathcal{L}_{\mathrm{SUSY}}$ follows then directly from Eqn. 1.29 by inserting the MSSM fields and the superpotential.

A general soft SUSY–breaking Lagrangian $\mathcal{L}_{\mathrm{soft}}$ can be written as

$$\begin{aligned}
\mathcal{L}_{soft} = \; & -\; \frac{1}{2}(M_1\tilde{B}\tilde{B} + M_2\tilde{W}_i\tilde{W}_i + M_3\tilde{g_j}\tilde{g_j}) + \text{h.c.} \\
& -\; \tilde{Q}^\dagger \mathbf{m}_Q^2 \tilde{Q} - \tilde{L}^\dagger \mathbf{m}_L^2 \tilde{L} - \tilde{U}^\dagger \mathbf{m}_u^2 \tilde{U} - \tilde{D}^\dagger \mathbf{m}_d^2 \tilde{D} - \tilde{E}^\dagger \mathbf{m}_e^2 \tilde{E} \\
& -\; m_{H1}^2 |H_1|^2 - m_{H2}^2 |H_2| m^2 - (m_{12}^2 \epsilon_{kl} H_1^k H_2^l + \text{h.c.}) \\
& -\; \epsilon_{kl}\left(\mathbf{a}_d H_1^k \tilde{q}_L^l \tilde{d}_R^* + \mathbf{a}_u H_2^k \tilde{q}_L^l \tilde{u}_R^* + \mathbf{a}_e H_1^k \tilde{l}_L^l \tilde{e}_R^*\right) + \text{h.c.}
\end{aligned} \tag{1.32}$$

with the 3×3 mass matrices $\mathbf{m}_Q \ldots \mathbf{m}_e$ for the sfermions in generation space, the 3×3 matrices $\mathbf{a}_e, \mathbf{a}_u$ and $\mathbf{a}_d$ in generation space, the bilinear coupling m_{12}, the Higgs mass parameters m_{H1} and m_{H2}, the mass parameters M_1, M_2 and M_3 for Binos, Winos and gluinos and the SU(2) indices k and l.

The Higgs Sector and electroweak symmetry breaking

In order to avoid gauge anomalies, connected to a non-vanishing trace of the hypercharge generator, to ensure optimal reduction of the radiative corrections to the mass of the (lightest) Higgs boson and to ensure mass terms for up-type and down-type fermions after EWSB, a second Higgs field with opposite sign of the hypercharge Y has to be introduced in minimal SUSY.

In unbroken minimal SUSY, the part of the scalar Higgs potential that is relevant in the potential minimum is given by:

$$W_H = \mu^2(H_1^2 + H_2^2) + \frac{1}{8}(g_1^2 + g_2^2)(H_1^{0\,2} - H_2^{0\,2})^2. \tag{1.33}$$

Since $W \geq 0$ ($W = 0 \Leftrightarrow H_1 = H_2 = 0$) no EWSB takes place. This changes after SUSY breaking, which introduces additional mass terms m_{H1} and m_{H2} and the bilinear coupling m_{12}:

$$W_H = m_1^2 H_1^2 + m_2^2 H_2^2 + \left[m_{12}^2 H_1 H_2 + \text{h.c.}\right] + \frac{1}{8}(g_1^2 + g_2^2)(H_1^{0\,2} - H_2^{0\,2})^2 \tag{1.34}$$

with $m_1^2 = m_{H1}^2 + \mu^2$, $m_2^2 = m_{H2}^2 + \mu^2$. For $m_1^2 + m_2^2 \geq 2|m_{12}^2|$ and $m_1^2 m_2^2 < m_{12}^4$ the potential has a SM-like shape and is minimal (without loss of generality) for $H_1 = \binom{\nu_1}{0}$ and $H_2 = \binom{0}{\nu_2}$, with ν_1 and ν_2 related by the well measured Z mass M_Z

$$\frac{1}{2}(g_1^2 + g_2^2)(\nu_1^2 + \nu_2^2) = M_\text{Z}^2 \tag{1.35}$$

such that they can be expressed in terms of $\tan\beta = \frac{\nu_2}{\nu_1}$. The MSSM Higgs sector is thus defined by 5 parameters: m_{H1}^2, m_{H2}^2, $m_{1,2}^2$, $\tan\beta$ and μ. Requiring the Higgs potential to have a non-trivial minimum removes two degrees of freedom:

$$\begin{aligned} m_{12}^2 &= \frac{-\sin(2\beta)}{2}\left[\frac{1}{\cos(2\beta)}(m_{H2}^2 - m_{H1}^2) - M_\text{Z}^2\right] \\ \mu^2 &= \frac{1}{\cos(2\beta)}(m_{H2}^2 \sin^2\beta - m_{H1}^2 \cos^2\beta) - \frac{1}{2}M_\text{Z}^2. \end{aligned} \tag{1.36}$$

In GUT models, M_{H1} and M_{H2} are effective values derived by radiative corrections from Higgs masses at GUT scale (*radiative electroweak symmetry breaking*).

The Higgs mass spectrum is determined by only two of the remaining parameters, for example the mass of the pseudoscalar Higgs boson M_A and $\tan\beta$. The masses of the Higgs bosons are given at leading order (LO) by.

$$M_\text{A}^2 = \frac{-2m_{12}^2}{\sin(2\beta)} \tag{1.37}$$

$$M_{\text{H,h}}^2 = \frac{1}{2}\left[M_\text{A}^2 + M_\text{Z}^2 \pm \sqrt{(M_\text{A}^2 + M_\text{Z}^2)^2 - 4M_\text{A}^2 M_\text{Z}^2 \cos^2(2\beta)}\right] \tag{1.38}$$

$$M_{\text{H}^\pm}^2 = M_\text{A}^2 + M_\text{W}^2. \tag{1.39}$$

The LO Higgs masses receive radiative corrections of both SM particles and SUSY particles. The dominant contribution comes from top-stop loops and increases with the stop

masses and with the top mass. In leading logarithmic approximation the correction can be expressed by [14]:

$$\Delta M_{\mathrm{h}}^2 \approx \frac{3{m_t}^4}{32\pi^2 \sin^2\beta M_W^2} ln \frac{m_{\tilde{\mathrm{t}}_1} m_{\tilde{\mathrm{t}}_2}}{{m_t}^2}. \tag{1.40}$$

At higher orders of perturbation theory (2-loop level) this leads to an upper limit on the mass of the lightest Higgs boson: $m_h \lesssim 135(140)\,\mathrm{GeV}$ for top masses of 175(180) GeV and SUSY masses of 1 TeV [18].

The phenomenological MSSM

The SUSY–breaking terms introduce more than 100 additional free parameters into the Lagrangian. The number can be reduced by a set of assumptions, which are a consequence of experimental constraints [13]:

- Large off-diagonal elements in the slepton mass matrices and in the trilinear sfermion-Higgs matrices would lead to FCNC effects in interactions of Standard Model particles via loop diagrams with SUSY particles. The strong upper limits on these effects constrain the off-diagonal elements in the corresponding matrices severely. The most prominent examples are the strong limits on additional contributions of squark-gluino loops to the $\mathrm{K}^0 - \bar{\mathrm{K}}^0$ mixing and the contribution of smuon-selectron loops to the BR($\mu \to \mathrm{e}\gamma$) with the strong upper limit of 1.2×10^{-11} [8]. In addition, the $\mathrm{K}^0 - \bar{\mathrm{K}}^0$ results limit severely the splitting between the masses of the first and the second generation squarks.
- The SUSY theory should observe the measured amount of CP violation, which constrains the amount of inter-generation mixing in the squark mass matrices and the trilinear squark-Higgs couplings. Additional contributions to CP violation could come from complex phases in the mass matrices and the trilinear sfermion-Higgs couplings

These constraints are fulfilled most easily [13] if the soft SUSY–breaking parameters are real, the mass matrices are diagonal, the masses of the first two sfermion generations are degenerate and the trilinear couplings are proportional to the Yukawa couplings ($\mathbf{a}_f = A_f \cdot \mathbf{y_f}$). With these assumptions, the SUSY parameter space is reduced to 22 degrees of freedom:

- 3 gaugino masses M_1, M_2 and M_3
- 5 sfermion masses $m_{\tilde{\mathrm{e}}_\mathrm{R}}$, $m_{\tilde{\mathrm{e}}_\mathrm{L}}$, $m_{\tilde{\mathrm{d}}_\mathrm{R}}$, $m_{\tilde{\mathrm{u}}_\mathrm{R}}$, $m_{\tilde{\mathrm{q}}_\mathrm{L}}$ of the 1st and 2nd generation
- 5 sfermion masses $m_{\tilde{\tau}_\mathrm{R}}$, $m_{\tilde{\tau}_\mathrm{L}}$, $m_{\tilde{\mathrm{b}}_\mathrm{R}}$, $m_{\tilde{\mathrm{t}}_\mathrm{R}}$, $m_{\tilde{\mathrm{q}^3}_\mathrm{L}}$ of the 3rd generation
- 6 trilinear couplings A_u, A_d, A_e, A_t, A_b, A_τ
- the mass of the pseudoscalar Higgs boson M_A
- the ratio of the Higgs vacuum expectation values $\tan\beta$
- the Higgs mass parameter μ.

This model or similar versions are often referred to as *phenomenological MSSM* [19].

The masses of the SUSY particles

After SUSY breaking and, as a consequence, electroweak symmetry breaking, the SUSY particles acquire masses which are a combination of direct mass terms in the SUSY–breaking Lagrangian and of scalar and fermion couplings to one of the two Higgs fields. Fields with different $\mathrm{SU(2)_L} \times \mathrm{U(1)_Y}$ quantum numbers can mix if they have the same quantum numbers of the remaining symmetries $\mathrm{SU(3)_C} \times \mathrm{U(1)_{EM}}$.

The 2×2 sfermion mass matrices in the base of the SU(2) eigenstates in case of the first generation are :

$$M^2_{\tilde{u},LR} = \begin{pmatrix} m_Q^2 + m_u^2 + (\frac{1}{2} - \frac{2}{3}s_w^2)Z_\beta^2 & m_u(A_u - \mu\cot\beta) \\ m_u(A_u - \mu\cot\beta) & m_U^2 + m_u^2 + \frac{2}{3}s_w^2 Z_\beta^2 \end{pmatrix} \tag{1.41}$$

$$M^2_{\tilde{d},LR} = \begin{pmatrix} m_Q^2 + m_d^2 + (-\frac{1}{2} - \frac{1}{3}s_w^2)Z_\beta^2 & m_d(A_d - \mu\tan\beta) \\ m_d(A_d - \mu\tan\beta) & m_D^2 + m_d^2 - \frac{1}{3}s_w^2 Z_\beta^2 \end{pmatrix} \tag{1.42}$$

$$M^2_{\tilde{e},LR} = \begin{pmatrix} m_L^2 + m_e^2 - (\frac{1}{2} - s_w^2)Z_\beta^2 & m_e(A_e - \mu\tan\beta) \\ m_e(A_e - \mu\tan\beta) & m_E^2 + m_e^2 - s_w^2 Z_\beta^2 \end{pmatrix} \tag{1.43}$$

with the abbreviations s_W^2 for $\sin^2\theta_W$ and Z_β^2 for $M_Z^2\cos 2\beta$. The parameters m_L^2, m_E^2 etc. are the explicit mass terms in the soft SUSY-breaking Lagrangian $\mathcal{L}_{Soft}$. The other terms are a consequence of the coupling to a Higgs field in $\mathcal{L}_{SUSY}$ or in $\mathcal{L}_{Soft}$. Since the off-diagonal elements are proportional to the masses of the SM partners, they can be neglected in the first two generations.

In the present MSSM, sneutrinos have only left handed fields:

$$M_{\tilde{\nu}}^2 = m_L^2 + c_w^2 Z_\beta^2. \tag{1.44}$$

Neutral higgsinos and gauginos mix to *neutralino* mass eigenstates, due to Higgs-higgsino-gaugino couplings in the basic SUSY Lagrangian ($\Phi\lambda\Psi$ terms, see Eqn. 1.27). Equation 1.45 shows the neutralino mass matrix in the base ($\tilde{B}$, $\tilde{W}^3$, $\tilde{H}_1^0$, $\tilde{H}_2^0$).

$$M_{\chi^0} = \begin{pmatrix} M_1 & 0 & -c_\beta s_w M_Z & +s_\beta s_w M_Z \\ 0 & M_2 & +c_\beta c_w M_Z & -s_\beta c_w M_Z \\ -c_\beta s_w M_Z & +c_\beta c_w M_Z & 0 & -\mu \\ +s_\beta s_w M_Z & -s_\beta c_w M_Z & -\mu & 0 \end{pmatrix} \tag{1.45}$$

with the abbreviations $s_\beta = \sin\beta, c_\beta = \cos\beta$, $s_W = \sin\theta_W$, and $c_W = \cos\theta_W$.

Diagonalization yields mass eigenstates and mass eigenvalues (see e.g. [20]), which are not presented here for lack of space. Neutralino masses for selected parameter combinations are given in Section 9.

Charged gauginos and higgsinos mix to *chargino* mass eigenstates. Equation 1.46 shows the chargino mass matrix in the $(\tilde{W^+}, \tilde{H_2^+}, \tilde{W^-}, \tilde{H_1^-})$ base:

$$M_{\chi^\pm} = \begin{pmatrix} 0 & X^T \\ X & 0 \end{pmatrix} \quad \text{with } X = \begin{pmatrix} M_2 & \sqrt{2}s_\beta M_W \\ \sqrt{2}c_\beta M_W & \mu \end{pmatrix}. \tag{1.46}$$

The chargino masses follow by diagonalizing:

$$m^2_{\tilde{\chi}^{\pm}_{1,2}} = \frac{1}{2}\Big[\,|M_2|^2 + |\mu|^2 + 2\,M_W^2 \mp \sqrt{(\,|M_2|^2 + |\mu|^2 + 2\,M_W^2\,)^2 - 4\,|\,\mu M_2 - M_W^2 \sin(2\beta)|^2}\,\Big]. \quad (1.47)$$

If the Higgs mass parameter μ is larger than the gaugino mass parameters M_i, the field contents of the lightest neutralinos are dominated by wino and bino components. The lightest chargino is also dominantly a wino. This region is called the *gaugino region*. The lightest neutralinos and the lightest chargino are then referred to as *gauginos*. The opposite case ($\mu << M_i$), where the lightest neutralinos are dominantly higgsinos, is called the *higgsino region*.

1.2.4 Integration into GUT theories: constraint MSSM

The assumptions done in section 1.2.3, motivated by experimental constraints on FCNC and CP violation, have reduced the SUSY parameter space considerably. A further simplification of the model is achieved by embedding the SUSY model in a GUT framework.

Regarding the MSSM as a low-energy effective theory of a more fundamental symmetry at a large energy scale (GUT scale) as implied by the apparent unification of the gauge couplings at the order 10^{16}GeV (see Fig.1.1), leads to simplifications of the soft SUSY–breaking terms, which comply with the phenomenological constraints mentioned in Section 1.2.3. The resulting MSSM model is called *constraint MSSM* (*cMSSM*). Apart from the unification of the couplings at the GUT scale the following assumptions are done:

- common gaugino mass $m_{1/2} = M_1 = M_2 = M_3$
- common sfermion mass $m_0^2 * \mathbf{1} = \mathbf{m}_Q^2 = \mathbf{m}_U^2 = \mathbf{m}_D^2 = \mathbf{m}_L^2 = \mathbf{m}_E^2$.

Further simplification is achieved by deriving also the trilinear couplings from a common GUT value and/or unify the Higgs masses with the other scalar masses at GUT scale.

- common scalar mass $m_0^2 = m_{H1}^2 = m_{H2}^2$
- common trilinear coupling $A_0 = A_t = A_b = A_\tau = A_u = A_d = A_e$.

These assumptions lead to very predictive models. The masses and couplings at the electroweak scale are effective values which are a consequence of radiative corrections from other particles (see renormalization in Section 1.1.1) and given by the *renormalization group equations*. Figure 1.3 gives an example for the running of the soft SUSY–breaking parameters from the GUT scale to the electroweak scale [21]. In various phenomenological studies, selected GUT conditions are relaxed in order to provide more model-independent statements or in order to select reference or benchmark scenarios.

If m_{H1} and m_{H2} are derived from a common scalar mass m_0 at GUT scale, Equations 1.36 can be used to calculate M_A^2 and μ^2 as a function of $\tan\beta$ and m_0 leaving only the sign of μ free, once $\tan\beta$ and m_0 are chosen.

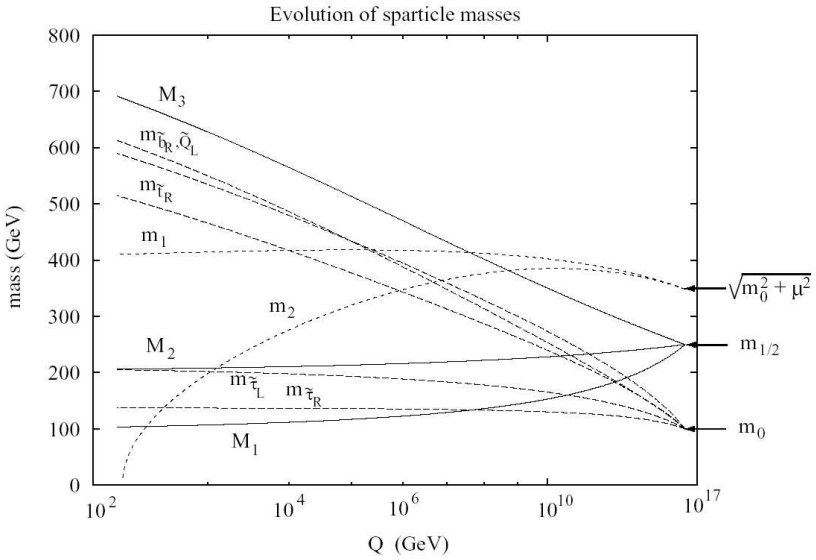

Figure 1.3: Renormalization group running of mass parameters from the GUT scale to the electroweak scale (from Ref. [21])

1.2.5 MSUGRA Grand Unification

Many of the assumptions, which lead to the simplifications of the SUSY model in the previous chapters can be derived by supergravity *SUGRA* [22], a locally supersymmetric model which is usually in addition constrained by an unspecified higher GUT symmetry at GUT scale. As in the case of the MSSM, only minimal models are considered in this section (*minimal Supergravity mSUGRA*). Not discussed here are the competing models for supersymmetry breaking: *Gauge Mediated Supersymmetry Breaking*, *Anomalous U(1)-Mediated Supersymmetry Breaking* and *Conformal Anomaly-Mediated Supersymmetry breaking* [9].

Supergravity is based on the invariance of the action under local supersymmetry, with the parameters α, $\bar{\alpha}$ from Eqn. 1.18 now becoming a function of space-time: $\alpha = \alpha(\mathrm{x})$. The variation of the locally SUSY-transformed action acquires additional terms due to the space-time derivatives of $\alpha(\mathrm{x})$, which have to be canceled in the canonical way by including a new gauge field with suitable transformation properties, the spin $\frac{3}{2}$ field *gravitino*, which forms part of a new superfield together with its spin-2 partner, the *graviton*. This way, gravity is introduced as a consequence of local supersymmetry.

MSUGRA also yields one of the most promising SUSY–breaking scenarios. SUSY is broken by at least one auxiliary component of a chiral superfield which belongs to a set of *hidden sector* fields that interact with the MSSM fields only by gravity. When one or more of the components acquire non-vanishing vacuum expectation values at the minimum of the scalar potential, the interaction with the fermionic component of the hidden sector field yields a mass term for the gravitino, most probably at the MSSM scale (*super Higgs effect*). Gravity scale interactions (*messenger*) with the components of the hidden superfields also yield the soft SUSY–breaking terms in Section 1.2.2 after SUSY is broken by the vacuum.

Imposing a higher GUT symmetry on the SUGRA potential reduces the SUSY degrees of

freedom to four continuous and one discrete parameter, commonly chosen as

- the ratio of the vacuum expectation values of the Higgs fields $\tan\beta$
- the common gaugino mass at GUT scale $m_{1/2}$
- the common scalar mass at GUT scale m_0
- the common trilinear coupling at GUT scale A_0
- the sign of the Higgs parameter μ.

Masses at the MSSM scale are again derived by renormalization group running from the GUT scale down to the MSSM scale. Over most of the model parameter space μ^2 is large (gaugino region) with the approximate relation

$$2m_{\chi_1^0} \approx m_{\chi_2^0} \approx m_{\chi_1^\pm} \approx \frac{1}{3} m_{\tilde{g}}. \tag{1.48}$$

MSUGRA has the advantage that it naturally appears as a low-energy effective scenario of string theories, after compactification of the extra dimensions [16, 23], which are currently the best candidate for a renormalizable fundamental theory.

1.2.6 Experimental constraints on SUSY

SUSY was proposed in the 70s of the last century and became popular when the stabilizing effect on the Higgs mass was recognized. Since then, many experiments have been searching for the new particles themselves or for indirect effects via radiative corrections and gravitational influence. In order to provide the effects presented as the core motivation for SUSY in Section 1.2.1, SUSY masses are desired to be in the range of $M \leq \mathcal{O}(1\text{ TeV})$. SUSY masses in this range are also preferred by present experimental evidence, as will be shown in this section.

Direct searches for MSSM particles

Searches for supersymmetric particles have been performed in e^+e^- collisions at LEP [24] and in $p\bar{p}$ collisions at D0 [25] and CDF [26]. No evidence for these particles has been found so far.

Direct searches at LEP II for the pair production of supersymmetric particles have resulted in lower limits on the masses of these particles, typically near the kinematic production threshold. The mass limits are then interpreted within a specific SUSY model on order to constrain the parameter space of the model. Figure 1.4a shows the part of the $m_{\tilde{\ell}_R}$-$m_{\chi_1^0}$ plane which is excluded by direct searches of the four LEP experiments. Selectron/smuon/stau masses lower than 99/94/86 GeV can be excluded for large slepton–LSP mass differences [27]. For low mass differences, selectron masses below 77(73) GeV are excluded by LEP in constrained MSSM models with negligible mixing with (without) Higgs searches for $M_{top} = 175\,\text{GeV}$ [28]. Figure 1.4b shows the lower limit on the mass of the lightest chargino as a function of the sneutrino mass. For large slepton/sneutrino masses,

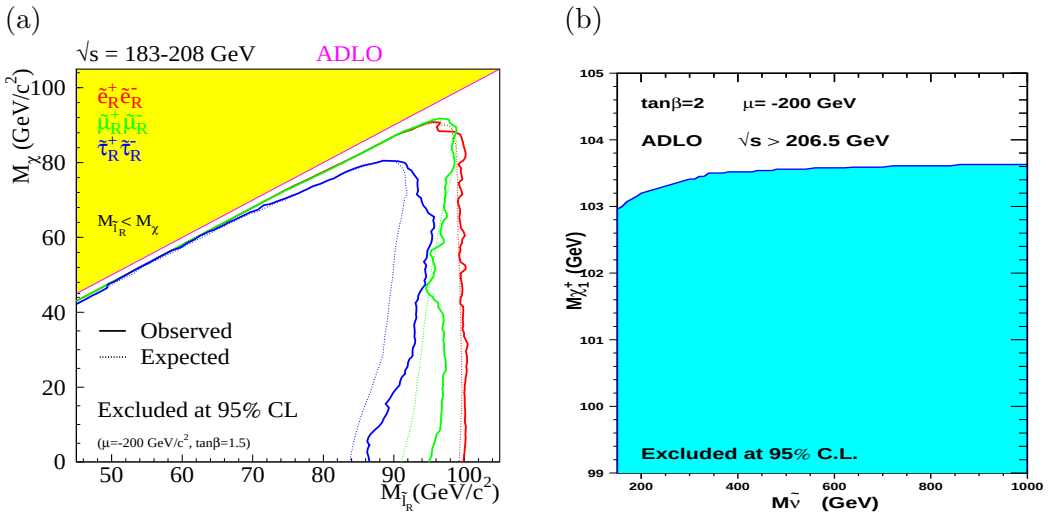

Figure 1.4: LEP combined lower limits in a constraint MSSM (a) on the slepton masses as a function of the mass of the lightest neutralino and (b) on the chargino mass as a function of the sneutrino mass.

chargino masses are excluded nearly up to the kinematic production threshold of 104 GeV at LEP [29] by direct searches.

Indirect evidence can be derived from the Higgs boson searches reinterpreted as the search for the lightest CP-even Higgs boson [30], which constrain the stop mass parameters due to the large impact of the stop loop corrections on the Higgs mass. As a consequence, the impact of the Higgs boson searches on the parameter space of a particular SUSY model depends strongly on the connection of the stop mass parameters to the other SUSY parameters. In mSUGRA models and constraint models with gaugino and scalar mass unification, the Higgs boson searches typically yield lower limits on $m_{1/2}$ as a function of m_0 and the degree of stop mixing ($A_t - \mu \cot\beta$, see Eqn. 1.43). Due to the strong dependence of the radiative corrections on the top quark mass, the impact of the Higgs searches is affected by the progress in the top mass measurement. The current world average of the top mass is $m_{\text{top}} = 174.3 \pm 3.4\,\text{GeV}$ [7]. In studies of the impact of the Higgs searches, m_{top} is usually varied in the range of $175\,\text{GeV} < m_{\text{top}} < 180\,\text{GeV}$.

Figure 1.5a shows the m_0–$m_{1/2}$ domain excluded by a combination of the results of the searches for charginos, sleptons and the Higgs boson within mSUGRA for $\tan\beta$=10, μ>0 and A_0=0. For large enough values of m_0, chargino searches exclude $m_{1/2}$ values up to 160 GeV. For low m_0, charginos decay invisibly into sneutrinos and the slepton searches fill the gap. Including the results from the Higgs boson searches extends the excluded $m_{1/2}$ domain up to nearly 300 GeV for modest values of m_0. Figure 1.5b shows the strong dependence of the impact of the Higgs mass limits on the trilinear coupling A_0 for a certain choice of $\tan\beta$ and μ. For $\tan\beta = 10$, typically values of $m_{1/2} < 180 - 250\,\text{GeV}$ are excluded for $100\,\text{GeV} < m_0 < 200\,\text{GeV}$ for any value of A_0 and $m_{\text{top}} = 175$ GeV [31]. The combination of the results of the searches for charginos, sleptons and Higgs bosons within a particular SUSY model leads also to a lower limit on the mass of the LSP in the corresponding model. Figure 1.6a shows the LSP mass domains excluded within a constraint MSSM for negligible mixing in the stau sector and $m_{\text{top}} = 178\,\text{GeV}$ as a func-

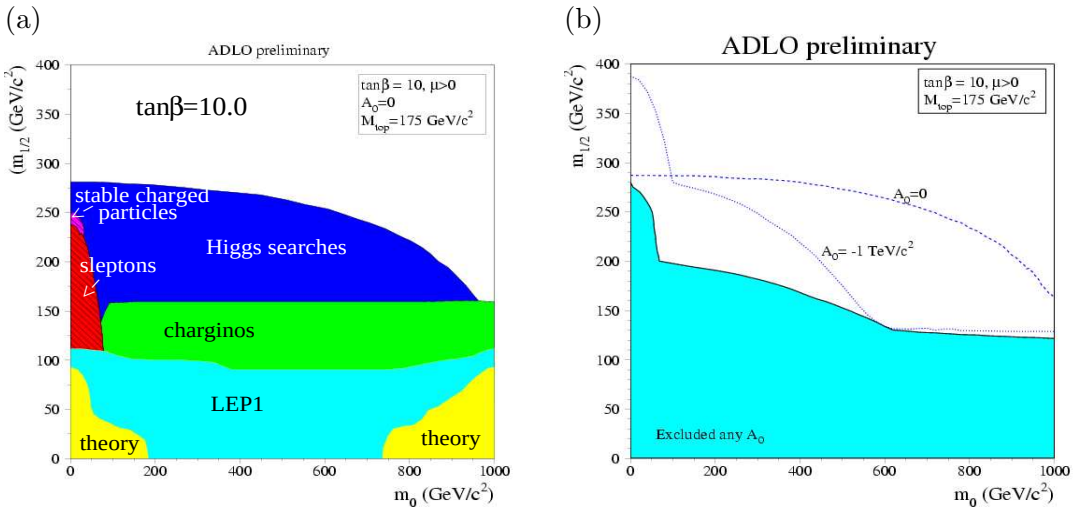

Figure 1.5: Region excluded in the mSUGRA $m_{1/2}$-m_0 plane by the combined results of the searches for charginos, sleptons and Higgs bosons at the four LEP experiments [31] for $\tan\beta$=10, $\mu > 0$ and $m_{top} = 175$ GeV (a) for A_0=0 and (b) for A_0=0, A_0=-1 TeV and for any A_0.

tion of $\tan\beta$ [32]. The overall limit is set by the slepton searches for large values of $\tan\beta$. For intermediate values of $\tan\beta$, the chargino searches set the limit. The Higgs searches contribute for small values of $\tan\beta$. LSP masses below 47 GeV are excluded within this framework. A lower limit of 42 GeV is obtained for any mixing in the stau sector [33]. Figure 1.6b shows the lower limit on the LSP mass derived within the mSUGRA model by the LEP experiments [31]. The LSP lower mass limit is found at 51 GeV for $m_{\text{top}} = 175\,\text{GeV}$, any value of $\tan\beta$ and any value of A_0.

The Tevatron experiments have been searching for SUSY in squark and gluino production and in associated chargino-neutralino production in leptonic final states which has resulted in the world most stringent limits on the chargino mass for a short while until LEP II has ruled out a larger mass region. Figure 1.7 shows the DØ [25] and CDF [26] 95% CL limits on the $\sigma_{\text{Prod}} \times \text{BR}$ into a specific subset of trilepton final states.

Indirect evidence from collider precision measurements

If SUSY exists, it is expected to influence the effective values of Standard Model parameters via radiative corrections. Hence the precise measurement of these values constrains the allowed SUSY parameter space.

- Measurement of muon g-2

  The anomalous magnetic moment of the muon $\alpha_\mu = \frac{1}{2}(g-2)_\mu$ receives radiative corrections from Standard Model and from SUSY particles. Figure 1.8a shows a subset of Feynman diagrams relevant for the SM calculation of $(g-2)_\mu$ [35]. Figure 1.8b shows the one and two-loop SUSY corrections for $(g-2)_\mu$ [35, 36] from SUSY particles. They yield the following approximate contributions to α_μ if all SUSY mass

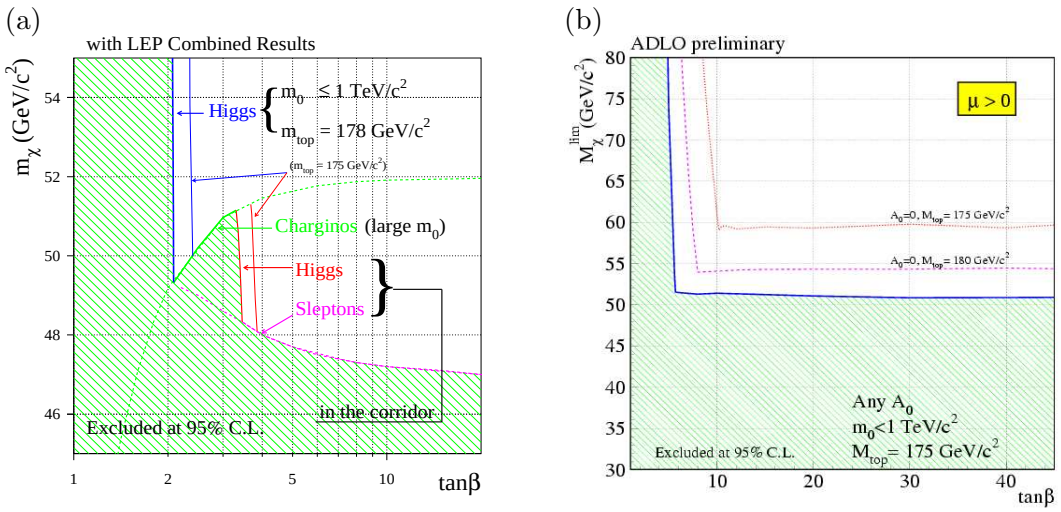

Figure 1.6: LEP combined lower limit on the LSP mass resulting from a combination of the search for sleptons, charginos and Higgs bosons as a function of $\tan\beta$ (a) in a constraint MSSM model with negligible stau mixing for a top mass of 178 GeV (b) in mSUGRA for $\mu > 0$, $m_0 < 1$ TeV, A_0=0 and top masses of 175 GeV and 180 GeV and for any A_0 and a top mass of 175 GeV.

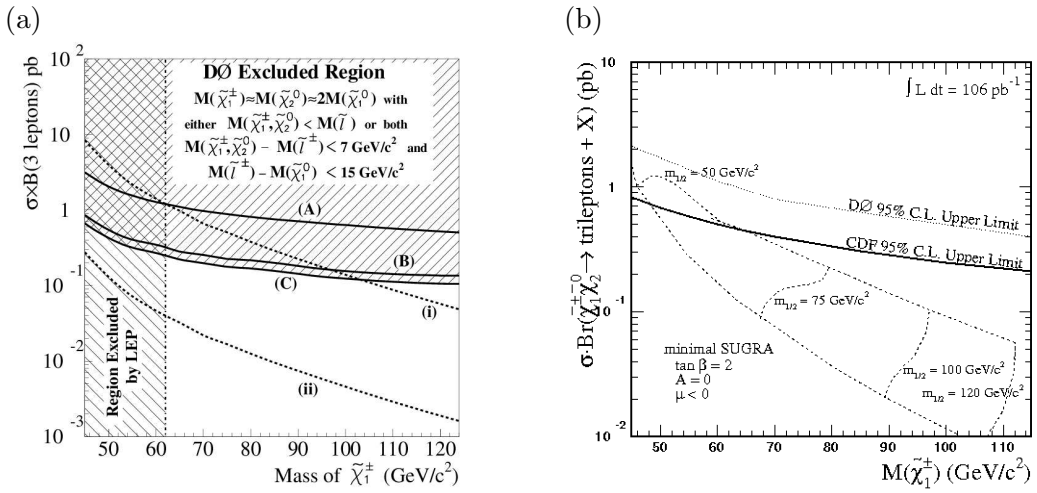

Figure 1.7: (a) DØ (a) 95% CL limit on the total cross section $\sigma_{\text{Prod}} \times$ BR into one of the nine trilepton final states compared with the predictions for different SUSY scenarios and (b) the CDF 95% CL limit on the $\sigma_{\text{Prod}} \times$ BR into final states with electrons and muons (four out of nine leptonic final states) compared with the mSUGRA prediction. The domain labeled *Region excluded by LEP* corresponds to an early chargino mass limit published by the OPAL collaboration in 1996 [34]. The final LEP chargino mass limit is at 103.5 GeV [29].

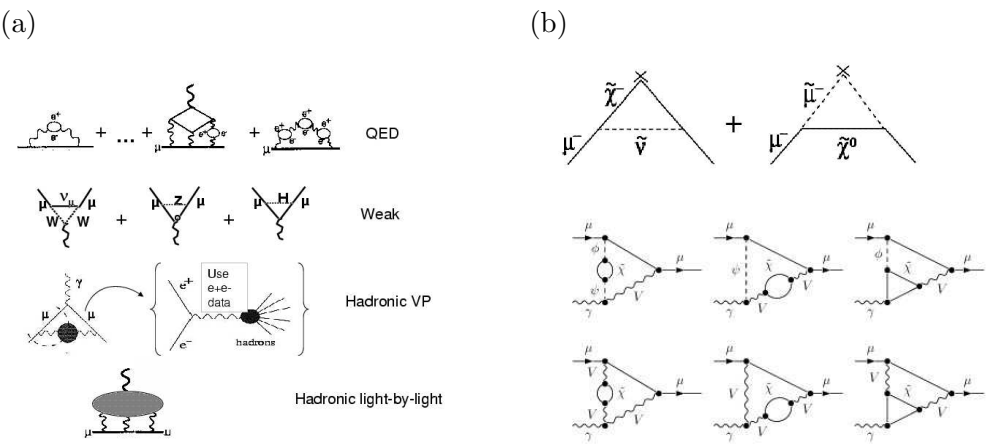

Figure 1.8: (a) Subset of Feynman diagrams relevant for the SM calculation of $(g-2)_\mu$ and (b) LO/NLO SUSY contributions from [35, 36]

scales are at M_{SUSY}:

$$\alpha_\mu^{\text{SUSY}_{1L}} = 13 \times 10^{-10} \left(\frac{100\ \text{GeV}}{M_{\text{SUSY}}}\right)^2 \tan\beta\, \text{sign}(\mu) \tag{1.49}$$

$$\alpha_\mu^{\text{SUSY}_{2L}} \approx 11 \times 10^{-10} \left(\frac{100\ \text{GeV}}{M_{\text{SUSY}}}\right)^2 \left(\frac{\tan\beta}{50}\right) \text{sign}(\mu). \tag{1.50}$$

The anomalous magnetic moment of the muon is measured with high precision at the Brookhaven National Laboratory [37]:

$$\alpha_\mu^{\text{exp}} = (11659208 \pm 6) \times 10^{-10}. \tag{1.51}$$

Depending on the evaluation of the hadronic contribution to the theoretical value (see Ref. [35, 38] and references therein) this corresponds to a 2-3σ derivation from the Standard Model expectation. The most recent calculation of the theoretical expectation[7] leads to a deviation of

$$\alpha_\mu^{\text{exp}} - \alpha_\mu^{\text{theo}} = (25 \pm 9) \times 10^{-10} \tag{1.52}$$

which is equivalent to a 2.7σ effect. This deviation agrees with SUSY models with positive sign of μ (see Eqn. 1.50) and a SUSY mass scale at the order of 100-1000 GeV for moderate values of $\tan\beta$ ($\tan\beta < 50$).

- Measurement of the rare decay $b \to s\gamma$

  Since the inclusive decay rate for the decay of the B meson into a strange meson and a photon, is determined by flavor-violating loop diagrams, it is rather sensitive to new physics. The branching ratio $b \to s\gamma$ has been measured by CLEO [39], Belle [40] and ALEPH [41], resulting in the present world average [38] of:

$$\text{BR}^{\text{exp}}(b \to s\gamma) = (3.54^{+0.30}_{-0.28}) \times 10^{-4} \tag{1.53}$$

which agrees with the theoretical value from the Standard Model [38]:

$$\mathrm{BR}^{\mathrm{theo}}(\mathrm{b} \to \mathrm{s}\gamma) = (3.70 \pm 0.30) \times 10^{-4}. \tag{1.54}$$

The exchange of charged Higgs bosons can enhance the branching ratio considerably. This contribution can be canceled by chargino-stop contributions, which interfere destructively with the Higgs contribution for positive μ. This imposes constraints on the SUSY parameter space, the most stringent ones for negative μ, which agrees with the preference for positive μ from the g-2 results, presented in the previous section.

- Measurement of the rare decay $\mathrm{B_s} \to \mu\mu$

  The theoretical prediction for this BR is [42]:

$$\mathrm{BR}^{\mathrm{theo}}(\mathrm{B_s} \to \mu\mu) = (3.4 \pm 0.5) \times 10^{-9}. \tag{1.55}$$

  The decay can be enhanced by contributions of non-SM-like neutral Higgs bosons (see Figure 1.9a) from models with two Higgs doublets, whose amplitude increases with $\tan^3\beta$ and which can completely dominate the value of the BR if $\tan\beta$ is large enough [43]. Searches of the Tevatron experiments DØ and CDF for this decay [38, 44, 45] result in the present combined 95% CL upper limit of:

$$\mathrm{BR}^{\mathrm{exp}}(\mathrm{B_s} \to \mu\mu) < (3.4) \times 10^{-7} \tag{1.56}$$

  which is still 2 orders of magnitude from the theoretical prediction. Figure 1.9b provides an estimate of the expected value of the cross section for a low–m_0 mSUGRA scenario, depending on $\tan\beta$. With the current sensitivity, Tevatron just starts to probe the region with $\tan\beta = 50$.

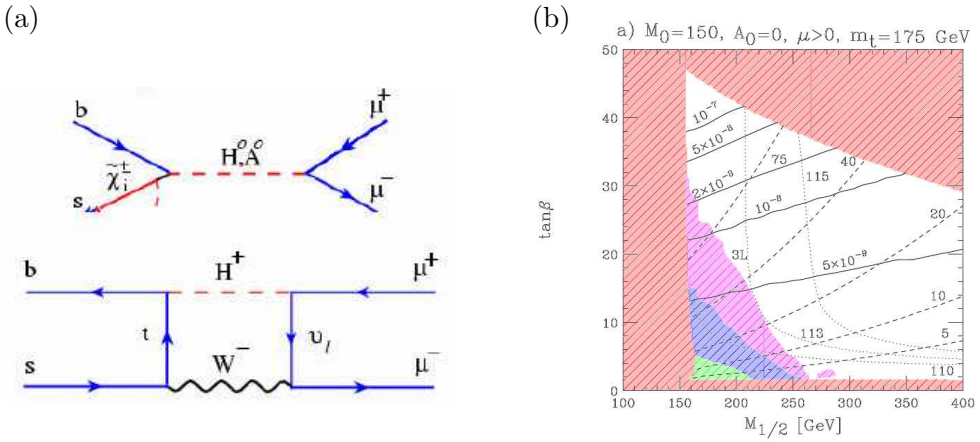

Figure 1.9: (a) Contributions to the amplitude of the decay $\mathrm{B_s} \to \mu\mu$ from models with two Higgs doublets and (b) sensitivity to the mSUGRA parameter space for $m_0 = 150$, $A_0 = 0$ and $\mu > 0$

Cosmological constraints

As stated earlier, the neutralino-LSP of a R-parity conserving SUSY theory provides a very good candidate for cold dark matter (CDM), such that measurements of dark matter densities can be reinterpreted as measurements of SUSY parameters.

- Measurement of the CDM relic density

  If RPC SUSY exists, the relic density of the LSPs (usually the lightest neutralinos) which result from the production in the early universe and the subsequent annihilation into Standard Model particles, must agree with the measured value for the current Dark Matter relic density. The value of the LSP relic density depends heavily on the SUSY particle mass spectrum and the couplings, such that a measurement of the dark matter density constrains the SUSY parameter space.

  The current Cosmic Standard Model (ΛCDM model) describes the universe as approximately flat and composed by roughly 5% baryonic matter, 25% dark matter and 70% dark energy. The parameters of the model are derived from

  – The precision measurement of the power spectrum of the anisotropies in the temperature of the cosmic microwave background (CMB)
  – The measurement of the red-shift of type Ia Supernovae as a function of their distance
  – The observation of the dynamics of galaxies and galaxy clusters

  Recent high precision measurements of the CMB anisotropies by the WMAP experiment [11] confirm the ΛCDM model and improve the accuracy of the combined fit of the input parameters, which results at 95 % confidence level (2σ) in:

  $$0.094 < \Omega_{\mathrm{CDM}} \mathrm{h}^2 < 0.129 \tag{1.57}$$

  where Ω_{CDM} is the ratio of the cold dark matter density and the critical matter density that leads to a flat universe and h is the dimensionless Hubble Constant, the current local expansion rate of the universe in units of 100km/s/Mpc [20, 11]. With h=0.72$\pm$0.05 this result corresponds to a CDM fraction of about 23 ± 4%. The upper bound yields a more stringent constraint on the LSP since additional sources for the CDM are possible.

  The standard annihilation cross section for the lightest neutralino (dominated by t-channel slepton exchange) decreases usually with its mass driving the relic density towards large values, which leads to the preferred LSP mass region very near the electroweak scale (*bulk region*). Nevertheless also heavier sparticles are possible along filaments in parameter space, provided there is a mechanism which increases the annihilation cross section [46, 47, 48]:

  – $\tilde{\tau}$–χ_1^0 co–annihilation allows for solutions with low relic densities even for larger values of $m_{1/2}$ provided m_0 is low enough such that the stau and the LSP are mass degenerated.

- In the *focus point region* for large values of m_0, the relic density is low due to a large higgsino component of the LSP, which allows for t-channel annihilation via chargino/neutralino exchange or co-annihilation with the lightest chargino or the second lightest neutralino.
- In the *rapid annihilation* region for large values of $\tan\beta$, the mass of the scalar or the pseudoscalar Higgs boson is approximately twice the LSP mass such that s-channel annihilation via a H(A) pole is enhanced.

Figure 1.10a shows the combined constraints on the $m_{1/2}$-m_0 parameter space of a constraint MSSM for four choices of the remaining parameters from the measurement of the CDM relic density, electroweak precision data and LEP II results, as of 2003 [48]. Varying, in addition, the trilinear coupling A_0 gives a more complete impression of the preferred parameter region. Figures 1.10b,c show the SUSY contribution to the anomalic magnetic moment α_μ and the branching fraction $B \to X_s\gamma$ for WMAP compatible cMSSM solutions versus $m_{1/2}$.

- Direct search for dark matter (*WIMP searches*)

  Direct detection of dark matter is based on the scattering off matter nuclei in earth based experiments. No evidence for dark matter has been found so far and the sensitivity of the present experiments is not large enough to seriously constrain SUSY but several more sensitive experiments are just starting or are under construction [20].

- Search for annihilation products

  In addition to detecting dark matter directly, one can search for the products of dark matter annihilations into neutrinos, positrons, anti-protons or photons in the solar system or in the galaxy. Two experiments have detected excesses, that can be interpreted as hints for the existence of dark matter. The HEAT telescope [49, 20] has registered an excess in the positron flux, that would correspond to a very large annihilation rate in the near solar system if interpreted as of dark-matter origin. The EGRET experiment has reported an excess of photons (*gamma-rays*), which could be interpreted as evidence for dark matter annihilation in the galactic center [50] and would be compatible with neutralino-CDM. The interpretations of both excesses are still under discussion awaiting clarification from a variety of future or recently started experiments [20].

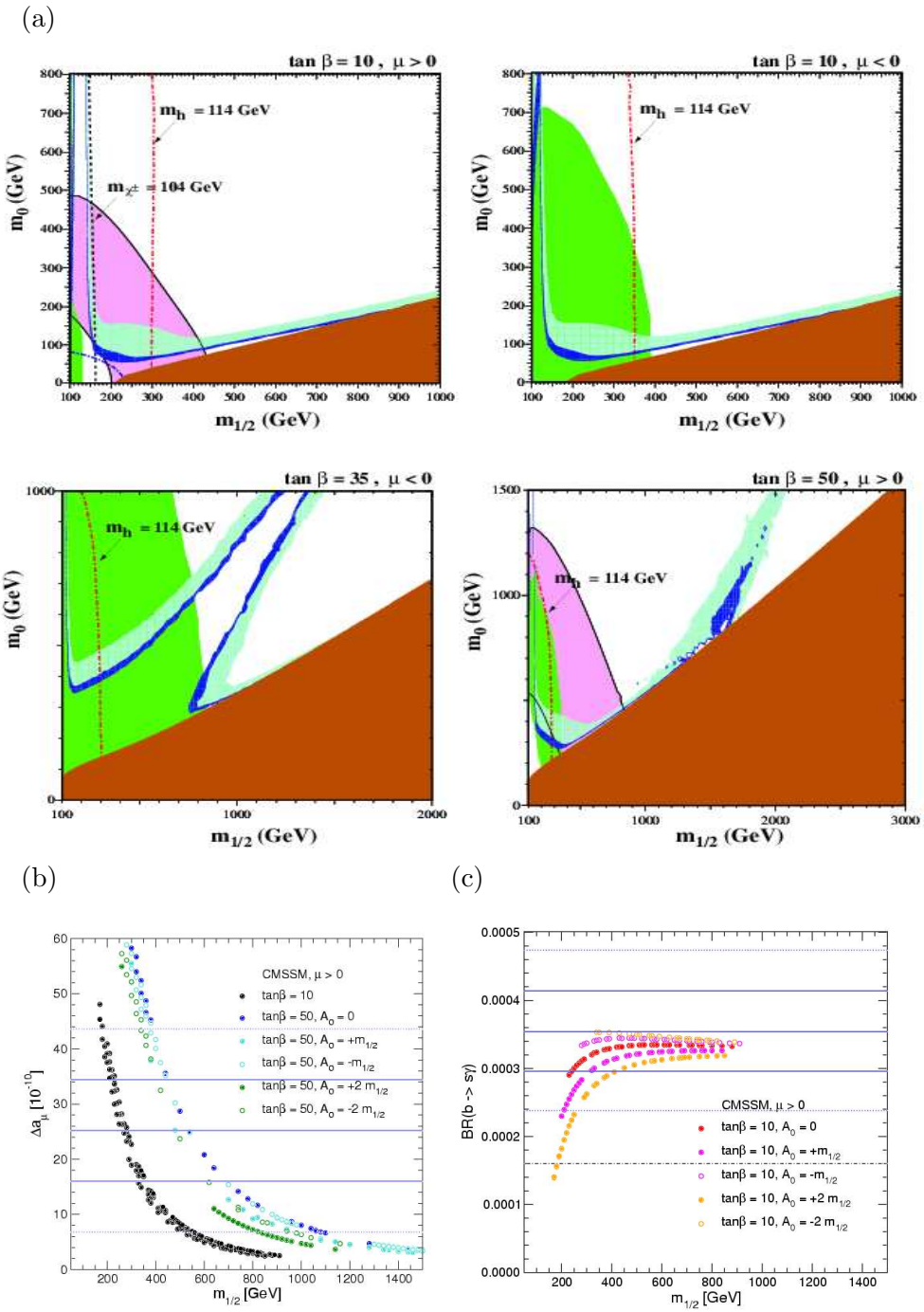

Figure 1.10: (a) Regions of the $m_{1/2}$-m_0 parameter space of a constraint MSSM preferred by the measurement of the CDM relic density, electroweak precision measurements and LEP II results, from [48]. The green shaded regions are excluded by $b \to s\gamma$. The pink shaded regions are favored by g_μ-2 at the 2σ level. The regions allowed by the older cosmological constraints are shaded light-blue and the regions allowed by the refined measurements, that include WMAP data, are shaded dark-blue. In the brown shaded region, the lightest $\tilde{\tau}$ would be the LSP. (b) SUSY contribution to the anomalic magnetic moment α_μ and (c) the branching fraction $b \to s\gamma$ as a function of the parameter $m_{1/2}$ for WMAP compatible constraint MSSM solutions. Solid lines show the central value and the 1σ range and dotted lines show the 2σ range for the constraining quantity, as measured experimentally.

2 Statistical methods

The statistical methods used in this analysis are presented in detail in the established text books [51, 52]. This Section intends just to give a brief overview over the methods chosen for this analysis, specifically in those cases where competing procedures are discussed in particle physics [8, 53].

2.1 Probability distributions

The probability of a certain outcome of an experiment is defined as the limit of the frequency with which this outcome occurs in a hypothetical series of N experiments for $\mathrm{N} \to \infty$. The probability density function (p.d.f) f(x) for a random variable x is then the limit of the frequency distribution in an infinite series of experiments.

The *expectation value* for any function a(x) of the random variable x with the p.d.f. f(x) is defined as

$$\mathrm{E[a(x)]} = \int_{-\infty}^{\infty} \mathrm{a(x)f(x)dx} \tag{2.1}$$

with the *mean* $\mu = \mathrm{E}\,[\mathrm{x}]$. The *variance*

$$V\,[x] = \mathrm{E}\left[(\mathrm{x} - \mathrm{E(x)})^2\right] = \mathrm{E}\left[\mathrm{x}^2\right] - \mu^2 \tag{2.2}$$

is a measure of how widely x is spread around the mean. The quantity $\sigma = \sqrt{V}$ is called the *standard deviation*. The covariance matrix $\mathrm{V_{ij}}$ of n random variables $\{x_1, x_2 \ldots x_n\}$ is defined by

$$V_{ij} = E\,[(x_i - \mu_i)(x_j - \mu_j)] = E\,[x_i x_j] - \mu_i \mu_j. \tag{2.3}$$

The correlation between the two random variables is best described by the correlation coefficient $\rho_{\mathrm{ij}} = \frac{\mathrm{V_{ij}}}{\sigma_\mathrm{i}\sigma_\mathrm{j}}$.

2.1.1 Probability distribution functions

The number k of successes in n trials of a random experiment with two outcomes and a success probability p is given by the *binominal distribution*

$$\mathrm{f_B(k;n,p)} = \binom{\mathrm{n}}{\mathrm{k}} \mathrm{p^k(1-p)^{n-k}}. \tag{2.4}$$

For $\mathrm{p} \to 0$, $\mathrm{n} \to \infty$ and $\mathrm{np} = \mu$, the binominal distribution can be approximated by the *Poisson distribution*

$$\mathrm{P_{Poiss}(n;\mu)} = \frac{\mathrm{e^{-\mu}\mu^n}}{\mathrm{n!}}. \tag{2.5}$$

For large μ the Poisson distribution approaches the *Gaussian distribution*

$$f(x;\mu,\sigma^2) = \frac{1}{\sqrt{2\pi\sigma^2}} exp\left(\frac{-(x-\mu)^2}{2\sigma^2}\right). \tag{2.6}$$

According to the *central limit theorem* the probability distribution of the sum x of n independent continuous random variables $\mathrm{x_i}$ becomes a Gaussian p.d.f with $\mu = \sum \mu_\mathrm{i}$ and $\sigma^2 = \sum \sigma_\mathrm{i}^2$.

The Gaussian distribution for the N-dimensional random variable $\mathbf{x} = \mathrm{x}_1, \mathrm{x}_2, \ldots \mathrm{x_N}$ with the mean $\boldsymbol{\mu} = \mu_1, \mu_2, \ldots \mu_\mathrm{N}$ can be expressed with the covariance matrix V:

$$f(\mathbf{x},\boldsymbol{\mu},V) = \frac{1}{(2\pi)^{N/2}|V|^{1/2}} exp\left[-\frac{1}{2}(\mathbf{x}-\boldsymbol{\mu})^T V^{-1}(\mathbf{x}-\boldsymbol{\mu})\right]. \tag{2.7}$$

The χ^2 distribution is defined as

$$\mathrm{f(z;n)} = \frac{\mathrm{z^{n/2-1}e^{-z/2}}}{\mathrm{2^{n/2}\Gamma(n/2)}} \tag{2.8}$$

for the number n of degrees of freedom and $\Gamma(x) = \int_0^\infty e^{-1}t^{x-1}dt$. If $\mathrm{x_1}$, $\mathrm{x_2}\ldots$ are independent Gaussian distributed random variables, the sum

$$\mathrm{z} = \sum_1^\mathrm{n} (\mathrm{x_i} - \mu_1)^2/\sigma_\mathrm{i}^2 \tag{2.9}$$

is distributed as a χ^2 with n degrees of freedom. If the $\mathrm{x_i}$ are not independent, the variable

$$\mathrm{z} = \sum_\mathrm{ij}^\mathrm{n} (\mathrm{x_i} - \mu_\mathrm{i})\mathrm{V_{ij}^{-1}}(\mathrm{x_j} - \mu_\mathrm{j}) \tag{2.10}$$

is χ^2 distributed.

2.2 Statistical tests

A physical theory, mostly formulated in terms of certain parameters, corresponds to a statistical *hypothesis*. It predicts the p.d.f. for an experimentally measurable random variable $\mathbf{x}$. An experiment produces only a finite amount of data, corresponding to a frequency distribution $\hat{\mathrm{f}}(\mathbf{x})$, from which we want to make a statement about the validity of the theory. Instead of the distribution of $\mathbf{x}$ usually the distribution of a function $\mathbf{t}(\mathbf{x})$, the *test statistics*, is analyzed. $\mathbf{t}(\mathbf{x})$ can be an *estimator* for a parameter of the theory or a variable, whose p.d.f is maximally different for competing hypotheses.

A parameter of the theory is estimated from the outcome $\hat{\mathrm{f}}(\mathbf{x})$ of the experiment. A *confidence region* can be defined on the *confidence level* α, which would cover the true value of the parameter in a fraction of $1-\alpha$ of a series of repeated experiments with the same prescription for constructing the confidence region.

In a search for a new effect, e.g. the search for new particles, the established theory corresponding to the *null hypothesis* H_0 is compared with the *alternative hypothesis* H_1 of a new theory. An experiment is performed in order to test the competing hypotheses.

Before the experiment is performed, a critical region C is defined for H_0. H_0 is rejected if $\mathbf{x} \epsilon$ C. The test is significant at the *significance level* η, if the probability for rejecting H_0 even though H_0 is true (type I error) is

$$\alpha = P(\mathbf{x} \in C|H_0) < \eta. \tag{2.11}$$

H_1 is rejected if $\mathbf{x} \notin$ C. The power of the test to reject H_1 is 1-β, with the probability β for the (type II) error of accepting H_0 and rejecting H_1 even though H_1 is true

$$\beta = P(\mathbf{x} \notin C|H_1). \tag{2.12}$$

In contrast to the power the significance level does not depend on the alternative hypothesis.

In order to increase the power to discriminate between the hypotheses, a test statistic $\mathbf{t}(\mathbf{x})$ is used whose probability distributions in the case of H_0 and in the case of H_1 are (ideally) maximally separated, which means that both α and β are small. It can be shown that the optimal test statistic is given by the ratio of the probability densities for H_0 and H_1(Neyman-Pearson lemma):

$$\lambda(\mathbf{x}) = \frac{f(\mathbf{x}|H_0)}{f(\mathbf{x}|H_1)}. \tag{2.13}$$

In practice, however, f is difficult to determine and a simpler test statistic is constructed.

A well established test statistic in particle physics is the number N of events with $\mathbf{x}$ in a certain signal region. H_0 predicts then a Poisson distribution of N with the mean b (the *background* distribution B). H_1 predicts a Poisson distribution of N with the mean s+b (the *signal+background* distribution S+B). The critical region for H_0 is then $C = \{N|N > N_0\}$ with N_0 chosen such as to fit the requirements on significance or power of the experiment.

2.2.1 Limit setting

In practice the alternative hypothesis is usually not a simple hypothesis but depends on a set of parameters which result in different predictions for s. Usually a significance level of $\alpha < 5.7 \cdot 10^{-5}$ is required for the rejection of the established theory whereas $\beta < 0.05$ is required for the rejection of an alternative theory. Both means can in general not be met in one test such that different critical regions are constructed for each purpose.

If H_0 is not rejected in this test on the required significance level, this does not exclude all alternative hypotheses, since the effects could be too weak to be measured. Formally a series of tests is performed for each alternative hypothesis H_1 with the critical region adjusted such that the power of the test is large enough (usually $\beta < \eta = 0.05$). The procedure starts with alternative hypotheses that predict small values of the mean s of the signal distribution and proceeds towards higher s until for $s = s_{max}$ the observed number of events is lower than the boundary N_0 for the critical region. All alternative hypotheses which predict a larger value of s_{max} are then excluded with the desired significance. No

statement is possible about the other hypotheses. This procedure is equivalent to constructing the minimal acceptance region for H_0 that still contains the observed number n_{obs} and solving:

$$\beta = \sum_{n=0}^{n_{obs}} P_{Poiss}(n|s_{max} + b) \leq \eta. \tag{2.14}$$

β is also denoted as the confidence level CL_{S+B} for the signal+background hypothesis for the upper limit on the expected signal s which corresponds to the interpretation of $\{s|s < s_{max}\}$ as a confidence region for the true value of s. 1-α is then denoted as the confidence level for the background hypothesis CL_B, describing the consistency of the hypothesis with the background.

In order not to overrate a downward-fluctuation of the background in deriving upper limits a common approach (*modified frequentist approach* [53]) modifies Eqn. 2.14 by normalizing β to the background confidence level $CL_B = 1 - \alpha$

$$CL_S = \frac{\beta}{1-\alpha} = \frac{CL_{S+B}}{CL_B} = \frac{\sum_{n=0}^{n_{obs}} P_{Poiss}(n|s_{max} + b)}{\sum_{n=0}^{n_{obs}} P_{Poiss}(n|b)} \leq \eta, \tag{2.15}$$

thus conservatively increasing the required power of the test[1].

2.2.2 Likelihood ratio and combination of different test statistics

Following the Neyman-Pearson lemma (see Eqn 2.13), the simple counter n is replaced by a more powerful test statistic Q, the *likelihood ratio* of the Poisson probabilities for the two competing hypotheses:

$$Q(n) = \frac{P_{Poiss}(n|s+b)}{P_{Poiss}(n|b)} = (1 + \frac{s}{b})^n e^{-s}. \tag{2.16}$$

Different test statistics Q_i (corresponding to different experiments, channels or bins of a distribution) can easily be combined with:

$$Q(n) = \prod \frac{P_{Poiss}(n_i|s_i + b_i)}{P_{Poiss}(n_i|b_i)} = \prod (1 + \frac{s_i}{b_i})^n e^{-s}. \tag{2.17}$$

The logarithm lnQ reduces then to the difference between the weighted sum of the candidate events, (with the event weight $\ln(1 + s_i/b_i)$ which depends on the local signal-to-background ratio) and the number of candidate events expected from the signal alone.

$$\ln Q(n) = \sum n_i \ln(1 + s_i/b_i) - s_i. \tag{2.18}$$

[1] this procedure follows for example from Bayesian statistics with a restricted prior density: The prescription for finding an upper limit on s which was presented above is equivalent with solving $\int_{s_{max}}^{\infty} P(s|n_{obs})ds < \eta$ with the unknown posterior probability density $P(s|n_{obs})$. It can be related to the well described model density P(n|s) (in our case $P_{Poisson}(n|s)$) by the classical Bayes theorem, if the model parameters are treated as random variables with a certain prior distribution $\pi(s)$, assuming a flat prior distribution, which is restricted to positive values for s yields Eqn. 2.15 [51].

The likelihood ratio Q replaces the counter n in the results derived in the last chapter, in particular :

$$\alpha = 1 - \mathrm{CL_B} = P(Q \geq Q_{obs}|B) \quad (2.19)$$

$$\beta = \mathrm{CL_{S+B}} = P(Q \leq Q_{obs}|S+B) \quad (2.20)$$

with the observed likelihood ratio $\mathrm{Q_{obs}}$

2.2.3 Sensitivity

The sensitivity of an experiment which aims to constrain the parameter of an alternative hypothesis can be derived by replacing $\mathrm{CL_S}$ (see Eqn 2.15) by the median $\mathrm{CL_S}$ in an ensemble of background-only Poisson experiments. The corresponding *expected limits* are used as a figure of merit to optimize the analysis. For low background means $\mathrm{b_i}$, the median $\mathrm{CL_S}$ can be replaced by the average $\mathrm{CL_S}$.

2.2.4 Systematic uncertainties

Statistical and systematic uncertainties in modeling the probability density for the random variables from which the test statistic is derived result in systematic errors on the predicted Poisson means $\mathrm{b_i}$ and $\mathrm{s_i}$ which enter the calculation. They are taken into account by integrating over possible values of the signal and background given their systematic uncertainty distribution, taking into account correlations. In practice they are assumed to be Gaussian-distributed with a cutoff that prevents negative values for $\mathrm{b_i}$ and $\mathrm{s_i}$.

3 The DØ-Experiment

Since the termination of the e^+e^- collider experiment LEP II by the end of 2000, the collider-based high-energy community has concentrated on two hadron accelerators:

- The Tevatron [54], located at the Fermi National Accelerator Laboratory (FNAL) [55] near Chicago, is a proton-antiproton collider with a center-of-mass energy of 1.96 TeV. It has started its second period of data taking with an upgraded accelerator and upgraded detectors in 2001.
- The Large Hadron Collider (LHC) [56], situated at CERN [57] at Geneva is a proton-proton collider with a center of mass energy of 14 TeV. It is scheduled to start data taking in 2007.

At present, the Tevatron collider [54] with the two multi-purpose experiments CDF [58] and DØ [59] provides the world highest center-of-mass energy. During the first data taking period (Run I) from 1992 to 1996, each experiment collected data corresponding to an integrated luminosity (see Section 4.1.1) of about 120 pb^{-1} at a center-of-mass energy of 1.8 TeV. After an upgrade of the accelerator and the experiments, the second period of data taking started in 2001 (Run II). Since then, each experiment has collected data corresponding to $\approx$1 fb^{-1}. By the end of Run II, an integrated luminosity of 8 fb^{-1} is expected per experiment.

Figure 3.1 shows the weekly and the total integrated luminosity from startup until July 2005. The development of the peak luminosity is shown in Fig. 3.2. Due to improvements in the accelerator, especially in the sector of antiproton storage and injection, the instantaneous luminosity has increased considerably, which is reflected in an increasingly steep rise of the integrated luminosity. Currently, typical peak luminosities are at the order of 10^{32} cm^{-1} s^{-1}. This analysis is based on data collected from April 2002 to June 2004 by the DØ detector. The following section gives an overview of the accelerator, the DØ detector and the data taking.

3.1 The accelerator

The *Tevatron*, the proton-antiproton collider at FNAL with a circumference of 6.3 km, is the last stage of a chain of accelerators which produce high-energy proton and antiproton beams. Figure 3.3 shows a sketch of the Tevatron and the accelerator chain at FNAL. The procedure starts with the *Cockroft-Walton* accelerator, which yields negatively charged hydrogen ions with a kinetic energy of 750 keV. The energy is increased to 400 MeV by the *LINAC* linear accelerator and the hydrogen ions are stripped off their electrons passing through a carbon fiber foil. The protons are then accelerated up to 8 GeV by the

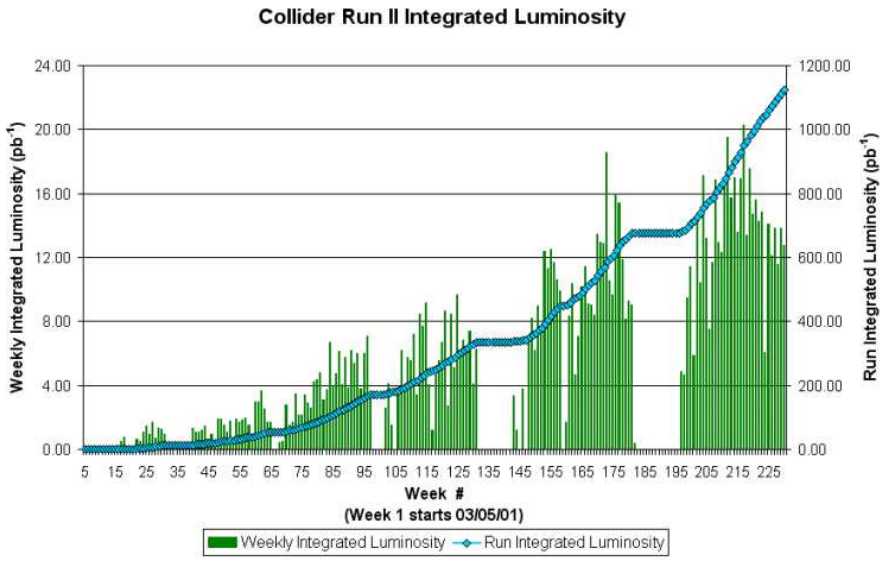

Figure 3.1: Tevatron total and weekly integrated luminosity

Booster synchroton, and transferred to the *Main Injector* synchroton ring, where they are accelerated to 150 GeV, arranged into a bunch structure and transferred to the Tevatron. Since the antiprotons are the limiting factor in increasing the luminosity of the Tevatron, much effort has gone into improving the production and storage of these particles. They are produced by directing 120 GeV proton bunches from the Main Injector at a nickel/copper target. The antiprotons that are produced in the hadronic reaction (1 in 50000 collisions) are collected, accelerated to 8 GeV, stochastically cooled in the *Debuncher* and stored in the *Accumulator*. A crucial part in increasing the antiproton rate has the *Recycler* [60], a storage ring parallel to the Main Injector, which has a much larger storage capability than the Accumulator. When enough antiprotons have been collected, they are passed to the Main Injector, where they are accelerated to 150 GeV and transferred into the Tevatron synchroton, where the bunches of protons and antiprotons are finally accelerated up to 980 GeV and brought to collisions.
In the final Tevatron collision stage, protons and antiprotons are arranged into 3 *super bunches*, separated by 2.6 μs, each composed by 12 small bunches, separated by 396 ns, which results in 36 bunches of protons and 36 bunches of antiprotons traveling the beam lines in opposite direction. The length of the bunches is about 60 cm, which corresponds to roughly 2 ns. The beam half-life is about 9-10 hours. The beams collide at two interaction points along the Tevatron, where CDF and DØ experiments are located, resulting in $p\bar{p}$ collisions at a center-of-mass energy of 1.96 TeV.

3.2 The DØ - detector

The DØ detector is a general purpose detector. It consists of several subdetectors which are arranged in the classical collider detector design, cylindrical around the interaction point.

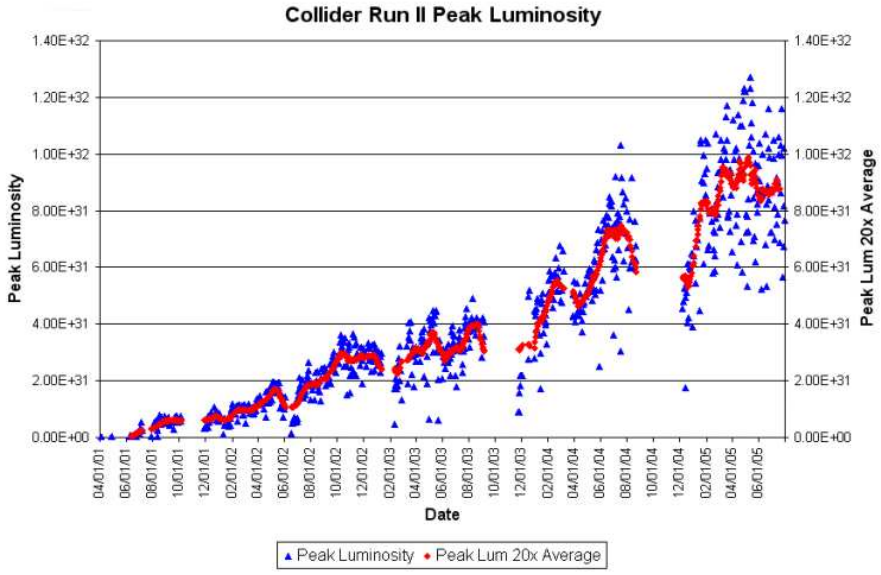

Figure 3.2: Tevatron peak luminosity

Starting at the beam line and moving outwards, the DØ detector consists of the silicon microstrip vertex detector (SMT) and the central fiber tracker (CFT), both immersed in the field of a superconducting solenoid magnet. It is surrounded by a liquid-argon sampling calorimeter followed by three layers of muon chambers, situated in a toroidal magnetic field. Data acquisition comprises a three-stage trigger system. The tracking system, the muon system and the calorimeter electronics have been upgraded considerably between Run I and Run II. The solenoid magnet has been introduced in Run II.

Figure 3.4 gives an overview over the arrangement of the various subdetectors. The detector components and in particular the upgrades that have been performed between the two stages of data taking are described in detail in reference [59]. This section intends to give only a short overview over the detector subsystems.

DØ uses a right-handed coordinate system originating at the detector center which corresponds to the main interaction point. The z-axis is along the proton direction and the y-axis is upward. Positions of particles are usually quoted in polar coordinates with the polar angle Θ replaced by the pseudorapidity η

$$\eta = -\ln(\tan\frac{\Theta}{2}) = \frac{1}{2}\ln\frac{2\cos^2\frac{\Theta}{2}}{2\sin^2\frac{\Theta}{2}} = \frac{1}{2}\ln\frac{\mathrm{E}(1-\cos\Theta)}{\mathrm{E}(1-\cos\Theta)} \approx \frac{1}{2}\ln\left[(\mathrm{E}+\mathrm{p_z})(\mathrm{E}-\mathrm{p_z})\right] = \mathrm{y} \qquad (3.1)$$

which approximates the true rapidity y for finite angles in the limit of vanishing ratio m/E. The direction of a particle trajectory is given by *physics-η* which is related to the vertex position. The position of a specific interaction of the particle in the detector is described by *detector-η* or η_{det} which is related to the origin of the coordinate system. The term *central* refers to $|\eta| \lesssim 1.0\,(1.6)$ in the calorimeter (tracker). The term *forward* describes the region of larger values of $|\eta|$.

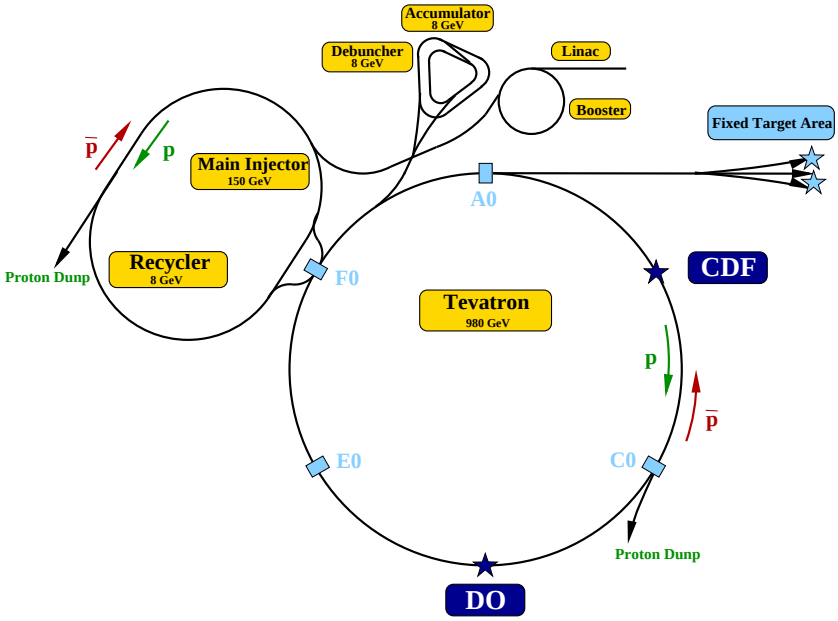

Figure 3.3: Schematic view of the Tevatron accelerator chain

3.2.1 The inner tracker

The inner tracker measures the trajectories of charged particles. Figure 3.5 shows the inner detector region and provides an overview over the central tracking detectors and their position relative to other subdetectors. The design of both tracking subsystems and of the magnetic coil is constrained by the available space within the cryostats of the Run I calorimeter.

The silicon microstrip tracker (SMT)

The SMT is the innermost detector, surrounding the beam pipe directly, starting at a radius of 2.7 cm. It provides both tracking and vertexing over nearly the full η coverage of the calorimeter and the muon systems. In order to provide a good position reconstruction in spite of the long interaction region, the SMT consists of barrel modules interspersed with discs in the center region and assemblies of disks in the forward region. Figure 3.6 provides an overview of the SMT design. The detector has six barrel modules in the central region with an outer radius of 9.4 cm and a length of 9 cm, each with four silicon readout layers. The innermost two layers have 12 double-sided silicon readout modules (*ladder*) each, the outermost layers have 24 ladders each. Each barrel module is capped at the high-|z| end with a disk of twelve double-sided wedge detectors (*F-disks*), with an outer radius of 10.5 cm. At the forward end of the barrel assemblies three additional F-discs are installed. In the far-forward regions (110 cm and 120 cm from the detector center) two large-diameter *H-disks* with an inner radius of 9.5 cm and an outer radius of 26 cm provide tracking at very large η.

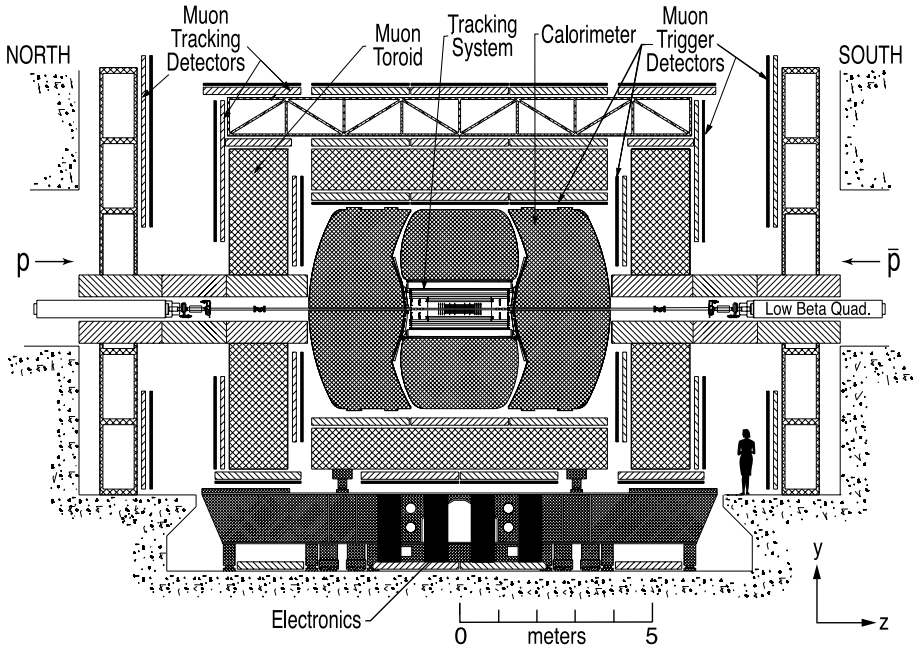

Figure 3.4: Diagram of the DØ detector (from Ref. [59])

The central fiber tracker (CFT)

The SMT is surrounded by the CFT (see Figure 3.5), which provides tracking in $|\eta_{\text{det}}| \lesssim 1.8$ and forms also part of the first level trigger.

It consists of scintillating fibers mounted on eight concentric support cylinders between radii of 20 and 52 cm. The two innermost cylinders are 1.66 m long; the outer six cylinders are 2.52 m long. Each cylinder supports one doublet layer of fibers oriented along the beam direction (*axial layers*) and a second doublet layer (*stereo layer*) at a stereo angle of +3° or -3° (in alternating mode). The scintillating fibers are 835 μm in diameter and have a multi-clad structure with a core of polystyrene doped with an organic fluorescent and a wave–shifter, surrounded by two optically denser claddings. Waveguides transport the light to the fast impurity-band silicon avalanche photon detectors, the *visible light photon counters (VPLC).*

3.2.2 The magnetic field

The solenoidal magnet consists of two concentric coils of superconducting CU:NbTi cable surrounding the CFT at a radius of 60 cm with a length of 2.7 m. The magnet is operated with a current of 4.7 kA at a temperature of 10 K. It provides a uniform 2 T magnetic field in the tracking volume, which allows for the momentum measurement of charged particles. The uniformity is achieved by a larger current density in the windings at the end of the coil. The material of the coil and of the cryostat wall corresponds to roughly one

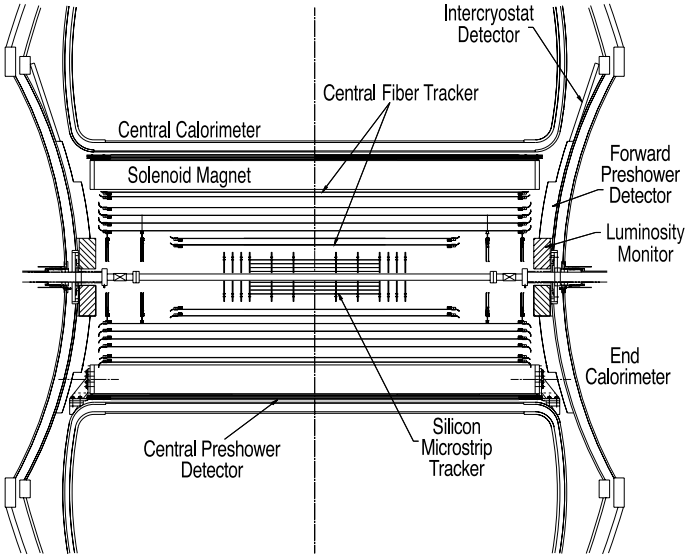

Figure 3.5: The central tracking system (from Ref. [59]).

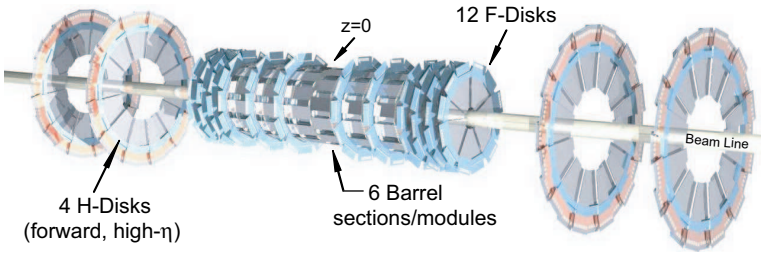

Figure 3.6: The disk/barrel design of the Silicon Microstrip Tracker (from Ref. [59])

electromagnetic interaction length [8] at $\eta = 0$. Figure 3.7 shows a sketch of the magnetic field in the detector provided by the solenoidal and the toroidal magnets.

3.2.3 The preshower system

Due to the presence of the solenoid, the electromagnetic energy resolution in the calorimeter is degraded. In order to improve the electron identification, scintillating fiber detectors, consisting of triangular scintillator strips, are installed between the magnetic coil and the cryostats of the central and forward calorimeter (see Figure 3.5).

The central preshower detector (CPS) consists of three cylindrical layers of scintillator strips, one with axial orientation, the others with stereo angles of -24° and +24° and a lead radiator of approximately one radiation length between the solenoid and the scintillators in the region $|\eta| < 1.3$ in order to induce electromagnetic showering. The material of the CPS, the coil and the cryostats corresponds to approximately two radiation lengths.

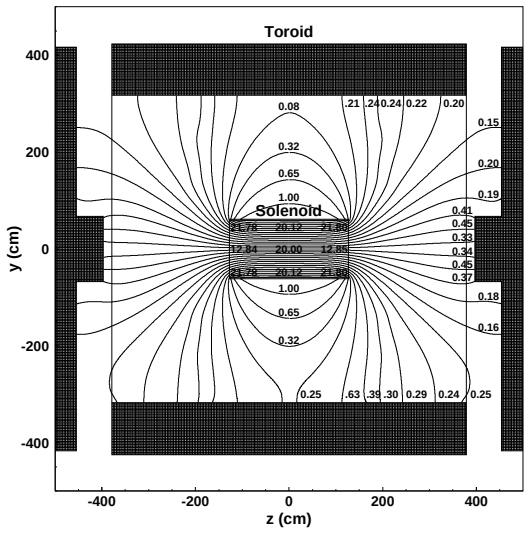

Figure 3.7: y-z projection of the DØ magnetic field (from Ref. [59]).

The forward preshower detectors (FPS) are located on the heads of the end–cap cryostats between the luminosity counters at the inner edge and the intercryostat detectors at the outer edge. Each FPS detector is made of two double layers of scintillator strips, separated by a lead-stainless-steel absorber, corresponding to two radiation lengths, in order to induce electromagnetic showers which can be detected in the outer layers.

The preshower system is not yet fully included into the electron identification such that the preshower information is not used in this analysis.

3.2.4 The calorimeter system

The DØ calorimeter system consists of three liquid argon sampling calorimeters. It is designed for the identification and energy measurement of electrons, photons and jets and for the measurement of the missing transverse energy.

Photons and electrons start electromagnetic cascades in the inner layers of the calorimeter. Hadron jets start hadronic showers [8], which, in general, have energy deposits in the electromagnetic and the hadronic layers of the calorimeter.

The liquid-argon calorimeters

Figure 3.8 shows the three parts of the central calorimeter (CC) which covers $|\eta| \lesssim 1.0$ and the two end calorimeters ECN (north) and ECS (south), denoted as EC in the following, which extend the coverage up to $|\eta| \lesssim 4$. The basic unit of each DØ calorimeter are cells, consisting of layers of absorber within the active medium, the liquid argon, which are situated within the calorimeter cryostat that keeps the temperature of the liquid argon at approximately 80 K. Figure 3.9 shows a typical calorimeter cell. The electromagnetic or hadronic showers develop in the compact material of the absorber plates. The liquid

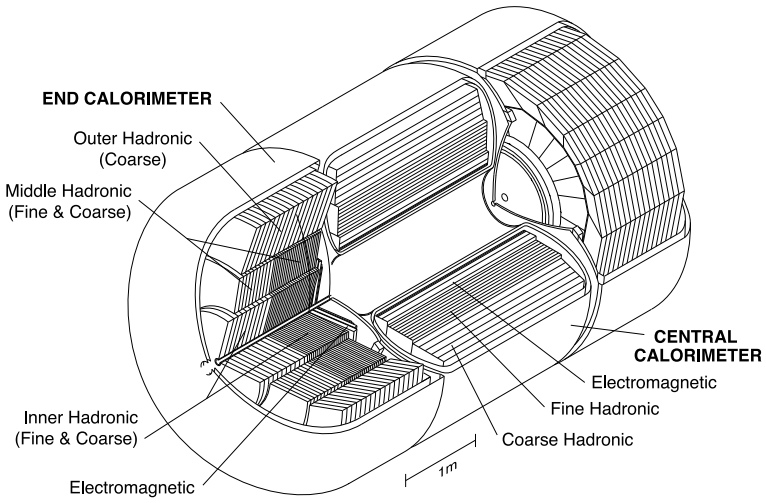

Figure 3.8: Isometric view of the central and two end calorimeters (from Ref. [59]).

argon in the gaps between the plates is ionized by the charged particles within a shower. The amount of ionization, representing a fraction of the energy of the shower, is collected on copper electrodes which are set on positive high voltage (typically 2 kV) relative to the grounded absorber plates. The typical drift time for the electrons across the gap is 450 ns.

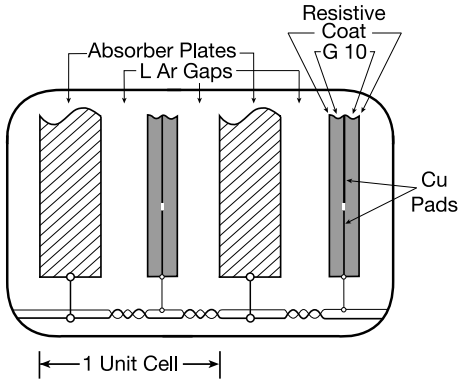

Figure 3.9: Schematic view of a calorimeter cell (from Ref. [59]).

Each calorimeter can be divided into three regions according to the difference in the size and material of the absorber plates. The absorber of the innermost electromagnetic (EM) sections is made of thin (3 mm in CC and 4 mm in EC) plates of depleted uranium, which correspond to roughly one radiation length in CC, the *fine* hadronic (FH) modules contain 6 mm-thick uranium-niobium plates and the *coarse* hadronic (CH) section uses 46.5 mm thick plates of copper (CC) or stainless steel (EC).

Figure 3.10 gives a schematic view of the transverse and longitudinal pattern of readout

cells. They form pseudo-projective towers, with the centers of the cells arranged on rays projecting from the center of the interaction region but with the cell boundaries and the absorber plates aligned with the cryostat borders. The cell boundaries lead to small non-sensitive regions in each layer which are called *ϕ-cracks*.

The lateral extension of a typical cell is 0.1 in η and 0.1 in ϕ. Cell sizes increase for $\eta > 3.2$ to 0.2×0.2 in $\eta - \phi$ in order to avoid very small absolute cell sizes.

The electromagnetic section of the central calorimeter (CC) has 4 cylindrical floors of cells (EM1-4) corresponding to 2, 2, 6.8 and 9.8 radiation lengths at $|\eta| = 0$, from which follows that the center positions of the cells are at a distance of 3, 5, 9.5 and 18 radiation lengths from the interaction point. The cells in the third electromagnetic layer, where the center of the electromagnetic shower is expected, have twice the granularity (0.05×0.05 in $\eta - \phi$) in order to allow for a more precise measurement of the location and the size of the shower.

The EM section of the endcap calorimeter (EC) consists also of 4 floors, corresponding to 0.3, 2.6, 7.9 and 9.3 radiation lengths. The cell granularity is comparable with the CC up to $|\eta| = 2.6$. For $2.6 < |\eta| < 3.2$ the cells in the third layer have the same size as the cells in the other layers. For $|\eta| > 3.2$ the size of the cells in all EM layers and in the hadronic modules is increased to 0.2×0.2 and continues to increase with increasing η up to 0.4×0.4 for $|\eta| \approx 4.0$.

The fine hadronic CC section consists of three floors, corresponding to 1.3, 1.0 and 0.8 hadronic interaction lengths. The innermost layer of the fine hadronic section can also be included into the identification of electromagnetic objects, in order to sample the energy deposition in the tail of the EM shower. The coarse hadronic section has a single cell layer with a depth of 3.2 hadronic interaction lengths.

The hadronic EC sections are arranged into three modules. The cylinder shaped innermost hadronic modules (ECIH) contain four fine hadronic layers of 1.1 hadronic interaction lengths each. The coarse hadronic layer has a depth of 4.1 hadronic interaction lengths. The middle hadronic modules (ECMH) have a fine hadronic section with four layers of 0.9 hadronic interaction lengths each and a coarse hadronic layer which corresponds to 4.4 hadronic interaction lengths. Three layers of additional coarse hadronic modules of 6 hadronic interaction lengths each (ECOH) are located in the outermost parts of the EC cryostat inclined at an angle of 60° with respect to the beam pipe.

Calorimeter readout

The DØ calorimeter has approximately 55000 readout channels, of which roughly 47000 are connected to physical readout modules in the cryostats. Figure 3.11 shows the schematic of the readout electronics. It had to be upgraded for Run II in order to cope with the reduced bunch spacing and the increased luminosity. The signals from the calorimeter cells are amplified and shaped in the preamplifiers and sent to the baseline subtractor system (BLS), where the signals are shaped and sampled at the peak (320 ns).

In parallel, faster shaped analog sums of the signal are picked off to provide prompt inputs to the calorimeter trigger system for both level 1 (L1) and level 2 (L2) trigger decisions. The signal is meanwhile kept in an analog buffer of Switched Capacitor Arrays (SCA)

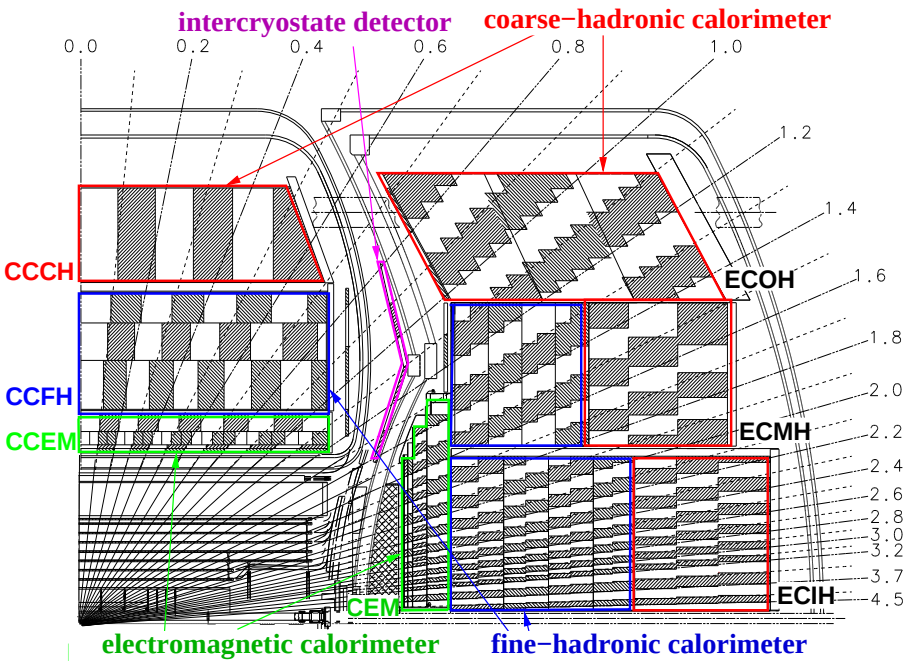

Figure 3.10: Schematic view of a portion of the DØ calorimeter showing the transverse and longitudinal segmentation pattern (from Ref. [59]).

awaiting the L1 decision. Upon a positive L1 decision, the corresponding signal from the SCA is read out and a baseline subtraction is performed in order to cope with the pile up (see also Section 4.1) over successive bunch crossings. The signals are then send to a similar storage pipeline (L2 SCA) awaiting the L2 trigger decision. After a positive L2 decision, the signals are digitized and send to the data acquisition (DAQ) in order to be processed by the level 3 trigger and stored to tape.

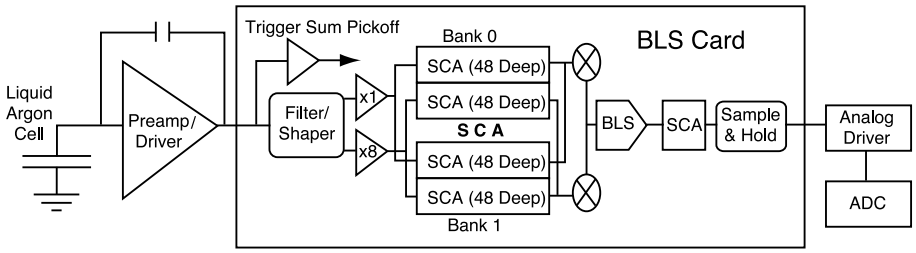

Figure 3.11: Schematic block diagram of the calorimeter readout chain (from Ref. [59]).

3.2.5 The intercryostat detectors

The η region between the central and the forward calorimeter ($1.1 < |\eta| < 1.4$) is characterized by only partial instrumentation of the EM and the fine hadronic sections and a

substantial amount of unsampled material from the solenoid and the cryostat walls. This problem is addressed by two detector systems which provide additional energy sampling (see Figure 3.5). The intercryostat detector (ICD) consists of a single layer of scintillating tiles, attached to the exterior surfaces of the EC cryostats. Additional readout cells without absorber, the *Massless Gaps (MG)*, are located inside the CC and the EC cryostat walls.

3.2.6 The muon system

In contrast other charged particles and hadrons, muons at Tevatron energies pass through the calorimeter without producing electromagnetic or hadronic showers (*minimum ionizing particles (MIPs)*). Muons can hence be identified in the muon system at the outside of the calorimeter. They leave, in addition, tracks in the tracking detectors.

The muon detector is located at both sides of an iron toroid magnet (see Figure 3.7), which surrounds the calorimeters at a distance of 318 cm $<$ r $<$ 427 cm to the beam pipe in the central part and in a distance of 454 cm $<$ z $<$ 610 cm from the interaction region in the forward parts and creates a magnetic field for momentum measurement in the muon system with a magnetic field strength of 1.8 T inside the iron.

The system consists of two parts. The central part (wide angle muon system, WAMUS) covers the range of $|\eta| \leq 1$. The forward angle muon system (FAMUS) extends the coverage up to $|\eta| \leq 2$. Each part is composed by scintillators for fast triggering and timing measurements and by proportional drift tubes (PDTs, central part) or mini drift tubes (MDTs, forward region) for precise position measurements, a rough momentum estimate and also for triggering (see Figure 3.12).

In addition, massive shielding structures (see Fig. 3.13) isolate the muon detectors from backgrounds generated near the beampipe and accelerator elements.

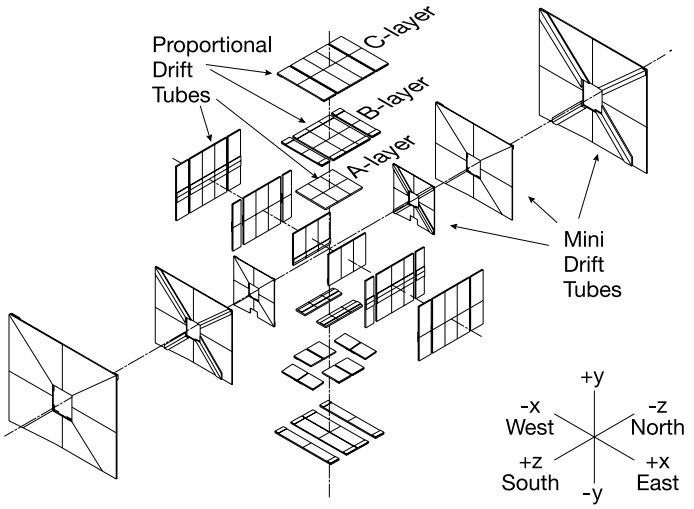

Figure 3.12: Exploded view of the muon wire chambers (from Ref. [59]).

Figure 3.13 shows the layout of the muon system. The PDTs and MDTs are arranged in three layers immediately inside (layer A), immediately outside (layer B) and further outside the toroid (layer C). The PDTs are made of aluminum tubes of 10.1 cm across and a maximum length of 5.79 m, filled with a mixture of 84% Argon, 8% freon and 8% Methane and holding an anode wire of gold plated wolfram (operated at 4.7 kV), parallel to the toroidal field lines, and vernier cathode patches alongside the wire (operated at 2.3 kV). They are arranged to chambers of 3-4 decks with 24 tubes each. The drift velocity is approximately 10 cm/μs and the drift time is of the order of 500 ns. For each PDT hit, the electron drift time, the difference in the arrival time to a neighboring hit and the charge deposition on the inner and outer cathode pads are recorded. The WAMUS is only partially instrumented at the bottom region (for $4 < \phi < 5.5$).

The faster and smaller MDTs consist of eight 1×1 cm^2 cells with a maximum length of 5.83 m, separated by aluminum combs and covered by a stainless steel foil. The tubes are filled with 90% freon-10% methane mixture and hold each a gold plated, grounded wolfram anode wire. They are operated at 3.2 kV. The maximum drift time is lower than 70 ns. Each MDT layer is associated with a scintillator layer.

A muon, identified in the muon system is matched to a central track (SMT, CFT) in order to get a precise momentum measurement. The MDTs contribute significantly to the muon momentum resolution at $\eta > 1.6$, where the tracking relies on the SMT.

Layers of fast scintillation counters are positioned alongside the PDTs and MDTs of layers A, B and C.

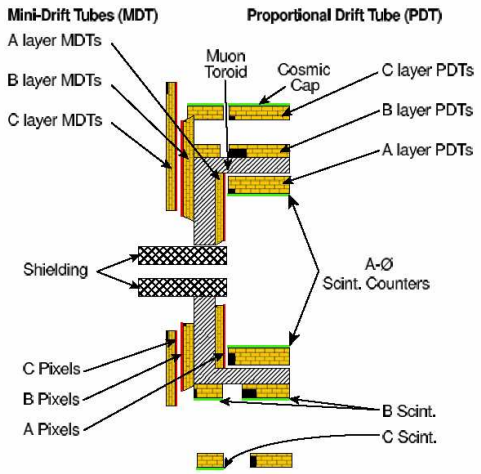

Figure 3.13: Schematic of the muon detector.

3.2.7 The forward-proton detector

The forward proton detector (FPD) measures proton and antiproton scatterings at small angles, that are missed by the main DØ detector.

The detector consists of a series of momentum spectrometers, that make use of the fields of accelerator magnets and of position detectors along the beam line. The position detectors are housed in special stainless steel containers (*Roman pods*) and can be moved away from the beam during instable beam conditions. The Roman pots are arranged in groups within stainless steel chambers (*castles*). The FPD consists of 6 castles with 18 Roman pots located at various distances from the interaction point.

3.2.8 The luminosity monitor

The luminosity monitor (LM) measures the rate of inelastic $p\bar{p}$ collisions in order to determine the Tevatron luminosity at the DØ interaction region. It also measures beam halo rates, makes a fast measurement of the z-position of the interaction vertex and identifies beam crossings with multiple $p\bar{p}$ interactions.

Figure 3.14 shows the location of the detectors in front of the end calorimeters at $|z| = 140$ cm, covering the region of $2.7 < |\eta| < 4.4$. Each LM corresponds to a circular array of twenty-four plastic scintillation counters with PMT readout.

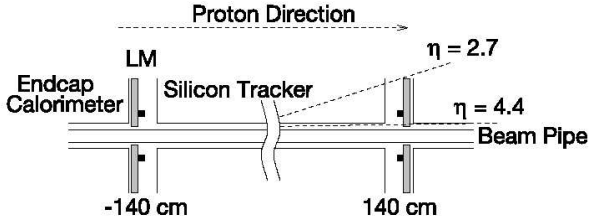

Figure 3.14: Schematic drawing showing the location of the LM detectors (from Ref. [59])

3.3 The trigger system

Due to the large inelastic cross section (approximately 70 mb, see Section 4) the collision rate is too large for each inelastic event to be recorded. DØ uses a three stage trigger system in order to select the interesting physics events. Figure 3.15 gives an overview over the trigger system. The first level (L1) consists of hardware trigger elements that reduce the data flow from approximately 2 MHz to 1.6 kHz within 5 μs. The second level (L2), a system of hardware engines and microprocessors, combines the information from different subdetectors in order to reduce the rate within 100 μs to 1 kHz. The software of the third stage (L3) runs on a farm of microprocessors. It performs within 200 ms a fast reconstruction on the full precision readout in order to reduce the data rate to 50 Hz, a limit given by the offline reconstruction capabilities. Figure 3.16a shows a block diagram of the DØ trigger system with the arrows indicating the flow of trigger-related data. The triggers are configured by a list of individual triggers that are defined by a set of requirements at L1, L2 and L3 (*trigger list*). This section gives a brief overview over the trigger system. The electron trigger chain will be discussed in more detail in section 6.

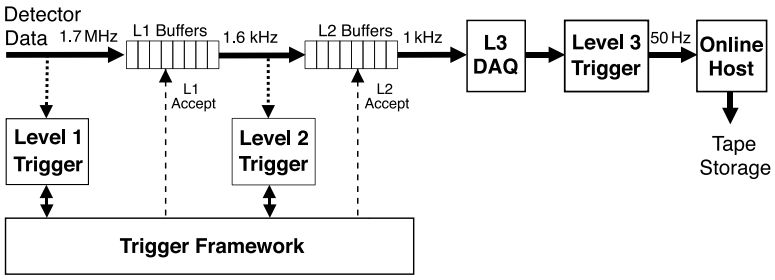

Figure 3.15: Overview of the DØ trigger and data acquisition system (from Ref. [59]).

The L1 trigger

In order to provide a dead-time less trigger decision within 5 μs, the L1 is implemented in a framework of field programmable gate arrays (FPGAs), which make their decisions based on simple objects created in the individual subdetectors from prompt detector data.

Figure 3.16a shows a block diagram of the DØ L1 and L2 trigger system. The calorimeter trigger (L1Cal) looks for energy deposition patterns exceeding programmed limits on transverse energy deposits. Basic trigger objects are the summed transverse energy deposition within the electromagnetic layers or the hadronic layers of a 0.2×0.2 calorimeter cell tower. The trigger coverage has been increased during the first two years of data taking from $|\eta| < 0.8$ to $|\eta| < 3.2$. The central track trigger (L1CTT) reconstructs the

(a) (b)

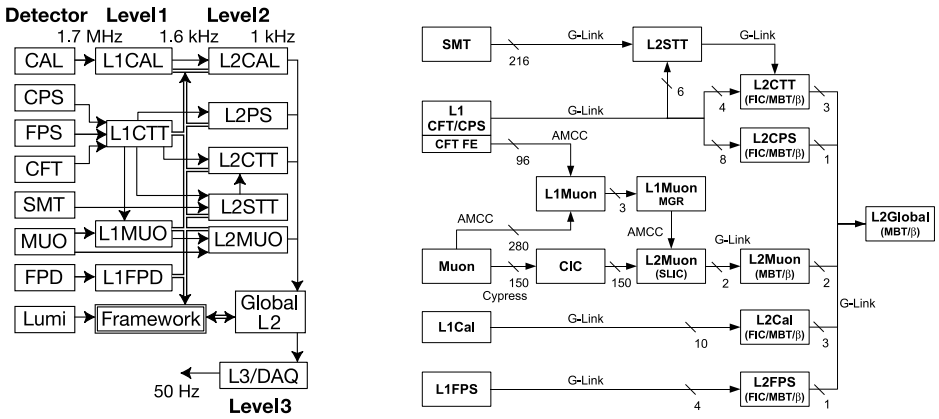

Figure 3.16: (a) Block diagram of the DØ trigger system and (b) L2 data paths and connections (from Ref. [59]).

trajectories of charged particles and measures their transverse momentum using fast discriminator data provided by the three scintillator based detectors (CFT, CPS and FPS). The objects are axial tracks in CFT and CPS, which are derived by comparing the CFT fiber information in a 4.5° sector in ϕ with a large set of predefined track patterns. The

forward tracks are derived from hits in FPS fiber layers. The trigger also calculates the phi-isolation of the tracks. The CFT part of the L1CTT has been fully commissioned and included into the data taking in June 2003 (trigger version 12). The CPS information has been included in summer 2004 (trigger version 13) after the data-taking for this analysis.

The muon trigger (L1Muon) looks for patterns consistent with muons using hits from wire chambers, muon scintillation counters and tracks from the L1CTT. The forward proton detector trigger (L1FPD) selects events in which the outgoing beam particles pass through one or a combination of the nine FPD scintillator spectrometers. If one of the trigger criteria of the configuration is fulfilled, the full event data is moved into the L2 buffer awaiting the L2 decision.

The L2 trigger

The L2 trigger is composed by preprocessing hardware engines and microprocessors, associated with a specific subdetector, that use data from front ends and L1 trigger processors in order to form physics objects. A global processing stage (L2Global) combines the preprocessor information in order to test for correlations across the detector subsystems and derive the trigger decision. A positive L2 decision tags the buffered event for full readout and further analysis in the L3 trigger. Figure 3.16b gives an overview over the preprocessor information that goes into the global processor.

The calorimeter preprocessor (L2Cal) identifies jets and electrons/photons and calculates the missing transverse energy for the global processor based on clusters of trigger towers around seed towers. The algorithms calculate the total energy, the isolation of the seed tower and the electromagnetic fraction of specific tower-combinations. The muon preprocessor (L2Muon) uses calibration and precise timing information in order to enhance the purity of the muon candidates. The preshower preprocessor (L2PS) uses the L1 PS clusters (CPS axial clusters, CPS stereo clusters and FPS clusters) in order to calculate the $\eta - \phi$ location and match the objects with CFT tracks. The CTT preprocessor (L2CTT) combines inputs from the L1CTT and the L2STT. The L2CTT refines the p_{T} measurement and calculates the azimuthal angle based on the full L1 information. The L2STT performs a pattern recognition in the SMT data. It improves the p_{T} measurement of the CTT tracks and measures the impact parameter in order to tag B-mesons.

The L2Global stage makes trigger decisions by creating global physics objects from a combination of the preprocessor objects and imposing cuts according to the configuration information from the trigger list. The information which of the L2 event criteria from the configuration (including the associated L1 criteria) are fulfilled, is stored in trigger bits (L1L2bits).

The L3 trigger

Upon a positive L2 decision, the L3 trigger, a fully programmable object oriented software trigger which runs on a CPU farm, receives the full precision readout of the detector in order to perform a fast reconstruction of the event and make a final trigger decision within 200 ms. Its decisions are based on complete physics objects as well as on the relationships

between such objects, which are generated by filter tools (based on reference parameter inputs from the trigger list) upon request from one of the filters. The filters apply simple cuts on the tool results, according to the trigger list configuration. An individual trigger corresponds to a L3 filter script that requires a certain L2 bit and runs a logical AND of several L3 filters. A logical OR of L3 filters is not possible. Figure 3.17 gives an example of a L3 execution tree.

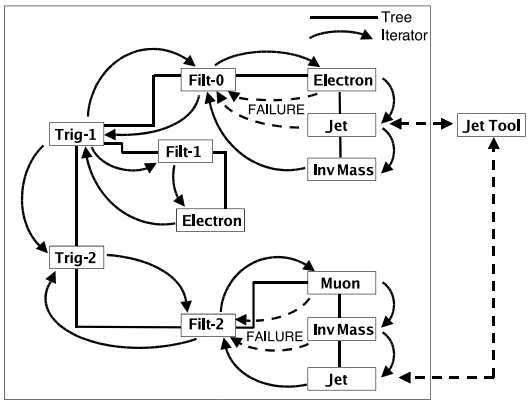

Figure 3.17: Example of a L3 execution tree (from Ref. [59]).

The jet tools perform simple cone algorithms based on calorimeter precision readout and on the primary vertex position. The electron tool is based on a $\Delta\mathcal{R} < 0.25$ cone jet with a minimum electromagnetic fraction and transverse shower shape requirements. A preshower match (in trigger versions > 12) or a spatial match to a L3 track can be required in order to further reduce the background rate.

The L3 muon tool uses wire and scintillator hits to reconstruct local muon track segments inside and outside the toroid. Scintillator hits are fitted along the track to the particle's velocity in order to improve the rejection of cosmic muons. The local muon can be matched to a central track in order to improve the momentum resolution. In addition, calorimeter isolation can be performed.

The missing transverse energy filter uses the corrected calorimeter cell energy and calculates the vectorial sum, the azimuthal angle and the scalar sum of the missing transverse energy. The HT tool calculates the scalar sum of L3 jets.

The L3 tracking uses CFT and SMT information. The CFT tracking performs a link-and-tree algorithm which connects hits from adjacent layers, starting with a seed in the outer layer. The longest extended path is stored as track candidate. CFT tracks are also used for determining the primary vertex. The SMT tracking connects segment paths of neighboring hits within a specified azimuthal angle, starting with a seed from an earlier tool's candidate or from hits in the outermost SMT layer and looking for the longest paths with the smallest χ^2. A global (CFT+SMT) high-momentum track finder starts from axial CFT seeds propagated towards the SMT by a linear fit in R-ϕ. Stereo clusters

are matched using a histogramming method. Global L3 tracks are used in electron and muon filters. The data flow from the readout crates to the processing nodes is controlled by the *L3DAQ* which forms part of the data acquisition system.

3.3.1 Data acquisition and event reconstruction

The data acquisition (DAQ) consists of the L3DAQ and the *online host system*, which receives event data from the L3 nodes and distributes that data to logging and monitoring tasks. Figure 3.18 shows a schematic of the architecture of this system. The L3 data is tagged with a data stream information and sent to a *collector* which distributes the events destined for physics analysis to different *data loggers* according to their stream tag. They write the data to files including meta data for the storage in a database, the mass storage system *ENSTORE*, which is accessed via the interface *SAM*. A copy of each event is sent to a *distributor*, which provides real-time event data for monitoring purposes. A diagnostic secondary path (*SDAQ*) bypasses the L3DAQ and is used in commissioning and calibration of detector components. The raw data is reconstructed with the software D0RECO [61]. The software provides two types of output: The DSTs (data summary tier) contain all event information that is necessary to perform an analysis including limited re-reconstruction of physics objects and correspond to approximately 150 kb per event. Dropping a part of the information and compressing the remaining data yields the summary format TMB (thumbnail) of approximately 20 kb per event, which provides sufficient information for most of the ongoing analyses. The reconstruction is discussed in more detail in Section 7.

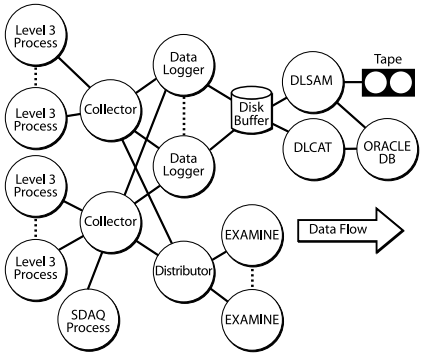

Figure 3.18: The online host system (from Ref. [59]).

3.3.2 Slow control

The DØ experiment uses EPICS (Experimental Physics and Industrial Control System), an integrated set of software building blocks for implementing a distributed control system which has to be extended in order to satisfy the slow-control needs of the detector. EPICS uses a distributed client-server architecture, consisting of host-level nodes (clients) that

run application programs and input/output controller (IOC) nodes (server) that interface directly with the detector hardware.

Figure 3.19 shows the architecture and the components of the controls and monitoring system. The *SES* collects and distributes all changes of state. The current (alarm) state of a detector component is relayed to users by the alarm display. The alarm watcher automatically pauses the run, if data quality is compromised.

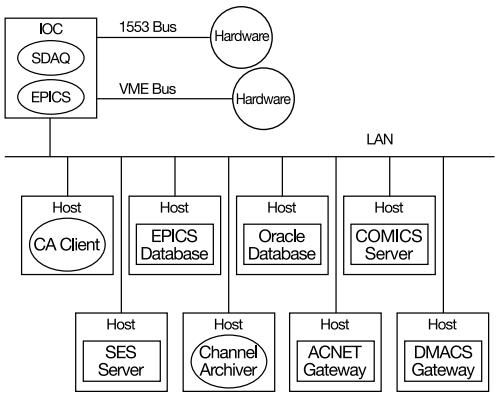

Figure 3.19: Organization of the control system components (from Ref. [59]).

The configuration of the detector is managed by the server program *COMICS*. The detector is represented as a tree, with nodes at successively deeper levels corresponding to smaller organizational units of the detector. The terminal (action-) nodes manage the configuration of this specific unit. A common PYTHON framework provides templates for visual displays (GUIs) that are used in monitoring and controlling detector components.

4 Phenomenology of $\mathrm{p\bar{p}}$ processes

This Section gives a brief overview over the processes at hadron colliders which are of interest for this analysis. It starts with the discussion of general terms and issues which are present at hadron colliders. These phenomena have to be taken into account in the simulation of physics events, which is discussed subsequently.

4.1 General Issues

4.1.1 Luminosity

The event rate $\mathrm{R} = \frac{\mathrm{dN}}{\mathrm{dt}}$ of a certain physical process is the product of the *cross section* σ, which depends on the type of the interaction and the energy scale, and the *luminosity* $\mathcal{L}$, a collider parameter, which is related to the number of particles that cross the collision region per unit of area and time.

$$\mathrm{R} = \sigma\mathcal{L}. \tag{4.1}$$

If two bunches containing n_1 and n_2 particles collide with frequency f, the luminosity is:

$$\mathrm{f}\frac{\mathrm{n}_1\mathrm{n}_2}{\mathrm{A}_{\mathrm{eff}}} \tag{4.2}$$

where $\mathrm{A}_{\mathrm{eff}}$ denotes the effective collision area given as

$$\mathrm{A}_{\mathrm{eff}} = 4\pi\sigma_{\mathrm{x}}\sigma_{\mathrm{y}} \tag{4.3}$$

where σ_{x} and σ_{y} are the standard deviations of the Gaussian beam profiles in horizontal and vertical direction. Luminosity is expressed in units of $\mathrm{cm}^{-2}\mathrm{s}^{-1}$. The total number N of events follows from the integrated luminosity:

$$\mathrm{N} = \sigma \int \mathrm{L}\,\mathrm{dt}. \tag{4.4}$$

Cross sections are expressed in units of *barn* with 1 barn = $10^{-28}\mathrm{cm}^2$. Since the typical cross sections of processes of interest at the Tevatron are in the range of picobarn (pb) or femtobarn (fb), the integrated luminosity is mostly quoted in units of pb^{-1} or fb^{-1} .

4.1.2 Factorization

Cross sections for processes that involve strong interactions can be factorized into a short-distance (hard) part which is calculable with perturbative QCD and depends on the particular process and a long-distance (soft) part which is not calculable with perturbative QCD

but universal and thus measurable experimentally. The non-perturbative component in the initial state of hadronic interactions is described by *parton distribution functions* (see Section 4.1.3). The soft component in the formation of hadronic final states is described by *fragmentation functions* (see Section 4.1.9). Separation is achieved with the introduction of a *factorization scale* μ_f which characterizes the boundary between the two energy regimes and is usually chosen at the order of the scale Q of the hard interaction. The infrared-divergent higher-order processes (see Section 4.1.5) in the initial state at scales below μ_f are absorbed into the PDFs.

The factorization is applicable in all orders of the perturbation expansion. The dependence of the cross section on the choice of the factorization scale decreases with increasing order of the calculation. The complete perturbation expansion is independent of the choice of μ_f. The variation of the cross section with the factorization scale yields an estimate of the size of higher-order corrections.

Renormalization (see Section 1.1.1) of the QCD expansion also introduces an arbitrary scale μ_R at which the coupling constant of the strong interaction is evaluated. Both scales are usually chosen to be equal (*factorization/renormalization scale*).

4.1.3 Parton distribution functions

A high-energy proton-antiproton collision at a center-of-mass energy $\sqrt{s}$ is considered as an interaction of constituents (partons) of the proton (valence quarks, sea quarks and gluons). The effective squared center-of-mass energy $\hat{s}$, also identified with the energy-momentum transfer Q^2 of the interaction, depends on the fraction x_1 and x_2 of the momentum carried by the interacting partons:

$$\hat{s} = x_1 x_2 s. \tag{4.5}$$

In order to simulate such an interaction, the distributions $f(x, Q^2)$ of the momentum fraction of the constituents (*parton distribution functions (PDFs)*) have to be known.

The dependence of the PDFs on Q^2 can be explained in a similar way as the evolution of masses and couplings towards their bare values with increasing energy scale (see Section 1.1). At low values of Q^2, an interaction of partons is performed by the partons and their surrounding cloud of gluons and quarks, which carry a part of the effective momentum in the interaction. With increasing Q^2 the measured momentum becomes the momentum of the *bare* parton.

Figure 4.1 shows the present parameterization of the PDFs of valence and sea quarks provided by the CTEQ group [62] for a typical Q^2 region for the processes of interest at the Tevatron. The sea quarks typically carry only a small momentum fraction x of the proton. Electron-proton scattering experiments measure the content of charged partons (quarks) which amounts to approximately half of the total proton momentum. The other half of the momentum is carried by a large number of gluons. Figure 4.1 shows that, on average, gluons carry a low momentum fraction of the proton.

The parton distribution functions for $Q^2 = 10000\,\mathrm{GeV}^2$ presented in Fig. 4.1 are the most up-to-date parameterizations based on results from deep inelastic scattering (DIS) of electrons, muons and neutrinos with nucleons (ZEUS, H1, BCDMS, E665, NMC, CCFR),

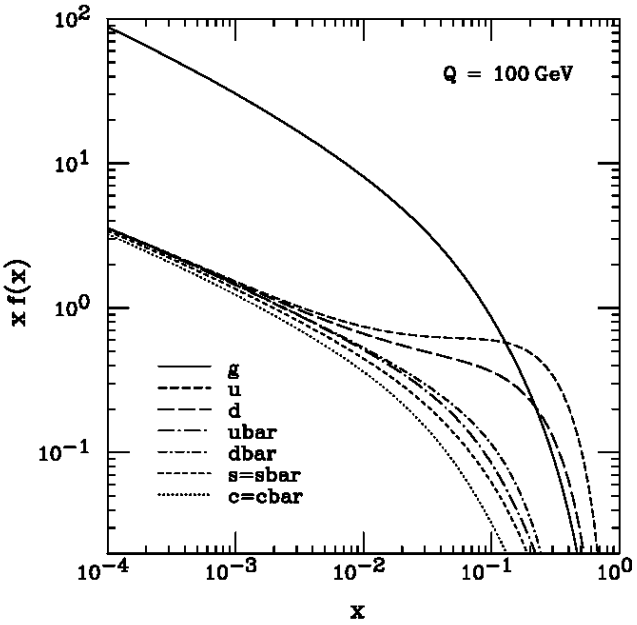

Figure 4.1: CTEQ Product of x and quark and gluon PDFs $f(x,Q^2)$ for $Q = 100$ GeV (version CTEQ6).

the Drell-Yan deuteron/proton ratio in E866 and E605, the W asymmetry from CDF, the inclusive jet cross section from CDF and the differential jet cross section from DØ [62]. The quark PDFs are mainly based on the DIS of electroweakly interacting particles with nucleons whereas the measurement of inclusive and differential jet production cross sections at hadron colliders is crucial to determine the gluon PDF.

In this analysis, CTEQ PDF fits are used for the calculation of the differential inelastic $p\bar{p}$ cross section in the simulation of signal and background final states expected at the Tevatron. In addition to the central PDF fits, the CTEQ group provides 1σ-variations of the PDFs resulting from various uncertainties (*error PDFs*) [62, 63].

4.1.4 Cross section

Figure 4.2a shows a schematic view of the leading order contribution to the electroweak production of leptons in a $p\bar{p}$ collider: $p\bar{p} \rightarrow \ell\ell X$ (Drell-Yan process), which constitutes a very important background for this analysis. The hard scattering process consists of the annihilation of two quarks into a lepton pair $q\bar{q} \rightarrow \ell\ell$. The remaining hadron remnants fragment into hadrons.

The leading order cross section for such a process is given by [64]:

$$\frac{d\sigma}{dQ^2} = \sum_{q,\bar{q}} \int dx_1 \int dx_2 \ \left[f_q(x_1,Q^2) f_{\bar{q}}(x_2,Q^2) + f_{\bar{q}}(x_1,Q^2) f_q(x_2,Q^2) \right] \frac{d\hat{\sigma}}{dQ^2} \qquad (4.6)$$

where $\hat{\sigma}$ is the cross section for the hard process $q\bar{q} \rightarrow \ell\ell$ and f_q and $f_{\bar{q}}$ are the PDFs for the quark and the antiquark. In the case of the Drell-Yan lepton pair production via a virtual

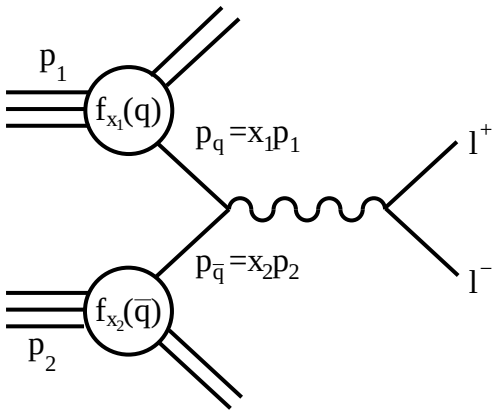

Figure 4.2: Schematic view of the Drell-Yan production of lepton pairs in a $p\bar{p}$ collision.

photon the hard process corresponds to the well-described cross section for electromagnetic quark-antiquark annihilation into a fermion-antifermion pair at a center-of-mass energy $\hat{s} = Q^2 = x_1 \cdot x_2 \cdot s$ taking into account the color combinations:

$$\hat{\sigma} = \frac{4\pi\alpha^2}{9\hat{s}} e_q^2 \tag{4.7}$$

which yields the differential cross section

$$\frac{d\hat{\sigma}}{dQ^2} = \frac{4\pi\alpha^2}{9Q^2} e_q^2 \delta(Q^2 - \hat{s}). \tag{4.8}$$

Figure 4.3 shows the cross sections for selected processes at the Tevatron. The cross section for all interactions that break up the proton structure (the total inelastic cross section) is approximately 70 mb. It is three orders of magnitude larger than the dijet cross section, which in turn is at least four orders of magnitude larger than the cross sections of the physics processes of interest. A typical cross section for the production of SUSY particles is eight orders of magnitude lower than the dijet cross section. As a consequence, sophisticated selections have to be developed in order to separate the interesting processes from the background.

4.1.5 Higher order QCD corrections

The process described in the previous Section, constitutes only the leading order (LO) contribution of a perturbation expansion as described in chapter 1.1. Next-to-leading order QCD corrections for this process, as shown in Fig. 4.4, lead to considerable corrections. The higher order contributions consist of virtual corrections (see Fig. 4.4 d,e,f) and emission (radiation) of real particles (see Fig. 4.4b,c and Section 4.1.6). In a full NLO calculation, the singularities from virtual corrections and the soft and collinear singularities of the real emission, cancel by negative interference such that the cross section receives a finite correction. The same cancellation occurs at all orders of perturbation theory.

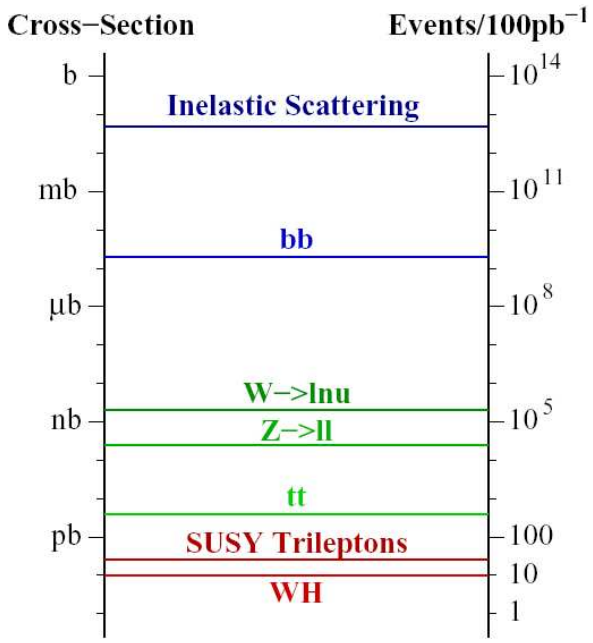

Figure 4.3: Cross sections (left) and number of events expected per 100 pb^{-1} integrated luminosity for selected processes at the Tevatron.

NLO cross sections are available for most of the processes of interest at hadron colliders whereas NNLO calculations have only been performed on a subset of processes so far. Higher order corrections affect not only the total cross section but also the kinematic and angular distributions in the final state. Nevertheless, in many cases, the effects of these corrections are small compared to the desired accuracy of the experiment, such that it is sufficient to simulate kinematic and angular distributions of the process under consideration at LO, use approximations for higher order effects on the topology (see Section 4.1.6) and correct the total cross section with the *K-factor*, the ratio of the higher order and the leading order cross section:

$$\mathrm{K_{NLO}} = \frac{\sigma_{NLO}}{\sigma_{LO}} \tag{4.9}$$

$$\mathrm{K_{NNLO}} = \frac{\sigma_{NNLO}}{\sigma_{LO}}. \tag{4.10}$$

This is the method used in this analysis.

4.1.6 Modeling initial and final state radiation (ISR, FSR)

In a process that contains colored/charged objects in the initial or final state, higher order effects (in particular gluon/photon radiation) result in large corrections not only of the cross section but also of the overall event topology by increasing the amount of final state particles. Since it is not possible to calculate the full perturbation expansion, two approaches exist for modeling these effects [65]:

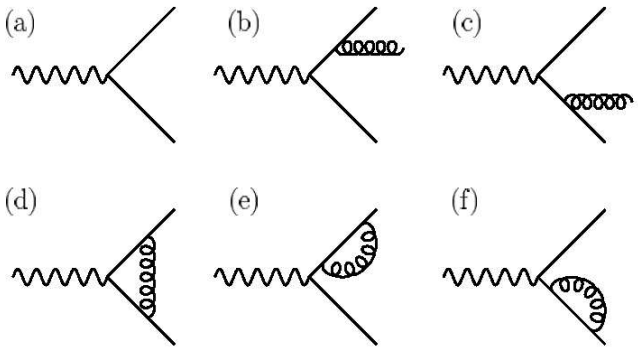

Figure 4.4: NLO QCD contributions for Drell-Yan processes.

- The *matrix element method* calculates amplitudes and phases of the QCD perturbation expansion at a given order in α_s. Currently only a few orders are calculated, such that multiple emissions of soft partons are not covered, whereas the radiation of a few hard partons is well described. The soft phase space region is usually cut out at generator level.
- The *parton shower method* approximates the higher order effects in a probabilistic approach by an evolution in a series of branchings of a parton into daughter partons with momentum fractions z and 1-z. The branching probability is described by the Altarelli-Parisi splitting functions P(z) [66]. Starting from the energy scale of the hard interaction the evolution of branchings is performed forwards (FSR) and backwards (ISR). The parton shower evolution corresponds to the resummation of the leading logarithmic divergent terms in the perturbation expansion for each order in α_s (*leading log approximation*). This leads to a good description of the radiation of collinear and soft partons where these terms are dominant but has limited predictive power for the emission of hard and wide-angle partons. [67]

The choice of one of the approaches is mostly motivated by the physics topic and the kinematic region of interest. The methods can be combined in order to achieve an improved description of a larger phase space region.

4.1.7 Beam remnants

The parton which participates in the hard interaction and its ISR products carry only a part of the energy-momentum of the beam hadron. The remaining part is carried by the hadron remnant. Apart from the momentum fraction in beam direction, the parton of the hard interaction is assumed to have a certain transverse momentum distribution in the hadron (*primordial* k_T), the recoil of which is also taken up by the hadron remnant. The fragmentation of the remnants leads to additional final state products. The products of ISR and beam remnants, are referred to as *underlying event*.

The underlying event is characterized by soft final state products, typically at low angles to the beam pipe, such that usually only a part of the underlying event is registered in the detector. This makes it impossible to reconstruct the initial momentum fraction x of the interacting partons. As a consequence, a final state particle's momentum component along the beam line is meaningless for most analysis purposes. Physics results are usually derived, using the transverse components of energy (E_{T}), momentum (p_{T}) and missing energy ($\not\!\!E_{\mathrm{T}}$).

4.1.8 Multiple interactions

Figure 4.3 shows that the total cross section for inelastic interactions in hadron colliders is several orders of magnitude larger than the cross section for processes of interest at the Tevatron which are connected with a larger energy-momentum transfer (*hard interactions*). A typical bunch crossing is therefore characterized by multiple soft inelastic interactions, the number of which depends on the luminosity and on the center-of-mass energy. This type of events is called *minimum bias event*.

At instantaneous luminosities of $3 \times 10^{31} cm^{-1} s^{-1}$, a typical average value at DØ during the epoch of data taking for this analysis, an average of 0.8 interactions per beam crossing is expected at DØ. These interactions are also present in events which are triggered by a hard interaction, and have to be included into the simulation. Final state particles from additional interactions can normally be identified by the fact that they do not come from the primary vertex.

If the readout of a detector signal for one event lasts longer then the bunch spacing, as is the case with the DØ calorimeter (see Section 3), the signal includes information from more than one inelastic interaction (*pile-up*). This fact is considered in the design of the readout electronics (see Section 3) and has to be modeled in the event simulation.

4.1.9 Fragmentation

Due to the confinement (see Section 1.1) the quarks and antiquarks created in an interaction cannot propagate freely but have to form colorless states (mesons and baryons). This process is called fragmentation. It cannot be calculated from perturbative QCD but is described in a probabilistic and iterative way in terms of branchings parameterized as *fragmentation functions* $\mathrm{d}_{\mathrm{q}}^{\mathrm{i}}(\mathrm{z}, \mathrm{E})$ which correspond to the probability that a quark produces a hadron i with a fraction (z) of the quark energy E. They have been measured experimentally at LEP [8]. The most successful approach is the *string fragmentation* [65, 67]. It models the linear confinement by a string with a certain energy density (energy per unit length) between the partons that are moving apart. Quark-antiquark pairs are created along the string, such that the string breaks up into hadrons. The products of the fragmentation process are stable and instable hadrons. The decay of the instable hadrons has to be simulated in the classical way, using decay matrix elements or results of measurements.

4.2 Event simulation

The complexity of the processes involved in a particle collision and the identification of the collision products makes a direct comparison of theoretical predictions and experimental results very complicated. This problem is solved by deriving explicit predictions for experimental quantities via a MC integration of the collision process.

The procedure starts with generating the 4-vectors of the final products expected from the interaction of interest, using Monte-Carlo (MC) techniques to select the relevant variables according to the predicted probability distributions. In the next step, they are processed through a detector simulation, the output of which has the same format as real measurements and can be further processed in exactly the same way as the real data. The simulated events are referred to as *MC events* in the following.

4.2.1 Event generation

Most of the signal and background processes of this analysis are generated with PYTHIA [65] version 6.2 and 6.3. The generator uses a string fragmentation model implemented in the program JETSET [65]. The software package TAUOLA [68] is used to simulate τ decays.

PYTHIA can simulate all Standard Model processes, that result from e^+e^-, $p\bar{p}$, pp and ep collisions. It generates in addition processes expected from new physics, as for example the production of SUSY particles. For most of the processes LO matrix elements are used. A PDF version of choice can be included. This analysis uses MC samples produced with the PDF versions CTEQ4-6.

ISR and FSR processes are simulated with the parton shower method (see Section 4.1.6), which is a reasonable approach for many physics processes that are important for this analysis. Problems may arise in simulating background processes where one or more leptons in the final state are faked by jets or photons with large transverse momenta (see Section 5.2). Implications of these drawbacks are discussed further in Section 9.

A better simulation of the problematic events is expected from the generator ALPGEN [69]. It uses tree-level matrix elements for multiparton final states which cover the multiple radiation of hard particles. ALPGEN is interfaced with PYTHIA, which includes parton showering for the emission of soft and collinear particles and the fragmentation into hadrons.

4.2.2 Detector simulation

The detector simulation is handled by the programs D0GSTAR [70] and D0SIM [71] in the DØ software software version p14.

The D0GSTAR program runs GEANT, version 3.21 [72], a software tool that simulates the interaction of high-energy particles with the detector material. It also models the decay of long-lived particles in the detector. This stage is the most time-consuming part of the MC production process, since the software has to model the particle interactions in great detail, including the ionization in the silicon detector and in the scintillating fibers, the development of electromagnetic and hadronic showers, interactions with the material of

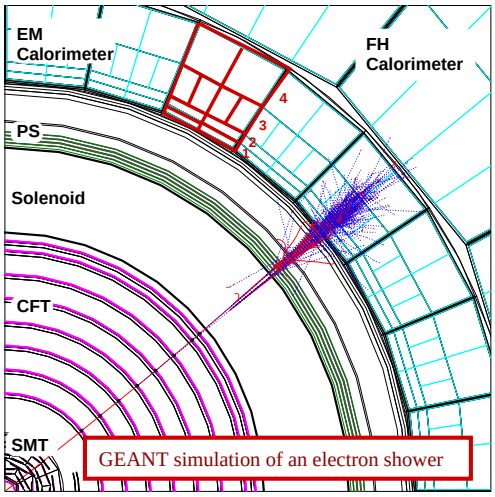

Figure 4.5: GEANT simulation of an electron in the DØ detector.

the superconducting coil and the border of the cryostats (see Section 3). Fig. 4.5 shows the simulation of an electron shower in the DØ detector. The D0GSTAR package simulates also the response of the readout electronics.

The D0SIM software performs the remaining steps that are necessary in order to bring the simulation data to the same level of detail as the data that is taken by the DAQ. It adds minimum bias events, Poisson distributed around a chosen mean value, in order to simulate the multiple interactions (see section 4.1.8). With the number of interactions depending on the luminosity, ideally a series of MC sets should be produced, each corresponding to a certain luminosity. Due to the limited computing capacity, the MC is produced with a fixed number of minimum bias events, that corresponds to the average luminosity for a certain data taking period. The MC sets used in this analysis are generated with a mean of 0.8 minimum bias events. D0SIM also adds calorimeter pile-up from previous crossings (see Section 4.1.8) and includes the simulation of SMT, CFT and calorimeter noise.

The D0SIM output has the same format as real data events but contains additional generator level information. It is reconstructed with the same reconstruction software D0RECO [61], which is used for real data. The trigger simulation D0TRIGSIM can be run in parallel. It models the L1 trigger and runs L2 and L3 algorithms on the output from the detector simulation and the L1 simulation.

A detailed list of the MC samples used for the analysis and the verification of the MC modeling is presented in Section 9.

5 Production and decay of SUSY particles and Standard Model background

This section describes the production and decay processes which result in the signal final states of interest for this analysis and presents the background processes which are expected in the framework of the Standard Model.

5.1 Production and decay of SUSY particles

SUSY particles are produced at hadron colliders in different types of processes. Squarks and gluinos are mainly produced in strong interactions. Electroweak interactions of quarks result in addition in charginos, neutralinos and sleptons. Since the couplings of the SUSY particles are identical to the couplings of their Standard Model partners, cross sections for SUSY particles are comparable to the cross sections of their partners at the same value of the energy-momentum transfer Q^2. Within R-parity conserving models, SUSY particles are produced in pairs. Each particle decays directly or via cascades into Standard Model particles and the LSP, which results in final states with jets, leptons and missing transverse energy.

If squarks and gluinos are sufficiently light, the strong production of these particles [73] is expected to be the dominant source of SUSY particles at hadron colliders, followed by the electroweak production of charginos and neutralinos. In GUT-constrained SUSY models, the squarks and gluinos are typically heavier than the uncolored SUSY particles (see Section 1.2.4) and the searches for SUSY particles at LEP II [24] result in lower limits of the order of 300-400 GeV on the squark and gluino masses. At this mass scale, the cross section for colored particles at the Tevatron is very low, which makes the production of light charginos and neutralinos an important source of SUSY particles [21].

5.1.1 Production of charginos and neutralinos at hadron colliders

Charginos and neutralinos are produced at hadron colliders at leading order in electroweak s and t-channel reactions of a quark and an antiquark [74] (mainly two valence quarks at the Tevatron) similar to the Drell-Yan process described in Section 4.1.4. The relative contribution of the s and t-channel amplitudes depends on the chargino and neutralino field content and on the squark masses. The vector boson in the s-channel couples to the gaugino and higgsino components of the charginos and neutralinos, whereas the squarks in the t-channel exchange, which are partners of the light quarks, couple mainly to the gaugino components. The t-channel contribution is suppressed for large squark masses. This leads to an enhanced cross section in the case of destructive interference between the amplitudes.

Fig. 5.1 shows the LO and NLO graphs from the QCD perturbation expansion for the production of two charginos/neutralinos. The NLO contributions increase the cross sections for charginos and neutralinos. NNLO corrections are expected to be small [74].

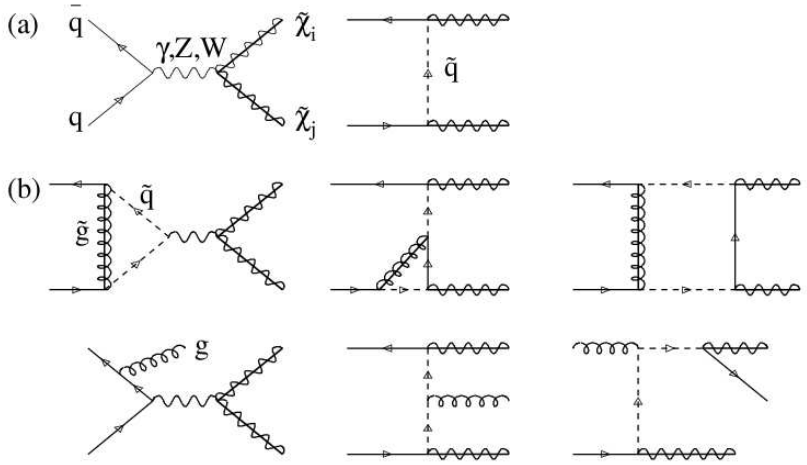

Figure 5.1: (a) LO and (b) NLO contributions to the associated production of charginos and neutralinos, from Ref. [74].

The NLO cross sections in the gaugino region are shown in Fig. 5.2a as a function of the gaugino mass for three processes of interest at the Tevatron: the pair production of the lightest chargino, the associated production of the lightest chargino and the second lightest neutralino and the pair production of the second lightest neutralino. All other combinations have either a very low cross section or lead to final states with a low multiplicity of particles which cannot be detected or separated from the background. The production rate decreases with increasing chargino/neutralino masses because the cross section for the hard interaction decreases with $\hat{s}$ and the density of valence quarks decreases with large values of x (see Section 4.1.4). Fig. 5.2b shows the resulting NLO K-factors.

The largest cross section is expected for the pair production of the lightest chargino and the associated production of the lightest chargino and the second lightest neutralino. In the mass range beyond the lower bounds of LEP II, between 100 GeV and 150 GeV, charginos and neutralinos are produced with cross sections of the order of 0.1 pb – 1 pb.

5.1.2 Decay of SUSY particles

In R-parity conserving SUSY models, charginos and neutralinos decay typically very rapidly directly or via cascades into the LSP and Standard Model particles, which yields a characteristic detector signature. The decays are mediated by gauge bosons or sfermions. Since the decays of charginos and neutralinos show substantial similarities they are discussed in parallel.

Figure 5.3 shows the decay modes of interest for a heavier neutralino. In large regions of the SUSY parameter space the 3-body decay via a virtual Z boson into a fermion pair

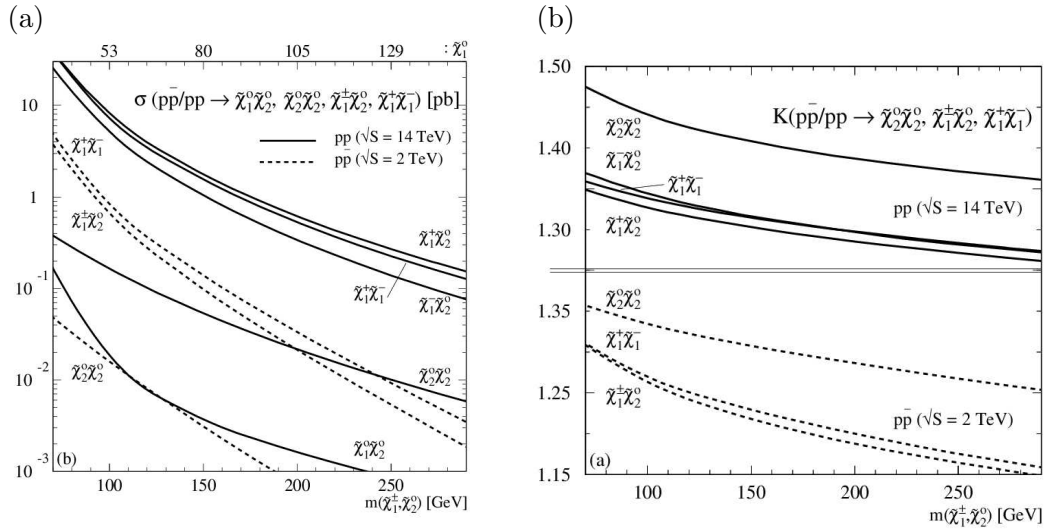

Figure 5.2: (a) NLO predictions for the cross section for the production of charginos and neutralinos and (b) the resulting K-factors for the LHC center-of-mass energy (continuous lines) and the Tevatron center-of-mass energy (dashed lines) from Ref. [74].

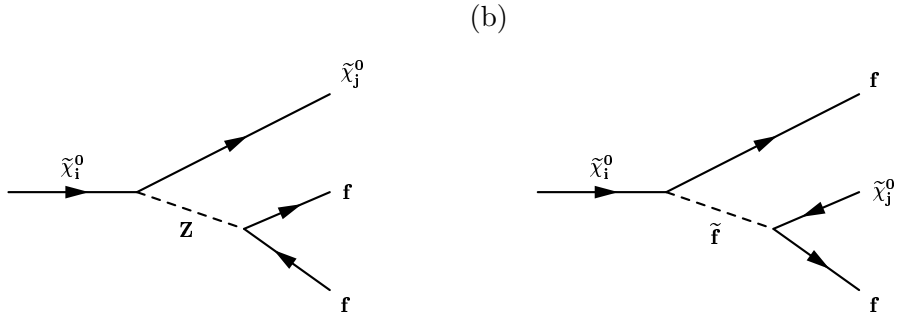

Figure 5.3: Decay modes of the neutralino (a) via a Z boson and (b) via a sfermion for i > j > 0.

and a lighter neutralino is dominant (see Fig. 5.3a). If the mass difference between the neutralinos is large enough, two body decays into the lighter neutralino and a real Z are possible, with the subsequent decay into a fermion pair.

The corresponding decay mode for charginos is shown in Fig. 5.4a. A chargino can decay via a virtual W boson into two fermions and a lighter neutralino. If the mass difference between the chargino and the lighter neutralino is large enough, 2-body decays into the lighter neutralino and a real W become dominant, with the subsequent decay of the W into two fermions. In case of leptonic W decays, the final state consists of the light neutralino, a charged lepton and a neutrino.

If sfermions are light enough or if the decay via a Z or W boson is suppressed, sfermion mediated 3-body decays become important (see Fig. 5.3b and 5.4b). The neutralino couples to a sfermion and its Standard Model partner whereas the chargino decays into a sfermion and the Standard Model weak isospin partner. The sfermion decays into its

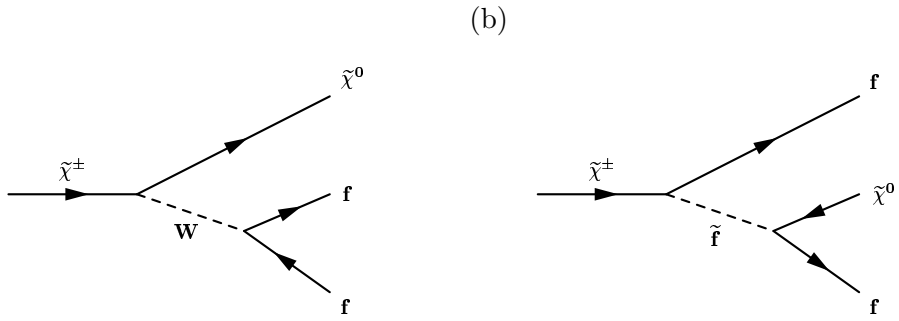

Figure 5.4: Decay modes of the chargino (a) via a W boson and (b) via a sfermion.

partner fermion and a lighter neutralino. The resulting final state differs from the one expected from gauge boson mediated decays only in the kinematics of the decay products. If the sfermion mass is low enough, 2-body decays into a real sfermion and a fermion become dominant.

In these processes, the branching ratio of the individual fermion types in the final state depends on the sfermion masses, the sfermion chirality and the field contents of the neutralino or the chargino. Wino-like neutralinos and charginos couple preferably to the left handed sfermions and fermions, higgsino-like neutralinos and charginos prefer the heavy leptons and photino-like neutralinos prefer the charged sfermions and fermions. A decay via a real sfermion or gauge boson is favored if it is kinematically allowed.

If the lighter neutralino is not the LSP, subsequent decays of the lighter neutralino can lead to further fermions in the final state. This process is of no relevance at the Tevatron because of the low cross section expected for the production of heavier neutralinos and charginos.

The detector signature which results from the production of two neutralinos or charginos is characterized by missing transverse energy carried by LSPs and neutrinos. In addition, various combinations of jets and charged leptons are expected in the final state. The pair production of the lightest charginos leads to final states with four jets, two jets and one charged lepton or two charged leptons only. The associated production of the lightest chargino and the second lightest neutralino leads to final states with four jets, two jets and one charged lepton, two jets and two charged leptons or three charged leptons only. Among these channels, the final state with three charged leptons (*trilepton final state*) stands out because of its low Standard Model background, which makes it the most promising channel for searches for charginos and neutralinos at the Tevatron.

The analysis presented in this thesis searches for the associated production of the lightest chargino and the second lightest neutralino in final states with two electrons, a third lepton and missing transverse energy ($\mathrm{e} + \mathrm{e} + \ell$). Results of searches in additional leptonic final states are reported in Ref.s [75] – [79]. The results of the analysis are combined with the results of searches for SUSY in the $\mathrm{e} + \mu + \ell$ final state [75], the $\mu + \mu + \ell$ final state [76] and a final state with two like-sign muons [77] (LS μ+μ).

Stau mixing effects

The leptonic final states are in general not equally composed by the three lepton generations. Due to the large mass of the Standard Model partner, the masses and field contents of the staus can be different from the values for the other two slepton generations, which leads to different branching ratios for final states with taus and final states with electrons or muons.

As described in Section 1.2.3, the off-diagonal elements in the stau mass matrix (see Eqn. 1.43), which are proportional to $A_\tau - \mu \tan\beta$ introduce a mixing between the two stau chirality states. As a consequence, the lightest stau can become considerably lighter than the lightest (the right-handed) selectron and smuon. It acquires, in addition, a left-handed component which couples to the $\mathrm{SU(2)_L}$ gauginos (important in the gaugino region, see Section 1.2.3). This leads to an enhanced BR into final states with τ-leptons for large values of $|A_\tau - \mu \tan\beta|$. If A_τ and μ are at the order of the electroweak scale, the degree of stau mixing is mostly dependent on $\tan\beta$. Figure 5.5 shows the dependence of the gaugino and slepton masses and of $\sigma \times$ BR into the individual lepton final states on the degree of stau mixing (introduced via scanning $\tan\beta$). The scan is performed for low values of m_0, where the light sleptons are lighter than the second lightest neutralino which, as a consequence, decays into a light slepton and its Standard Model partner (2-body decays). For large values of $\tan\beta$, final states with τ-leptons are dominant.

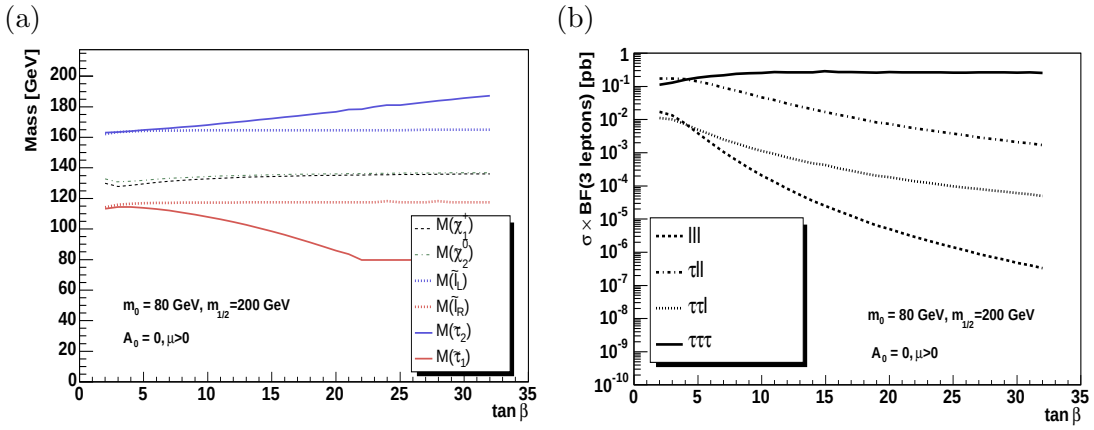

Figure 5.5: (a) Masses of SUSY particles and (b) total cross section of the associated production of the lightest chargino and the second lightest neutralino into various trilepton final states as a function of $\tan\beta$ for $\mu > 0$, $m_{1/2} = 200\,\mathrm{GeV}$, $m_0 = 100\,\mathrm{GeV}$ and $A_0 = 0$ (from Ref. [80]).

5.1.3 Signal topologies

If both the chargino and the neutralino decay into charged leptons, the associated production of the lightest chargino and the second lightest neutralino leads to final states with three charged leptons (two opposite sign leptons of the same generation and another lepton of any generation), one neutralino and two LSPs. The four leading order graphs for this process are presented in Fig. 5.6.

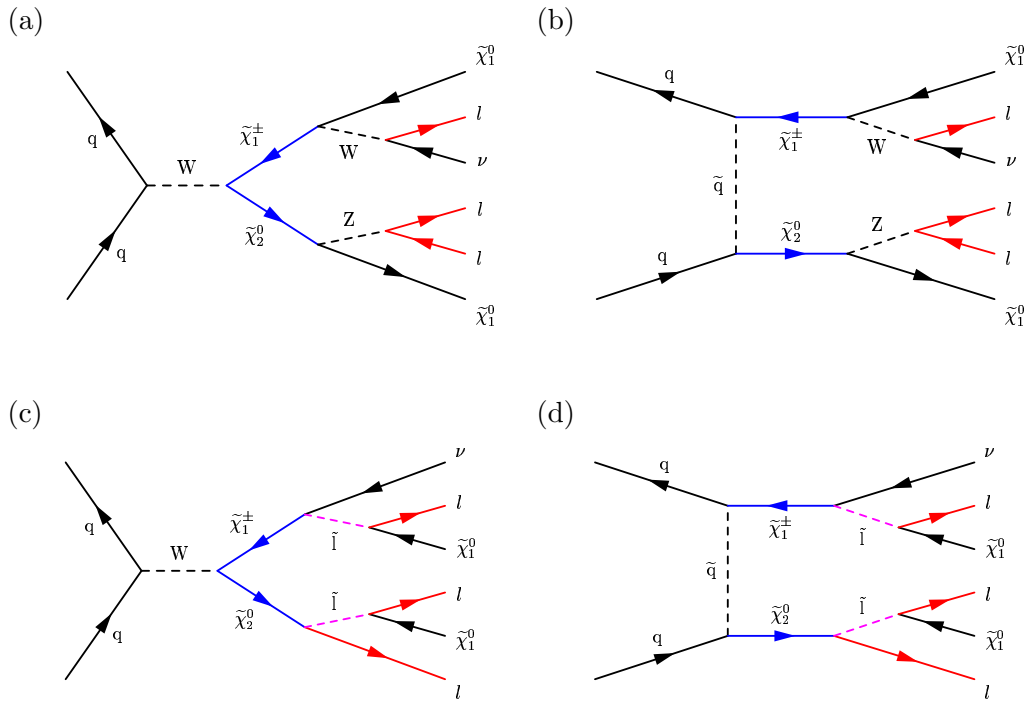

Figure 5.6: Production and decay modes for associated chargino/neutralino production in trilepton final states.

The phase space available for the three leptons depends strongly on the mass differences involved. Figure 5.7 shows the distribution of the transverse momenta of the tree final state leptons (electrons or muons), as generated with PYTHIA for three slepton mass scenarios in mSUGRA models with a chargino mass of 106 GeV and a neutralino mass of 110 GeV. Fig. 5.7a corresponds to the case that the slepton mass is larger than the gaugino masses such that the gauginos decay via 3-body processes. If the slepton is considerably lighter than the gauginos, 2-body decays into real sleptons are dominant (see Fig. 5.7c). Both scenarios lead to three leptons with asymmetrically distributed transverse momenta, which are usually large enough for the event to be reconstructed with high efficiency. Problems occur at the transition between the two decay scenarios. Figure 5.7b shows the momentum distribution for a slepton mass slightly smaller than the gaugino masses. In this case the 2-body decay of the neutralino becomes dominant but the phase space for the lepton which is produced together with the slepton is very small, which leads to a very asymmetric momentum distribution of the two leptons which stem from the neutralino.

Search for SUSY in electron/muon final states at the Tevatron

Due to stau mixing (see Section 5.1.2) large regions of the SUSY parameter space are characterized by final states dominated by tau leptons. Electron-muon based analyses are most sensitive in two regions of interest:

- low degree of stau mixing: $\mu \tan\beta \approx A_\tau$

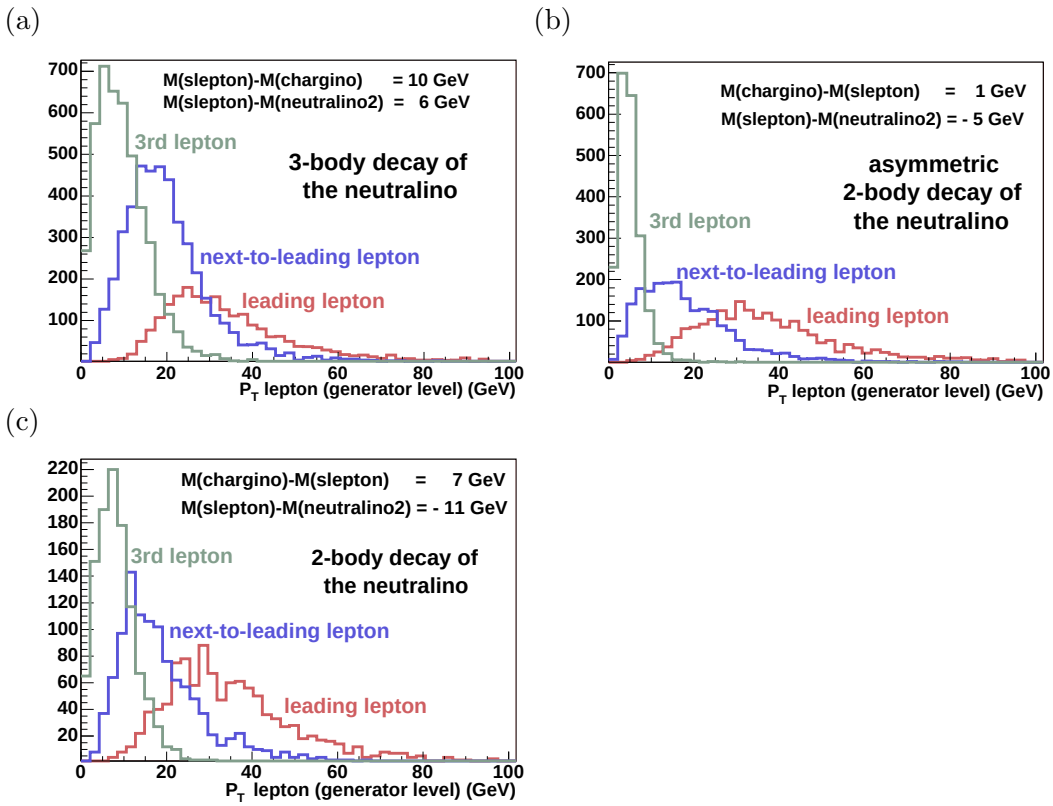

Figure 5.7: Distribution of the transverse momenta of leptons resulting from the associated production of charginos and neutralinos for different mass relations.

- large slepton masses (large m_0 in GUT models) $\Rightarrow$ stau-selectron mass differences are small compared to the slepton mass scale and gaugino decays via virtual sleptons are suppressed.

Both scenarios are consistent with GUT-constrained MSSM models in the light of the results from LEP II searches, electroweak precision measurements and cosmological data (see Section 1.2.6). The first region contains the scenarios where the dark matter relic density is adjusted by direct neutralino annihilation and neutralino-stau co-annihilation and the second region of interest corresponds to the focus-point scenario (see Section 1.2.6). A large mass of the lightest Higgs boson, beyond the LEP II limit, is possible with a large average stop mass (see Section 1.2.3), which corresponds to large values of $m_{1/2}$ (in the first case) or large m_0 (in the second case).

Since the scalar mass unification is only desired but does not follow from theoretical requirements or experimental results, this requirement can be dropped or loosened such that the stop mass is decoupled from other SUSY masses and the Higgs boson can be heavy for models with both light sleptons and light charginos and neutralinos. The relic density of the dark matter is adjusted in these models by direct neutralino annihilation (bulk region, see Section 1.2.6).

So far, the Tevatron has produced roughly 10% of the integrated luminosity of 8 fb^{-1} per experiment expected for Run II in 2008 (see Section 3 and Fig. 3.1). With the present data set, sensitivity for SUSY in final states with electrons is limited to SUSY models with

- low chargino and neutralino masses ⇒ large $\chi_2^0\chi_1^\pm$ cross section (see Fig. 5.2)
- low slepton masses ⇒ large leptonic BR of χ_2^0 and $\chi_1^\pm$ (see Sections 5.1.2)
- low degree of stau mixing ⇒ large electron fraction in the final state (see Section 5.1.2).

5.2 Standard Model background

Most of the Standard Model processes can be suppressed in the selection of SUSY candidates by requiring three charged leptons and missing transverse energy in the event.

Nevertheless, there are a couple of Standard Model processes which can produce a SUSY-like detector signature (*background processes*). The reconstructed final state leptons are composed by real leptons or photons and jets that are misidentified as leptons. The background events can contain true missing transverse energy (carried for example by a neutrino in the final state) or the energy imbalance is a consequence of an energy mismeasurement.

Table 5.1 gives an overview over the most important SM processes which can lead to a trilepton signature in the detector.

Process	# leptons	$\not\!\!E_T$	remarks
$(W \to e\nu) + \gamma$/jet	1	yes	photons/jets fake second electron and third lepton
$(Z/\gamma \to ee) + \gamma$/jet	2	no	photon/jet fakes third lepton, mismeasured $\not\!\!E_T$
$WZ \to ee\ell\nu$	3	yes	
$WW \to ee\nu\nu$	2	yes	photon/jet fakes third lepton
$ZZ \to eeXX$	2-4	no/yes	misidentifid leptons/mismeasured $\not\!\!E_T$
$t\bar{t} \to ee + 2$jets	2	yes	jet fakes third lepton
$q\bar{q} \to$ jets	0	no	jets fake three leptons, mismeasured $\not\!\!E_T$

Table 5.1: Standard Model backgrounds for the SUSY trilepton selection.

The most important irreducible background consists of the associated production of a W and a Z boson (see Fig. 5.8a,c) with subsequent leptonic decays of both gauge bosons, which is the Standard Model equivalent of the associated chargino neutralino production in the gaugino region. Since the Z boson decays directly into two leptons, the invariant mass of two opposite sign leptons of the same generation in the final state corresponds to the Z mass. The missing transverse energy stems from the neutrino.

The production of two Z bosons (see Fig. 5.8e) can lead to the second irreducible final state with two electrons and two tau-leptons. The neutrinos from the tau decay provide the missing transverse energy. As in the case of the WZ processes, the invariant mass of

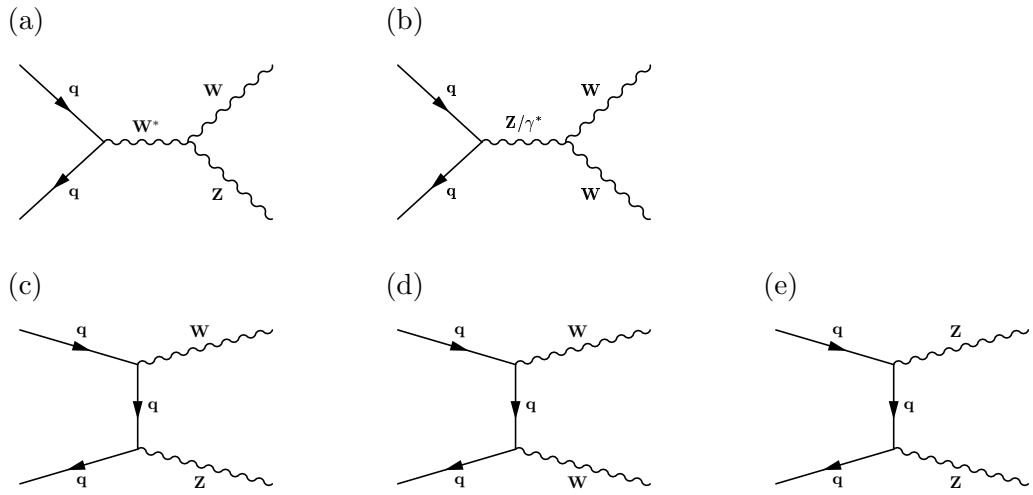

Figure 5.8: LO graphs for di-Boson production.

two opposite sign electrons is expected to be in the range of the Z mass. Other decay modes of the Z bosons lead to final states with four electrons or two electrons and two muons which are balanced in the transverse plane or to final states with two leptons and two jets, one of which is misidentified as the third lepton. The event is selected if detector readout noise or a mismeasurement of the energy of one of the objects fake large missing transverse energy.

The production of two W-bosons (see Fig. 5.8b,d) leads to two opposite sign leptons in the final state and missing transverse energy, carried away by the two neutrinos. A jet or a photon from the underlying event can be misreconstructed as a third lepton.

The production of a single W-boson which provides a lepton and true missing transverse energy can also be a background, if additional jets and/or photons are misidentified as the second and the third lepton. Figure 5.9 shows the LO graphs for W+photon and W+jet production. This background will be discussed further in Section 9.

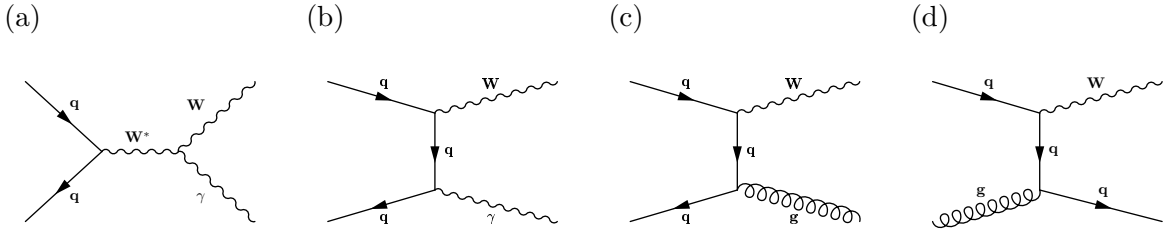

Figure 5.9: LO graphs for W + jet/γ production at the Tevatron.

Final states with two opposite sign leptons are created in Drell–Yan processes (see Section 4.1.4) and on the Z resonance. An additional jet or photon can be misreconstructed as a third lepton. The events are expected to be balanced in the transverse plane but are selected in case of a mismeasurement of the missing transverse energy. Figure 5.10 shows the most important LO contributions for Z/γ+photon and Z/γ+jet production.

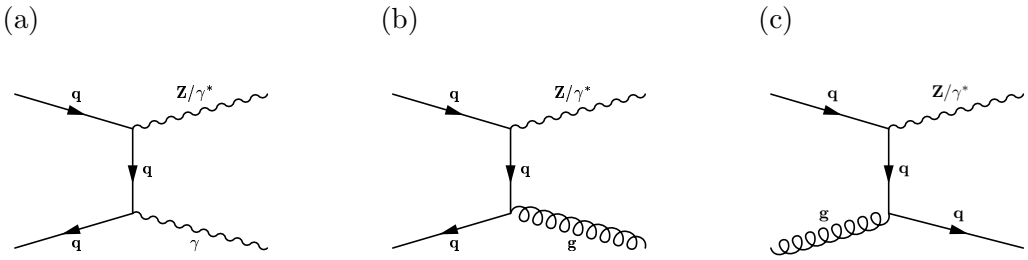

Figure 5.10: LO graphs for Z + jet/γ production at the Tevatron.

The production of two top quarks which decay semileptonically leads to two leptons, two hard b-jets and missing transverse energy in the final state. The event is selected, if one jet is misidentified as a third lepton. Fig. 5.11 shows the LO graphs for $t\bar{t}$ production.

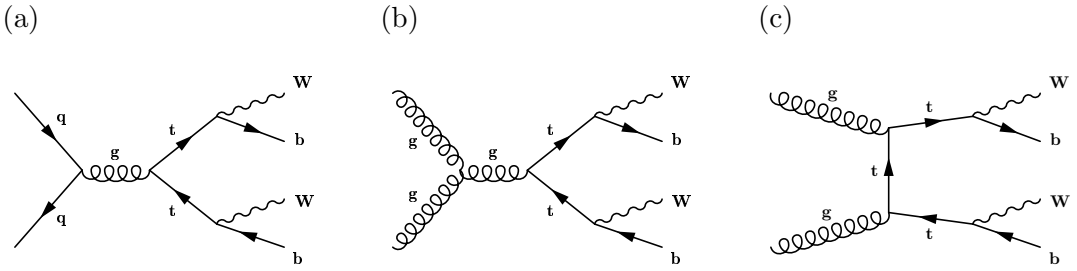

Figure 5.11: LO graphs for $t\bar{t}$ production at the Tevatron.

Due to its very large cross section (see Fig. 4.3), the production of jets has also to be considered as a possible background source, even though no isolated lepton is produced in the process. Three jets can be misidentified as leptons and a mismeasurement of the jet energy can fake missing transverse energy. This background is called *QCD background* in what follows.

Cross sections for the most important backgrounds are presented in Section 9. The selection strategies applied to suppress these backgrounds are discussed in detail in Section 10.

6 The electron trigger

As shown in the previous section, the final states from associated production of charginos and neutralinos which are the subject of this thesis are characterized by at least two electrons with asymmetrically distributed lepton transverse momenta in a broad kinematic range, from very soft up to modest p_{T} values. They contain, in addition, a third charged lepton and missing transverse energy.

These events are not stored unless the DØ trigger system (see Section 3.3) has filtered them out of a large background of inelastic proton-antiproton reactions, mostly resulting in two or more soft jets. A part of this thesis has thus been devoted to the development of the DØ L3 electron triggers for the complete phase of data taking for this analysis. A special emphasis has been put on the efficient coverage of the low-to-modest momentum range and on the triggering of events with two electrons in the final state. This section presents a few examples of development and performance studies for the L3 trigger of trigger version 12, with which 2/3 of the data for this analysis has been collected. It is designed for a luminosity of $6 \times 10^{31}\mathrm{cm}^{-2}\mathrm{s}^{-1}$.

In the following, the standard reconstruction of electrons and photons (see Section 7) is denoted as *offline reconstruction*, in order to distinguish it from the reconstruction in the trigger. All electron triggers that do not require a track are also used for photon triggering. Electrons and photons are denoted as *EM objects*. Triggers that require one EM object are referred to as *Single-EM triggers* in the following and triggers that require two EM objects are called *Di-EM triggers*.

6.1 The L1 electron trigger

The L1 electron triggering makes use of the calorimeter trigger L1Cal and the track trigger L1CTT (see Section 3.3). The relevant quantity for the L1Cal is the energy in the electromagnetic (EM) trigger towers. The trigger uses a reference set of four E_{T} thresholds. The L1CTT compares the momentum of a track in the CFT with a reference set of three thresholds. An isolation of the track in azimuthal direction (ϕ) can be required in addition. Table 6.1 shows the notation used in the following for L1 triggers.

notation	description
CEM(N,x)	N L1 electromagnetic towers with E_{T} >x GeV
TTK(N,x)	N tracks with p_{T} >x GeV
TIS(N,x)	N isolated tracks with p_{T} >x GeV

Table 6.1: Notation for L1 triggers.

L1 triggers that require a minimum energy in two EM trigger towers do not only serve as Di-EM triggers but are also used to recover the events where the energy of one EM object is spread over two adjacent trigger towers.

Table 6.2 gives an overview over the L1 electron triggers used in version 12. The set contains three calorimeter-only triggers. E1, the main Single-EM trigger, and E2, the main Di-EM trigger, are complemented by E3 which triggers asymmetric Di-EM events and single electrons and photons, where the energy is spread in an asymmetric way over adjacent trigger towers. The kinematic range for electron triggering is extended to low energies by adding additional CTT requirements. Single electrons can be triggered down to calorimeter energies of 9 GeV and 6 GeV by the triggers E4, E5 and E6 if their track is reconstructed in the CTT with $p_{\mathrm{T}} > 10$ GeV. A low-p_{T} Di-EM trigger for J/ψ and low-mass SUSY events is provided by E7. Trigger E8, which requires one calorimeter object and two tracks addresses final states with one electron and an additional lepton.

Trigger name	description
E1	CEM(1,11)
E2	CEM(2,6)
E3	CEM(1,9)*CEM(2,3)
E4	CEM(1,9)*TTK(1,10)
E5	CEM(1,6)*CEM(2,3)*TTK(1,10)
E6	CEM(1,6)*TIS(1,10)
E7	CEM(1,6)*CEM(2,3)*TTK(1,5)*TTK(2,3)
E8	CEM(1,6)*TTK(2,5)*TIS(1,5)

Table 6.2: Version 12 L1 triggers. The symbol $*$ denotes a logical AND.

The efficiency of the L1 triggers is studied for offline reconstructed EM objects in data (see EM candidates in Section 7.2.1) triggered by a muon trigger or by a minimum bias trigger as a function of the offline measured transverse momentum. The resulting efficiency curve is referred to as the *turn-on* of the trigger. Figure 6.1a shows the turn-on for four single L1 trigger thresholds (5 GeV, 10 GeV, 15 GeV and 20 GeV). The turn-on of the combined L1Cal trigger set of trigger version 12 is shown in Fig. 6.1b. The L1Cal set of version 12 is fully efficient for single electrons and photons with $p_{\mathrm{T}} > 20$ GeV. From the CEM(1,5) turn-on in Fig. 6.1a follows, that events with two electrons or photons with $p_{\mathrm{T}} > 10$ GeV are expected to be triggered with large efficiency by the low-p_{T} Di-EM calorimeter triggers.

6.2 The L2 electron trigger

In the data used for this analysis only very simple L2 calorimeter triggers are used which build clusters of two adjacent trigger towers. The L2 triggers are denoted with EM(x), where x is the minimum E_{T} sum of both trigger towers. In trigger version 12, L2 terms are applied in the J/Ψ trigger E7. The trigger is split into two triggers with different L2 conditions. The trigger E7A requires two L2 EM clusters with $p_{\mathrm{T}} > 3\,\mathrm{GeV}$ and $p_{\mathrm{T}} > 5\,\mathrm{GeV}$ in $|\eta| < 1.6$. Trigger E7B requires one L2 EM cluster with $p_{\mathrm{T}} > 9\,\mathrm{GeV}$ in $|\eta| < 1.6$. A

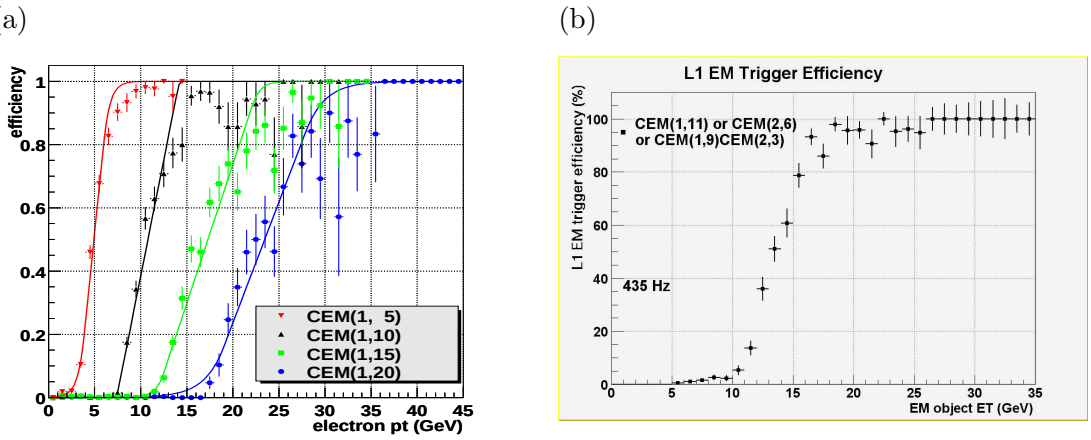

Figure 6.1: L1Cal trigger efficiency for single offline reconstructed EM candidates as a function of the offline measured p_T for (a) four Single-EM L1 trigger thresholds (5 GeV, 10 GeV, 15 GeV and 20 GeV) and (b) for the OR of the version 12 L1Cal triggers in trigger-unbiased data (from Ref. [81]).

more sophisticated L2 trigger set, which is able to calculate the calorimeter isolation and to match tracks to the calorimeter is used starting from trigger version 13 [82].

6.3 The L3 electron trigger

In the data taking period covered by this analysis, the L3 electron trigger reduces the EM trigger rate from several hundred events per second down to approximately 20 events per second. This section gives an overview over the L3 triggers and the general L3 trigger strategy.

The EM suite uses loose conditions at large transverse momenta and tightens the requirements with decreasing p_T thresholds. Two strategies are used in parallel:

- Tighten the electron/photon identification (EM-ID) requirements
- Require additional objects in the event

Table 6.3 shows the notation used in the following for the L3 triggers. The triggers will be described in more detail in the following sections. Tables 6.4 presents the L3 electron triggers of trigger version 12.

The version 12 Single-EM menu triggers very loose L3 EM clusters with $E_T > 70$ GeV (VL70). The EM-ID is tightened successively with decreasing p_T threshold down to $E_T > 20$ GeV by tightening the EM fraction, and requiring the shower shape to agree with the shape expected for electrons and photons (L50, SH30 and SHT20). The kinematic threshold for central electrons can be lowered to 15 GeV by requiring a track or a track-match (SHT15_TK13 and T13L15). Triggers based on calorimeter variables and triggers based on track requirements can be used in a complementary way in order to increase the

notation	description
NCx	Simple cone cluster ($\Delta R < 0.25$), $E_{\mathrm{T}} >$ x GeV
VLx	Very loose EM cluster (Energy fraction in the EM Cal.>0.8), E_{T}>x GeV
Lx	Loose EM cluster (EM energy fraction>0.9), $E_{\mathrm{T}} >$ x GeV
SHx	Loose shower shape requirement, $E_{\mathrm{T}} >$ x GeV
SHTx	Tight shower shape requirement, $E_{\mathrm{T}} >$ x GeV
RLx	Road method, loose, $p_{\mathrm{T}} >$ x GeV
RTx	Road method, tight, $p_{\mathrm{T}} >$ x GeV
METx	Missing transverse energy $\not\!\!E_{\mathrm{T}} >$ x GeV
TKy	Global track $p_{\mathrm{T}} >$ y GeV
Ty	Match between track and calorimeter cluster ($\Delta\mathcal{R}$<0.1), track p_{T}>y GeV

Table 6.3: Notation for L3 trigger terms.

efficiency for electrons and to provide enough redundancy for systematic trigger studies. Triggers with loose EM-ID conditions which require another object ($\not\!\!E_{\mathrm{T}}$, a track or a second electron) in the event can be used in a complementary way with a Single-EM trigger with tight ID in order to increase the efficiency for final states with more than one object.

The EM-ID is successively tightened for the Di-EM trigger set from two loose EM clusters with $E_{\mathrm{T}} > 20$ GeV (2L20) to two EM objects with loose shower shape requirement and $E_{\mathrm{T}} > 8$ GeV (2SH8), complemented by a di-electron trigger which requires only a track match for one of the electrons (2L8_T8L8). An asymmetric trigger (5_11_SH5_T4L5) with one track-based electron and one electron identified in the calorimeter with $E_{\mathrm{T}} > 5$ GeV and 11 GeV is designed for SUSY events. A trigger for two central electrons with $E_{\mathrm{T}} > 5$ GeV (2T5SH5) requires both a loose shower shape and a matched track. Two soft central electrons with $p_{\mathrm{T}} > 3$ and 5 GeV are triggered efficiently by the road trigger, which uses the energy within a narrow tube along the extrapolation of a track into the calorimeter [83].

6.4 Development and performance studies of L3 electron triggers

This section shows a few examples of the studies for the development of triggers used in the version 12 trigger set. Since they are part of an ensemble of triggers which observe the overall trigger strategy outlined above, the performance of the whole set has to be optimized.

The signal efficiency is studied with MC and data samples processed with the updated version 12 trigger simulation. The background rates are measured using a *special run* triggered with the new L1Cal triggers without L3 requirements, which is also processed with a trigger simulation of the new triggers.

Trigger name	L1/L2 terms	L3 terms
Single-EM triggers		
E1_VL70	E1	VL70
E1_L50	E1	L50
Ex_SH30	E1-E4	SH30
Ex_T25VL30	E1-E4	T25VL30
Ex_SHT20	E1-E4	SHT20
Ex_L20_M25	E1-E4	L20_M25
Ex_T13L15	E1-E6	T13L15
Ex_SHT15_TK13	E1-E6	SHT15_TK13
Ex_SHT15_M15	E1-E6	SHT15_M15
Ex_T7SHT8_2TK5	E1-E8	T7SHT8_2TK5
Ex_T7SHT8_M10	E1-E8	T7SHT8_M10
Di-EM triggers		
Ex_2T5SH5	E2,E5,E7,E8	2T5SH5
Ex_2SH8	E1-E6,E8	2SH8
Ex_2L8_T8L8	E1-E8	2L8_T8L8
Ex_2L15_SH15	E1-E6	2L15_SH15
Ex_2L20	E2-E6	2L20
Ex_5_11_SH5_T4L5	E2-E7A,E8	5_11_SH5_T4L5
Ex_2RL3_RT3_RL5	E7A,E7B	2RL3_RT3_RL5

Table 6.4: Version 12 triggers.

6.4.1 The shower width

The transverse shower-shape cuts applied in trigger version 5-11 use the shower widths in the first three EM layers of the calorimeter, defined as:

$$\mathrm{Width_{layer}} = \frac{1}{\mathrm{E_{layer}}} \sum_{\mathrm{layer}} \mathrm{E_i} \Delta \mathrm{R_i} \tag{6.1}$$

which corresponds to the energy-weighted average of the distance $\Delta\mathcal{R}$ of the center of the cells in one layer of the cluster from the cluster axis.

Figures 6.2 shows the distribution of the shower width for probe electrons from a $\mathrm{Z}/\gamma \rightarrow \mathrm{ee}$ selection. The electron selection requires two opposite sign electrons from the primary vertex with $|\eta| < 2.5$ (at least one in CC) with an electron likelihood larger than 0.8. One (tag) electron is required to have triggered a Single-EM trigger.

The typical background consists of jets with a large EM-fraction which are reconstructed as a loose EM-Object by the L3 trigger. An unbiased sample of these jets is selected from $\mathrm{Z}/\gamma + \mathrm{jet} \rightarrow \mathrm{ee} + \mathrm{jet}$ events, which are triggered by the electrons from the Z decay. The additional jet is required to match to a loose L3 EM-object. The distribution of the shower width for these jets is shown in Fig. 6.2 as a comparison.

The reconstructed shower width in layer 3 is smaller because of the finer granularity in this layer (see Section 3.2.4). The version 5-11 shower shape triggers require the shower width to be smaller than 0.09, 0.08 and 0.05 in layer 1, 2 and 3 respectively.

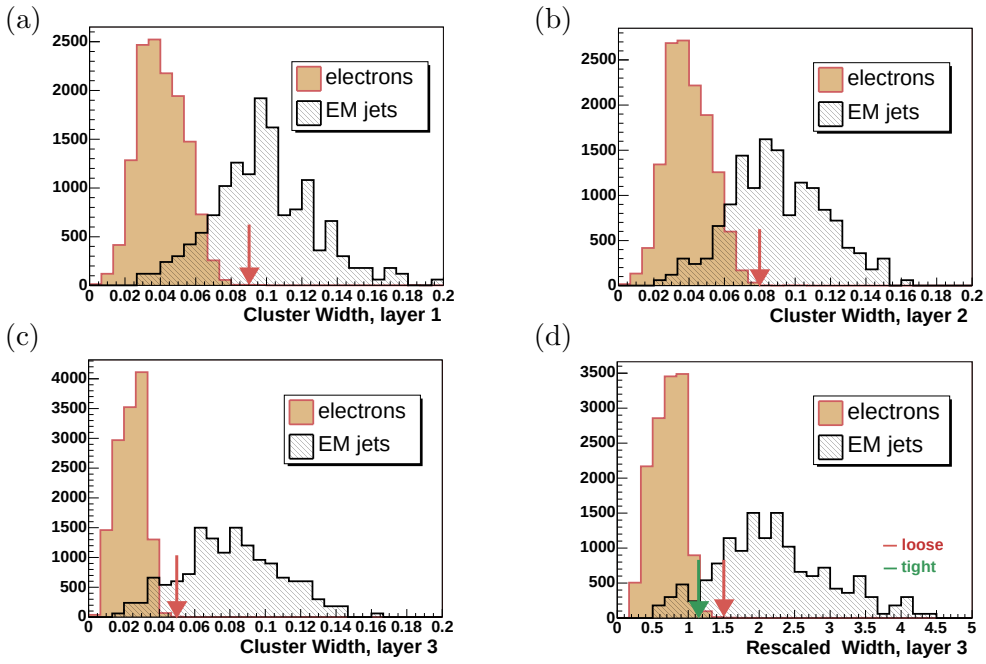

Figure 6.2: (a-c) Shower width in the first three EM layers and (d) rescaled shower width in layer 3 for unbiased probe electrons from a tight offline $Z/\gamma \rightarrow ee$ selection and for jets that match with a loose L3 EM cluster (arbitrary normalization). The position of the cuts on the shower width in trigger versions 5-11 (a-c) and the position in CC of the loose and the tight cut on the rescaled shower width (d) are marked on the plots.

The average width increases with η since the absolute size of the calorimeter cells becomes smaller for large η. It becomes also larger if the electron passes through a layer near the border of a cell. The rejection is increased for trigger version 12 at a comparable efficiency level by rescaling the shower width as a function of the η position of the cluster and of the ϕ position of the cluster axis in the calorimeter cell in order to compensate for these effects, which yields the *rescaled widths*. The distribution of the rescaled width is shown for layer 3 in Fig. 6.2d for unbiased probe electrons and jets from data. Two sets of thresholds for CC and EC objects are introduced, specifying the loose trigger (SH), and the tight trigger (SHT).

The shower width triggers within the trigger set

The two shower shape triggers are part of the version 12 Single-EM trigger set. The trigger thresholds are adjusted such that the overall L3 EM rate keeps within the specifications of 20 events per second. Approximately three quarters of the rate are assigned to Single-EM triggers. One quarter of the electron budget is used for Di-EM triggers.

The basic Single-EM trigger set, consisting of the loose shower-shape trigger, the tight shower-shape trigger and the tight shower-shape trigger with additional track is designed for a trigger rate of 14 events per second. Figure 6.3 shows the rate expected for the OR of SHy, SHTx and SHT15*TK12 as a function of the E_T thresholds x, y for the shower shape

triggers. The desired trigger rate is achieved with thresholds of x=20 GeV and y=30 GeV respectively.

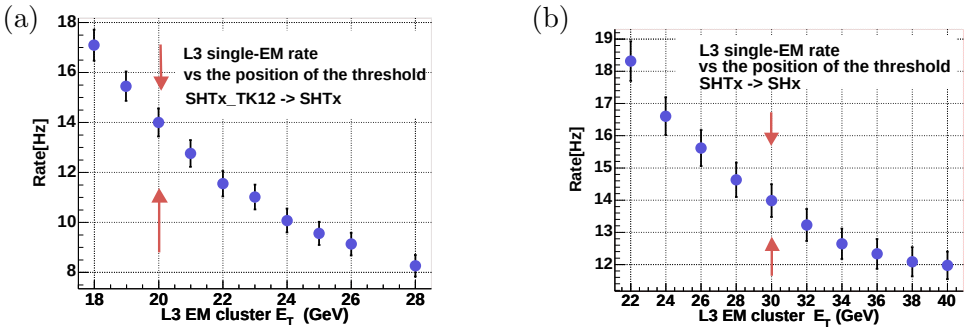

Figure 6.3: L3 rate for the basic Single-EM trigger suite at a luminosity of $6 \times 10^{31}\mathrm{cm}^{-2}\mathrm{s}^{-1}$ depending (a) on the threshold where the track requirement is dropped and (b) on the threshold where the shower shape requirement is loosened. The remaining trigger thresholds are fixed at 20 GeV and 30 GeV respectively.

The target rate for the basic Di-EM trigger set consisting of triggers requiring two loose EM objects with shower shape requirements for both, one or none of the EM objects is 4-5 events per second. Figure 6.4 shows the rate for the OR of 2SH8, 2Lx_SHx and 2Ly as a function of the E_{T} thresholds x and y. The desired rate is achieved with thresholds of x=15 GeV and y=20 GeV respectively.

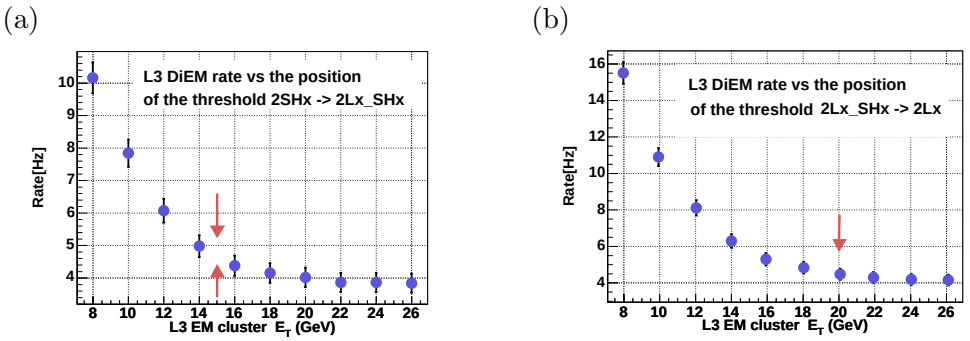

Figure 6.4: L3 rate for a basic Di-EM trigger suite of 2SH8-2LySHy-2Lz at a luminosity of $6 \times 10^{31}\mathrm{cm}^{-2}\mathrm{s}^{-1}$ depending on the threshold where the shower shape requirement is dropped (a) for one electron and (b) for both electrons.

Efficiency of the shower width triggers

After the implementation of the new trigger, the efficiency is cross–checked using L3-unbiased probe electrons from the offline $\mathrm{Z}/\gamma \rightarrow$ ee selection. Figure 6.5 shows the trigger efficiency as a function of the offline reconstructed transverse momentum of the probe electron for a SH8 trigger and the Single-EM triggers SHT20 and SH30. The 50% points of the turn-on are located at 9 GeV, 21.5 GeV and 31.5 GeV for trigger SH8, SHT20 and

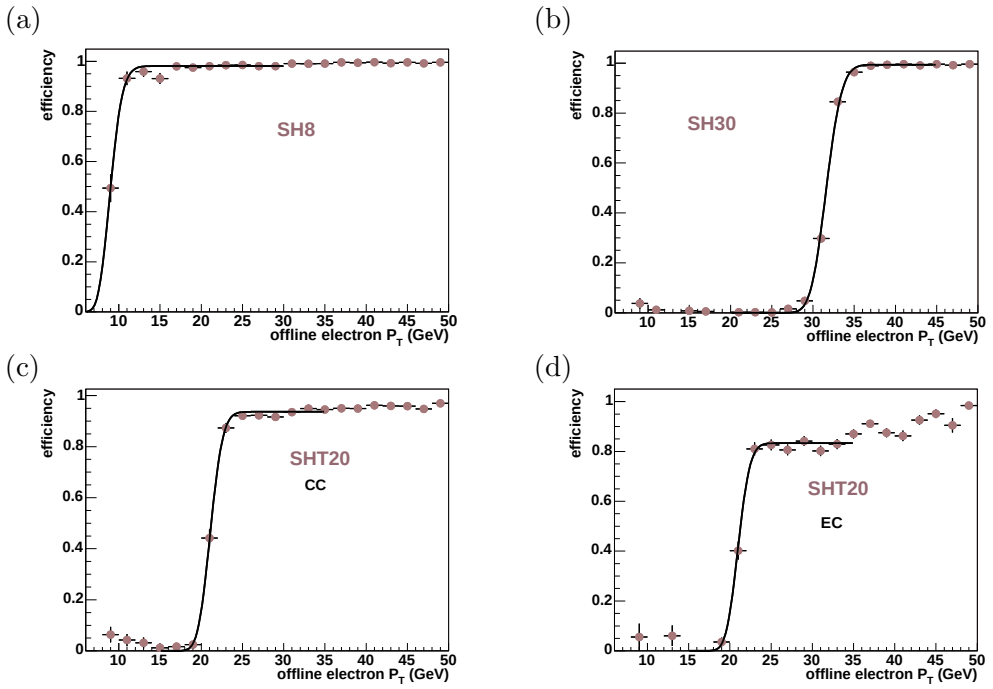

Figure 6.5: L3 efficiency as a function of the transverse momentum of a L3-unbiased offline electron in a tight $Z/\gamma \rightarrow ee$ selection in data for (a) SH8 and (b) SH30 and SHT22 in (c) CC and (d) EC.

SH30 respectively. The turn-on is shifted with respect to the offline measured transverse momentum by approximately 10%. The inefficiency of the SHT20 trigger is partly due to a missing correction for the alignment of calorimeter and tracker in the DØ detector.

6.4.2 The L3 track match

The version 8-11 trigger in the low-p_T range, requires a track in addition to the narrow-width electron cluster. The version 12 trigger software can propagate the track into the calorimeter and perform a simple spatial match with the L3 electron cluster.

Figures 6.6a and b show the p_T distribution of the leading track in the special L1Cal run mentioned above for all tracks, tracks with a $\Delta\phi$ match or tracks with a $\Delta\mathcal{R}$ match with the L3 electron cluster. Requiring a L3 track in the event to match in $\Delta\mathcal{R}$ with the electron leads to a considerable background rejection.

The efficiency is studied with MC electrons from a $Z \rightarrow ee$ sample. Figure 6.6c shows the $\Delta\mathcal{R}$ between L3 track and L3 calorimeter cluster for electrons with offline spatial track match, which results in a large matching efficiency for reconstructed L3 tracks for electrons matched offline to a track.

A considerable inefficiency for the L3 track-match trigger stems from the low L3 tracking efficiency of 70%. Figure 6.6d shows the L3 tracking efficiency as a function of the offline reconstructed track p_T in tracks matched offline to electrons from $Z \rightarrow ee$ events (from [80]).

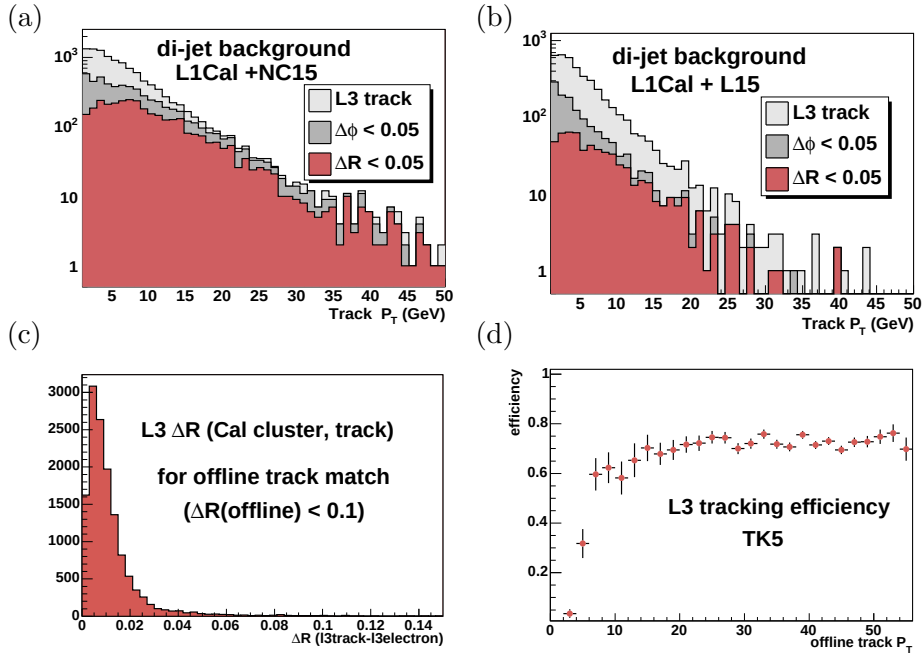

Figure 6.6: Distribution of the transverse momentum of the leading track with different grades of matching (a) to a L3 cluster without EM fraction requirement with $E_{\mathrm{T}} > 15$ GeV (NC15) and (b) to a standard loose L3 EM cluster with $E_{\mathrm{T}} > 15$ GeV (L15) in events that are triggered by the version 12 L1Cal trigger. (c) $\Delta\mathcal{R}$ between L3 track and L3 calorimeter cluster for electrons from $Z \rightarrow$ ee MC with offline spatial track match in $\Delta\mathcal{R} < 0.1$. (d) L3 tracking efficiency (p_{T}(track) > 5 GeV, TK5) for offline reconstructed tracks that match to electrons from $Z \rightarrow$ ee in $|\eta_{\mathrm{det}}| < 1.6$.

Fig. 6.7 shows the efficiency for offline selected probe electrons for the combination of shower shape triggers only which require $E_{\mathrm{T}} > 20$ and for a combination of the shower shape triggers with the low-p_{T} track match triggers. Since the L3 tracking relies on the CFT, the track-match trigger contributes only for central electrons ($|\eta_{det}| < 1.6$). For electrons with $10\,\mathrm{GeV} < E_{\mathrm{T}} < 20\,\mathrm{GeV}$, the track-match trigger recover 60% of the efficiency.

6.4.3 Triggering of electrons from SUSY events in trigger version 12

The associated production of charginos and neutralinos with leptonic decays results in signatures of three charged particles with very asymmetrically distributed and in average comparably low transverse momenta (see Section 5.1.3). SUSY events selected by this analysis are required to have at least two electrons with transverse momenta larger than 12 GeV and 8 GeV in the final state (see Section 10.1).

Studies are performed in order to determine whether the kinematic range of the SUSY final states with two electrons of $p_{\mathrm{T}} > 8$ GeV is sufficiently covered by the L3 electron trigger menu in trigger version 12. The study is performed with a MC simulation of associated production of a chargino and a neutralino with masses of 110 GeV and 114 GeV respectively which decay via 3-body processes into final states with three electrons or with

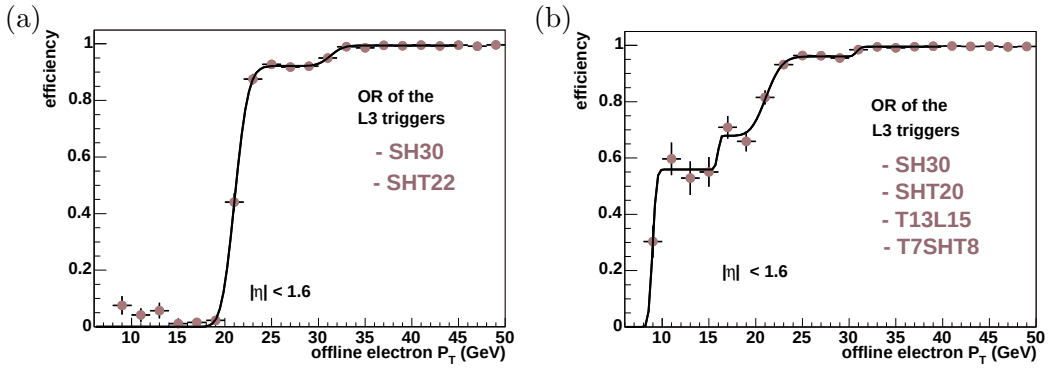

Figure 6.7: L3 efficiency as a function of the transverse momentum of a L3-unbiased offline electron of a tight $Z/\gamma \rightarrow ee$ selection for (a) an OR of the Single-EM triggers SHT20 and SH30 and (b) for the combination T7SHT8, T13L15, SHT20 and SH30 for electrons in $|\eta_{det}| < 1.6$.

two electrons and one muon (SUSY reference point M6, see Section 9.2). The trigger simulation is applied directly after the detector simulation, such that the results of the offline electron reconstruction are not available. The preselection for the trigger study requires two loose L3 EM objects with $p_{\mathrm{T}} > 6$ GeV (2L6). This sample is expected to contain the events selected offline with $p_{\mathrm{T}} > 8$ GeV, taking into account the L3 turn-on (see Figure 6.5a). The Di-EM mass is calculated with the two leading L3 EM objects.

Figure 6.8 shows the results from the trigger study for SUSY events with three electrons in the final state. In this case the event can be triggered by electrons from the neutralino and from the chargino. The selection of events in the kinematic range of the analysis selection mentioned above (2L6), is marked by a red, empty histogram. Figures 6.8a and b present the efficiency as a function of the Di-EM mass of the main low-p_{T} Di-EM triggers, the asymmetric Di-EM trigger 5_11_SH5_T4L5 and the symmetric low-p_{T} Di-EM trigger 2SH8. A large part of the SUSY events within the detector acceptance is selected by the asymmetric Di-EM trigger or the symmetric low-p_{T} Di-EM trigger alone.

Figure 6.8c shows the Di-EM mass coverage by the logical OR of the two low-p_{T} Di-EM triggers with the high-p_{T} Di-EM triggers 2L15_SH15 and 2L20. The low-p_{T} Di-EM triggers recover the efficiency in the low invariant mass range, that is not triggered by the high-p_{T} Di-EM triggers. A combination with the Single-EM triggers improves the efficiency.

The Di-EM mass coverage by the logical OR of the Single-EM triggers SH30, SHT20 and T13L15 is shown in Fig. 6.8d. The trigger SH30 is only efficient in the high-mass region. Important contributions in the low-mass region come from triggers at lower thresholds of 20 GeV and 15 GeV. As in the case of the Di-EM triggers, the combination of Single-EM and Di-EM triggers improves the efficiency for SUSY events.

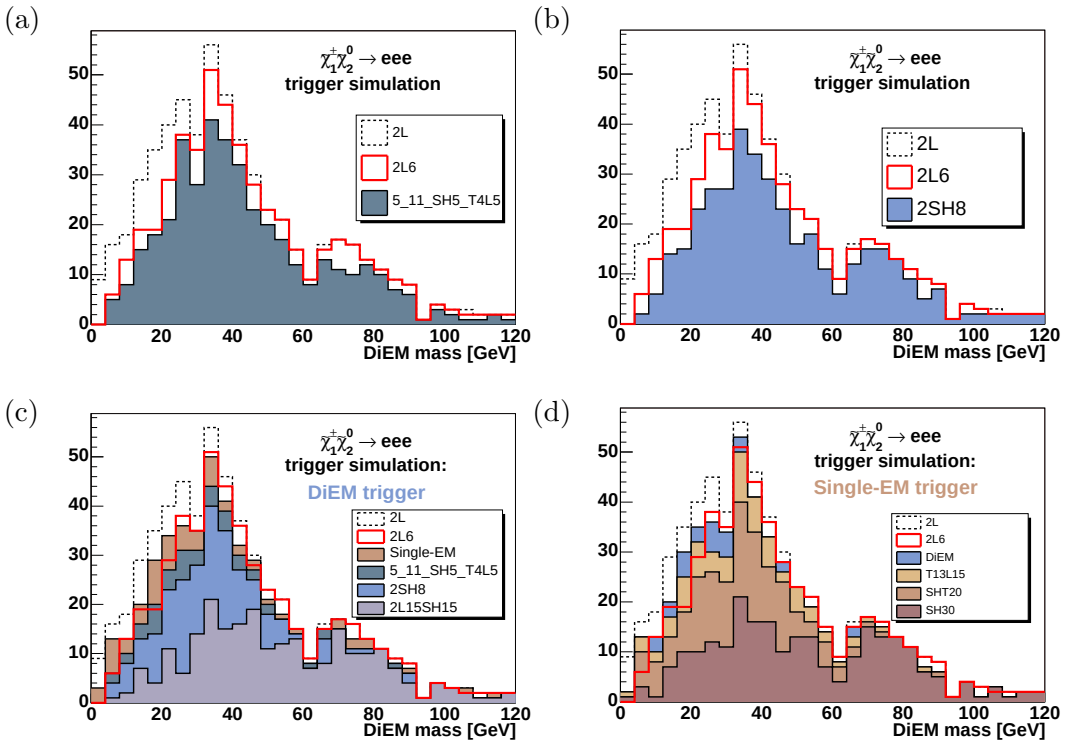

Figure 6.8: Trigger coverage of the invariant Di-EM mass spectrum with two L3 EM clusters expected for $\chi_1^{\pm}\chi_2^0 \rightarrow$ eee + X with a chargino mass of $m_{\chi^{\pm}} = 110$ GeV (point M6, see Section 8) for (a) the asymmetric Di-EM trigger 5_11_SH5_T4L5 , (b) the low-p_T Di-EM trigger 2SH8, (c) the OR of the Di-EM triggers 2SH8,5_11_SH5_T4L5, 2L15_SH15 and 2L20 and (d) the OR of the Single-EM triggers T13L15, SHT20 and SH30.

Final states with two electrons and one muon show different kinematic distributions of the reconstructed electrons due to the fact, that both electrons stem exclusively from the neutralino. In particular, the average invariant mass is considerably lower than in the case of final states with three electrons. Figure 6.9 shows the trigger coverage of the Di-EM mass range for these events with the same triggers as studied for Fig. 6.8.
The efficiency of the asymmetric Di-EM trigger for e+e+μ final states is larger than the efficiency of the 2SH8 trigger due to the larger fraction of events with one low-p_T electron from the neutralino (see Fig.s 6.9a and b). As in the case of e+e+e final states, substantial parts of the e+e+μ final states are covered by both the Single-EM trigger set and the Di-EM trigger set (see Fig.s 6.9c and d). The contribution of the asymmetric Di-EM trigger and of the 2SH8 trigger is more important for final states with only two electrons. Combining Single-EM and Di-EM triggers improves the efficiency. The single-EM trigger set enhances in particular the efficiency for events where one electron is not reconstructed in the calorimeter or has a transverse momentum below the Di-EM trigger threshold (see Fig. 6.9c).

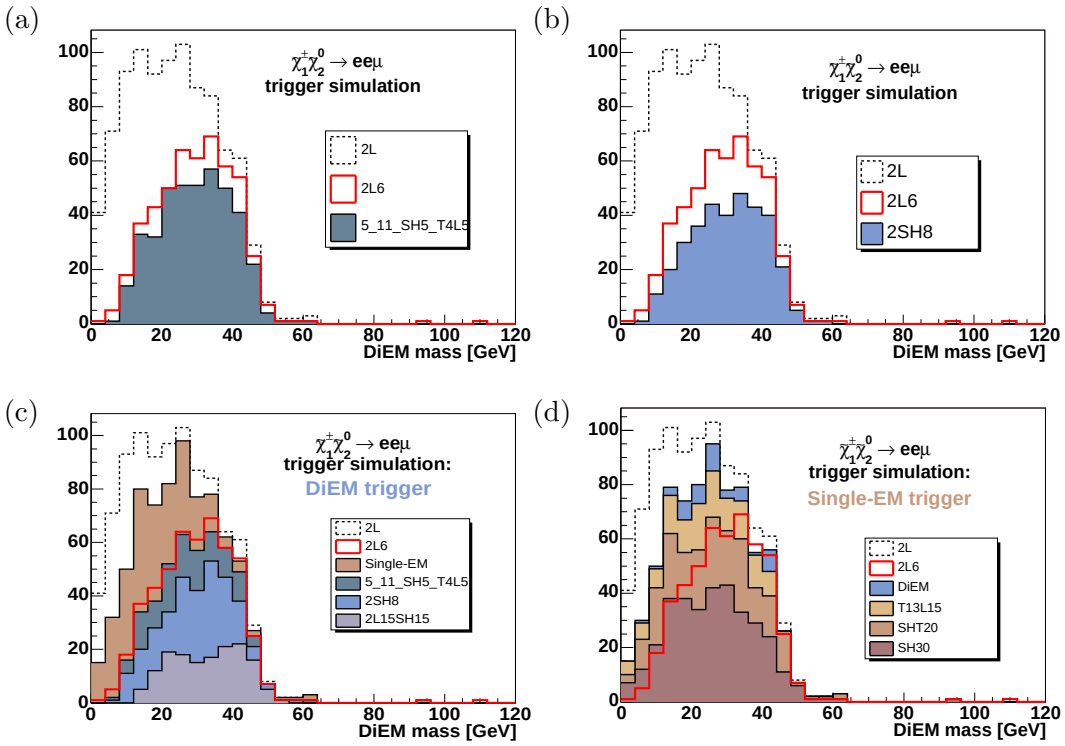

Figure 6.9: Trigger coverage of the invariant Di-EM mass spectrum with two L3 EM clusters expected for $\chi_1^\pm\chi_2^0 \to ee\mu + X$ with a chargino mass of $m_{\chi^\pm}$= 110 GeV (point M6, see Section 8) for (a) the asymmetric Di-EM trigger 5_11_SH5_T4L5 , (b) the low-p_T Di-EM trigger 2SH8, (c) the OR of the Di-EM triggers 2SH8,5_11_SH5_T4L5, 2L15_SH15 and 2L20 and (d) the OR of the Single-EM triggers T13L15, SHT20 and SH30.

7 Event reconstruction and object identification

The stream of digital readout signals from the detector (raw data) is processed in order to extract candidates of basic physical objects (tracks, jets, electrons/photons, taus, muons and the primary vertex). The raw energy of the objects is calibrated to reconstruct the event kinematics (4-momenta of the physics objects and missing transverse energy) as precisely as possible.

Other objects in the event or signals which are related to readout problems in the detector can be misidentified as a physics object of interest (*background*). The criteria employed for the identification are therefore optimized for a large object purity while at the same time keeping the selection efficiency high. The algorithms for reconstruction and identification are collected in the software package D0RECO[61].

This analysis uses the properties of electrons, tracks, jets and missing transverse energy in the event for the isolation of the signal final state. The following chapter presents the strategies applied to reconstruct these physics objects from the detector response and separate them from the background.

7.1 Tracks

A track is the reconstruction of the trajectory of a charged particle based on the energy deposition (*hits*) in successive layers of the SMT and the CFT (see Section 3.2.1).

The CFT is used for tracking in $|\eta_{det}| \lesssim 1.6$. Charged particles in the forward region ($|\eta_{det}| \gtrsim 2.0$) provide only hits in the SMT. The hits in the axial layers of the CFT are used to estimate the projection of the trajectory in the $r-\phi$ plane. Adding the hits in the CFT stereo layers provides information about the z position of the charged particle. SMT tracking uses the hits in the barrel modules and in the F-discs. The tracking detectors yield a better estimate for the position of the trajectory of an electron than the calorimeter.

The track candidates are then filtered in order to reject the misreconstructed tracks based on the χ^2 value per degree of freedom (χ^2/Ndf) of the track fit and the number of misses of hits in different layers. Fig. 7.1 compares the number of hits and the χ^2 value per degree of freedom of the track fit for electron tracks and for tracks that are not matched to any calorimeter object in a selection of $Z \rightarrow ee$ events.

The transverse momentum of the track is calculated from the curvature of the trajectory in the homogeneous longitudinal magnetic field in the tracker. The momentum resolution becomes worse with increasing momentum ($\frac{\Delta P}{P} \sim P$) whereas the energy resolution in the calorimeter improves with the increasing energy ($\frac{\Delta E}{E} \sim \frac{1}{\sqrt{E}}$) such that for electrons in

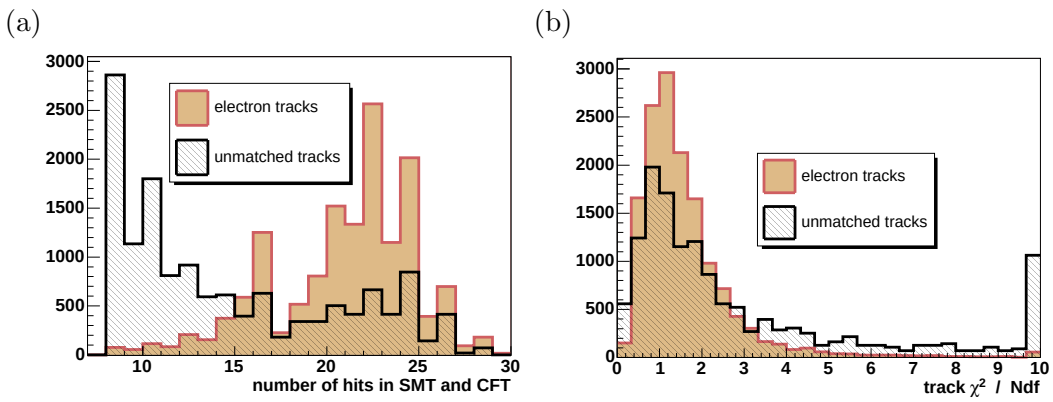

Figure 7.1: (a) Number of hits and (b) χ^2 per degree of freedom of the track fit for electron tracks (shaded) and tracks that are not matched to a calorimeter object in a selection of $Z \rightarrow ee$ events. The tracks are required to have a $p_T > 5\,\text{GeV}$.

the momentum range of interest for this analysis the calorimeter yields a more accurate measurement of the kinematics. The momentum measurement in the tracker is worse for electrons than for heavier charged particles due to the radiation of *bremsstrahlung*.

Figure 7.2 compares the invariant mass of two electrons from $Z \rightarrow e\ e$ events measured with the calorimeter and with the tracker. The invariant mass resolution is considerably worse in the tracker. The tracker measures, in addition, a systematically lower Z mass because of the energy loss due to bremsstrahlung. The track momentum resolution is worse in the forward region.

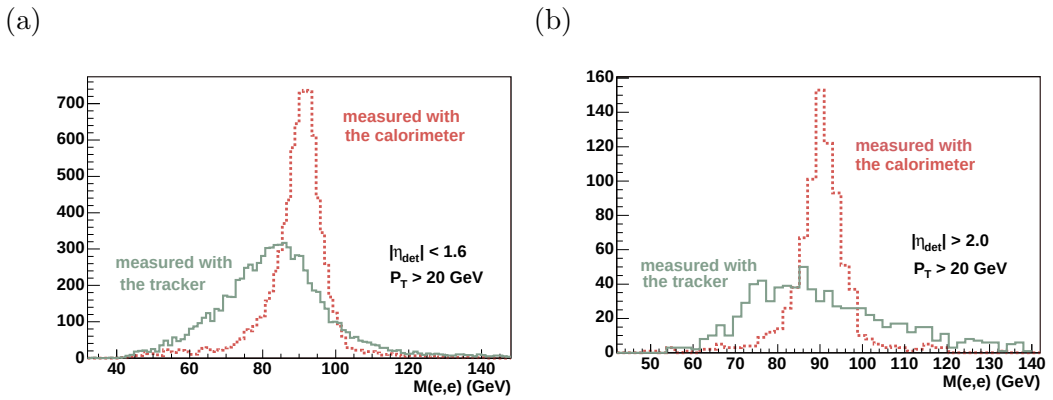

Figure 7.2: Invariant mass of two electrons as measured with the calorimeter (dashed line) and with the tracker (continuous line) for electrons with $E_T > 20\,\text{GeV}$ measured in the calorimeter and a matched track with $p_T > 20\,\text{GeV}$ in the tracker for (a) both electrons in $|\eta| < 1.6$ and (b) one electron in $|\eta| > 2.0$.

7.2 Electrons

The electron and photon identification is based on electromagnetic showers in the calorimeter [8], which deposit their energy mainly in a narrow region within the first four calorime-

ter layers (EM layers, see Section 3.2.4). Electrons are distinguished from photons by the association with a track in the central tracker.

Figure 4.5 shows a simulation of an electron shower in the DØ calorimeter. The shower maximum in uranium is expected at shower depths between 6.5 and 8 radiation lengths for electrons with energies from 10 GeV to 50 GeV and the main part of the shower is contained within 20 radiation lengths [8]. The longitudinal shower profile in the DØ central calorimeter (at $\eta = 0$) is sampled at depths of roughly 3-4, 5-6, 7-13 and 14-23 radiation lengths in the EM layers *EM1, EM2, EM3* and *EM4* respectively. The shower maximum is expected in the third layer which has a higher granularity. The first fine-hadronic layer (*FH1*) is used to sample the tail of the shower (see Section 3.2.4).

The lateral shower development is characterized by the Moliere radius [8] of roughly 2 cm. As a consequence, the main part of the shower in the CC (cell size of the order of 10×10 cm^2 at $\eta = 0$) is expected to be contained in one calorimeter cell tower.

7.2.1 The EM candidate

Calorimeter objects consist of cell towers in the first five calorimeter layers (EM1-FH1) in a cone of $\Delta\mathcal{R} < 0.4$. They are formed by the *Simple Cone Algorithm*. The EM towers with the largest energies are selected as seeds. A *precluster* is formed by adding adjacent cell towers to the seed if they are within a cone of $\Delta\mathcal{R} < 0.3$ in CC or of 10 cm radius (layer EM3) in EC and the precluster axis is calculated. All EM towers within $\Delta\mathcal{R} < 0.4$ with respect to this axis are added to the precluster and the axis is recalculated. This procedure is repeated until the cone is stable. The clusters are required to have a minimum transverse energy $E_{\mathrm{T}} > 1.5$ GeV.

The reconstructed EM clusters are dominated by background from hadronic jets. The jets are characterized by broad showers with a large fraction of energy deposited in the hadronic calorimeter. In order to enhance the purity of real electrons and photons, additional requirements are imposed on the fraction of the cluster energy deposited in the four EM layers

$$\mathrm{EMfrac} > 0.9 \tag{7.1}$$

and on the isolation of the shower in the EM layers of the $\Delta\mathcal{R} < 0.2$ core of the cluster versus the remaining cluster:

$$\mathrm{Iso} = \frac{\mathrm{E_{EM+HAD}}(\Delta\mathcal{R} < 0.4) - \mathrm{E_{EM}}(\Delta\mathcal{R} < 0.2)}{\mathrm{E_{EM}}(\Delta\mathcal{R} < 0.2)} < 0.2. \tag{7.2}$$

EM clusters which fulfill these requirements are called *EM candidates*. Figure 7.3 shows the EM candidate reconstruction efficiency versus detector η and the position in a calorimeter cell (from Ref. [84]). The efficiency is stable in detector η, apart from the ICR region between $1.05 < |\eta_{det}| < 1.5$, where it drops considerably (the efficiency is not calculated for this region in the figure). The EM candidate efficiency decreases substantially if the shower axis is close to one of the boarders of a calorimeter trigger tower (0.2×0.2 in η and ϕ) where a layer of inactive material surrounds the cells.

The cluster center is calculated as the energy-weighted mean of the positions of the cluster cells in the third layer. The energy of the calorimeter cluster corresponds to the sum of

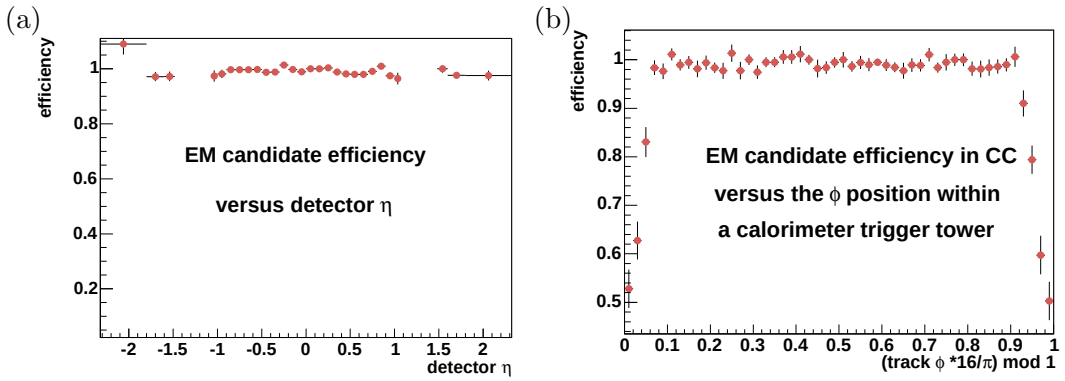

Figure 7.3: Reconstruction efficiency versus (a) detector eta and (b) the azimuthal position within a calorimeter trigger tower ($(\phi * 16/\pi)$mod1). The efficiency is calculated for $|\eta_{det}| < 1.05$ and $1.5 < |\eta_{det}| < 2.3$ for an isolation requirement of Iso < 0.15 (from Ref. [84]).

the energy deposition in the four EM layers and the first FH layer. It is calibrated by the EM energy scale (*EM scale*) which is derived from Z $\rightarrow$ ee and $J/\Psi \rightarrow$ ee events [85].

The four momentum of the EM object is calculated with the best estimate for the direction in η and ϕ. If the calorimeter cluster can be loosely matched to a track the direction is taken from the track. If no matching track is found (not relevant for this analysis) the direction is calculated from the primary vertex and the cluster center. In the following, only EM candidates with a transverse energy E_{T} in excess of 7 GeV are considered.

The track match algorithm searches in a window of $\Delta\mathcal{R} < 0.1$ from the calorimeter cluster center for candidate tracks extrapolated into the calorimeter. The *spatial track match* is based on the difference of the z position and the azimuthal angle ϕ of track and cluster axis. The track with the largest χ^2 probability, with

$$\chi^2 = (\frac{\Delta \mathrm{z}}{\sigma \mathrm{z}})^2 + (\frac{\Delta\phi}{\sigma\phi})^2 \tag{7.3}$$

is selected. An EM candidate that is matched with a track in the central calorimeter becomes a *loose electron*.

The track momentum is expected to match the measurement of the transverse energy in the calorimeter. An alternate track χ^2 fit uses in addition the ratio of the track transverse momentum p_{T} and the transverse energy E_{T} measured in the calorimeter:

$$\chi^2 = (\frac{\Delta \mathrm{z}}{\sigma \mathrm{z}})^2 + (\frac{\Delta\phi}{\sigma\phi})^2 + (\frac{\frac{\mathrm{E_T}}{\mathrm{p_T}} - 1}{\sigma\frac{\mathrm{E_T}}{\mathrm{p_T}}})^2. \tag{7.4}$$

The performance of the criterion suffers from the worse momentum resolution in the tracker.

EM-ID criteria [86, 87] are implemented in the reconstruction software em_evt [88] and emreco [89] included in the postprocessing package d0correct, version 07 [90].

7.2.2 The Electron Likelihood

The sample of loose electrons still contains a substantial amount of background. It is mainly composed by

- narrow jets with a large electromagnetic energy deposition, caused by:
  - showers from π_0 decays which overlap with a track of a charged particle (main background source)
  - π_0 decays with a photon conversion in the inner part of the tracker
  - charged pions
  - non-isolated electrons from meson decays
- radiated photons which convert in the inner part of the tracker.

The rejection of spurious electrons is increased by the *electron likelihood* [91], which combines several quantities measured in the calorimeter and in the tracker.

The likelihood requires an EM candidate that is matched with a track in the central calorimeter using the track match procedure that includes the $E_{\mathrm{T}}/p_{\mathrm{T}}$ ratio. This track is called *electron track* in what follows. An important quantity which enters the likelihood calculation is the *track isolation*. The electron track is required to be isolated in a large isolation cone which rejects pions and electrons within jets. Isolation in a small cone rejects photon conversions, which result in electrons and positrons with a small distance in $\mathcal{R}$.

The most important calorimeter variable is a χ^2 function of eight correlated shower shape observables: the energy fractions of the four EM layers, the total EM energy, the vertex z-position and the transverse shower width in z and ϕ, which measures how well the shape of the cluster agrees with an electromagnetic shower from an electron. The inverse of the corresponding 8x8 covariance matrix is called *HMatrix H* [92].

$$\mathrm{HMatrix}\,\chi^2 = \sum_{\mathrm{ij}}^{\mathrm{n}} (\mathrm{x_i} - \mu_{\mathrm{i}})\mathrm{H_{ij}}(\mathrm{x_j} - \mu_{\mathrm{j}}) \tag{7.5}$$

with the observed values x_i and the means μ_i for the shower shape observables (see Section 2).

The input variables for the likelihood calculation are:

- the EM fraction
- the shower shape HMatrix χ^2
- the χ^2 probability (for two degrees of freedom) for the spatial match of the electron track
- the number of tracks with $p_{\mathrm{T}} > 0.5\,\mathrm{GeV}$ in a 0.05 cone around and including the electron track

- the p_T sum of all tracks with $p_T > 0.5\,\text{GeV}$ in a 0.4 cone around and excluding the electron track

- the distance of closest approach (DCA) of the track to the primary vertex in the transverse plane.

Figure 7.4 shows the distribution of the EM fraction, the HMatrix χ^2, the spatial track match χ^2 probability and the p_T sum of tracks in an isolation cone of $\Delta\mathcal{R} < 0.4$ for electrons from Drell-Yan $Z/\gamma \rightarrow ee$ processes and for jets that are misidentified as electrons (background) in a background-dominated preselection of events with two loose electron candidates with $15 < M(e,e) < 60$. Whereas the Drell-Yan process results in two electrons with opposite charge (opposite-sign), the background consists of 50% OS events and 50% events with electrons of the same charge (like-sign). The distribution for the Drell-Yan electrons is thus extracted by subtracting the like-sign events from the opposite-sign events. The background distributions are derived from the like-sign events.

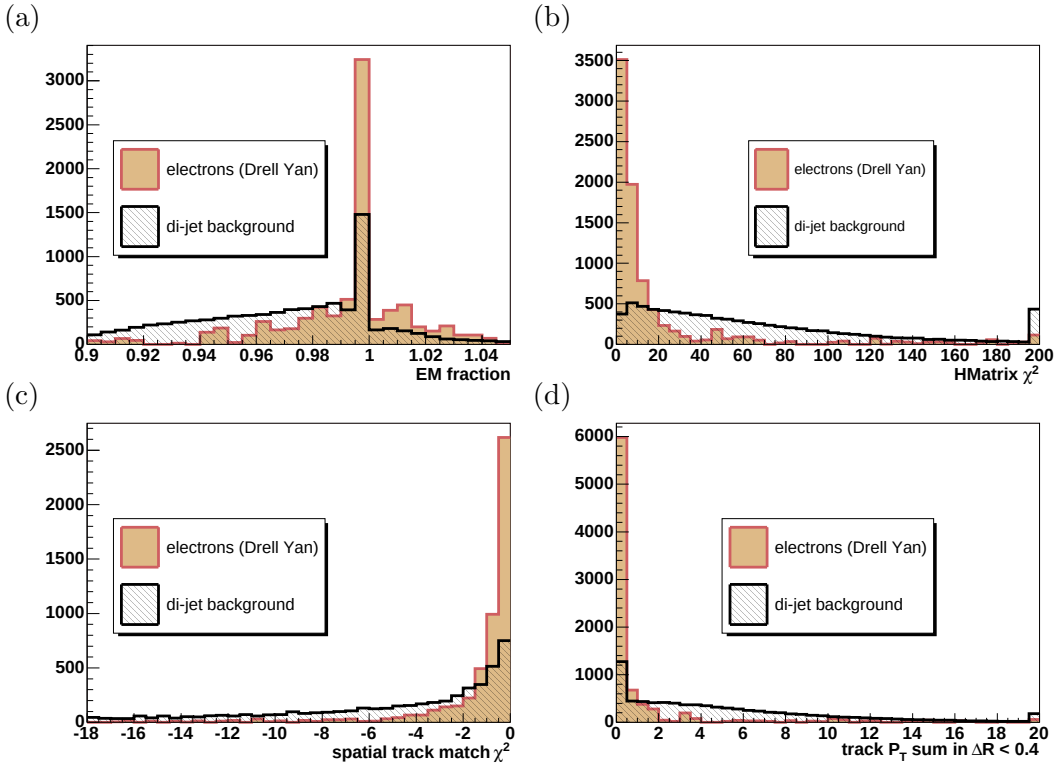

Figure 7.4: Distributions of input quantities for the electron likelihood for electrons (shaded) and electron fakes (hatched) after a preselection of an EM candidate with loose spatial track match in events with two EM candidates with $15\,\text{GeV} < M(e,e) < 60\,\text{GeV}$: (a) EM fraction, (b) HMatrix χ^2, (c) spatial track match χ^2 and (d) p_T sum of tracks in an isolation cone of $\Delta\mathcal{R} < 0.4$.

Figure 7.5 shows the distribution of the electron likelihood for electrons and jets in CC and EC. The loose electron is called *tight* if its likelihood exceeds the value of 0.2.

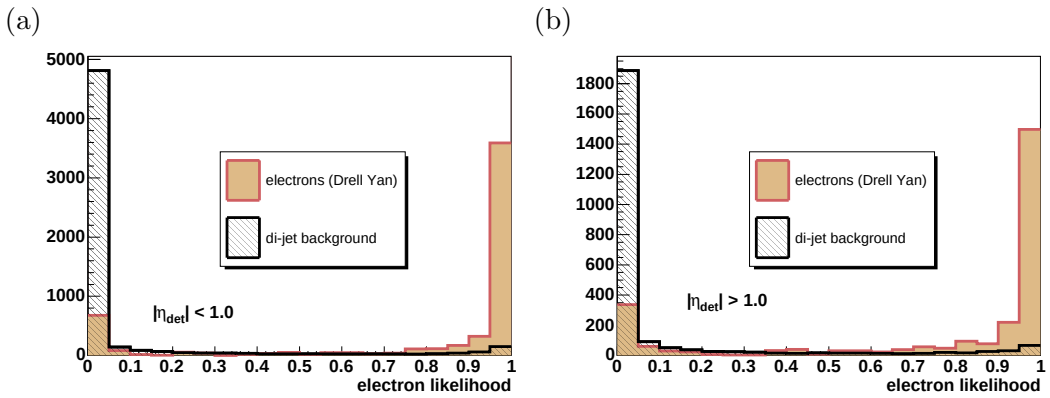

Figure 7.5: Distribution of the electron likelihood for electrons (shaded) and jets (hatched) after a preselection of an EM candidate with loose spatial track match in events with two EM candidates with $15\,\text{GeV} < \text{M(e, e)} < 60\,\text{GeV}$ for (a) $|\eta_{det}| < 1.0$ and (b) $|\eta_{det}| > 1.0$.

7.3 Jets

The jets are reconstructed using the *improved legacy cone* algorithm [93]. It uses cell towers as seeds. Proto-jets are created with a simple-cone algorithm from these seeds and around the midpoints of two seeds. Overlapping cones are separated with a split-and-merge procedure. This analysis uses $\Delta\mathcal{R} < 0.5$ cone jets which are in addition required to be separated ($\Delta\mathcal{R} > 0.5$) from an EM candidate. In the following, jets with a low fraction of the jet energy deposited in the EM layers of the calorimeter (EM fraction < 0.9) are called *hadronic jets* and jets with a larger EM fraction (EM fraction > 0.9) are called *EM jets*.

Hadronic jets are calibrated with the Jet-energy-scale (JES) implemented in the package JetCorr [94], version 05-03-00. The JES corrects for the calorimeter response to jets (determined from E_{T}-balanced photon+jets events), for the energy offset due to the underlying event, pile-up, multiple interactions (see Section 4), electronic and uranium noise (determined by minimum bias events) and for the shower leakage outside the jet cone, which is determined from measured energy profiles of jets. Since the calorimeter response is not modeled correctly in the MC simulation (see Section 9), corrections are derived separately for MC and data. Figures 7.6 and 7.7 show the JES correction factors and their errors derived as a function of the energy and the η position of a jet. Hadronic jets with $\text{E} < 15\,\text{GeV}$ are calibrated with the JES for jets with $\text{E} = 15\,\text{GeV}$. EM Jets are corrected with the EM scale from the electron/photon reconstruction (see Section 7.2.1).

Patterns of calorimeter noise, dominated by the fraction in the coarse hadronic layers (see Section 3.2.4) can be misidentified as jets. They are suppressed by quality requirements which define *good jets* [95] in the following:

- energy fraction in the coarse hadronic layers CHF < 0.4
- L1 confirmation: The ratio of the jet energy measured by the L1 system to the jet energy measured by the precision readout must be larger than 0.4.

Only good jets with corrected transverse energy $\text{E}_{\text{T}} > 15\,\text{GeV}$ are used for this analysis.

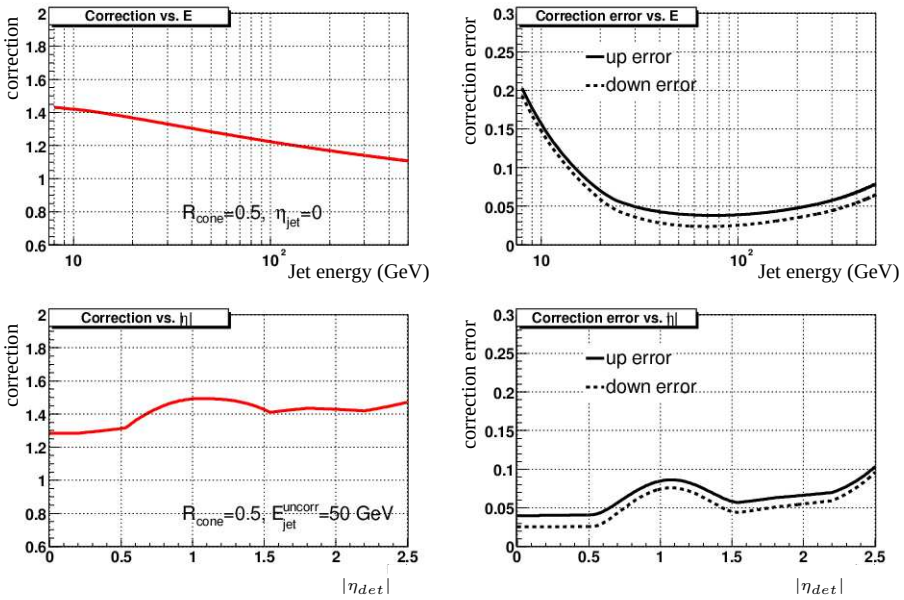

Figure 7.6: Jet energy scale calibration factors and the corresponding errors for data depending on the uncalibrated jet energy for $\eta = 0$ (top) and depending on η for $E_{jet} = 50\,GeV$ (bottom).

7.4 Missing transverse energy

The missing transverse energy ($\not\!\!E_T$) corresponds to the (negative) vector sum of the calibrated energy depositions in the detector. It measures the imbalance of the visible energy, which is usually due to the presence of objects that do not deposit their energy in the detector. A certain resolution in the missing transverse energy is caused by the finite energy resolution of the detectors. The resolution is worsened by additional detector effects such as noise and crosstalk in the readout electronics.

The raw missing transverse energy is calculated in the d0correct package [90] (version 07). The algorithm computes the vector sum in the transverse plane of the energies in all cells within the electromagnetic and the fine hadronic layers of the calorimeter (see Section 3.2.4). In order to avoid mismeasured missing transverse energy from noise in the coarse hadronic layer, cells from this layer are only included into the calculation of the missing transverse energy if they are located within a good jet.

This quantity is corrected for the calorimeter response of the physics objects. The JES calibration (see Section 7.3) is propagated into the calculation of the missing transverse energy. The value of the $\not\!\!E_T$ is also corrected for the EM scale by calculating the difference of the fully calibrated energy of EM candidates and the sum of the energies of the corresponding calorimeter cells. Since muons in Tevatron energy ranges do not develop electromagnetic showers in the calorimeter, the small energy deposition in the calorimeter by direct ionization is corrected by the difference to the full muon transverse momentum, as measured in the muon system and in the tracker. Insufficient calibration of the energy measurement of the physics objects can deteriorate the resolution of the missing transverse energy.

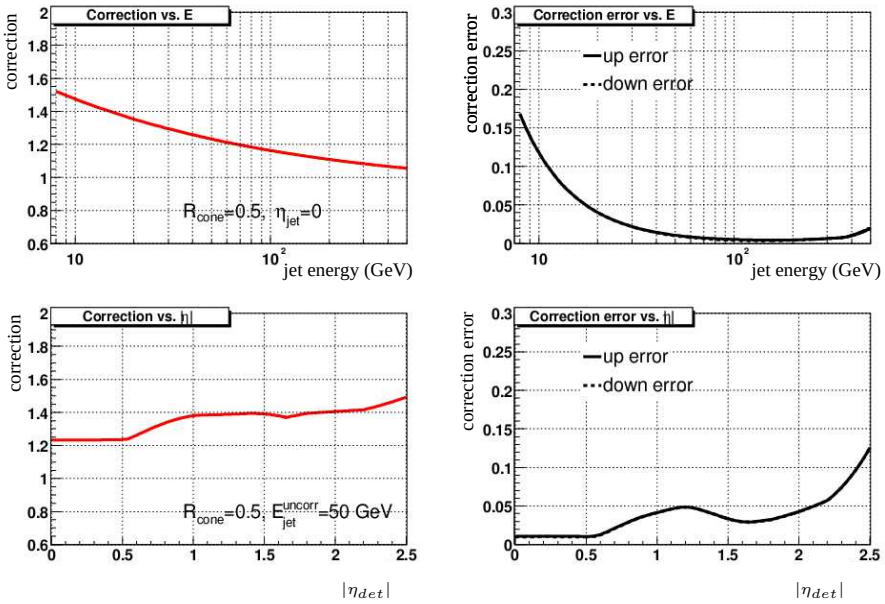

Figure 7.7: Jet energy scale calibration factors and the corresponding errors for MC depending on the uncalibrated jet energy for $\eta = 0$ (top) and depending on η for $E_{jet} = 50\,GeV$ (bottom).

A measure of the $\not\!\!E_T$ resolution is the distribution of the reconstructed $\not\!\!E_T$ in $Z \rightarrow ee$ events which have no true $\not\!\!E_T$. Figure 7.8a shows the effect of the correction for the detector response on the (mismeasured) missing transverse energy in $Z \rightarrow ee$ events. The average $\not\!\!E_T$ is smaller after the response corrections.

Significance of the missing transverse energy

Figure 7.8b shows the distribution of the corrected $\not\!\!E_T$ for $Z \rightarrow ee$ events with and without jets. The missing transverse energy in events with jets is still considerably larger than in events without jets. This is attributed to fluctuations of the energy deposition of jets in the calorimeter. Events where $\not\!\!E_T$ is related to the jet resolution are identified by comparing the size and azimuthal direction of the missing transverse energy with the energy deposition of jets.

A $\not\!\!E_T$ *significance* $\mathrm{Sig}(\not\!\!E_T)$ is calculated by dividing the missing transverse energy by a measure of the jet energy resolution of good jets $\sigma_{E_T(jet)}$ projected into the direction of the missing transverse energy:

$$\mathrm{Sig}(\not\!\!E_T) = \frac{\not\!\!E_T}{\sqrt{\sum_{\mathrm{Jets}} \sigma^2_{E_T(jet)||\not\!\!E_T}}}. \tag{7.6}$$

7.5 Primary vertex

A bunch crossing results in a hard interaction and additional softer minimum-bias interactions at locations spread around the nominal interaction point in the center of the

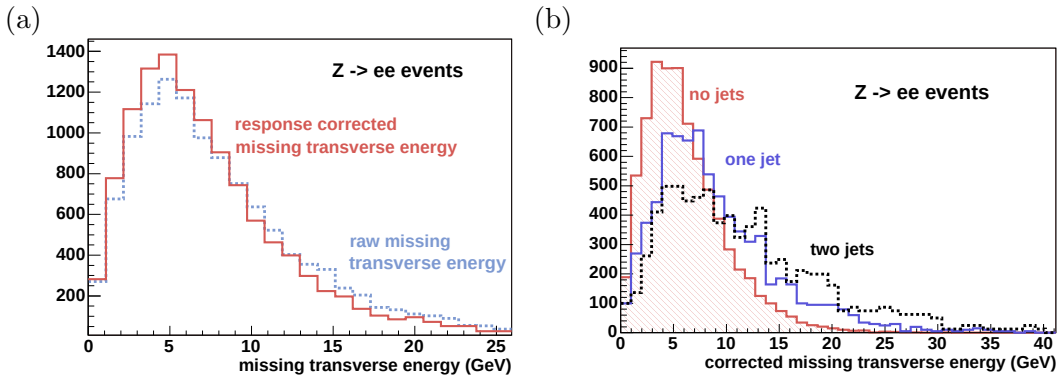

Figure 7.8: (a) Raw (dashed line) and response corrected (continuous line) missing transverse energy in $Z \rightarrow$ ee events and (b) corrected missing transverse energy in in $Z \rightarrow$ ee events without reconstructed jets (hatched), with one good jet (continuous line) and with at least two good jets (dashed line).

detector where the two beams are focussed. The vertex of the hard scattering process is called *primary vertex*. Vertices in a bunch crossing are reconstructed with at least three tracks with SMT hits, which point to the vertex. The exact position is determined with a fit which uses the tracks associated to the vertex. The primary vertex is picked among the vertex candidates based on the multiplicity and the transverse momentum of the associated tracks. Figure 7.9 shows the distribution in z and R = $\sqrt{x^2 + y^2}$ of the primary vertices for Z $\rightarrow$ ee events. The RMS of the z distribution of the vertex position in these events is 24 cm. The RMS of the spread in transverse direction is 0.1 mm. The center value of the distribution (*beam spot*) is shifted with respect to the center of the detector.

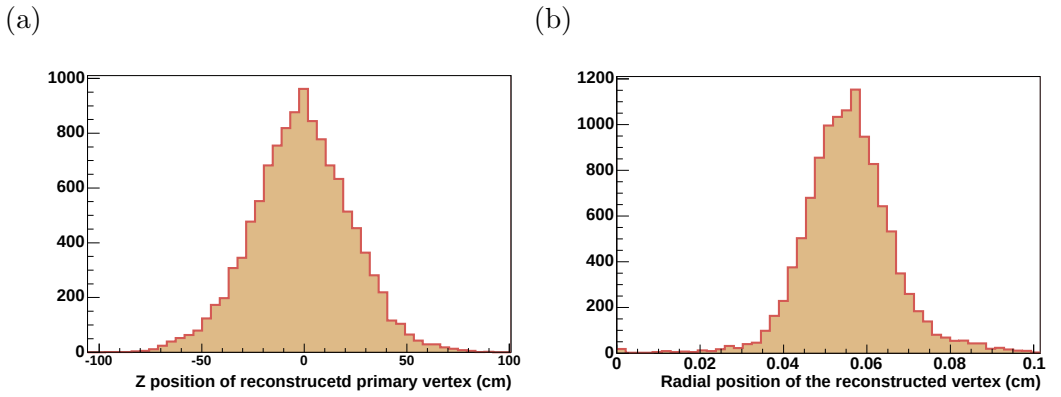

Figure 7.9: (a) Z and (b) R position of the reconstructed vertex in the DØ coordinate system for data taken with trigger version 12.

8 The data sample

The analysis searches for the associated production of charginos and neutralinos in data collected from April 2002 to June 2004 with the DØ detector. This Section gives an overview over the data sample, the trigger requirements and the quality criteria for the data used for the selection.

8.1 Data skims

In order to reduce the processing effort for the individual analyses, the DØ experiment produces subsets of the data [96], characterized by the presence of reconstructed objects with certain quality requirements and momentum ranges.

This analysis uses the *Di-EM skim* which selects events with two EM candidates (see Section 7.2) with $p_{\mathrm{T}} > 7\,\mathrm{GeV}$.

8.2 Data quality selection

The signal selection (see Section 10) relies on the identification of two electrons, three tracks, additional jets and on the reconstruction of the missing transverse energy. Various quality requirements are imposed in order to make sure that all detector components needed for the reconstruction of these objects have been working well. The data quality can be evaluated for a whole *run*, a data unit with a constant DAQ setting that corresponds usually to several hours of data taking. In order to address detector problems, which occurred for a short period within the run, quality flags can be assigned per *luminosity block (LBN)* which is the fundamental unit of time for the luminosity measurement and corresponds to one minute of data taking [97]. The individual quality criteria are discussed in the following.

8.2.1 The calorimeter quality selection

The analysis relies on a good measurement of all calorimeter objects in the event: electrons, jets and missing transverse energy. As a consequence, data units where the direct run control or the distributions of characteristic quantities indicate a calorimeter problem, are discarded from the analysis sample. The quality selection [98, 99, 100, 101] removes:

- LBNs with
  - large average $\not\!\!E_{\mathrm{T}}$
  - large RMS of the $\not\!\!E_{\mathrm{T}}$
  - peaks in the ϕ distribution of jets
  - a large multiplicity of bad jets and a low multiplicity of good jets
  - external noise, picked up by the calorimeter high voltage distribution
  - severe problems in at least one ADC crate
  - large positive and large negative energies in the same event
- runs with
  - identified *hot cells*, that are not removed in the processing
  - other known hardware problems
- events with a pedestal shift in one or several ADCs (*coherent noise*)

These requirements remove about 16% of the Di-EM skim data (see Section 8.1). The fraction of events with coherent noise is estimated from the preselection with two electrons to be $2.3 \pm 0.5\%$.

8.2.2 The tracking quality selection

Since the analysis requires three tracks per event it is very important to ensure a good tracking. As a consequence, all runs with known problems in the SMT or in the CFT [101] are discarded, which removes in addition 1% of the data.

8.2.3 The luminosity quality selection

In order to have an accurate integrated luminosity estimate, the LBNs with problems at the luminosity data acquisition or the luminosity HV settings, online losses, incomplete events, L3 losses, unreadable tapes and problems with the reference triggers that are used to calculate the luminosity are discarded from the data sample [102]. The additional data loss corresponds to roughly 1% of the reconstructed data that has passed the previous selection.

8.2.4 Trigger selection

The data for this analysis is taken with trigger versions 5-12. Table 8.1 shows the set of L3 triggers that is used for this analysis. It is chosen such that it ensures a good coverage of the kinematic range expected from SUSY events as detailed in the trigger study in Section 6. The selection uses the full L1L2 trigger set available for each L3 trigger. A detailed description of the L1, L2 and L3 trigger terms can be found in Section 6.

Triggers	L1 [L2] terms	L3 terms
Trigger Version 5-11		
Di-EM trigger		
2EM_2MD7	CEM(2,5) [2EM(6)*EM(8)]	2L7
2EM_MD12_CEM10	CEM(2,5)*CEM(1,10)	2L7L12
2EM_HI	CEM(2,10)	L20
2EM_HI_SH	CEM(2,10)	SH15
2EM_HI_SH_TR	CEM(2,10)	SH12*TK12
Single-EM trigger		
EM_HI[_2EM5]	CEM(1,10) [CEM(2,5)] [EM(12)]	L30
EM_MX	CEM(1,15)	
EM_HI[_2EM5]_SH	CEM(1,10) [CEM(2,5)] [EM(12)]	SH20
EM_MX_SH	CEM(1,15)	
EM_HI[_2EM5]_SH_TR	CEM(1,10) [CEM(2,5)] [EM(12)]	SH15*TK12
EM_MX_SH_TR	CEM(1,15)	
Trigger Version 12		
Di-EM trigger		
Ex_2T5SH5	E2,E5,E7,E8	2T5SH5
Ex_2SH8	E1-E6,E8	2SH8
Ex_2L8_T8L8	E1-E8	2L8_T8L8
Ex_2L15_SH15	E1-E6	2L15_SH15
Ex_5_11_SH5_T4L5	E2-E7A,E8	5_11_SH5_T4L5
Single-EM trigger		
Ex_SH30	E1-E4	SH30
Ex_SHT20	E1-E4	SHT20
Ex_T13L15	E1-E6	T13L15

Table 8.1: Triggers used for this analysis in different epochs of data taking. See Section 6 for further details

8.3 Integrated luminosity

The rate of inelastic collisions measured with the luminosity monitor (see Section 3.2.8) is used to calculate the integrated *delivered luminosity* at the DØ detector [103]. The fraction of the luminosity that corresponds to crossings when a certain trigger was capable of processing data from the detector is called *exposed luminosity* [97] for this trigger. The fraction of the exposed luminosity that is not lost in the readout process (see Section 3.3.1) is called *recorded luminosity* [104]. The *reconstructed luminosity* corresponds to the fraction of the recorded events that is reconstructed.

The luminosity is calculated for the two high-p_T single-EM triggers which have collected the largest integrated luminosity: EM_MX for trigger V5-11 and E1_SH30 for trigger V12 (see Table 8.1). The data fractions where other triggers have been turned off or prescaled are considered as additional inefficiencies for these triggers. Table 8.2 shows the

integrated luminosity for different trigger versions and data taking periods for the data used for this analysis. The term *good* corresponds to the fraction of events that pass the quality requirements presented in Section 8.2.

trigger version	reference trigger	exposed luminosity	recorded luminosity	recorded good lumi.	reconstructed good lumi.
V5-V11	EM_MX	179.0pb^{-1}	153.1pb^{-1}	116.1pb^{-1}	115.7pb^{-1}
V12	E1_SH30	246.4pb^{-1}	227.0pb^{-1}	200.8pb^{-1}	199.2pb^{-1}
sum		425.4pb^{-1}	380.2pb^{-1}	316.9pb^{-1}	314.9pb^{-1}

Table 8.2: Exposed, recorded and reconstructed luminosity for the data of the two trigger epochs used in this analysis as calculated with the luminosity package lm_access v01–05–01 combined with the estimate for the coherent noise fraction

The systematic uncertainty of the luminosity estimate of 6.5% is dominated by the error on the measurement of the inelastic $\text{p}\bar{\text{p}}$ cross-section followed by the uncertainty on the kinematic distributions for diffractive processes [105]. An additional uncertainty of 0.5% stems from the calculation of the fraction of events with coherent noise.

This resulting luminosity for the data set used for this analysis is

$$\int \text{L}\,\text{dt} = 315 \pm 21\,\text{pb}^{-1}. \tag{8.1}$$

9 Monte-Carlo generation and data-MC comparison

In order to test the Standard Model versus a SUSY hypothesis, it is crucial to translate both theories into an accurate prediction of measurable variables. Most of the expectations are derived from MC simulations. Standard Model contributions with large uncertainties, as for example the background from QCD jet production, and the verification of the MC modeling are derived with data from regions of phase space, where the signal contribution can be neglected, such that no bias is introduced.

9.1 The MC samples

9.1.1 Standard Model processes

The Standard Model backgrounds for this analysis have been discussed in Section 5.2. Apart from the background from QCD jet production (QCD background) which is derived from data, they are simulated with MC methods, as described in Section 4.2. All MC samples are generated with Pythia except for the WW sample, which is generated with Alpgen, interfaced with Pythia.

Further details about the individual MC samples used for this analysis, are listed in Table 9.1. Apart from the WW sample, all samples are produced with leading-order matrix elements (LO ME) and LO PDF versions. The LO cross section is scaled with a K-factor. It corresponds to the ratio of the cross section calculated with the matrix element at the highest available order of perturbation expansion and NLO Cteq6 PDFs to the ratio of the cross section calculated with LO matrix element and the LO PDF used for the MC production.

$$\mathrm{K_{(N)NLO}} = \frac{\sigma(\text{(N)NLO ME, NLO PDF})}{\sigma(\text{LO ME, LO PDF})} \tag{9.1}$$

The errors due to the PDF uncertainty and the errors from varying the factorization and renormalization scale [63, 106] are also listed in Table 9.1 if available. The PDF-related errors on the cross section, calculated according to [63], are dominated by the uncertainty on the position of the global χ^2 minimum of the PDF fit, quantified in terms of a set of eigenvectors [62]. The errors on the cross sections are derived by comparing the cross section that results from the central NLO fit to the cross sections calculated with error PDFs to the various eigenvectors. The contributions from the uncertainty about the renormalization and the factorization scale (see Section 4.1.2) used in the simulation is taken into account by varying the scales within 50% and 200% of the mass scale of the hard interaction. The error on the background expectation is calculated by varying the cross sections within the corresponding errors.

Process	Ref.	K_{QCD}	σ (pb)			# events
Z→ee (60-130)	[107]	NNLO	241.6	$^{+8.7}_{-7.7}(PDF)$	$\pm 0.7(scale)$	300000
Zγ →ee (15-60)	[107]	NNLO	409.3	$^{+15.1}_{-14.7}(PDF)$		1062520
Zγ →ee (12-15)	[107]	NNLO	303.8	$^{+14.3}_{-14.9}(PDF)$		166500
Zγ →ee (5-15)						
$E_T(e) > 7\,GeV$	[107]	NNLO	9.7	$\pm 0.5(PDF)$	$\pm 1.0(stat)$	20650
W→eν incl.	[107]	NNLO	2583	$^{+93}_{-83}(PDF)$	$\pm 5(scale)$	2428687
Z→ ττ (15-60)	[107]	NNLO	409.3	$^{+14.6}_{-13.5}(PDF)$		303500
Z→ ττ (60-130)	[107]	NNLO	241.6	$^{+8.7}_{-7.7}(PDF)$	$\pm 0.7(scale)$	300000
Z→ ττ (130-250)	[107]	NNLO	1.92	$^{+0.5}_{-0.6}(PDF)$		104000
ZZ incl.	[106]	NLO	1.42	$\pm 0.06(PDF)$	$\pm 0.05(scale)$	10000
WW → ℓℓ	[106]	NLO	12.0	$\pm 0.6(PDF)$	$\pm 0.3(scale)$	170350
WZ incl.	[106]	NLO	3.68	$\pm 0.22(PDF)$	$\pm 0.12(scale)$	15000
$t\bar{t}$ → eebbνν	[108]	NNLO	0.078	±0.005		9750
Y(1S)→ee	from data		35	±10		30000
Y(2S)→ee	from data		25	±7		29750

Table 9.1: $\sigma_{Prod} \times BR$ and the number of generated events for the background processes of this analysis. The order of QCD perturbation expansion at which the cross section has been calculated and a reference for the cited cross section value are included in the table.

9.1.2 Signal samples

The selection of SUSY candidates is by a large part based on the different distributions of kinematic quantities as compared to Standard Model processes. As a consequence, the selection efficiency is highly dependent on the masses and mass differences of the SUSY particles involved. A large number of parameter combinations (*SUSY points*) have been generated in order to perform a scan of the gaugino masses and the slepton masses (see Section 11). This section presents a small subset of *benchmark points* which are used for the optimization of the signal selection. They are chosen such that they comply with the LEP limits from direct sparticle searches, as outlined in Section 1.2.6, in particular the lower limit on the chargino mass and the lower limits on the slepton masses. Stau-mixing is turned off, which leads to equal branching ratios into the three lepton generations. The properties of these samples are summarized in Table 9.2. The points are chosen from two kinematic regions, depending on the decay type of the second neutralino:

- *3-body region*: the slepton mass is larger than the mass of the second neutralino → 3-body decays of the second neutralino (points M4, M6, M12);
- *2-body region*: the slepton mass is smaller than the mass of the second neutralino → 2-body decays of the second neutralino into a real slepton and the Standard Model partner (DM3).

SUSY points M4 and DM3 have a chargino mass directly beyond the lower limit from LEP II of 103.5 GeV. Point M12 is characterized by large chargino and neutralino masses,

beyond the expected sensitivity of the analysis with the current data set. Point M6 with a modest chargino mass of 110 GeV is chosen as the most important reference point for the optimization of the kinematic cuts.

The MSSM input parameters are calculated with SOFTSUSY [109]. The samples are generated with PYTHIA, version 6.3 using CTEQ 6 PDFs. NLO K-factors are calculated according to the prescription in [74].

Pt	$m_{\chi_2^0}$ [GeV]	$m_{\chi^\pm}$ [GeV]	$m_{\tilde{\ell}_R}$ [GeV]	$m_{\chi_1^0}$ [GeV]	BR(χ_2^0) e$\mu\tau$	BR(χ_2^0) $\tilde{\ell}$	BR($\chi^\pm$) e$\mu\tau$	BR($\chi^\pm$) $\tilde{\ell}$	BR(3ℓ)	$\sigma\times$BR(3ℓ) [pb]
M4	108	104	109	58	0.70	0.00	0.52	0.00	0.37	0.346
M6	114	110	115	61	0.70	0.00	0.51	0.00	0.36	0.265
M12	152	150	153	82	0.58	0.00	0.42	0.00	0.24	0.046
DM3	108	104	101	58	0.00	0.99	0.57	0.01	0.57	0.486

Table 9.2: Slepton and gaugino masses, branching ratios of the gauginos and the product of the cross section and the leptonic branching fraction $\sigma\times$BR(3ℓ) of the SUSY benchmark points used in the optimization of the analysis.

9.2 Background from QCD jet production

The contribution of the QCD background, which corresponds to jets that are misidentified as electrons, can not reliably be simulated in MC and is instead determined from data. In order to obtain a data sample, which is dominated by QCD jet production, a part of the electron identification requirements is reversed. This sample is used to calculate the efficiency for the selection cuts which are not correlated to the reversed electron identification criteria. The efficiency for the correlated cuts is determined separately. The sample is referred to as *QCD sample* in what follows.

In the analysis presented here, the QCD sample is selected by requiring two EM objects with a broad shower shape (HMatrix$\chi^2 > 35$) and without any likelihood requirement for the electron candidates. This sample corresponds to events with at least two jets with a large EM fraction, which are broader than the jets that fake electrons in the analysis preselection.

The difference in the jet width leads to differences in the trigger efficiency and in the reconstruction efficiency, which have an impact on the p_T and η distributions of the electron candidates: The low-p_T electron triggers (see Section 6) are designed to have a lower efficiency for broader EM-jets than for electron-like jets, which leads to a different p_T turn-on in the QCD sample and the real QCD background. In addition, the η-acceptance for the broad jets differs from the acceptance for narrow jets, especially close to the boarder of the calorimeter cryostats. Since the number of events with broad jets is different from the number of events with jets which fulfill the electron identification requirements, the QCD sample has to be normalized.

Overall normalization factors and corrections for p_T and η distributions are derived from an additional QCD background sample. It consists of the subsample of the analysis with

like-sign electrons, which is dominated by QCD events at the preselection level (see Section 10.2.1) and is called *like-sign sample* in what follows. Since a typical jet is composed of numerous hadronization and conversion products, the charges of the jet hadrons which fake the two electron tracks are not related. As a consequence, the like-sign subsample corresponds to half of the QCD background in the analysis preselection. The sample is corrected for the small number of $Z/\gamma \to \ell\ell$ events with misidentified charge. Since the leading two electrons from a SUSY signal are expected to be like-sign in a considerable fraction of the events, the like-sign sample cannot be used to model the QCD background within stages of the analysis, where the signal contribution cannot be neglected. It is used though to remove the trigger bias and correct the η distribution in the QCD sample at preselection level. This is done iteratively for the leading and the next-to-leading electron and for the η and p_T corrections. The corrections are derived separately for trigger versions 5-11 and 12. Global normalization factors of 0.0034±0.0007 and 0.0061±0.0008 are derived at large values of p_T for both electrons for trigger version 5-11 and trigger version 12 respectively.

The η-dependent correction factors for the QCD sample are summarized in Table 9.3.

η range	0.75-1.0	1.0-1.3	1.3-1.9	1.9-2.5	2.5-3.0
Trigger V5-11					
correction, leading electron	0.7±0.1	1.0±0.2	2.7±0.4	3.8±0.5	1.0±0.3
correction, next-to-leading electron	0.7±0.1	1.2±0.2	1.9±0.3	3.2±0.5	3.2±0.8
Trigger V12					
correction, leading electron	0.8±0.1	1.2±0.1	2.6±0.3	3.8±0.5	3.8±0.5
correction, next-to-leading electron	0.8±0.1	1.2±0.2	2.1±0.3	3.3±0.4	3.3±0.4

Table 9.3: Scale factor for the QCD sample derived with the like-sign sample for different bins in η, for the leading and the next-to-leading electron candidate.

Figure 9.1 shows the ratio of the p_T distribution in the like-sign sample and the QCD sample for the last iteration step at preselection level after the global normalization and after the final η corrections. This ratio is fitted with a fifth order polynom in case of the leading electron and with a third order polynom of in case of the next-to-leading electron. The event weight of the QCD sample is corrected for each electron if the correction is larger than 1.0.

Normalization and p_T and η corrections are calculated once at preselection level and used for the whole selection. Apart from the cuts on HMatrix χ^2 and the likelihood, all selection cuts are applied to the QCD sample. The rejection of additional likelihood cuts which are performed after the normalization at preselection level is calculated with the like-sign sample and used to scale the QCD sample at this selection level.

9.3 MC efficiency and resolution corrections

The MC samples, although produced with a full detector simulation, do not reproduce the data correctly. This is partly due to the fact that the triggers are not simulated in

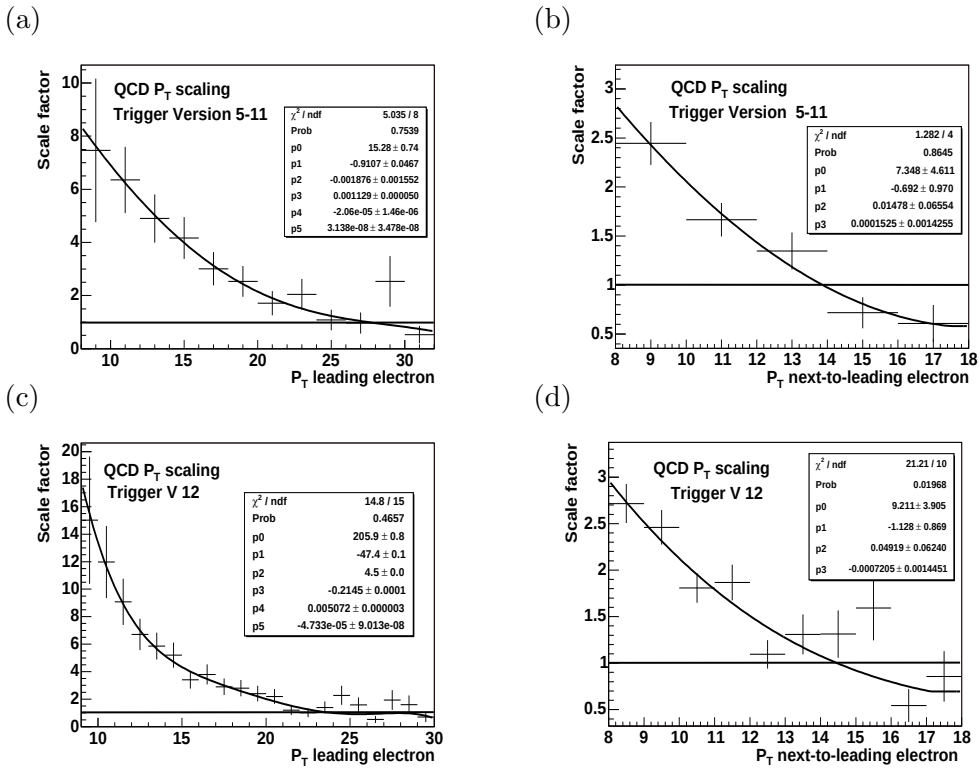

Figure 9.1: Ratio of the large HMatrix QCD sample and the like-sign sample as a function of the p_{T} of the leading and of the next-to-leading electron at the preselection stage in data taken (a,b) with trigger versions 5-11 and (c,d) with trigger version 12. The fit is used to scale the large HMatrix χ^2 sample for scale factors larger than 1.0.

MC. Additional corrections have to be derived for the p_{T} resolution of the tracker and the calorimeter. The incomplete implementation of the detector in GEANT and additional effects, mainly in the readout electronics which are not simulated lead also to corrections of the electron identification efficiency, the rate of photon conversions in the tracker and the resolution of the missing transverse energy. The approximation of ISR by parton showers models certain areas of the final state phase space only poorly.

Many of the corrections applied in the following sections affect mainly the modeling of the Z/γ and W backgrounds and are crucial for the optimization of the selection cuts. Since these backgrounds are successfully rejected in the course of the analysis selection, the impact of these corrections on the total background expectation in the final result is comparably small. The uncertainties of all corrections are included into the systematical error on the final analysis result.

9.3.1 Data samples for efficiency studies

MC corrections are derived using a preselection of $\mathrm{Z}/\gamma \rightarrow \mathrm{ee}$ candidates with two tight electrons with $p_{\mathrm{T}} > 7$ GeV in $|\eta_{det}| < 3.0$ and with an invariant di-electron mass $\mathrm{M(e,e)} > 18\,\mathrm{GeV}$ corresponding to the analysis preselection (see Section 10.2.1). If the p_{T}

dependence of the correction can be neglected or if the purity of the sample is crucial for deriving corrections, the preselection sample is tightened to a $Z \to ee$ sample by requiring $p_T > 25\,GeV$ and by selecting events with M(e,e) in a window around the Z resonance (usually $|M(e,e) - M(Z)| < 20\,GeV$). Since tightening the likelihood cut increases the electron purity in the $Z \to ee$ sample, a cross check with tighter likelihood requirements is performed. The expected contribution from SUSY events is too small to have a significant effect on the distributions analyzed in the following studies.

The modeling of true large $\not{E}_T$ and of the electron misidentification probability of jets and photons is studied with a subset of the Di-EM skim with W candidates: the *W+EM* sample. The basic W+EM selection requires one electron with $p_T > 25\,GeV$ and likelihood > 0.8, and a second EM object with $20\,GeV < M(e,e) < 50\,GeV$ and $p_T > 8\,GeV$. The missing transverse energy is required to have a large significance and to be in excess of 25 GeV. The transverse mass with the leading electron (see Section 10.2.4) must be larger than 40 GeV. The $W + \gamma$ fraction within this sample can be enriched by requiring a small HMatrix $\chi^2 < 20$ for the second EM object.

9.3.2 Trigger efficiency

The triggers which are used for this analysis are shown in Table 8.1. Since the triggers are not yet simulated in the standard MC, trigger efficiencies have to be measured in data and then folded into signal and background MC. The tag-and-probe method described in Section 6 yields trigger efficiencies, which can in principle be combined to calculate the efficiency of the OR of all triggers of a trigger set.

Since the explicit trigger turn-on is of no immediate interest for the analysis but only the resulting MC efficiency corrections in the low-p_T region, an alternative approach is used. The corrections for the p_T turn-on of the logical OR of the triggers in the trigger set is calculated by comparing the p_T distributions of the two leading electrons in Drell-Yan $Z/\gamma \to ee$ events in data and MC.

The procedure is performed for the di-electron preselection sample described above. The lower p_T thresholds for the electrons (8 GeV and 7 GeV for the leading and the next-to-leading electron) are below the analysis thresholds of 12 GeV and 8 GeV respectively. All corrections described in the following sections are applied on the MC events. Since the number of $Z \to ee$ events selected in data and MC shows a good agreement for both trigger versions, no further normalization of the MC is required. Figures 9.3a+c and e+g show the p_T distributions of both electrons without the trigger corrections for trigger versions 5-11 and 12 respectively. The fraction of Drell-Yan Z/γ events within the di-electron preselection in data is obtained by subtracting the number of events expected from the QCD background (see Section 9.2) from the total preselection sample. The trigger efficiency correction corresponds to the ratio of the number of Z/γ events in data and MC as a function of the electron p_T. The correction is then fitted using a sum of two Gaussian error functions (integrated Gaussian distributions) in order to model contributions of individual triggers:

$$\epsilon^{\text{trig}} = P_0 + 0.5 \times P_2 \times (1 + \text{Errfct}(\frac{p_T - H_2}{\sqrt{p_T} \times S_2})) + 0.5 \times P_1 \times (1 + \text{Errfct}(\frac{p_T - H_1}{\sqrt{p_T} \times S_1})) \quad (9.2)$$

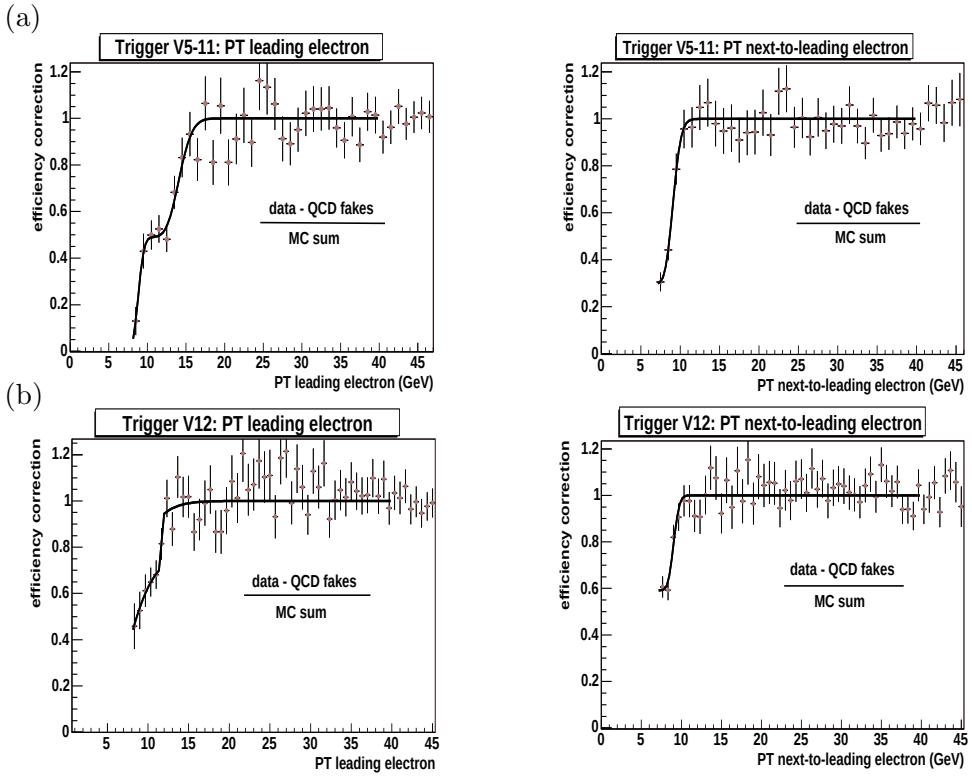

Figure 9.2: Number of data divided by number of expected background events (mainly Drell-Yan events) as a function of the p_{T} of the leading electron and of the p_{T} of the next-to-leading electron at the preselection level for (a) trigger version 5-11 and (b) trigger version 12.

with the plateau efficiencies P_0, P_2 and $\mathrm{P}_1 = 1 - \mathrm{P}_2 - \mathrm{P}_0$, the half points H_1 and H_2 and the *slopes* S_1 and S_2 which correspond to the difference of the p_{T} resolution at trigger level and in the offline reconstruction. The procedure is performed iteratively for the leading electron in order to correct for the trigger efficiency of the single electron triggers and for the next-to-leading electron in order to describe the fraction of events, which have not been triggered by a single electron trigger. The fit results for the last iteration step are shown in Table 9.4. The MC events are corrected depending on the p_{T} of the two leading electrons with the fit values for both electrons.

	P_0	P_2	H_1	H_2	S_1	S_2
V5-11, 1st	0.000±0.005	0.49±0.05	14.13±0.45	8.84±0.23	0.49±0.31	0.26±0.13
V5-11, 2nd	0.297±0.049	–	9.11±0.16	–	0.36±0.11	–
V12, 1st	0.000±0.016	0.78±0.10	11.67±0.00	7.73±0.92	0.000±0.001	0.12±0.51
V12, 2nd	0.592±0.040	–	9.04±0.18	–	0.25±0.11	–

Table 9.4: Fit results for the trigger turn-on

The trigger turn-on is calculated separately for data taken with trigger versions 5–11 and for data taken with trigger version 12, because of major changes in the trigger menu for

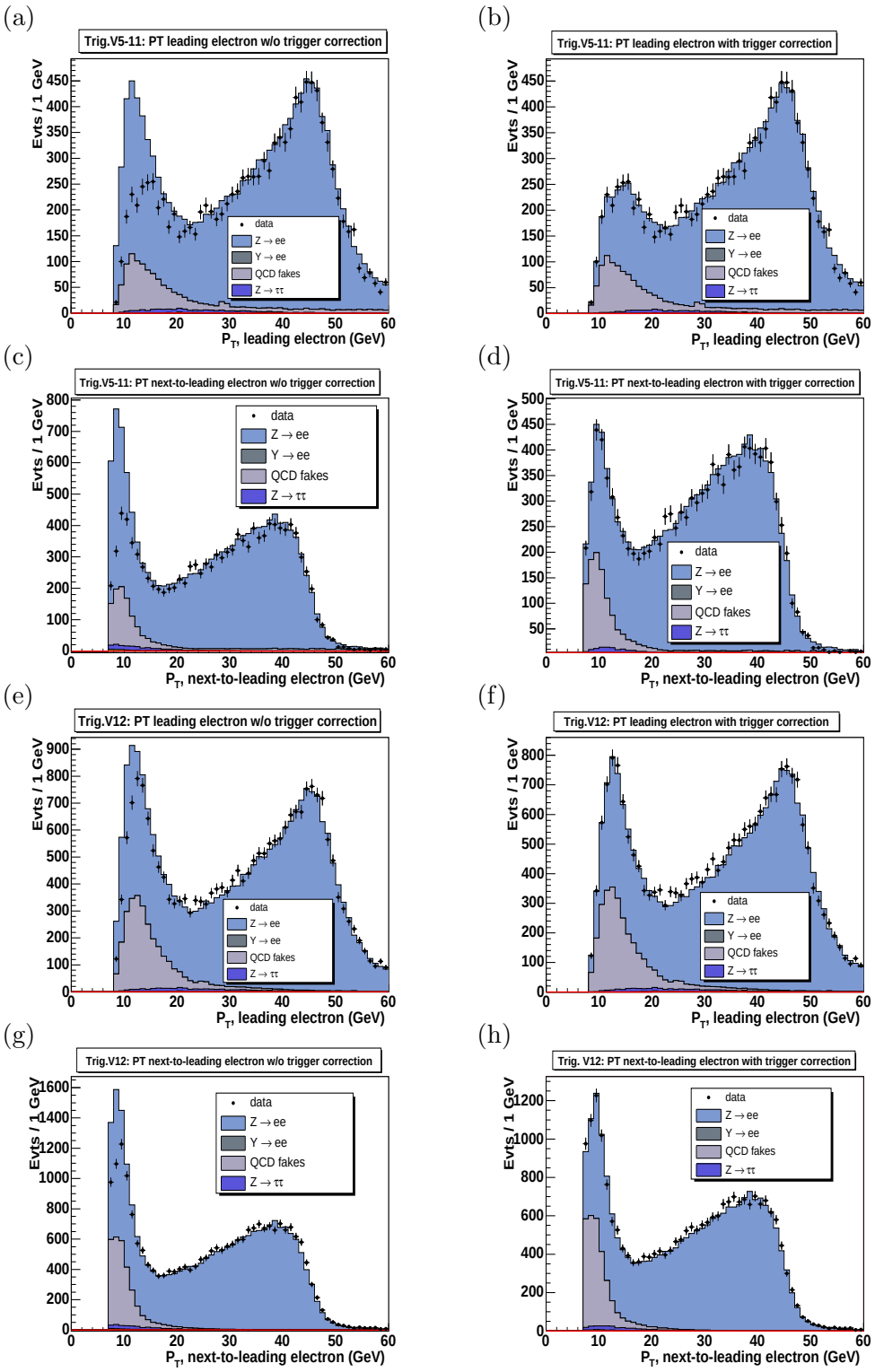

Figure 9.3: Distribution of the transverse momentum of the leading and the next-to-leading electron in data (points with error bars) and MC and QCD sample (histograms) before (a,c,e,g) and after (b,d,f,h) applying the p_{T} dependent trigger corrections to the MC for (a-d) trigger versions 5-11 and (e-h) trigger version 12.

trigger version 12 (see Section 6). Figure 9.2 shows the turn-on corrections for leading and next-to-leading electron for both trigger versions. The p_{T} distributions of both electrons after the trigger corrections are shown in Fig. 9.3b+d and f+h for trigger versions 5–11 and 12 respectively. The analysis selection uses a weighted average of the corrections for both trigger versions, with the weights corresponding to the luminosity share.

9.3.3 Electron resolution corrections

The calorimeter energy resolution for electrons is not properly modeled in the detector simulation. This fact has been subject of many ongoing studies since several years, which focus mainly on refined calibration, electronic noise and wrong description of the detector in GEANT [110]. As a consequence the reconstructed electron energies in MC have to be smeared in order to reproduce the resolution in data. In addition, the center value of the energy distribution has to be corrected. The smearing and scaling parameters are derived by comparing the distribution of M(e,e) for $\mathrm{Z} \to \mathrm{ee}$ events in data and MC. For this case the $\mathrm{Z} \to \mathrm{ee}$ selection uses a broader mass window of $|M(\mathrm{e},\mathrm{e}) - M(Z)| < 30\,\mathrm{GeV}$.

The analysis in this thesis uses electrons up to $|\eta|_{det} < 3.0$ without constraints on the azimuthal angle ϕ. This includes less sensitive detector regions (*non-fiducial* regions) which consist of the ϕ *cracks* at the boarders of a calorimeter tower in CC ($|\eta| < 1.0$) and the intercryostat region which corresponds roughly to $1.0 < |\eta|_{det} < 1.5$ (see Section 3.2.4). These regions are characterized by a worse electron p_{T} resolution. As a consequence, electron energies are smeared and rescaled separately for fiducial electrons in CC, non-fiducial electrons in CC, electrons in the ICR and electrons in EC ($|\eta| > 1.5$). Electron energies are smeared with a Gaussian of rms $= \sigma_{\mathrm{el}}$ and scaled with a factor $\mathrm{corr}_{\mathrm{el}}$ according to

$$\mathrm{E}_{\mathrm{new}} = \mathrm{E}_{\mathrm{old}} * \mathrm{corr}_{\mathrm{el}} * (1. + \mathrm{Gaussian}(\sigma_{\mathrm{el}})) \tag{9.3}$$

The smearing and scaling parameters for the four detector regions are listed in Table 9.5.

region	σ_{el}	$\mathrm{corr}_{\mathrm{el}}$
CC fiducial	0.040±0.004	1.006±0.001
CC non-fiducial	0.080±0.004	0.950±0.002
ICR	0.055±0.010	0.984±0.001
EC	0.035±0.006	0.990±0.001

Table 9.5: Smearing parameters for electrons

The MC overestimates the probability to reconstruct the ϕ coordinate of an electron in the critical region around the ϕ cracks, defined as $|\phi - \phi_0| < 0.02$, where ϕ_0 is the center of the ϕ crack. This problem is probably related to a poor modeling of the energy deposition at the border of a cell [84]. As long as this feature is not corrected for in the detector simulation, the fiducial and non-fiducial fractions in MC are reweighted in order to fit the fraction in the data such that the total number of expected CC events is not changed.

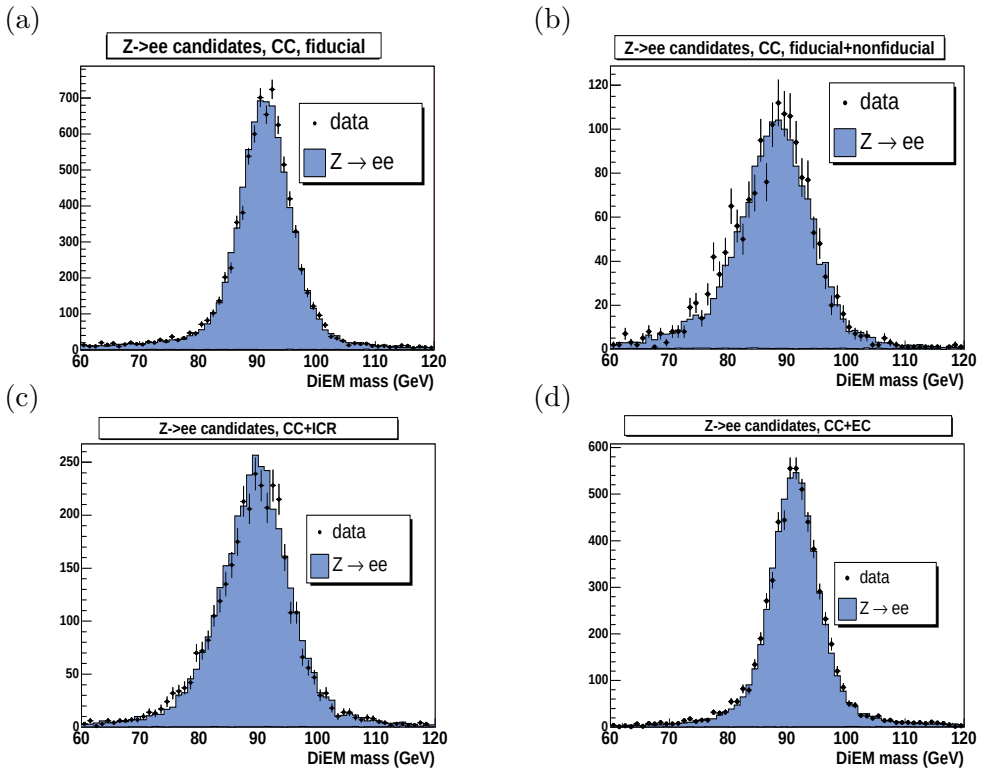

Figure 9.4: Distribution of M(e,e) in Z → ee events in data and smeared MC (a) for both electrons in fiducial detector regions in CC, (b) for one electron near a phi crack (CC non fiducial), (c) for one electron in $1.0 < |\eta_{\rm det}| < 1.5$ (ICR) and (d) for one electron in $1.5 < |\eta_{\rm det}| < 3.0$ (EC). All electron efficiency corrections described in this note are applied.

The weights are determined by comparing the fiducial and non-fiducial electron fractions in CC+CC Z → ee events in data and MC. The resulting values are 0.56± 0.01 for the non-fiducial fraction and 1.08± 0.02 for the fiducial fraction.

Figure 9.4 shows the distribution of the Di-EM mass in Z → ee events in data and smeared MC for the four detector regions. All electron energy corrections are propagated into the $\not\!\!E_{\rm T}$ calculation.

9.3.4 Electron identification efficiency corrections

Efficiencies for the identification of EM candidates (see Section 7.2.1), which comprises the calorimeter clustering and the requirements on the EM fraction and the isolation, have been measured in data for Z → ee candidates in [84] using a tag-and-probe method. The probe sample requires one identified electron and a second track, with the invariant mass of electron and track within the Z mass window.

These efficiencies are compared with the electron identification efficiency measured in MC obtained by matching a reconstructed EM candidate to a generated MC electron from Z → ee MC samples. The resulting efficiencies for data and MC are shown in Table 9.6 for

different $|\eta_{\text{det}}|$ regions. Since MC and data efficiencies agree within the errors no correction is applied for the electron identification.

	$\lvert\eta_{\text{det}}\rvert < 1.05$	$1.5 < \lvert\eta_{\text{det}}\rvert < 2.3$
data efficiency	0.988±0.003	0.995±0.011
MC efficiency	0.991±0.001	0.991±0.001
MC correction factor	0.997±0.003	1.004±0.011

Table 9.6: Data and MC efficiencies and the resulting correction for MC for probe electrons in Z → ee events. The data efficiencies are taken from Ref. [84].

cut		CC	
		fid	non-fid
tr. match	ϵ_{data}	0.973±0.010	0.965±0.010
tr. match	ϵ_{MC}	0.983±0.001	0.984±0.001
tr. match	corr	0.990±0.010	0.981±0.011
Lhd>0.2	ϵ_{data}	0.878±0.009	0.792±0.012
Lhd>0.2	ϵ_{MC}	0.932±0.001	0.913±0.002
Lhd>0.2	corr	0.942±0.010	0.867±0.013
Lhd>0.8	ϵ_{data}	0.813±0.009	0.675±0.013
Lhd>0.8	ϵ_{MC}	0.903±0.001	0.863±0.003
Lhd>0.8	corr	0.900±0.010	0.782±0.015

cut		EC				
		$1.1 < \eta < 1.5$	$1.5 < \eta < 1.7$	$1.7 < \eta < 2.0$	$2.0 < \eta < 2.3$	$2.3 < \eta < 3.0$
tr. match	ϵ_{data}	0.940±0.011	0.860±0.012	0.677±0.013	0.568±0.016	0.561±0.018
tr. match	ϵ_{MC}	0.985±0.001	0.947±0.002	0.874±0.003	0.857±0.004	0.844±0.005
tr. match	corr	0.954±0.013	0.909±0.013	0.774±0.015	0.662±0.019	0.665±0.022
Lhd>0.2	ϵ_{data}	0.794±0.013	0.810±0.012	0.643±0.013	0.534±0.017	0.468±0.020
Lhd>0.2	ϵ_{MC}	0.916±0.003	0.925±0.003	0.854±0.004	0.835±0.005	0.756±0.006
Lhd>0.2	corr	0.867±0.014	0.876±0.014	0.753±0.016	0.639±0.020	0.619±0.026
Lhd>0.8	ϵ_{data}	0.633±0.015	0.731±0.013	0.585±0.014	0.480±0.017	0.348±0.021
Lhd>0.8	ϵ_{MC}	0.799±0.005	0.883±0.004	0.812±0.004	0.775±0.006	0.591±0.008
Lhd>0.8	corr	0.792±0.019	0.828±0.015	0.720±0.018	0.618±0.023	0.590±0.037

Table 9.7: Data and MC efficiencies for probe electrons in Z → ee events and efficiency corrections for the electron spatial track match (tr.match) and the electron Likelihood (Lhd).

Efficiencies for loose spatial track match and various likelihood cuts have been measured separately for electrons in fiducial CC, non-fiducial CC, and in several detector-η bins in the EC region, using the tag and probe method in Z → ee events in data and MC. The Z → ee candidates in data are required to pass a loose Di-EM trigger without shower shape or track requirements and to have two electrons with $p_{\text{T}} > 25\,\text{GeV}$ and $|\text{M(e, e)} - \text{M(Z)}| < 30$. The tag electron is required to be in the fiducial CC region, to have a standard spatial track match (see Section 7) and an electron likelihood in excess of 0.9. The QCD background

is fitted and subtracted. The results are presented in Table 9.7. The resulting difference in data and MC is applied as efficiency correction for all MC electrons.

9.3.5 p_{T}(Z) reweighting

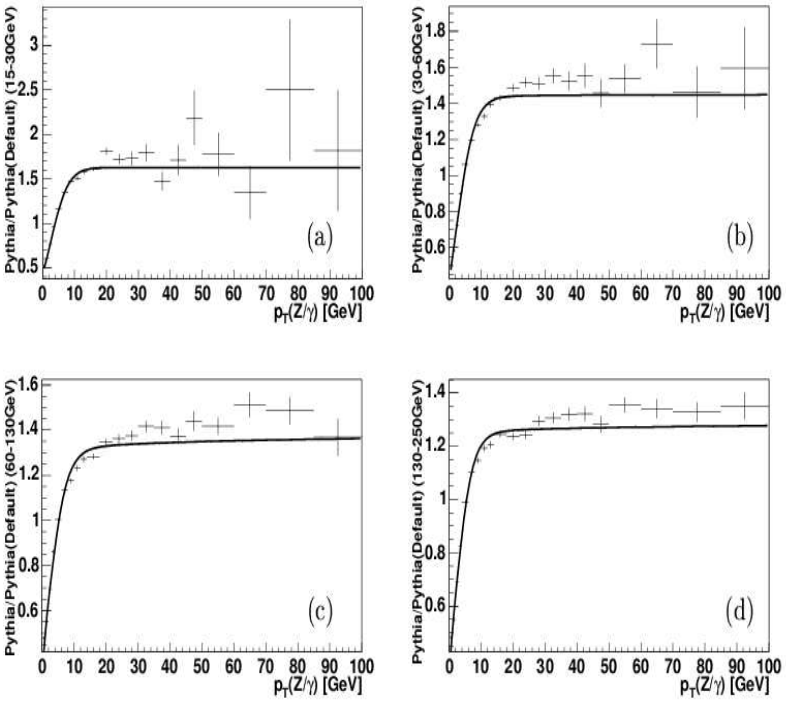

Figure 9.5: Ratio between tuned and default PYTHIA MC as a function of generated p_{T}(Z) for the mass ranges: (a) 15 GeV < M(Z/γ) < 30 GeV, (b) 30 GeV < M(Z/γ) < 60 GeV, (c) 60 GeV < M(Z/γ) < 130 GeV and (d) 130 GeV < M(Z/γ) < 250 GeV (from Ref. [111]).

The distribution of the transverse momentum p_{T}(Z) of the Z boson is not properly described in the default PYTHIA 6.2. This problem can be addressed by tuning effective parameters of PYTHIA which enter the modeling of the (ISR) parton showers. In [111], the primordial k_{T} and the QCD scale for parton showering in PYTHIA samples are tuned via four input parameters based on the differential Z boson production cross section as a function of p_{T} as measured in $\mathrm{Z} \to \mu\mu$ events in Run I and Run II data. The ratio of the number of events in tuned and in default MC as a function of p_{T}(Z) is fitted in [111] separately for four invariant mass windows (see Figure 9.5). The $\mathrm{Z}/\gamma \to \ell\ell$ MC which is used in this analysis is reweighted with this ratio using the fit results presented in [111]. Figure 9.6 shows the distribution in data and MC of the reconstructed p_{T}(Z) before and after p_{T}(Z) reweighting for a $\mathrm{Z} \to \mathrm{ee}$ sample and for the low-mass preselection ($\mathrm{M(e,e)} < 60\,\mathrm{GeV}$, see Section 10.2.1).

The corrections are tuned based only on the p_{T}(Z) distributions. It has been checked, that the tuning has no negative impact on the description of the other quantities that are used in this analysis (see Section 10).

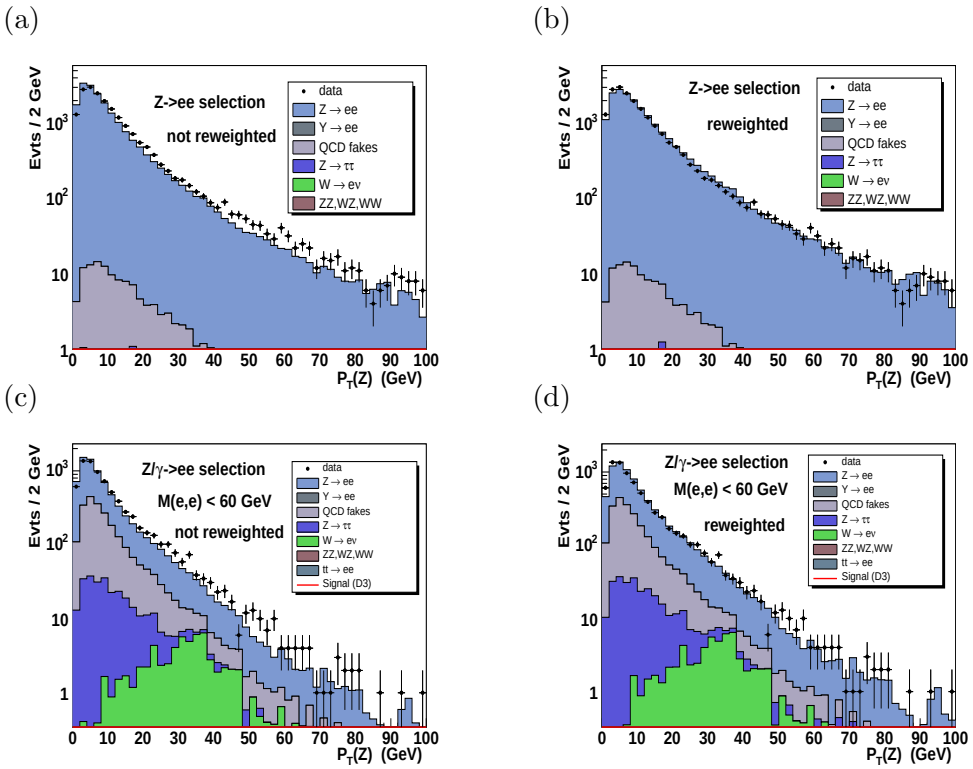

Figure 9.6: Distribution of the reconstructed transverse momentum of the (e, e) system (a,b) for a $Z \to ee$ selection and (c,d) at the low-mass preselection level (a,c) before and (b,d) after the $p_T(Z)$ reweighting.

9.3.6 Description of the ISR processes

Due to the true large missing transverse energy, $W \to e\nu + \text{jet}/\gamma$ processes constitute an important background for this analysis such that the correct modeling of this background is important for the optimization of the analysis.

The W+γ production consists of photon radiation from a W (see Fig. 5.9a), denoted with WWγ in the following, and ISR photon radiation (see Fig. 5.9b). Figure 9.7a compares the angle $\Delta\mathcal{R}$ between the electron and the second EM-object in W+γ candidates in data and Pythia W-inclusive MC. Events with very low and events with very large $\Delta\mathcal{R}$ between the reconstructed electrons are not well simulated in MC. This is attributed to the fact, that the Pythia the parton shower method (see Section 4.1.6), does not correctly reproduce the p_T and angular distribution of the radiated ISR photon. This effect is compensated by rescaling the fraction of WWγ events in the W inclusive sample by a factor of 1.8. The WWγ candidates are selected by requiring a photon at generator level with $p_T > 5\,\text{GeV}$ which stems from the W and is matched with the next-to-leading reconstructed electron. Figure 9.11b shows the $\Delta\mathcal{R}$ distribution after the rescaling.

The distribution of the W+jet fraction has not been analyzed in detail due to the fact that the most obvious discrepancies between data and MC are observed in a selection of W+γ events. The modeling of the second jet/photon which can be misidentified as a third

(a) (b)

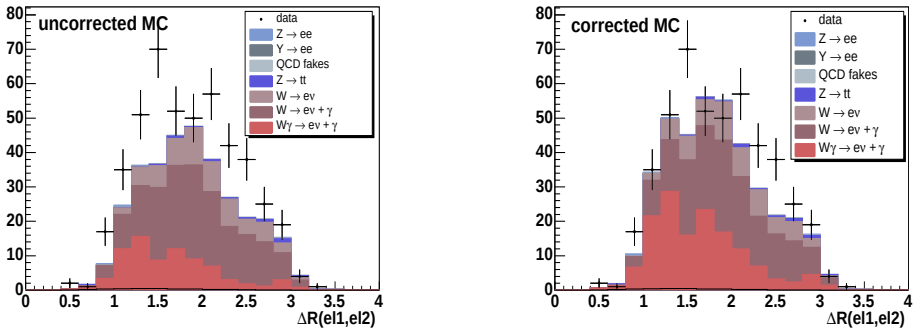

Figure 9.7: Distribution in data and MC of the angle $\Delta\mathcal{R}$ between the electron and the second EM-object in W+γ candidates (a) before and (b) after the correction for ISR. The W-inclusive MC is subdivided into events with a photon with $p_T > 5\,\text{GeV}$ radiated from the W which is matched to the second electron (dark red), events with such a photon which is not radiated from the W boson (dark purple, mostly photons from π_0 and ρ_0) and events without such a photon (light purple).

lepton in the analysis selection has not been checked due to the lack of statistics. In this regard the analysis will profit from ongoing studies of the p_T distribution and multiplicity of jets in W+jets events which have more statistics because the leading jet is not required to fake the second electron.

9.3.7 Conversion probability

Another discrepancy is observed when comparing the fraction of events with track match for the second electron within the W+γ events in data and MC. Figure 9.8a,c shows the number of SMT hits in CFT tracks and the $\Delta\mathcal{R}$ between the electron and the second EM object in $W + \gamma$ candidates (corrected for ISR graphs) with a track matched to the second EM object. Whereas there is a reasonable agreement between MC and data for the fraction of tracks that have many SMT hits (presumably charged pions from jets), the fraction of data with no or very few SMT hits is strongly underestimated in MC. Since the material density is larger in between the SMT and the CFT tracker than in the sensitive region of the SMT itself, photons which convert early enough to provide CFT hits most likely do so at the SMT/CFT border. As a consequence, no (or very few) SMT Hits are measured. The signature of the events underestimated in MC corresponds thus to the signature expected from photon conversions. This is a strong hint, that the number of EM radiation lengths within the tracker is not properly represented in the current GEANT parameterization.

The conversion probability is corrected for by scaling the W-inclusive MC events which contain a conversion candidate with a factor of 2.5. The conversion candidates are selected by requiring a photon at generator level matching with the second reconstructed electron and the track matched to the second electron having less than 5 SMT hits. The correction factor has been adjusted to fit the the number of W+γ candidates with tracks with exactly 0 SMT hits (first bin in Figure 9.8a), which are not part of the signal selection of the

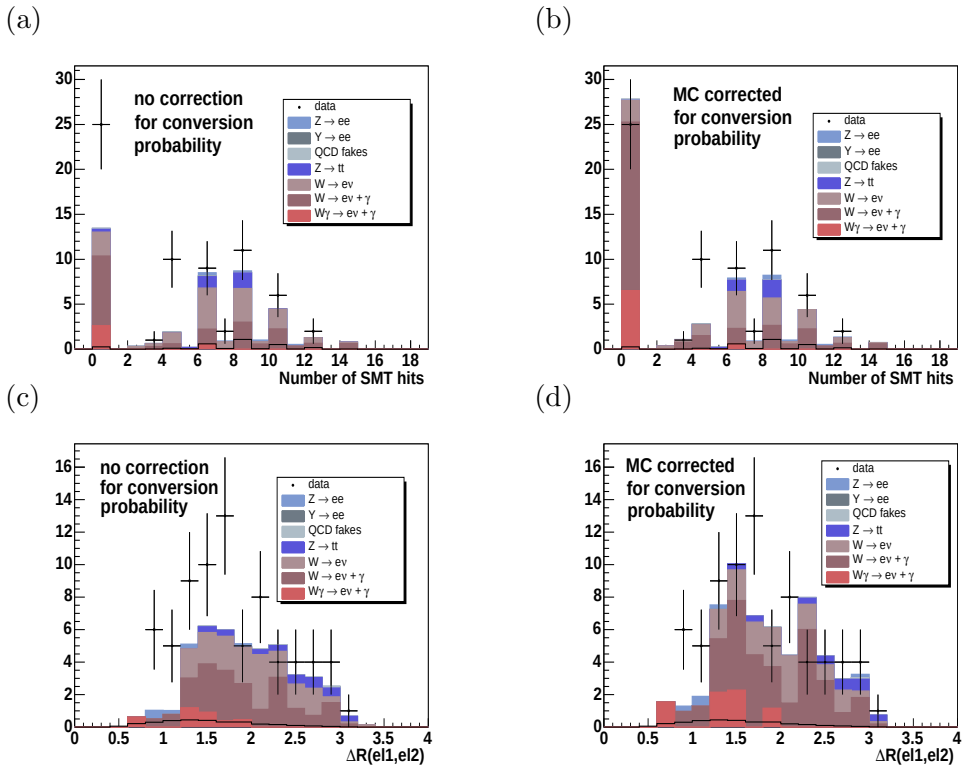

Figure 9.8: Distribution in data and MC (a,b) of the number of SMT hits in events with CFT tracks matching the second electron and (c,d) of the $\Delta\mathcal{R}$ between the first and the second electron in W+γ candidates (a,c) before and (b,d) after the correction of the conversion probability. The contribution from SUSY events expected in this selection ($m_{\chi^{\pm}}$=110 GeV, black, empty histogram) is negligible.

analysis (see Section 10.2.1). Figure 9.8b,d shows the number of SMT hits and the angle between the electron and the second EM object after the conversion corrections are applied.

9.3.8 Jet corrections

Similar to the case of the electrons (see Section 9.3.3), the jet energy resolutions in MC and in data are also different. The jet-p_{T} in MC is smeared with the difference in resolution in data and MC, as derived in [112]. The p_{T} resolutions in data and MC are derived for $p_{\mathrm{T}}(jet) \leq 50\,\mathrm{GeV}$ with events where a jet recoils against a photon radiated from an initial state quark. For $p_{\mathrm{T}}(jet) \geq 50\,\mathrm{GeV}$ they are derived with di-jet events. The fit parameterizes the p_{T} resolution as a combination of noise (N), sampling (S) and constant (C) contribution for different bins in detector η:

$$\frac{\sigma \mathrm{p_T}}{\mathrm{p_T}/\,\mathrm{GeV}} = \sqrt{\mathrm{C}^2 + \left(\frac{\mathrm{S}}{\sqrt{\mathrm{p_T}/\,\mathrm{GeV}}}\right)^2 + \left(\frac{\mathrm{N}}{\mathrm{p_T}/\,\mathrm{GeV}}\right)^2} \tag{9.4}$$

Figure 9.9 shows the transverse momentum of the leading jet for a preselection dominated by Drell-Yan $\mathrm{Z}/\gamma \rightarrow$ ee events (cut 2 in Section 10) after all corrections from Section 9.3

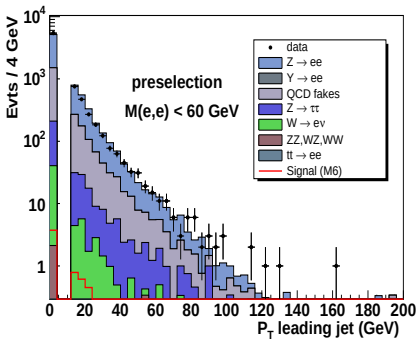

Figure 9.9: Distribution of the leading p_{T}(jet) in data (points with error bars) and MC+QCD (histograms) at the level of the low mass preselection (see Section 10).

applied. MC and data are in reasonable agreement.

9.3.9 $\not\!\!E_{\mathrm{T}}$ correction

Since the missing transverse energy is an important quantity in the signal selection, the correct modeling of this quantity in background events is important for the successful optimization of the analysis.

The smearing of good jets and electrons in the event is propagated into the calculation of the missing transverse energy. Figure 9.10a shows the $\not\!\!E_{\mathrm{T}}$ distribution in Z → ee candidates in data and MC at the preselection level. The $\not\!\!E_{\mathrm{T}}$ distribution is obviously not modeled properly in MC, in particular the large-$\not\!\!E_{\mathrm{T}}$ tail, which would correspond to the signal region in a disjoint selection with low invariant masses. This effect is also attributed to problems in the calorimeter simulation, which affect not only the energy of the clustered objects but also the unclustered energy. To correct for this effect, the x-component and the

(a) (b) (c)

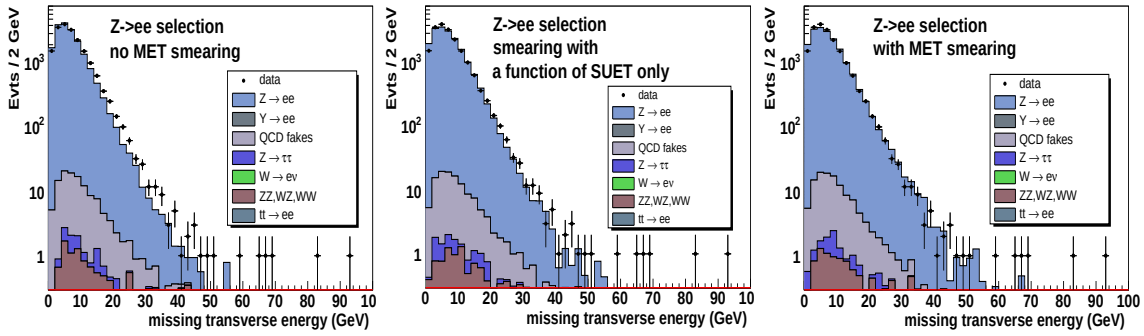

Figure 9.10: Distribution of the $\not\!\!E_{\mathrm{T}}$ in a Z → ee selection (a) without the smearing of the $\not\!\!E_{\mathrm{T}}$, (b) after the SUET-related smearing and (c) after the complete smearing of the $\not\!\!E_{\mathrm{T}}$ in data (points with error bars) and background simulation (filled histograms).

y-component of the missing transverse energy in MC is smeared according to the description in [113] using a Gaussian with $\sigma_1 = 2.55 + 0.00895 * \text{SUET}$, proportional to the scalar sum of the unclustered transverse energy SUET. The $\not\!\!E_T$ and its azimuthal direction are then recalculated from the smeared x and y contributions.The resulting $\not\!\!E_T$ distribution is shown in Figure 9.10b.

The remaining discrepancies in the large-$\not\!\!E_T$ region are attributed to events with problems in the readout electronics (*calorimeter noise*), which are not discarded by the standard data quality procedures described in Section 8.2. This is corrected for by smearing the x component and the y component of the $\not\!\!E_T$ in addition in 2% of the events, with a Gaussian of $\sigma_2 = 15.0\,\text{GeV}$. Figure 9.10c shows the $\not\!\!E_T$ distribution in $Z \to ee$ events after all corrections applied. Since the background after the final signal selection (see Section 11) is dominated by events with true $\not\!\!E_T$, the impact of the $\not\!\!E_T$ corrections derived in this section on the number of background events in the final selection is only at the order of 5%. Nevertheless, the corrections are crucial for the optimization of the selection at earlier stages.

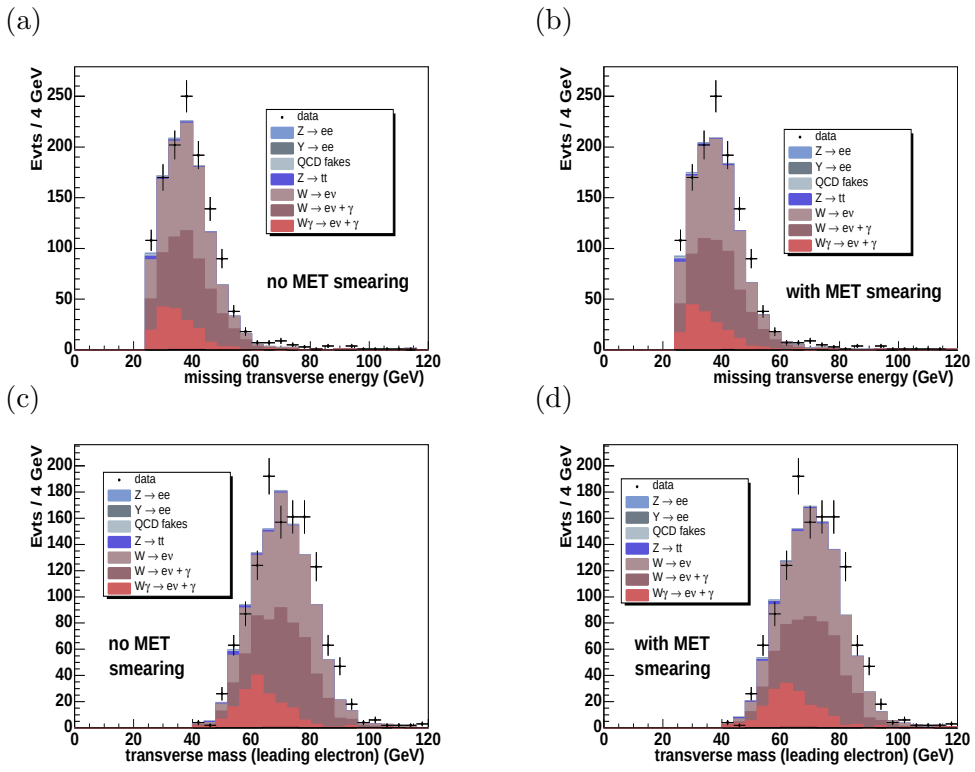

Figure 9.11: Distribution of (a,b) the $\not\!\!E_T$ and (c,d) the transverse mass of the leading electron in W+EM events in in data and MC (a,c) before and (b,d) after the smearing of the $\not\!\!E_T$.

The W+EM selection can be used to check the impact of the $\not\!\!E_T$ smearing on events with true $\not\!\!E_T$. In Figure 9.11, the distribution of the missing transverse energy and of the transverse mass in W events is compared before (a,c) and after (b,d) the $\not\!\!E_T$ smearing. The data-MC agreement is still reasonable after the smearing.

9.3.10 Track smearing

The $1/p_{\mathrm{T}}$ resolution of the tracker is not modeled correctly in the detector simulation. In order to correct for this fact, the simulated track p_{T} is smeared according to:

$$\frac{1}{p_{\mathrm{T}}} \rightarrow \frac{1}{p_{\mathrm{T}}} + (A + B/p_{\mathrm{T}}) * Gaussian(0,1) \tag{9.5}$$

with A=0.0013(0.0023) and and B=0.017(0.028) for tracks with(without) SMT hits respectively. The parameters are derived from comparing the width of $\mathrm{Z} \rightarrow \mu\mu$ and $\mathrm{J}\psi \rightarrow \mu\mu$ events in data and MC [114].

10 The signal selection

The signal selection is optimized for the associated production of the second lightest neutralino and the lightest chargino decaying into final states with two electrons, a third lepton, two LSPs and a neutralino. A set of cuts has been developed in order to separate the signal from the background of Standard Model processes.

10.1 Selection overview

The selection requires two isolated tight electrons with $p_{\mathrm{T}} > 8$ and 12 GeV. A third reconstructed charged lepton is not required in the final state in order to gain efficiency. Instead, the selection requires an additional isolated track with $p_{\mathrm{T}} > 4\,\mathrm{GeV}$. The LSP and the neutrinos typically result in substantial missing transverse energy which is used to further reduce the background.

Since the sensitivity of the analysis with the present data set is limited to a small chargino mass region beyond the LEP limit of 104 GeV, optimization of the analysis has been derived based on a point in SUSY parameter space with $m_{\chi^{\pm}} = 110\,\mathrm{GeV}$, $m_{\chi_2^0} = 114\,\mathrm{GeV}$ and $m_{\tilde{\mathrm{e}}_{\mathrm{R}}} \approx m_{\chi_2^0}$ (point M6 in Table 9.2). The selection efficiency has been checked for a large chargino and slepton mass range. Figure 10.1 shows the most important kinematic variables of the selection for the point M6 which was used for the optimization, for a SUSY point with low slepton masses with 2-body decays of the neutralino into a slepton (DM3) and for a point with a large chargino mass (M12).

Table 10.1 summarizes briefly the selection procedure. The selection is optimized for a maximal sensitivity of the analysis (see Section 2.2.3). The individual cuts will be justified and described in more detail in the following sections.

The number of events selected in data and expected from Standard Model processes (backgrounds) are presented in Table 10.2. The number of events expected from a SUSY model point with a chargino mass of 110 GeV (M6) and the corresponding selection efficiency is shown as a reference.

Due to the limited MC statistics, the statistical error for the number of $\mathrm{Z}/\gamma \rightarrow \mathrm{ee}$ and $\mathrm{W} \rightarrow \mathrm{e}\nu$ events expected for the last selection stages is very large. In order to reduce this error, the rejection of the last three cuts (9–11) for $\mathrm{Z}/\gamma \rightarrow \mathrm{ee}$ and $\mathrm{W} \rightarrow \mathrm{e}\nu$ events is calculated based on samples where some of the prior cut are loosened such that they have a larger statistics. This rejection is then applied on the number of events expected after applying cut 8. The loose $\mathrm{Z}/\gamma \rightarrow \mathrm{ee}$ sample is created by extending the invariant mass range towards the Z resonance and by loosening the requirements on the quality and the isolation of the third track. The $\mathrm{W} \rightarrow \mathrm{e}\nu$ sample is increased by loosening the electron identification (likelihood and number of SMT hits), the track isolation and the

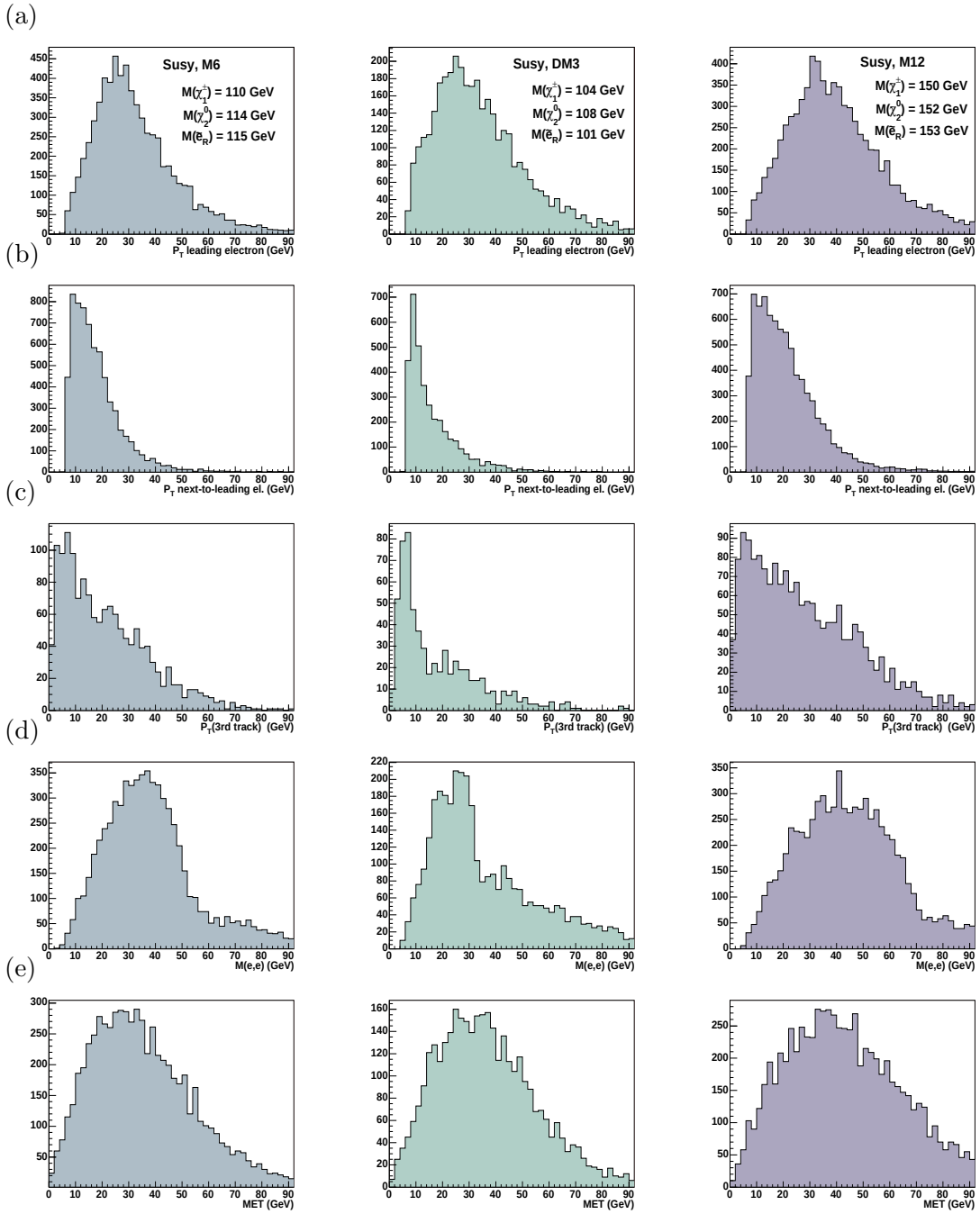

Figure 10.1: Distribution of the transverse momentum (a) of the leading electron, (b) of the next-to-leading electron and (c) of the the third track and of (d) the invariant electron mass and (e) the missing transverse energy for the SUSY reference points M6 which was used for the optimization (first column), DM3 with 2-body decays of the neutralino into a slepton (second column) and M12 with a larger chargino mass (third column).

(1) Di-EM preselection	$p_T > 8, 12$ GeV
	spatial track match $\chi^2 > 10^{-18}$
	Hmatrix $\chi^2 < 35$ for at least 1 electron
	electron likelihood > 0.2
	electrons from primary vertex
	no ECEC
	2nd electron with | z0 |$<$ 35cm: at least 1 SMT hit
	2nd electron with | z0 |$>$ 35cm: likelihood > 0.8
(2) Anti Z $\rightarrow$ ee: M(e,e)	$18\,\text{GeV} < \text{M(e,e)} < 60\,\text{GeV}$
(3) Anti Z/$\gamma \rightarrow$ ee: $\Delta\phi$(electrons)	$\Delta\phi(\text{electrons}) < 2.9$
(4) Anti-top: H_T: $\Sigma p_T(jet)$	scalar sum of p_T of jets: $H_T < 80$ GeV
(5) 3rd quality track with track isolation	p_T (track) > 4.0 GeV, $\Sigma p_T(\text{isolation cone}) < 1\,\text{GeV}$
(6) Track calorimeter isolation	$E_{iso} < 3.0$, $E_{iso} < 0.6 * \sqrt{p_T(\text{track})}$
(7) Track: Anti-W cut	electron likelihood > 0.8 for p_T(track) < 15.0 GeV
(8) Missing transverse energy	$\not\!\!E_T > 22$ GeV
(9) $\not\!\!E_T$ from jets	$\not\!\!E_T > 6.0 \times \sigma(\text{jet}(\|\not\!\!E_T))$
(10) $\not\!\!E_T$ from electrons	transverse mass (e, $\not\!\!E_T$) > 20 GeV for both electrons
(11) $\not\!\!E_T$ and track p_T	$\not\!\!E_T \times p_T(\text{track}) > 220$ GeV^2

Table 10.1: Overview over the cuts of the selection. The cuts are discussed in detail in the following sections.

track quality cuts. The cuts that are loosened are chosen such that the correlation with the variables used for the last selection steps is small. The samples are checked for possible correlations by comparing the rejection of the last three selection cuts at an early stage of the selection, where both the tight sample and the loose sample have a large statistics. The error on the normalization of the loose sample and correlations to the loosened cuts are taken into account in the calculation of the systematic error.

10.2 Cut flow and data-MC comparison

10.2.1 Di-electron selection

The preselection requires two tight electrons (likelihood > 0.2, see Section 7.2) with $p_T(\text{max}) > 12$ GeV and $p_T(\text{min}) > 8$ GeV, stemming from the same vertex (distance of the vertex z positions $\Delta z_0 < 1$ cm). This vertex is required to be identical to the primary vertex ($\Delta z_0 < 2$ cm). The misvertexing probability is underestimated in MC which leads to a correction of 0.983 ± 0.005 on the MC event efficiency, estimated from comparing data and MC using a tight Z $\rightarrow$ ee selection (see Section 9.3.3).

In order to avoid phase space regions with unfavorable signal-to-background ratio, both electrons must be detected in $|\eta_{\text{det}}| < 3.0$ and at least one of the electrons is required to be in CC ($|\eta_{\text{det}}| < 1.0$).

Cut	Data	Sum BG	SUSY M6	
			expected events	ϵ(3 lep) [%]
1 Presel	33468	31646±67±3291	8.70±0.14±0.93	10.43±0.17
2 low mass	7569	7240±22±753	6.69±0.12±0.72	8.02±0.14
3 low $\Delta\phi$	3921	3975±18±413	6.14±0.12±0.66	7.36±0.14
4 p_{T} jet	3850	3932±18±409	5.98±0.11±0.64	7.17±0.13
5 3rd track	257	265.4±4.7±27.6	3.63±0.09±0.39	4.35±0.11
6 trk cal iso	115	129.3±3.3±13.8	3.31±0.08±0.35	3.97±0.10
7 anti-W	92	94.7±2.9±10.1	3.15±0.08±0.34	3.77±0.10
8 $\not\!\!E_{\mathrm{T}}$	5	2.27±0.52±0.59	2.44±0.07±0.26	2.92±0.09
9 scaled $\not\!\!E_{\mathrm{T}}$	1	0.75±0.06±0.25	2.28±0.07±0.24	2.73±0.08
10 $\mathrm{M_T}$	1	0.58±0.05±0.19	2.11±0.07±0.23	2.53±0.08
11 p_{T}(tr)×$\not\!\!E_{\mathrm{T}}$	0	0.20±0.03±0.07	1.93±0.06±0.21	2.31±0.08
	Z/$\gamma\rightarrow$ee	W$\rightarrow$eν	QCD jets	Z$\rightarrow\tau\tau$
1 Presel	28448±66	88.31±4.91	2561±8	290.2±5.8
2 low mass	4954±20	55.85±3.93	1959±7	257.1±6.0
3 low $\Delta\phi$	2783±17	52.19±3.84	1044±5	82.6±4.0
4 p_{T} jet	2765±17	52.19±3.84	1026±5	77.4±3.9
5 3rd track	172.2±4.3	1.87±0.62	85.6±1.5	4.24±0.90
6 trk cal iso	82.9±3.0	0.94±0.42	42.7±1.1	1.64±0.58
7 anti-W	75.6±2.8	0.31±0.22	16.23±0.42	1.48±0.58
8 $\not\!\!E_{\mathrm{T}}$	0.96±0.32	0.21±0.21	0.408±0.050	0.48±0.34
9 Sig $\not\!\!E_{\mathrm{T}}$	0.30±0.03	0.21±0.03	0.042±0.015	0.00±0.03
10 $\mathrm{M_T}$	0.19±0.03	0.20±0.03	0.014±0.006	0.00±0.001
11 p_{T}(tr)×$\not\!\!E_{\mathrm{T}}$	0.008±0.005	0.035±0.014	0.008±0.005	0.00±0.001
	WW	ZZ	WZ	$\mathrm{t\bar{t}}\rightarrow$ ee
1 Presel	18.82±0.17	10.56±0.093	13.72±0.12	8.776±0.132
2 low mass	7.686±0.111	1.174±0.017	0.703±0.010	2.729±0.073
3 low $\Delta\phi$	7.119±0.107	1.112±0.017	0.645±0.010	2.658±0.072
4 p_{T} jet	7.113±0.107	0.725±0.011	0.523±0.008	0.546±0.032
5 3rd track	0.096±0.010	0.219±0.024	0.224±0.024	0.052±0.010
6 trk cal iso	0.046±0.007	0.044±0.044	0.208±0.029	0.022±0.007
7 anti-W	0.039±0.006	0.044±0.044	0.205±0.030	0.021±0.006
8 $\not\!\!E_{\mathrm{T}}$	0.034±0.006	0.000±0.044	0.157±0.026	0.021±0.006
9 Sig $\not\!\!E_{\mathrm{T}}$	0.033±0.006	0.000±0.022	0.129±0.022	0.021±0.006
10 $\mathrm{M_T}$	0.031±0.006	0.000±0.022	0.118±0.021	0.021±0.006
11 p_{T}(tr)×$\not\!\!E_{\mathrm{T}}$	0.021±0.004	0.000±0.018	0.118±0.022	0.021±0.006

Table 10.2: Number of candidate events observed and background events expected at different stages of the selection. The errors for the numbers of the individual backgrounds are statistical. For the sum of all backgrounds statistical and systematic errors are given. The number of expected events and the selection efficiency (based on all leptonic final states) for SUSY point M6 ($m_{\chi^{\pm}}$=110 GeV) are added to the table.

SMT hit requirement

The process $W \rightarrow e\nu + \gamma$, with the photon either being radiated from the W or stemming from a π^0 or ρ^0 decay and converting into an e^+e^- pair is an important background of this analysis. The genuine electron is mostly reconstructed as the leading electron whereas the conversion electron is reconstructed as the next-to-leading electron. Since the second electron is required to match with a track, the conversion must take place in the tracker. This background is reduced by requiring the next-to-leading electron to have at least one hit in the inner layers of the SMT (see Section 3.2.1). The cut is not applied for events with the primary vertex outside the SMT ($|z_0| > 35$ cm). Figure 10.2 shows the number of hits in the inner part of the SMT for the next–to–leading electron expected from SUSY events and from $W \rightarrow e\nu$ events which pass the preselection. The efficiency for electrons is slightly overestimated in MC. A correction factor of 0.971 ± 0.002 is derived from comparing data and MC using a tight $Z \rightarrow ee$ selection.

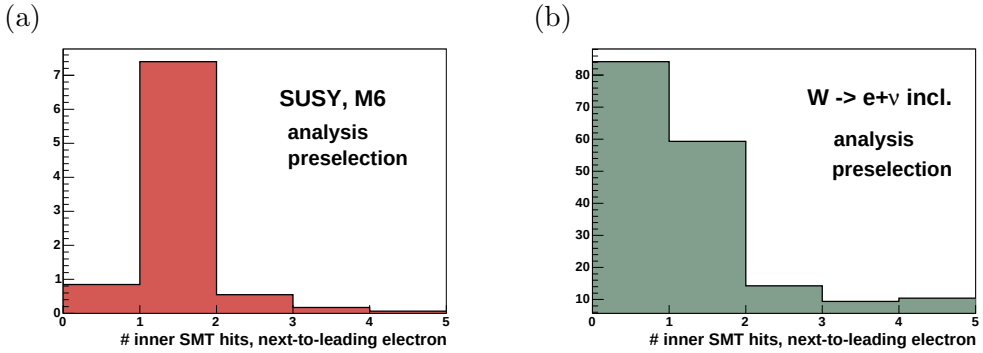

Figure 10.2: Number of SMT hits of the next-to-leading electron track at the preselection level for (a) SUSY MC (point D4) and (b) $W \rightarrow e\nu$ MC.

The electron likelihood provides also an efficient tool to reduce not only events with jets that are reconstructed as electrons but also events with photon conversions due to the large e/p, a large track DCA and the track isolation. The likelihood requirement for the next-to-leading electron is therefore tightened to likelihood > 0.8 instead of requiring SMT hits for events with the primary vertex outside the SMT acceptance.

Di-EM mass

Figure 10.3 shows the distribution in data, background and signal (point M6) of the Di-EM mass M(e,e) at this stage. The invariant mass distribution of the background, dominated by $Z/\gamma \rightarrow ee$ events at this selection stage is well described by the MC simulation, except for the low-mass shoulder of the Z-resonance, where the MC underestimates the number of events found in data. This discrepancy is mainly attributed to an incorrect description of the DØ detector in GEANT [110] and is expected to be reduced in future versions of MC production. In order to reject the $Z \rightarrow ee$ events, the Di-EM mass is required to be in the range $18\,\text{GeV} < M(e,e) < 60\,\text{GeV}$. Data and background are in reasonable agreement within this range. The cut on the Di-EM mass reduces the background by a factor of 4.4 while losing 23% of the SUSY signal.

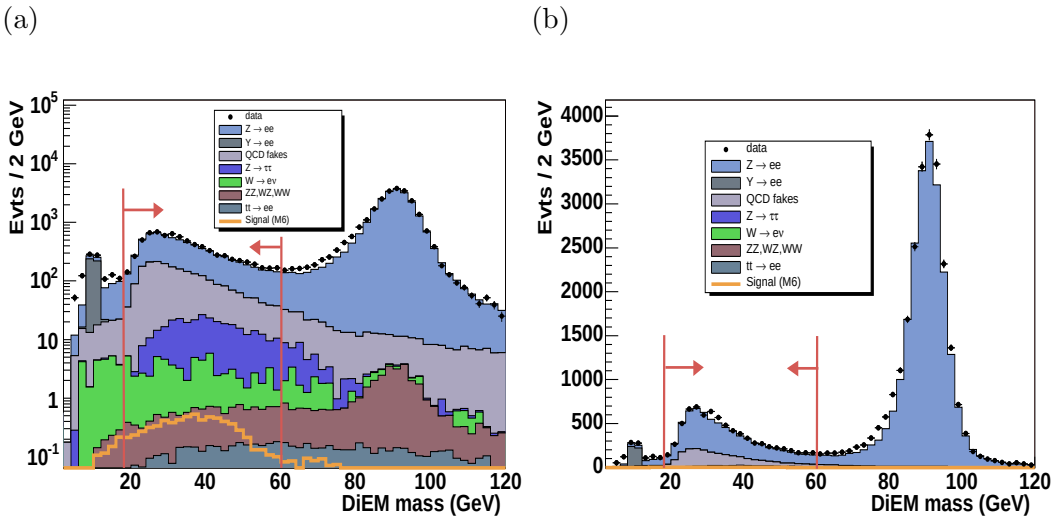

Figure 10.3: Distribution of the invariant Di-EM mass M(e,e) at preselection level (cut1) in data (points with error bars), SM background (filled histograms) and expected signal (SUSY point M6, empty histogram) with (a) logarithmic scale and (b) linear scale. The selected M(e,e) range is marked with bars.

The resulting sample is referred to as *low-mass preselection* in what follows and the distribution of all quantities relevant for the analysis will be presented also for this stage. At the low-mass preselection stage, the sample consists mainly of $Z/\gamma \rightarrow ee$ and misidentified jets from QCD production (QCD background). Of further importance are also $Z \rightarrow \tau\tau$ events.

Azimuthal angle between the electrons

Electrons from $Z/\gamma \rightarrow ee$, $Z/\gamma \rightarrow \tau\tau$ and QCD events are mainly back-to-back in the transverse plane, whereas the electrons from chargino and neutralino decays have no preferred angle $\Delta\phi_{e,e}$. The distribution of this quantity in data, background and signal (point M6) is shown in Fig. 10.4 at the preselection level. Data and background expectation are in good agreement after the $p_T(Z)$ reweighting (see Section 9.3.5) of the PYTHIA MC. The azimuthal angle between the electrons is required to be less than 2.9, which reduces the background by a factor of 1.8 with a signal efficiency of 92%.

10.2.2 Sum of the jet transverse momenta H_T

Due to the true missing transverse energy, $t\bar{t}$ events become an important background source in later stages of the selection. In contrast to the signal they are characterized by the presence of at least two hard jets, stemming from the t-decay (see Fig. 5.11). As a consequence, the $t\bar{t}$ contribution can be reduced by a cut on on H_T, the scalar sum of the p_T of the good jets in the event. The distribution of the quantity is shown in Fig. 10.5 at the low-mass preselection level and before the cut is applied. Requiring $H_T < 80\,\text{GeV}$

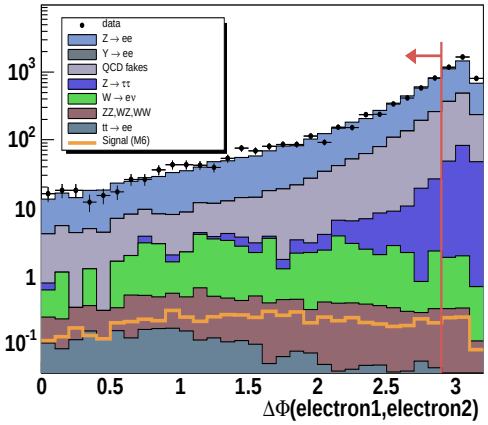

Figure 10.4: Distribution of the azimuthal angle between the two electrons in data (points with error bars), SM background (filled histograms) and expected signal (SUSY point M6, empty histogram) at the low-mass preselection level. A vertical bar marks the cut position.

rejects 80% of the $t\bar{t}$ background with a signal efficiency of 97%. Data and background expectation are in reasonable agreement in the selected H_T range.

10.2.3 Selection of a third track

The remaining background consists mainly of processes with at most two leptons in the final state. It is dominated by $Z/\gamma \rightarrow ee$ and QCD background at this stage of the selection. $W \rightarrow e\nu$ events, characterized by genuine $\not\!\!E_T$, become important once the other events are reduced by the $\not\!\!E_T$ related cuts. The W events and to a minor extent also the $Z \rightarrow ee$ and the QCD events can be significantly reduced by exploiting the fact, that there is a third charged lepton expected in the SUSY final state, which produces a track in the central tracker. The analysis requires an isolated, high-quality track, well-separated from the two electron candidates ($\Delta\mathcal{R} > 0.4$), which stems from the same vertex as the electrons ($\Delta z_0 < 1$cm). A large track p_T is found to be faked mostly by poorly measured low-p_T tracks. To ensure a good p_T measurement, the χ^2 per degree of freedom of the track fit (see Section 7.1) is required to be lower than four and the track is required to have at least 17 hits or 14 CFT hits. Tracks without CFT hits are rejected.

An alternate approach [25] consists in requiring a third identified lepton (electron, muon or τ) in the event. With the lepton identification efficiency decreasing for low values of p_T, this method has a lower signal-to-background ratio as compared to the third-track requirement. In the search for signals with more than three charged leptons in the final state [17], the efficiency for the identification of three leptons is large enough to result in a large sensitivity.

The MC efficiency corrections derived for the tracking and the photon conversion probability in Section 9.3.4 and 9.3.7 are also applied on the third track.

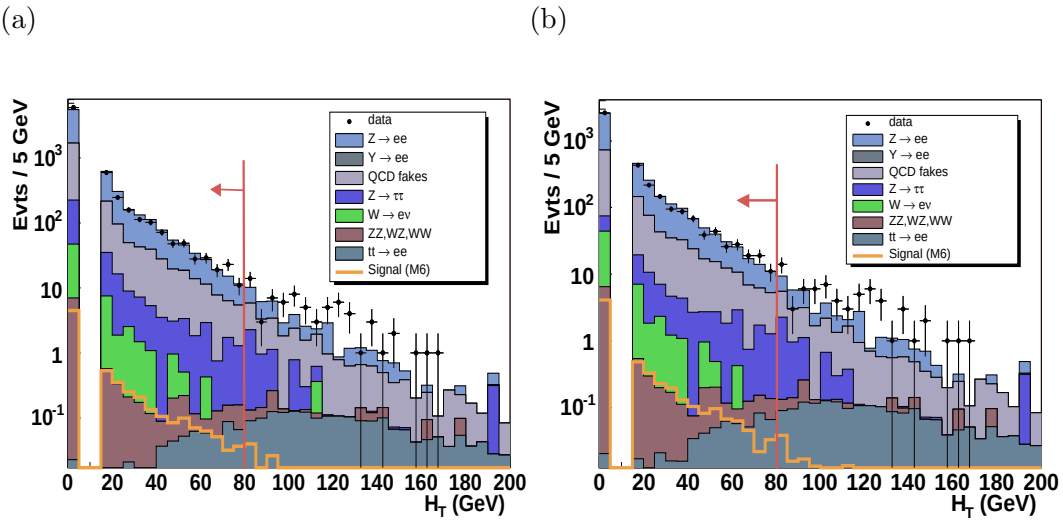

Figure 10.5: Distribution of the H_T in data (points with error bars), SM background (filled histograms) and expected signal (SUSY point M6, empty histogram) (a) at the low-mass preselection level and (b) before the cut on H_T is applied. A vertical bar marks the cut position.

Isolation in the tracker

For most of the background events in the preselection, the third track does not stem from a third lepton but from one of the charged hadrons within a jet and is therefore not isolated.

This background is reduced by requiring the third track to be isolated in the tracker. The scalar sum of all tracks in a hollow cone of $0.1 < \Delta\mathcal{R} < 0.4$ around the third track, which originate from the same vertex and have $p_T > 0.3$ GeV, is required not to exceed 1 GeV. The isolation criterion is designed to be efficient for tracks from electrons, muons and taus. All tau decay modes (leptonic, hadronic (1 prong), hadronic (3 prong)) either produce only one track or a set of tracks in a very narrow region in η and ϕ [115]. Figure 10.6 shows the scalar sum of the p_T of all tracks in the isolation cone around reconstructed tracks of $p_T > 3$ GeV that match to an electron, a muon or a tau-lepton from SUSY events (point M6) and of the third reconstructed track in Drell-Yan MC. The tracks from Drell-Yan events are characterized by a larger energy in the isolation cone. Within the SUSY sample, the tau-tracks are the least isolated, which is mainly due to the fraction of 3 prong decays.

In the following, the *third track* is defined as the leading additional track, which fulfills all above mentioned quality and isolation requirements.

Figure 10.7 a,b shows the distribution in data and background of the transverse momentum of the third isolated track at the low-mass preselection level and before the cut on the p_T(track) is applied. The analysis requires a track with $p_T > 4$ GeV, which corresponds to an average rejection factor of 15 for the backgrounds (the W background is reduced by a factor of 30). This large rejection is achieved at the expense of 40% of the signal efficiency, the largest fraction of which are e+e+τ events with the τ decaying into low-p_T hadrons, which do not pass the p_T threshold of the selection.

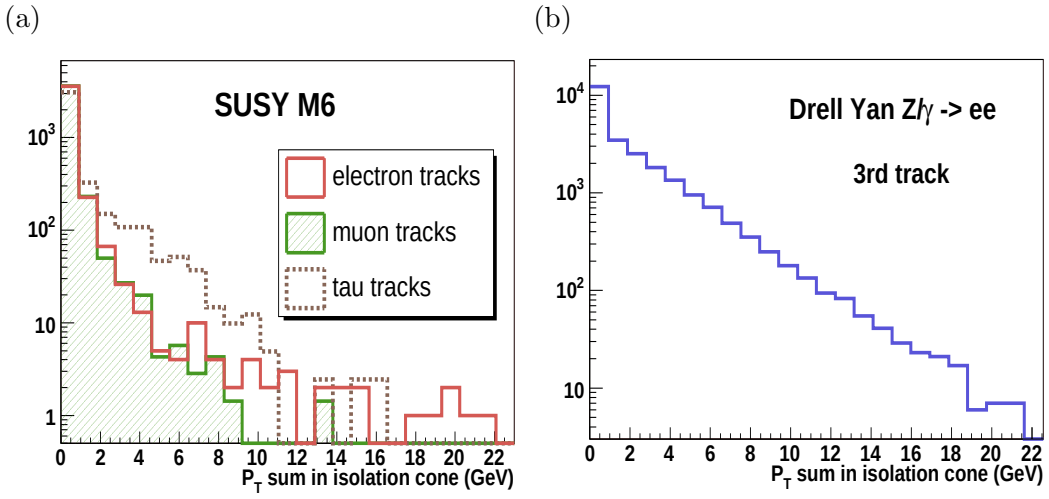

Figure 10.6: Distribution of the p_{T} sum of tracks in the track-isolation cone around tracks with $p_{\mathrm{T}} > 3$ GeV (a) for electron tracks (continuous line), muon tracks (hatched histogram) and τ-tracks (dashed line) in SUSY MC (point M6) and (b) for the third track in Drell-Yan $\mathrm{Z}/\gamma \rightarrow$ ee MC.

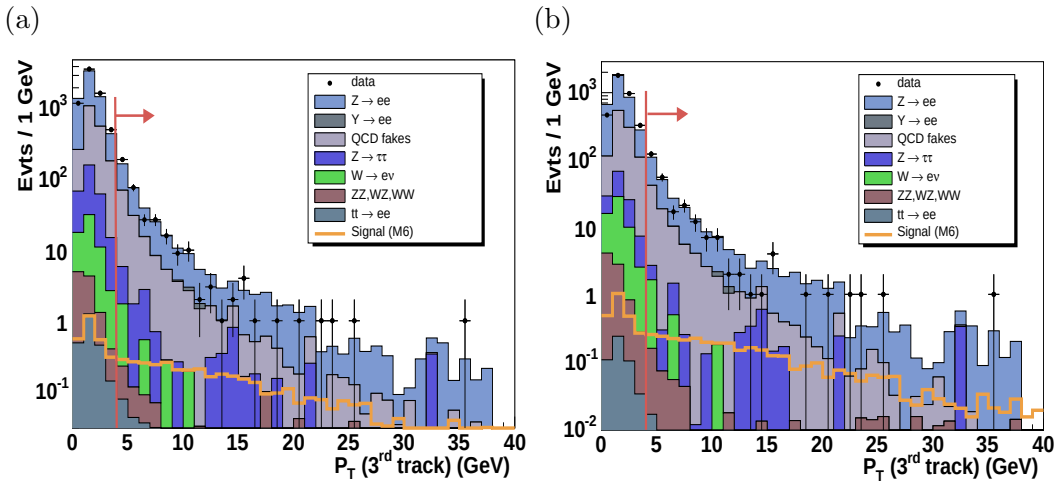

Figure 10.7: Distribution of the transverse momentum of the selected third track in data (points with error bars), SM background (filled histograms) and expected signal (SUSY point M6, empty histogram) (a) at the low-mass preselection level and (b) before the cut on p_{T}(track) is applied. A bar marks the cut position.

Isolation in the calorimeter

A further reduction of the number of events, where the third track stems from a jet is achieved by requiring the third track to be, in addition, isolated in the calorimeter. The electrons, muons and tau-leptons which produce the track in the signal final state, deposit energy in the calorimeter only in a small cone around the track, whereas the jets are characterized by calorimeter energy deposition in a large cone.

The calorimeter isolation uses the scalar sum of the transverse energy deposition in the cells of the electromagnetic (EM) and the fine-hadronic (FH) layers of the calorimeter in a hollow isolation cone of $0.2 < \Delta R < 0.4$ around the extrapolation of the third track into the calorimeter (Cal E_{T} sum). Figure 10.8 shows the E_{T} sum in the calorimeter isolation cone as a function of the track p_{T} for W and Drell-Yan events and for SUSY events with lepton tracks. The background events are characterized by large values of the E_{T} sum in the calorimeter isolation cone, mostly combined with low values of the track p_{T}. The lepton tracks in the signal are distributed over a large p_{T} range and have low values of the E_{T} sum in the calorimeter isolation cone, slightly increasing with the transverse momentum of the track. Figure 10.9 shows the rejection for various backgrounds versus the efficiency for lepton-tracks from SUSY events for varying the cuts on the the maximum Cal $\mathrm{E_T}$ sum and the maximum ratio of the Cal E_T sum and $\sqrt{p_{\mathrm{T}}(\mathrm{track})}$. Events with

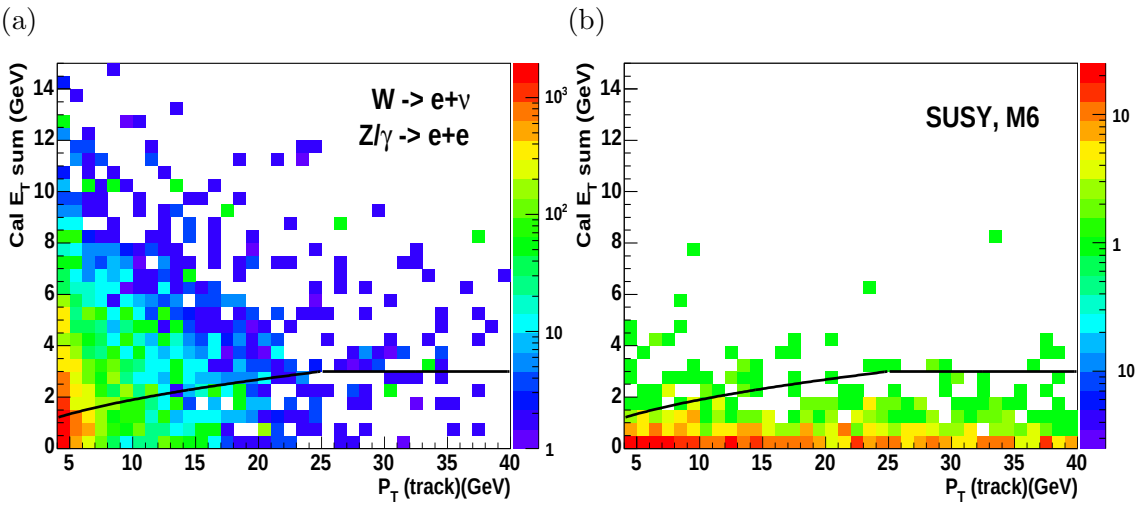

Figure 10.8: E_{T} sum in the calorimeter isolation cone as a function of p_{T}(track) for (a) W and Drell Yan events and (b) SUSY events with lepton tracks (point M6, $m_{\chi_1^{\pm}} = 110$ GeV). The selected domain is marked with a line.

Cal $\mathrm{E_T}$ sum $< 60\%\sqrt{p_{\mathrm{T}}(\mathrm{track})}$ and Cal $\mathrm{E_T}$ sum $< 3\,\mathrm{GeV}$ are selected. The selected domain is marked with a line in Figure 10.8.

Figure 10.10 shows the distribution in data and background expectation of the E_{T} in the calorimeter isolation cone of the third track for $p_{\mathrm{T}}(\mathrm{track}) > 4\,\mathrm{GeV}$ at the low-mass preselection level and before the cut on the calorimeter isolation is applied. The calorimeter isolation rejects an additional 50% of the background, with an efficiency loss of 10% in the remaining SUSY events.

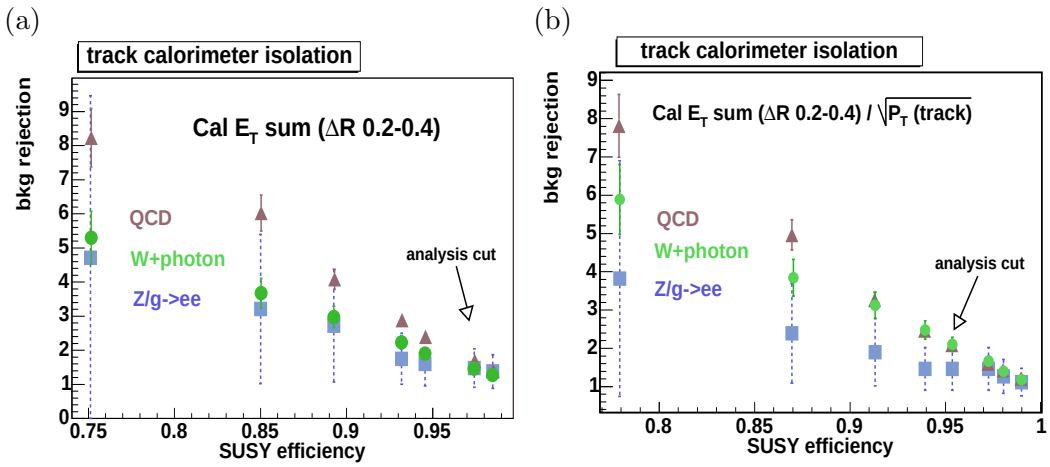

Figure 10.9: Rejection for QCD, W+γ and Drell-Yan events versus the efficiency for SUSY events with $m_{\chi_1^\pm} = 110$ GeV where the third track is matched to a charged lepton for different requirements on (a) the maximum Cal E_T sum and (b) the maximum ratio of the Cal E_T sum and $\sqrt{p_T(\text{track})}$.

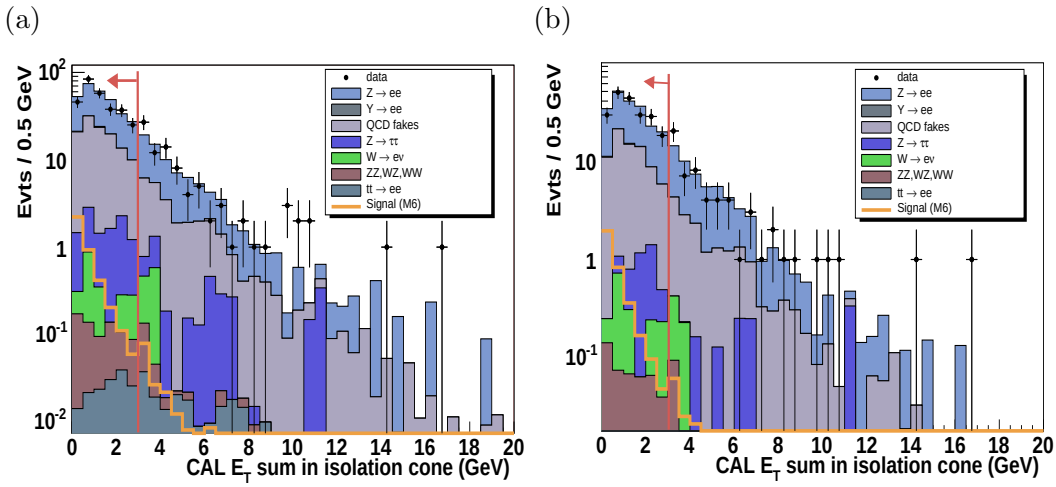

Figure 10.10: Distribution of the E_T sum in the calorimeter isolation cone of the third track with $p_T(\text{track}) > 4$ GeV in data (points with error bars), SM background (filled histograms) and expected signal (SUSY point M6, empty histogram) (a) at the low-mass preselection level and (b) before the cut on the calorimeter isolation is applied. The position of the p_T- independent cut is marked with a bar.

Additional Anti-W cut

$W \to e\nu$ and QCD background are expected to have both a low transverse momentum of the third track and a worse electron ID for the second EM-object. In order to reduce the remaining W contribution, the likelihood requirement for the second electron is tightened to 0.8 for events with $p_T(\text{track}) < 15$ GeV. This reduces the background by 25% (the QCD and the W fraction are reduced by a factor of 3) with a signal efficiency of 95%.

All track-related cuts together reduce the background by a factor of 40 at the expense of 50% of the signal. After applying the track requirements, the W fraction is at the order of the WZ fraction. The remaining background is dominated at this stage by $Z \to ee$ and QCD events. In what follows this selection stage is referred to as e+e+*track* stage.

10.2.4 Selection of events with large significant $\not\!\!E_T$

$Z/\gamma \to ee$ and QCD events, the dominant fractions after the e+e+track selection are characterized in general by small values of $\not\!\!E_T$, whereas the two LSPs and the neutrinos in the signal final state lead to considerable amounts of true $\not\!\!E_T$. Figure 10.11 shows the distribution in data and background of the $\not\!\!E_T$ at the low-mass preselection level and before the cut on this quantity is applied. Since this analysis does not reconstruct an additional muon in the event, the missing transverse energy is not corrected for the energy of muons. Data and MC are in reasonable agreement. All events with $\not\!\!E_T < 22$ GeV are discarded.

The $\not\!\!E_T$ requirement reduces the background expectation by a factor of 40, with a loss of 23% in the signal. The $Z \to ee$ and QCD background fractions are reduced to the order of the $W \to e\nu$ and the $Z \to \tau\tau$ background fractions.

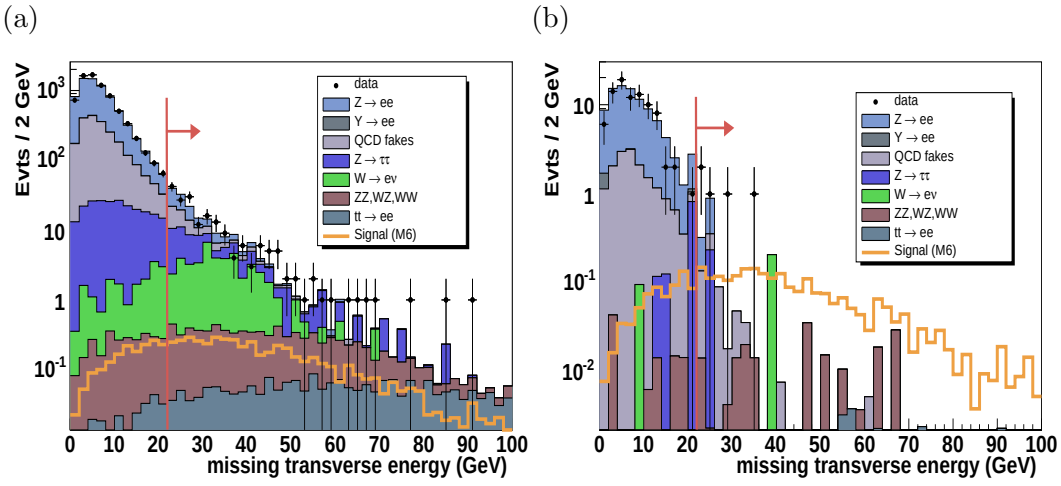

Figure 10.11: Distribution of the $\not\!\!E_T$ in data (points with error bars), SM background (filled histograms) and expected signal (SUSY point M6, empty histogram) (a) at the low-mass preselection level and (b) before the cut on the $\not\!\!E_T$ is applied. The cut position is marked by a vertical bar.

$\not\!\!E_T$ significance

Large values of the missing transverse energy in $Z/\gamma \rightarrow ee$ and QCD events are mostly due to fluctuations of the reconstructed jet energies. These events are characterized by small values of the missing transverse energy significance $Sig(\not\!\!E_T)$ (see Section 7.4). Figure 10.12 shows the distribution of this quantity in data and background expectation for the low-mass preselection sample, the e+e+track stage and before the cut on $Sig(\not\!\!E_T)$ is applied. The $\not\!\!E_T$ significance is required to be in excess of 6.0. This cut reduces the background by a factor of 3 with a signal efficiency of 93%. One event is selected at this stage in agreement with the background prediction of 0.75 events.

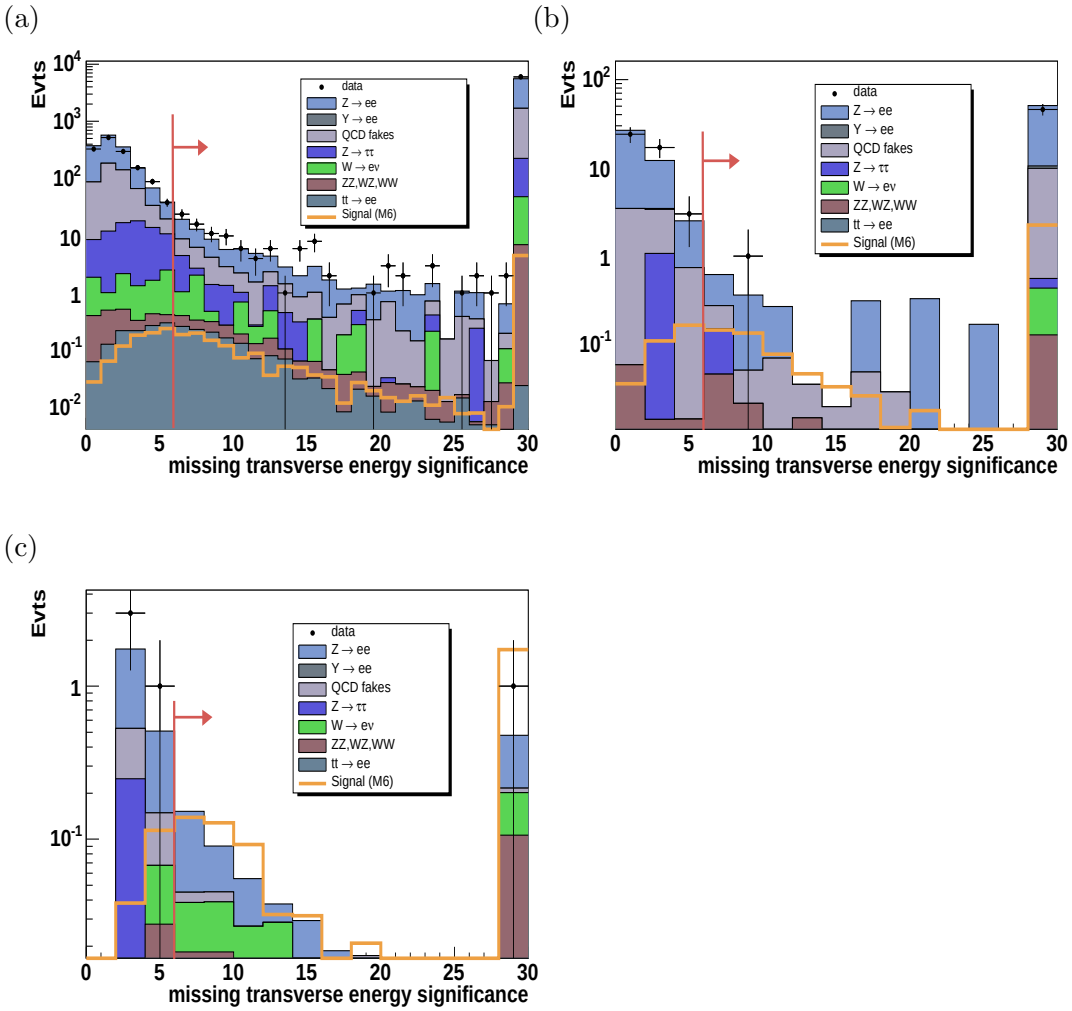

Figure 10.12: Distribution of the $\not\!\!E_T$ significance in data (points with error bars), SM background (filled histograms) and expected signal (SUSY point M6, empty histogram) (a) at the low-mass preselection level, (b) at the e+e+track level and (c) before the cut on $Sig\not\!\!E_T$ is applied (c). The events without jets are presented in the last bin of the histogram. Plot (c) is derived with the loose $Z \rightarrow ee$ and the loose $W \rightarrow e\nu$ sample (see Section 10.1).

Transverse mass

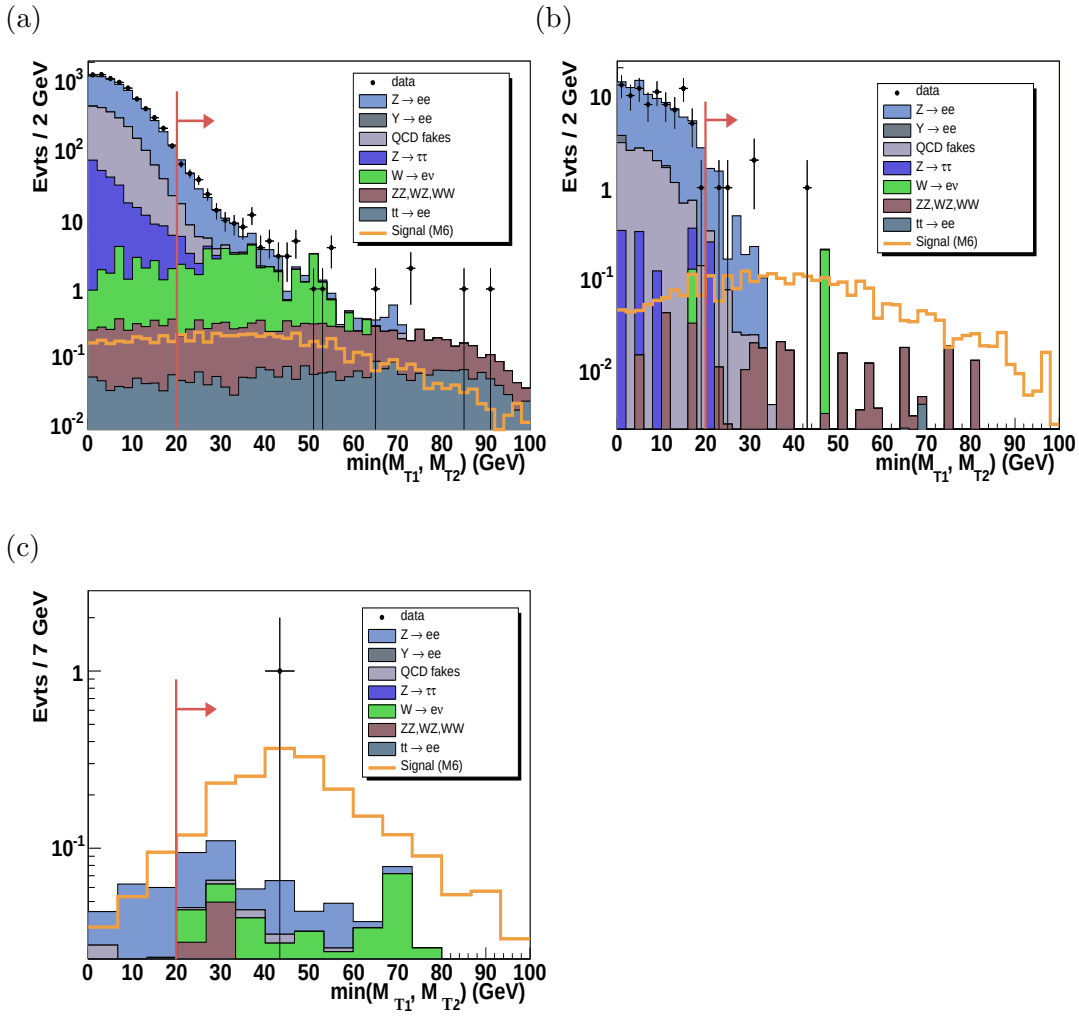

Figure 10.13: Distribution of the minimum of the electron transverse masses in data (points with error bars), SM background (filled histograms) and expected signal (SUSY point M6, empty histogram) (a) at the low-mass preselection level, (b) at the e+e+track level and (c) before the cut on the transverse mass is applied. The latter plot is derived with the loose $Z \to ee$ and the loose $W \to e\nu$ sample.

Large reconstructed $\not\!\!E_T$ in background events without true $\not\!\!E_T$ is often due to a poorly measured electron energy. As a consequence, the azimuthal angle between the $\not\!\!E_T$ and one of the electrons is small. This leads to small values of the *transverse mass* M_T of the electron with the missing transverse energy, $M_T = \sqrt{2 \cdot \not\!\!E_T \cdot p_T(e) \cdot (1 - cos(\Delta\phi(\not\!\!E_T, e))}$, whereas the signal is characterized by larger transverse masses.

Figure 10.13 shows the distribution of the minimum transverse mass of both electrons in data and background at the low-mass preselection level, at the e+e+track stage and before the cut on the transverse mass is applied. Events with a $M_T < 20\,GeV$ for one of the electrons are discarded. This cut reduces the $Z/\gamma \to ee$ background by 40% with a signal efficiency of 93%.

10.2.5 Combined cut on $\not\!\!E_T$ and p_T(track)

The remaining background is dominated by WZ, Z → ee and W → eν events. Whereas the final states of the WZ events are comparable to the final states of chargino and neutralino production, Z → ee and W → eν events are characterized by mismeasured $\not\!\!E_T$ and/or a third track from a jet or from a photon conversion and are therefore expected to differ in the $\not\!\!E_T$ and the p_T(track) distribution from the SUSY signal.

Figure 10.14 shows the distribution of $\not\!\!E_T$ as a function of p_T(track) for a background consisting of equal fractions of Z/γ → ee and W → eν events and for the SUSY signal (point M6). Z/γ → ee events are characterized by low values of $\not\!\!E_T$ and W → eν events have large $\not\!\!E_T$ but low values of p_T(track) whereas the SUSY events show a flat distribution over a large part of the $\not\!\!E_T$-p_T(track) plane. The combined background follows roughly a hyperbolic shape, which suggests a cut on the product of $\not\!\!E_T$ and p_T(track), in order to separate the signal from the background. Lines of constant product of $\not\!\!E_T$ and p_T(track) are added.

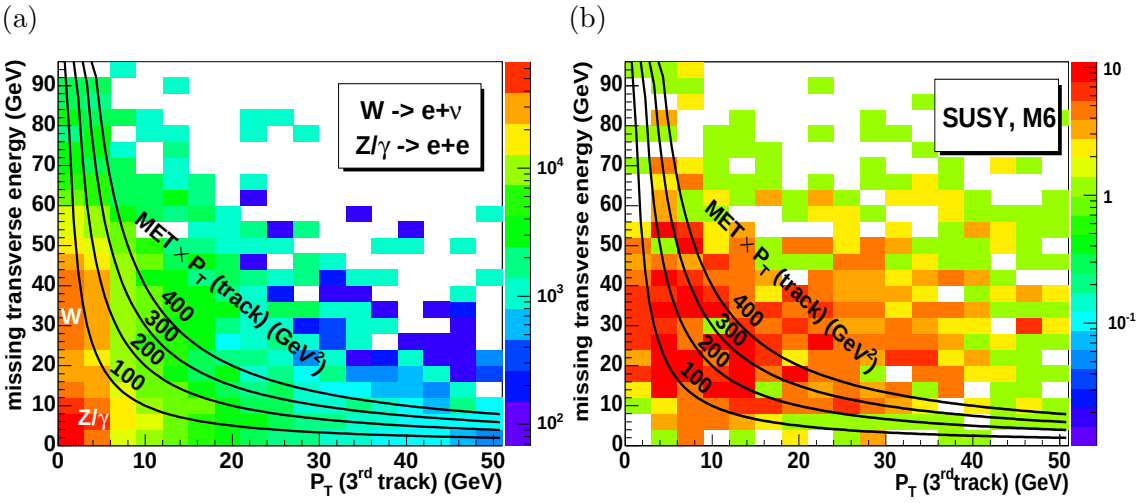

Figure 10.14: Distribution of $\not\!\!E_T$ as a function of p_T(track) at the low-mass preselection level (a) in background and (b) signal (point M6, b). Additional lines correspond to points of constant $\not\!\!E_T \times p_T$(track).

Figure 10.15 shows the distribution of $\not\!\!E_T \times p_T$(track) in data and background expectation at the low-mass preselection level, at the e+e+track stage and before the cut on this quantity is applied.

Optimization of the cut on $\not\!\!E_T \times p_T$(track)

Since the last cut of the selection exploits the two most important characteristics of the signal final state, the presence of a third lepton and substantial missing transverse energy, particular effort has been put into the optimization of this requirement. The position of the cut is chosen such that is gives the best expected 95% CL limit on the signal cross section in the absence of SUSY.

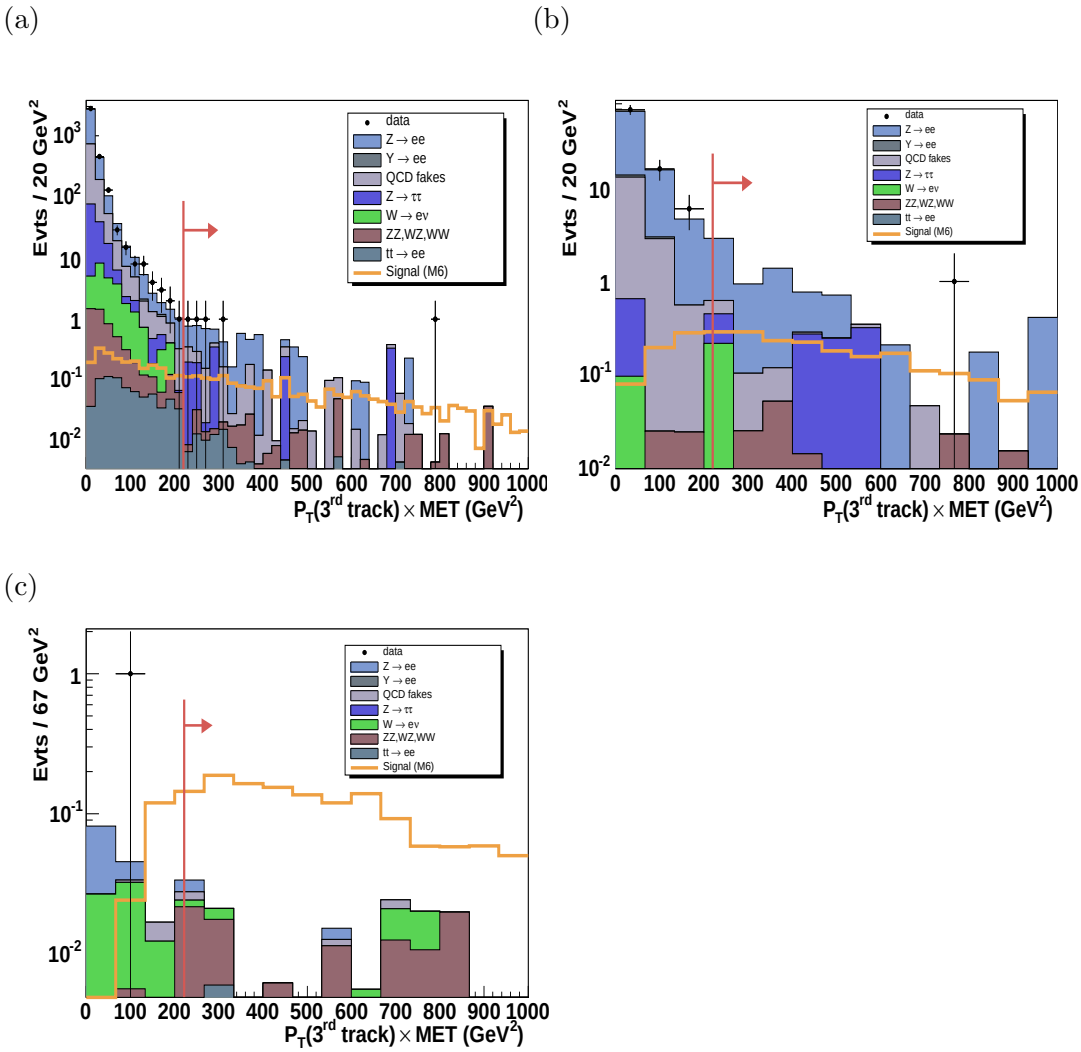

Figure 10.15: Distribution of the product of $\not\!\!E_T$ and the transverse momentum of the third track in data (points with error bars), SM background (filled histograms) and expected signal (SUSY point M6, empty histogram) (a) at the low-mass preselection level, (b) at the e+e+track level and (c) before the cut on $\not\!\!E_T \times p_T$(track) is applied. Plot (c) is derived with the loose $Z \to ee$ and the loose $W \to e\nu$ sample.

Since the background statistics is extremely low at this stage of the selection, the cut on $\not\!\!E_T \times p_T(\text{track})$ is optimized using a loose sample, which is selected by loosening the quality cuts for the objects involved but keeping the kinematic thresholds of the analysis selection in order not to bias the efficiency for the last cut. The positions of the loosened cuts are chosen such that the relative fractions of the most important background sources correspond to the fractions in the analysis selection before applying the last cut. In detail, the loose sample is derived without requirements on the number of SMT hits and with the electron likelihood loosened to likelihood > 0.1. The Di-EM mass range is extended up to 90 GeV. The minimum value of $\text{Sig}(\not\!\!E_T)$ is reduced by a factor of 4. The third track is selected without quality and isolation requirements.

Figure 10.16a shows the distribution of the $\not\!\!E_T \times p_T(\text{track})$ in the loose background sample. The distribution is fitted with a sum of two exponentials which is multiplied by an error function in order to account for the turn-on for low values of $\not\!\!E_T \times p_T(\text{track})$ due to the previous plain cuts on $p_T(\text{track})$ and $\not\!\!E_T$. The expected number of background events, which follows from the fit after the normalization is shown in Fig. 10.16b as a function of the position of the cut on $\not\!\!E_T \times p_T(\text{track})$. Figure 10.16c shows the corresponding expected number of events for a SUSY point with $m_{\chi_1^\pm} = 110$ GeV in the 3-body region.

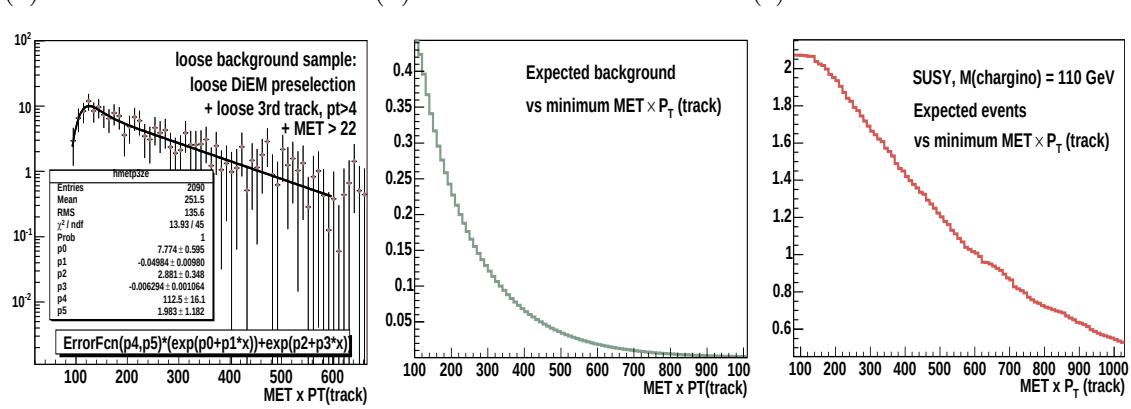

Figure 10.16: (a) Fit of the $\not\!\!E_T \times p_T(\text{track})$ distribution for the sum of all backgrounds, (b) expected background as a function of $\not\!\!E_T \times p_T(\text{track})$ and (c) expected signal ($m_{\chi_1^\pm} = 110$ GeV) as a function of the cut at $\not\!\!E_T \times p_T(\text{track})$.

These values are used to calculate the expected 95% CL limits on the total cross section into trilepton states, $\sigma \times \text{BR}(3\ell)$, for a SUSY point with $m_{\chi_1^\pm} = 110$ GeV in the absence of a signal as a function of the position of the cut on the product of $\not\!\!E_T$ and $p_T(\text{track})$. The limits are calculated as described in Section 2.2.1, using the likelihood-ratio method. The results are shown in Fig. 10.17a. The plot suggests an optimal cut position in the range of $150\ \text{GeV}^2 < \not\!\!E_T \times p_T(\text{track}) < 220\ \text{GeV}^2$.

The analysis is combined with the results of three other SUSY channels [75, 76, 77] (see Section 5.1.2 and detailed results in the next section). The optimal cut position on the product of $\not\!\!E_T$ and $p_T(\text{track})$ in the $e + e + \ell$ channel is chosen such that it minimizes the expected combined limit on the signal cross section. Figure 10.17b shows the 95% CL limit expected in the absence of signal for the same SUSY point with the combined analysis

as a function of the position of the cut on the product of $\not\!\!E_T$ and p_T(track) in the e+e+ℓ analysis. The optimal cut position is in the range 180 GeV^2 $< \not\!\!E_T \times p_T(\text{track}) <$ 300 GeV^2.

The product of $\not\!\!E_T$ and p_T(track) is required to be larger than 220 GeV, which yields an optimal sensitivity for the combined analysis, while at the same time preserving a good efficiency for the stand-alone analysis in the e + e + ℓ channel. The optimal cut position depends on the kinematics of the signal final state. Within the chargino mass range of interest (directly beyond the LEP II limits, see Section 11), this dependence can be neglected. With increasing data statistics, the sensitivity of the analysis will be extended towards larger chargino masses (see Section 12) such that a reoptimization of the cut position will be necessary.

The last cut reduces the expected background to 0.20±0.03(stat)±0.07(sys) events, dominated by WZ events. Further background contributions stem from WW, W, $t\bar{t}$, QCD and $Z/\gamma \rightarrow$ ee events. The single data event selected in the previous stage is discarded due to its low value of the product of $\not\!\!E_T$ and p_T(track) of 123 GeV^2 which is clearly below the selection threshold. The efficiency of the selection for leptonic final states of the SUSY reference point M6 is (2.3±0.1)%, which results in 1.9±0.1 events expected for this SUSY point after the selection.

(a) (b)

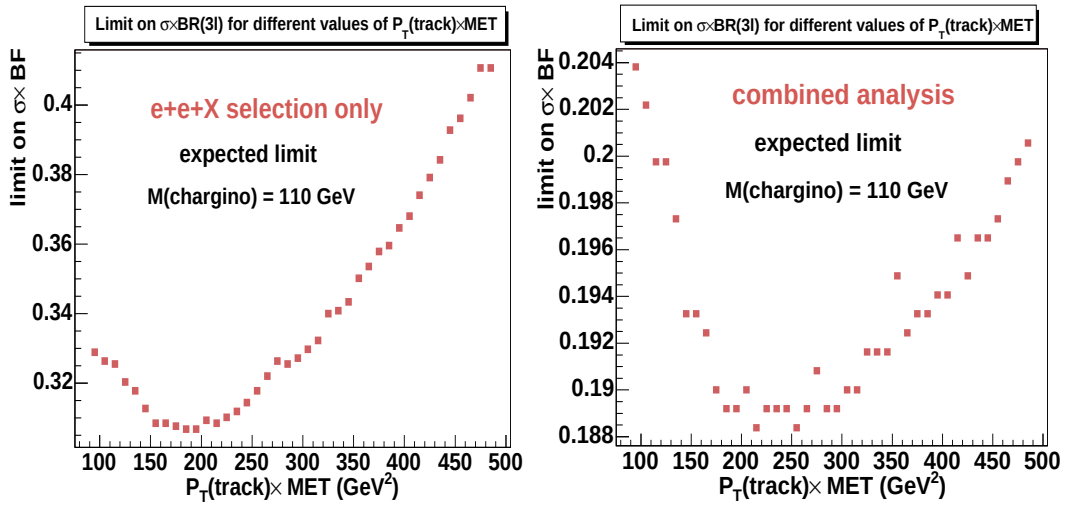

Figure 10.17: Expected limit on $\sigma \times \text{BR}(3\ell)$ for a SUSY point with $m_{\chi_1^\pm} = 110$ GeV as a function of the position of the cut on $\not\!\!E_T \times p_T$(track) in the e+e+ℓ selection (a) resulting from the e+e+ℓ analysis only and (b) calculated for the combined analysis.

10.2.6 Systematic uncertainties

The systematic uncertainties on the number of events expected from Standard Model processes and for SUSY events are composed of a variety of contributions:

- detector modeling (efficiency, resolution, calibration)

- modeling of the trigger efficiencies
- modeling of the physics process (PDFs, NLO processes)
- calculation of rejection factors with loose samples
- calculation of the expected QCD background
- measurement of the integrated luminosity.

The total systematic error is calculated as the square root of the quadratic sum of the individual errors, assuming that they are independent. The errors derived for the individual contributions are listed in Table 10.3. Details of the calculation of the individual errors are discussed in the following sections.

Since the systematic errors depend on the selected phase space region, which changes within the cut flow and since the composition of the background changes also for each step of the selection, the systematic error on the total background expectation depends on the selection stage.

The systematic errors are calculated for three stages of the analysis:

- low mass preselection (cut2), dominated by $Z/\gamma \rightarrow ee$, and QCD events
- large $\not\!\!E_T$ and large p_T(track) (cut8), dominated by $Z/\gamma \rightarrow \ell\ell$, $W \rightarrow e\nu$ and QCD events
- final selection (cut11), dominated by WZ events.

In order to increase the MC statistics for the selection stage 8 and 11, loose samples are used for the calculation of the systematic errors. The loose selection requires two electrons with $p_T > 12$ GeV and $p_T > 8$ GeV and track match, 18 GeV $<$ M(e,e) $<$ 120 GeV, a loose track with $p_T > 4$ GeV and $\not\!\!E_T > 22$ GeV. The individual fractions of the background are reweighted in order to reproduce the background composition at cut stage 8 and 11 as presented in Table 10.2. The resulting statistical uncertainty of this loose sample is 1.7% and 1.4% for cut 8 and cut 11 respectively.

Modeling of the detector and the trigger

An important contribution to the systematic error stems from the modeling of the electron reconstruction efficiency, in particular the efficiency for reconstructing an EM candidate (see Section 7.2.1) and the efficiency of the cut on the likelihood. Both contributions are calculated by varying the MC efficiency corrections within their errors, as listed in Tables 9.6 and 9.7.

The reweighting of the fraction of MC events with electrons reconstructed near a border of a calorimeter tower (ϕ crack, see Section 9.3.3) leads also to a non negligible contribution to the systematic error, which is estimated by composing the difference of the numbers of selected events in corrected and uncorrected MC.

source	background			signal
	presel	large p_{T}(track)/$\not\!\!E_{\mathrm{T}}$	final	final
modeling of the detector and the trigger				
electron reconstruction	2.6%	3.1%	3.0%	3.5%
CC phi cracks	–	2.1%	0.8%	0.5%
conversion probability	0.1%	2.1%	2.7%	0.2%
track isolation	–	2.3%	3.1%	1.0%
jet energy scale	–	10.1%	1.6%	0.9%
jet smearing	–	12.3%	3.1%	0.1%
electron smearing	0.2%	2.5%	0.6%	0.4%
MET smearing	–	17.2%	3.3%	0.4%
trigger turn-on	3.0%	2.4%	2.3%	1.5%
modeling of the physics process				
PDF/scale errors on the cross section	2.6%	3.1%	6.0%	3.5%
PDF error on the acceptance	–	–	–	6.5%
W: ISR correction	0.1%	0.4%	0.9%	0.2%
p_{T}(Z) modeling	0.7%	4.4%	0.3%	–
calculation of rejection factors with loose samples				
loose MC samples (rejection)	–	–	24.5%	–
loose MC samples (normalization)	–	–	19.2%	–
QCD background	6.5%	4.3%	0.4%	–
quadratic sum	8.1%	25.1%	32.6%	8.5%
integrated luminosity	6.5%	6.5%	6.5%	6.5%
coherent noise fraction	0.5%	0.5%	0.5%	0.5%
quadratic sum total	10.4%	26.0%	33.2%	10.7%

Table 10.3: Systematic uncertainties on the number of events expected from Standard Model processes for different selection stages and from SUSY processes after the last selection cut (relative errors are quoted).

The uncertaintiy in the correction derived for the modeling of the photon conversion probability in MC (see Section 9.3.7) are taken into account by calculating the difference between corrected and uncorrected MC.

Electronic noise in the calorimeter readout can have an impact on the efficiency of the track calorimeter isolation requirement. If this noise is badly described in the detector simulation, the MC may overestimate the signal efficiency for this cut. This effect is taken into account by adding random noise distributed as a Gaussian with $\sigma = 0.5$ GeV, a value corresponding to the maximal noise that can be added without destroying the good agreement of the distribution of the E_{T} sum in the isolation cone for background tracks in data and MC shown in Fig. 10.10.

The calibration of the jets (jet energy scale) is an important source of systematic uncer-

tainty for cut stages with a large $Z/\gamma \rightarrow ee$ component due to the fact that it is propagated into the missing transverse energy. The contribution is calculated by varying the jet energy scale corrections for data and MC within their error (see Figures 7.7 and 7.6).

Electron and jet smearing in MC have an impact on the number of selected events, mainly via the propagation of the modification of the transverse momenta into the $\not\!\!E_T$ calculation. The contribution from the smearing process is estimated by 50% of the difference between smeared and unsmeared MC. The impact of the smearing is large after the cut on the $\not\!\!E_T$ (cut 8) and decreases with the $Z/\gamma \rightarrow ee$ fraction in the background.

The smearing of $\not\!\!E_T$ in MC increases the number of $Z/\gamma \rightarrow ee$ and $Z/\gamma \rightarrow \tau\tau$ events considerably, that are expected to pass the requirement of large $\not\!\!E_T$. Since the origin of the discrepancy of the $\not\!\!E_T$ distribution in data and MC is not fully understood yet, the uncertainty is conservatively taken into account by calculating the difference of the number of events expected for the background with smeared and unsmeared MC. The contribution is large for cut stage 8 and decreases with the $Z/\gamma \rightarrow ee$ fraction in the background. For the final selection, it is much less important.

The effect of the trigger turn-on in the early stages of the selection is calculated by varying the parameters of the MC turn-on correction within the error of the fit, as listed in Table 9.4. The background at the final stage of the selection and the signal have a large fraction of events with three real electrons. The trigger efficiency for these events could be larger than the efficiency that is calculated based on the leading two electrons. This is conservatively taken into account by estimating the systematic contribution with 50% of the difference between the uncorrected MC and the trigger-corrected MC. The $Z/\gamma \times \rightarrow ee$ contribution for the error on the trigger turn-on is calculated from the low mass preselection instead of the loose sample, which has a larger fraction of high-p_T electrons.

Modeling of the physics process

The signal and background cross sections are calculated with NLO CTEQ6 PDFs. The PDF-related errors on the background cross section are calculated according to [63] and presented in Table 9.1. The PDF uncertainty on the signal cross section increases with the chargino and neutralino masses. For chargino masses of 106 GeV and 130 GeV the errors are calculated as 3.5% and 4.5% respectively.

The uncertainties of the PDF fit have also an impact on the shape of the distribution of kinematic variables which are used in the selection, resulting in an error on the acceptance. The impact of the PDF uncertainty on the acceptance is estimated for the signal by comparing the selection efficiencies for a SUSY point with $m_{\chi_1^\pm} = 106$ GeV measured in MC generated with the CTEQ6 central PDF fit and in MC generated with the PDF error functions. In this case, the errors are estimated with PDF error functions to eigenvector 4 [62], which have the largest impact on the kinematic distribution of the quarks in the kinematic region that corresponds to the production of a chargino-neutralino pair.

The error from the $p_T(Z)$ reweighting (see Section 9.3.5) is estimated by varying the fit weights within the errors. This contribution is relevant after the cut on the azimuthal angle between the electrons (cut 3).

The uncertainties in the corrections derived for the ISR modeling in the PYTHIA $W \to e\nu$ MC (see Section 9.3.6) are taken into account by calculating the difference between corrected and uncorrected MC. The contribution depends strongly on the fraction of W events in the background.

Calculation of rejections with loose MC samples

The dominant error for the background estimate in the three final selection steps comes from the loose sample which is used for modeling the rejection of the last three cuts. The uncertainty results from the normalization of the sample at cut stage 8 (large $\not\!\!E_T$) and from the assumption that the loosened cuts have no correlation to the variables used for the last cut stages (Sig($\not\!\!E_T$), M_T, $\not\!\!E_T$ and p_T(track)). The error on the normalization is 100% for the W sample and 40% for the $Z/\gamma \to ee$ sample.

The largest correlation to the final cuts is expected from the extension of the invariant mass range of the $Z/\gamma \to ee$ sample towards the Z resonance (M(e,e) < 90 GeV), since the average $\not\!\!E_T$ increases with the Di-EM mass. This contribution is estimated by comparing the rejection of the last three cuts for the loose and the tight sample in a Di-EM preselection without a third track requirement, where both samples have sufficient statistics. Since the track information cannot be used in the preselection stage, cut 11 which requires $\not\!\!E_T \times p_T(\text{track}) > 220\,\text{GeV}^2$ is replaced by a tightened cut on the missing transverse energy, $\not\!\!E_T > 30$. The resulting relative differences of 10%, 24% and 8% for the efficiencies of cut 9, cut 10+cut 9 and the large-$\not\!\!E_T$ requirement are used to estimate the error on the background efficiency for the last cuts.

Description of the QCD background

The contribution from the description of the QCD background, in particular the low-p_T and the η reweighting of the QCD sample (see Section 9.2), is taken into account by varying these corrections within the errors presented in Table 9.3 and Fig. 9.1.

Measurement of the integrated luminosity

Since the MC is normalized to the measured luminosity, the error on the luminosity measurement and on the coherent noise fraction which is removed by the data quality selection (see Section 8.3) is added to the systematics.

All contributions result in a systematic error for the background estimate of 10% in the preselection, 26% after requiring large-$\not\!\!E_T$ and 33% in the final selection. The systematic error on the signal expectation adds up to 11%.

The size of the systematic error in signal and background is mainly due to an insufficient understanding of the detector and to the small number of MC events available. Various ongoing studies [110] are expected to improve the understanding of the detector. Improved data processing capabilities are expected to allow for a substantially increased MC production. As a consequence, the systematic error is expected to be reduced in the future.

11 Results

Since no evidence for associated production of charginos and neutralinos is observed, upper limits on the product of the cross section and the leptonic branching ratio are extracted from the result of the previous section. The upper limits are compared with predictions from different SUSY models, in order to derive constraints on SUSY model parameters.

The results are derived and interpreted for this analysis alone and in combination with three other analyses that search for associated production of charginos and neutralinos in final states with muons.

11.1 Efficiencies for the signal selection

The signal efficiency and therefore also the limit on the total cross section depend mainly on the kinematics of the final state particles which in turn follows from the chargino and neutralino masses and from the mass difference of the gauginos and to the sleptons.

The selection efficiencies are derived for SUSY models with $m_{\chi_1^\pm} \approx m_{\chi_2^0} \approx 2 \cdot m_{\chi_1^0}$, similar to the benchmark points presented in Table 9.2. The motivation for this choice of chargino and neutralino mass relations for the reference point comes from GUT-oriented SUSY scenarios and is discussed in detail in Section 11.3. If not stated otherwise, results are quoted in the following for chargino and neutralino decays into leptonic final states with equal branching ratios into the three lepton flavors. The dependence of the results on the flavor composition of the final state and the impact of the mass relations between charginos and neutralinos and within the neutralinos is discussed in Section 11.2.2.

Figure 11.1a shows the selection efficiency for associated production of charginos and neutralinos with leptonic final states as a function of the mass difference between the second neutralino and the lightest slepton for $m_{\chi_2^0}$=108 GeV and $m_{\chi_1^\pm}$=104 GeV at the LEP II chargino mass limit. Two domains of large selection efficiency are separated by a *channel* of low efficiency:

The selection efficiency is large for slepton masses larger than the mass of the second neutralino, where the neutralino and the chargino decay mainly via virtual sfermions and gauge bosons (3-body decays). The efficiency increases slightly with increasing slepton mass, approaching a stable level, such that efficiencies calculated for sleptons only slightly heavier than the neutralino can be used to derive predictions for very large slepton masses. This region is referred to as *3-body region* in the following.

The second domain with large selection efficiencies is found for sleptons that are substantially lighter than the second neutralino. In this case, the neutralino decays mainly into a real slepton and a lepton. The efficiency increases with increasing mass difference between the neutralino and the slepton. This region is called *2-body region* in what follows.

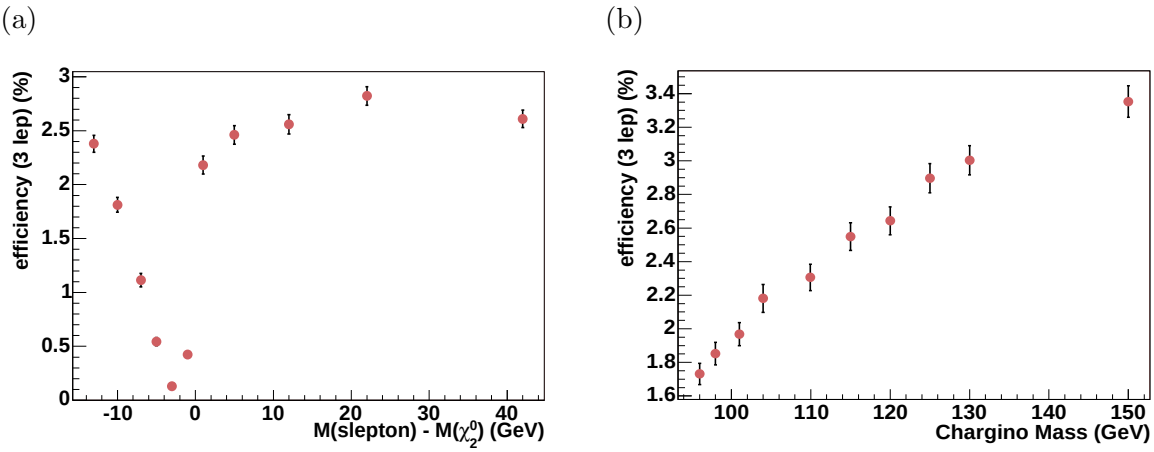

Figure 11.1: Selection efficiency for SUSY points with equal electron, muon and tau branching ratios of chargino and neutralino for $m_{\chi_1^\pm} \approx m_{\chi_2^0}$ and $m_{\chi_2^0} \approx 2 \cdot m_{\chi_1^0}$ (a) as a function of the mass difference between the lightest slepton and the second lightest neutralino for $m_{\chi^\pm}$=104 GeV and (b) as a function of the chargino mass in the 3-body domain.

A channel of low selection efficiency between the two domains of large efficiency corresponds to the region where the neutralino decays into a real slepton and a very soft lepton, often below the kinematic threshold of the selection, due to the small mass difference between the slepton and the neutralino, as discussed in Section 5.1.3 (see Fig. 5.7b).

The dependence of the efficiency on the chargino and the neutralino mass is investigated in Fig. 11.1b for SUSY models in the 3-body region. The mass difference between slepton and neutralino is fixed to $m_{\tilde{\ell}}$ - $m_{\chi_2^0} \approx 1$ GeV and the chargino mass is scanned. The selection efficiency increases with increasing chargino mass due to the increasing transverse momenta of the final state particles.

11.2 Extraction of cross section limits

No candidate event remains in the data after the selection in agreement with the expectation of 0.20±0.03(stat)±0.07(sys) events from Standard Model processes (see Section 10). This result is translated into upper limits on the product of the cross section for associated production of charginos and neutralinos and the branching ratio into three leptons, $\sigma(\chi_2^0\chi_1^\pm) \times \mathrm{BR}(3\ell)$, which is referred to as *trilepton cross section* in what follows. The limits are derived using the selection efficiencies for SUSY signals presented in the previous section as a function of the slepton-neutralino mass difference and as a function of the chargino mass in the 3-body region. The limits are calculated with the likelihood-ratio method in the modified frequentist approach as described in Section 2.2.2. Since the same selection cuts are used for all SUSY masses the shape of the limits reflects directly the shape of the signal efficiency, presented in Fig. 11.1.

Figure 11.2 shows the resulting upper limits on the trilepton cross section as a function of the mass difference between the slepton and the neutralino for $m_{\chi_1^\pm}$=104 GeV and as a function of the chargino mass in the 3-body region. The expected limits are very similar to

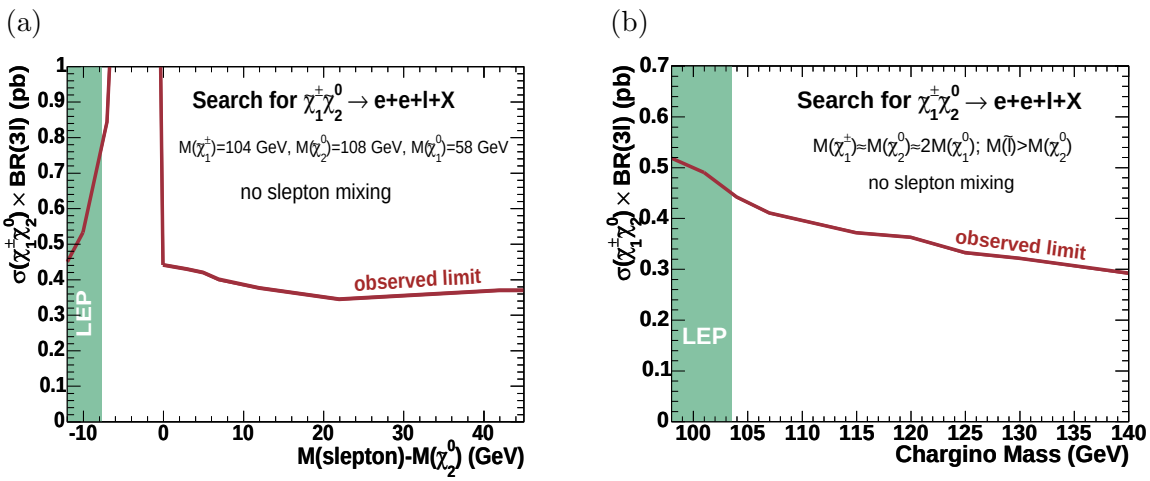

Figure 11.2: Upper limits on the trilepton cross section $\sigma(\chi_2^0\chi_1^\pm) \times \mathrm{BR}(3\ell)$ set by this analysis (red line) (a) as a function of the mass difference between the second neutralino and the slepton for $m_{\chi^\pm} = 104\,\mathrm{GeV}$ and (b) as a function of the chargino mass in the 3-body domain. The parameter domains excluded by direct searches for selectrons and charginos at LEP II ($m_{\tilde{\mathrm{e}}} < 100$ GeV for large mass difference to the LSP and $m_{\chi_1^\pm} < 103.5$ GeV) are marked as a reference.

the observed limits and not shown in the plot. The parameter domains excluded by direct searches for selectrons and charginos at LEP II ($m_{\tilde{\mathrm{e}}} < 100$ GeV for large mass difference to the LSP and $m_{\chi_1^\pm} < 103.5$ GeV, see Section 1.2.6), are marked as a reference.

The scan of the slepton-neutralino mass difference, shown in Figure 11.2a, results an upper limit on the trilepton cross section in the range of 0.4 pb in the 3-body region. As expected, the cross section limit is large in the channel of low efficiency (see Fig. 11.1a). In the 2-body region, the limit falls again below 0.4 pb and decreases with decreasing slepton mass. The results of the chargino mass scan in the 3-body region are shown in Fig. 11.2b. The limit decreases with increasing chargino and neutralino masses due to the increasing signal efficiency (see Fig. 11.2b) from 0.5 pb for $m_{\chi_1^\pm}$=100 GeV to 0.3 pb for $m_{\chi_1^\pm}$=140 GeV.

The limits from this analysis restrict the cross section range for associated production of charginos and neutralinos with SUSY masses beyond the LEP II kinematic reach and beyond the Tevatron Run I analyses performed by the DØ and the CDF experiments (see the limits on the $\sigma \times \mathrm{BR}(\mathrm{e}/\mu)$ derived for $\sqrt{\mathrm{s}}$=1.8 TeV in Fig. 1.7).

11.2.1 Combination with other analyses

The sensitivity is significantly improved by a combination [116] with the results from three additional analyses that search for associated production of charginos and neutralinos in trilepton final states with muons:

- final states with one electron, one muon and a third lepton, $\mathrm{e} + \mu + \ell$ selection [75]
- final states with two muons and a third lepton, $\mu + \mu + \ell$ selection [76]

- final states with two like sign muons, LS $\mu + \mu$ selection [77].

Table 11.1 shows the number of events observed in data and the number of expected background and signal events (reference point M6, $m_{\chi^\pm} = 110\,\text{GeV}$) expected for the four analyses.

Analysis	Data	Total Background	Signal (M6)
e+e+ℓ	0	0.20±0.03±0.07	1.93±0.06±0.21
e+μ+ℓ	0	0.31±0.13±0.03	1.60±0.06±0.14
μ+μ +ℓ	2	1.75±0.34±0.48	1.30±0.04±0.18
LS μ+μ	1	0.66±0.36±0.14	0.70±0.10±0.16
sum (– overlap)	3	2.92±0.51(stat)±0.52(sys)	5.08±0.14±0.41

Table 11.1: Number of candidate events observed and events expected from Standard Model processes and from a reference signal point (M6, $m_{\chi_1^\pm}$=110 GeV) in the four analysis channels. Correlations in the systematic errors are taken into account in deriving the total systematic error.

Combining all four selections, a total background of 2.9±0.5(stat)±0.5(sys) is expected after all cuts while 3 events are observed in the data. No evidence for associated production of charginos and neutralinos is observed. An upper limit on the total cross section is extracted using the likelihood ratio method. Systematic and statistical errors, which are discussed in detail in the individual analysis descriptions are taken into account in the combination including their correlations.

To avoid double-counting, signal events selected by more than one analysis channel are assigned to one channel and removed from the other channels. The channel which the overlap is assigned to is chosen such that it maximizes the combined sensitivity. These overlaps amount to about 16% between the e+e+ℓ and the e+μ+ℓ analyses, 15% between the e+μ+ℓ and the μ+μ+ℓ analyses and 14% between the μ+μ+ℓ and the LS μ+μ analyses. The overlap between backgrounds is negligible.

The results of the combined analysis are used to derive upper limits on the trilepton cross section which are shown in Fig. 11.3. The expected limit (see Section 2.2.3) is added as a comparison. The observed limit is slightly tighter than the expected limit because the distribution of the number of expected Standard Model events within the four analyses differs slightly from the distribution of the data events. The upper limit on the trilepton cross section is approximately 0.2 pb for large slepton masses (see Fig. 11.3a). In the channel with degenerated slepton and neutralino masses, the efficiencies of all analyses which select three leptons, are low and the limit is determined by the LS μ+μ analysis. In the 2-body region, the limit decreases again with increasing slepton-neutralino mass difference. The chargino mass scan in the 3-body region, presented in Fig. 11.3b, shows that the combined limit improves with increasing chargino mass, reaching a value of 0.16 pb for $m_{\chi^\pm} = 140$ GeV.

The results from the combined analysis restrict the trilepton cross section considerably more than the Tevatron Run I analyses performed by the DØ and the CDF experiments

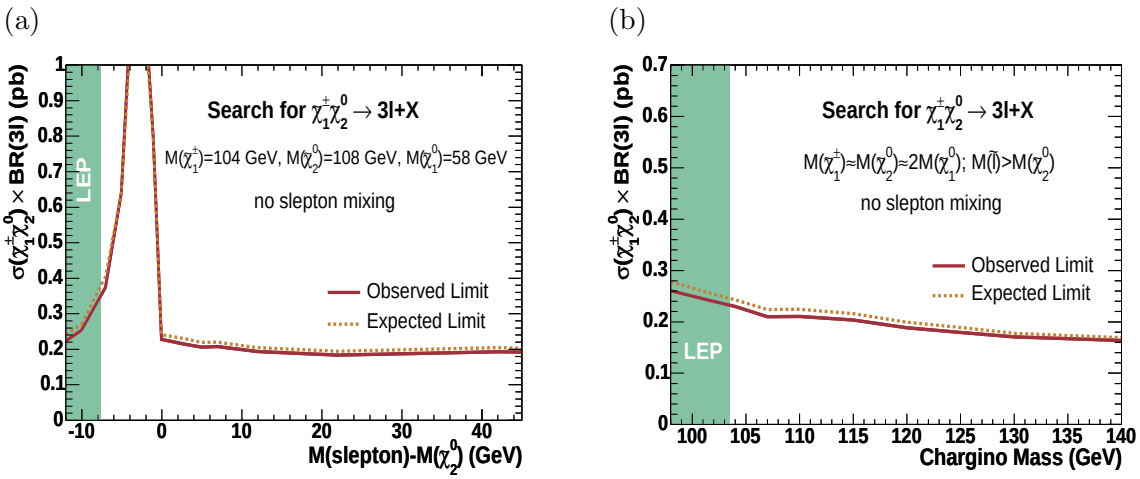

Figure 11.3: Observed (continuous line) and expected (dashed line) upper limits on the trilepton cross section $\sigma(\chi_2^0\chi_1^\pm) \times \mathrm{BR}(3\ell)$ set by the combined analysis (a) as a function of the mass difference between the second neutralino and the slepton for $m_{\chi^\pm} = 104\,\mathrm{GeV}$ and (b) as a function of the chargino mass for sleptons mass degenerated with the second lightest neutralino. Chargino masses below 103.5 GeV and selectron masses < 100 GeV (with large mass differences to the LSP) are excluded by direct searches at LEP.

(see Fig. 1.7) and constitute the most stringent limits on the associated production of charginos and neutralinos with chargino and neutralino masses beyond the LEP II kinematic reach.

The selection efficiency depends in addition on the mass difference between the chargino or the second lightest neutralino and the LSP. Large mass differences lead to large lepton transverse momenta, which are expected to result in larger selection efficiencies. For low mass differences, the selection efficiency is expected to decrease due to low transverse momenta of the final state particles.

If the mass difference between the chargino or the second neutralino and the LSP becomes larger than the W mass or the Z mass respectively, decays into real W and Z bosons become dominant for large slepton masses, which leads to background-like kinematic distributions in the signal. This case is discussed in detail in Section 12.1.

11.2.2 Dependence on the flavor composition of the final state

The limits presented in the previous section are derived assuming degenerated slepton masses which leads to equal branching ratios of the neutralino and the chargino into the three lepton flavors. The dependence of the results on this assumption is studied in this section.

The final states selected in this analysis, consist mainly of two electrons and an additional electron, muon or τ-lepton, such that the efficiency for leptonic topologies depends on the branching ratio of the second neutralino into electrons. Since the probability for a lepton to fulfill the requirements of a third track is different for each lepton flavor, the total efficiency depends in addition on the flavor composition of the chargino decay products.

Table 11.2 shows the selection efficiencies for various final states for the three SUSY reference points presented in Fig. 10.1. The largest efficiencies are derived for the e+e+μ and the e+e+e final states. In the 3-body region (M6, M12), the e+e+μ efficiency is slightly larger than the e+e+e efficiency because the probability for an electron to be reconstructed as an isolated track is slightly lower than for a muon due to bremsstrahlung of the electron. In the 2-body region (DM3), the efficiency for final states with three electrons is larger because the transverse momentum of the second electron from the neutralino decay is comparably low and the e+e+e final state provides an additional possibility to identify the electron from the chargino as a tight electron instead of the second electron of the neutralino. In both regions, the number of selected e+e+τ final states is lower than the number of selected e+e+e or e+e+μ events. The inefficiency is mainly connected to hadronic tau decays which result in charged pions with low transverse momenta. The small number of selected τ+τ+e final states corresponds to events where a τ-lepton decays into an electron.

point	$m_{\chi_1^0}$,$m_{\tilde{e}_R}$[GeV]	ϵ(e+e+e) [%]	ϵ(e+e+μ)[%]	ϵ(e+e+τ) [%]	ϵ(τ+τ+e) [%]
M6	114, 115	8.05±0.43	9.11±0.46	3.49±0.28	0.15±0.06
M12	152, 153	9.94±0.48	13.65±0.56	6.06±0.37	0.47±0.11
DM3	108, 104	5.17±0.40	3.41±0.32	1.17±0.18	0.09±0.07

Table 11.2: Selection efficiencies of this analysis for various final states of three SUSY reference points. Final states not listed here have negligible efficiencies

The number of final states with two muons selected by the analysis in this thesis is negligible but these signatures are selected with a large efficiency by the other analyses of the combination. As a consequence, the final results of the combination are mainly independent of the electron/muon ratio in the final state.

As described in Section 1.2.3, in many SUSY models the $\tilde{\tau}$ masses and couplings are different from the values of the other two generations due to a considerable degree of $\tilde{\tau}$-mixing which leads to different branching ratios for final states with τ-leptons. Unlike the muon efficiency, the efficiency for final states with two τ-leptons is substantially lower in all four analysis such that the branching ratio into τ-leptons is expected to have a sizeable impact on the cross section limits derived in the combination.

This effect is studied by scanning the branching ratios of both the chargino and the second neutralino into final states with τ-leptons at the same time by varying the ratio of stau and selectron/smuon masses in the 3-body range for $m_{\chi_2^0}$=108 GeV and $m_{\chi_1^\pm}$=104 GeV. Figure 11.4a shows the resulting selection efficiencies for the four analyses as a function of the τ-fraction within the leptonic decay products of the second neutralino. The efficiencies of all electron/muon based analyses decrease with increasing τ branching ratios of the neutralino and the chargino. The corresponding combined upper limit on the trilepton cross section as a function of the τ-fraction is shown in Fig. 11.4b. As expected, the upper limit increases with increasing τ branching ratio. The combination with the results of additional analyses that search for SUSY in final states with identified τ-leptons [78, 79] is expected to improve the sensitivity for large τ branching ratios.

(a) (b)

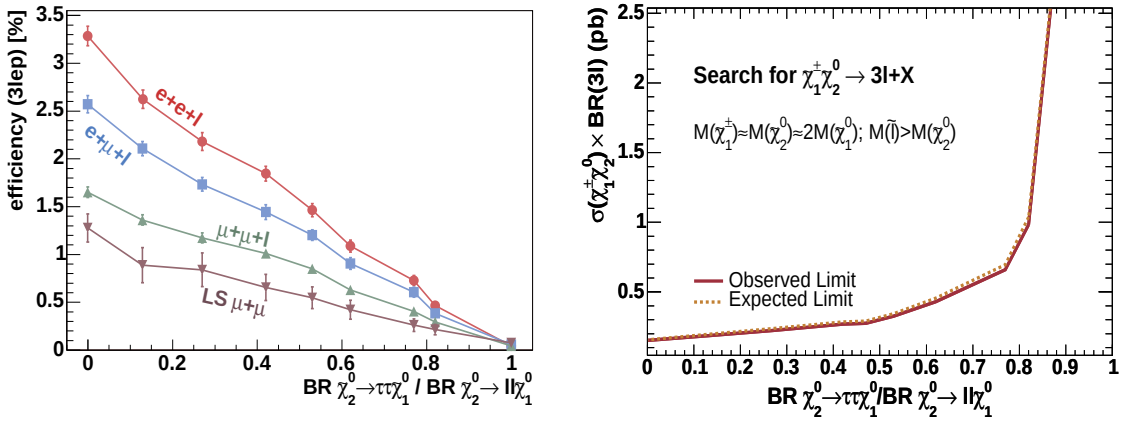

Figure 11.4: Scan of the BR of the chargino and the second neutralino into final states with τ-leptons for $m_{\chi_1^\pm}$=104 GeV, $m_{\chi_1^\pm} \approx m_{\chi_2^0}$ and $m_{\chi_2^0} \approx 2 \cdot m_{\chi_1^0}$ in the 3-body domain. (a) Efficiency of the four analyses and (b) observed and expected upper limit on the trilepton cross section $\sigma(\chi_2^0\chi_1^\pm) \times \mathrm{BR}(3\ell)$ as a function of the BR of the second neutralino into τ-leptons.

11.3 Interpretation of the cross section limits

The upper limits on the cross section, derived in the last sections, are compared with predictions from the MSSM in order to restrict the allowed SUSY parameter space further. Due to the large number of degrees of freedom in the general MSSM (see Section 1.2.3), resulting from the parameterization of the SUSY breaking, limits on masses or SUSY parameters are usually not extracted for the general MSSM. The limits are instead compared with selected benchmark models. The constraints on chargino, neutralino and slepton masses that are derived for these benchmark scenarios can be applied to any MSSM model with comparable mass relations and branching ratios.

The benchmark scenarios for this analysis are derived from GUT-constraint SUSY models with different degrees of scalar mass unification and are motivated by the two focus regions of electron/muon based trilepton studies at the Tevatron: SUSY parameter combinations with low $\tilde{\tau}$-mixing and parameter domains with large slepton masses, both resulting in comparable branching ratios for all lepton flavors (see Section 5.1.3). Common features of the GUT-constraint models at the SUSY mass scale of interest are the wino-like lightest chargino and second lightest neutralino (gaugino region) and the specific mass relations, $m_{\chi_1^\pm} \approx m_{\chi_2^0}$ and $m_{\chi_2^0} \approx 2 \cdot m_{\chi_1^0}$, for which the selection efficiencies in the previous section are derived. The benchmark points are modeled with mass degenerated sleptons.

The upper limits on the trilepton cross section in the 3-body region are compared with the predictions for chargino mass scans from three benchmark scenarios:

- Models where the sleptons are mass degenerated with the second neutralino and the latter decays dominantly via sfermion mediated 3-body graphs (*3l–max scenario*), such that the leptonic branching ratio for 3-body topologies is maximally enhanced. Unification of squark and slepton masses is assumed in calculating the cross section.

The scenario provides an upper bound on the trilepton cross section for 3-body topologies within mSUGRA-inspired models with negligible $\tilde{\tau}$-mixing.

- A variation of the 3l–max scenario, where the unification of slepton and squark masses is dropped. The squarks are assumed to be very heavy (masses at TeV scale), which suppresses the destructive interference from the t-channel contribution to the production cross section such that the cross section is enhanced (see Section 5.1). This model provides an upper bound on the trilepton cross section for 3-body topologies with negligible $\tilde{\tau}$-mixing (*heavy-squarks scenario*).
- mSUGRA-inspired models with large slepton (and squark) masses obtained by raising m_0 to the TeV scale, assuming scalar mass unification (*large-m_0 scenario*). For large slepton masses the impact of the $\tilde{\tau}$-mixing on the branching ratios is negligible, since the slepton mass difference is small compared to the slepton mass and the charginos and neutralinos decay via gauge boson mediated 3-body decays.

Starting from the 3l–max and the heavy-squarks benchmark points with $m_{\chi_1^\pm}$= 104 GeV and $m_{\chi_2^0}$=108 GeV, the trilepton cross section is also scanned as a function of the slepton mass for fixed chargino and neutralino masses assuming negligible $\tilde{\tau}$-mixing. The corresponding benchmark models are denoted as *mSUGRA inspired* and *heavy squarks* respectively. Both models unify for very large slepton and squark masses (large-m_0 scenario).

The comparison of the observed upper limit on the trilepton cross section with the values predicted in the benchmark scenarios leads to excluded mass ranges for these scenarios and other SUSY models with comparable mass relations and field contents.

11.3.1 Interpretation of the results in the e+e+ℓ channel

Figure 11.5a compares the upper limit on the trilepton cross section from Fig. 11.2a for $m_{\chi^\pm}$=104 GeV derived by the e+e+ℓ analysis as a function of the mass difference between the second neutralino and the slepton with the predictions from the mSUGRA-inspired and the heavy-squarks model. The trilepton cross section increases for both scenarios with decreasing slepton mass as expected from the increasing contribution of slepton mediated neutralino decays. The leptonic branching ratio is further enhanced when the slepton mass drops below the neutralino mass and the neutralino decays via a real slepton (2-body region). For mass-degenerated slepton and neutralino, the phase space for the lepton and the real slepton is extremely small, such that this decay is suppressed. As a consequence, for a small mass range of about 1 GeV the trilepton cross section vanishes and the second neutralino decays instead dominantly via 3-body modes into invisible neutrinos.

The e+e+ℓ analysis alone is not sensitive to GUT–constraint SUSY models with sfermion universality beyond the LEP II limits. Models with enhanced cross sections due to heavy squarks, though, are accessible for this analysis and slepton masses with $m_{\chi_2^0} < m_{\tilde{\ell}} < m_{\chi_2^0} + 8\,\text{GeV}$ are ruled out for $m_{\chi^\pm} = 104\,\text{GeV}$. A second region of sensitivity for the heavy-squark scenario opens in the 2-body domain for $m_{\tilde{\ell}} < m_{\chi_2^0} - 7\,\text{GeV}$.

Figure 11.5b compares the limit observed in the 3-body domain (see Fig. 11.2b) as a function of the chargino mass with the trilepton cross sections predicted by the 3l–max,

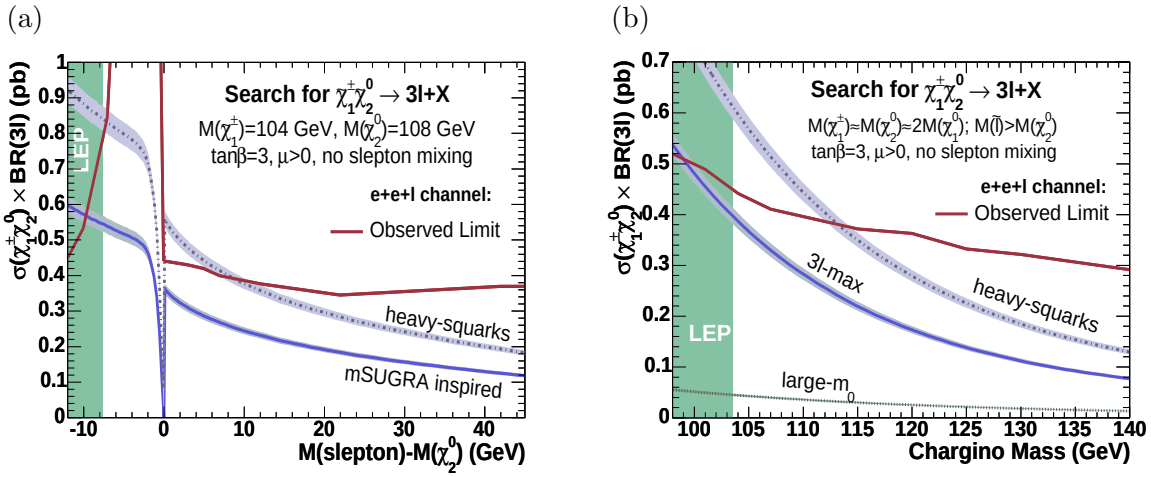

Figure 11.5: Upper limits on the trilepton cross section $\sigma(\chi_2^0\chi_1^\pm) \times \mathrm{BR}(3\ell)$ set by this analysis (continuous line) for constraint SUSY models with negligible slepton-mixing (a) as a function of the mass difference between the second neutralino and the slepton for $m_{\chi^\pm} = 104\,\mathrm{GeV}$ and (b) as a function of the chargino mass in the 3-body domain. The MSSM benchmark model lines that are plotted as a reference correspond to the 3l–max scenario, the heavy-squarks scenario and the large-m_0 scenario (see detailed explanation in the text). PDF-related errors on the cross section are shown as shaded bands. Chargino masses below 103.5 GeV and slepton masses < 100 GeV (with large mass differences to the LSP) are excluded by direct searches at LEP.

the heavy squark and the large-m_0 benchmark scenario. The cross section range between these benchmark lines corresponds to typical trilepton cross sections expected from GUT-constraint SUSY models. The stand-alone analysis is not yet sensitive to constraint SUSY models with sfermion universality beyond the LEP II limits but excludes scenarios with heavy squarks up to chargino masses of 112 GeV.

11.3.2 Interpretation of the results of the combined analysis

As has been demonstrated in Section 11.2.1, the sensitivity of the search for associated chargino neutralino production at DØ is considerably enhanced by a combination with the results of the other three electron/muon based analyses. The limit on the trilepton cross section decreases from 0.4 pb to 0.2 pb for typical SUSY masses near the LEP II mass limits. The improved cross section limits result in considerably enhanced excluded mass regions for the investigated SUSY models.

Figure 11.6 compares the predictions from the MSSM benchmark scenarios with the cross section limits derived by the combined analysis. The results of the slepton mass scan (see Fig. 11.3a) are interpreted in Fig. 11.6a. The observed upper limit for the 3-body region around 0.2 pb excludes a slepton mass range of $m_{\chi_2^0} < m_{\tilde{\ell}} < m_{\chi_2^0} + 20\,\mathrm{GeV}$ for models with unified sfermion masses. Slepton masses with $m_{\chi_2^0} < m_{\tilde{\ell}} < m_{\chi_2^0} + 40\,\mathrm{GeV}$ are excluded for models with heavy squarks for low chargino masses ($m_{\chi^\pm} = 104\,\mathrm{GeV}$).

The combination is also sensitive in the 2-body region and excludes slepton masses with $m_{\tilde{\ell}} < m_{\chi_2^0} - 6\,\mathrm{GeV}$. For heavy squarks, slepton masses with $m_{\tilde{\ell}} < m_{\chi_2^0} - 4\,\mathrm{GeV}$ are excluded. The slepton mass range covered by the combined analysis shrinks with increasing

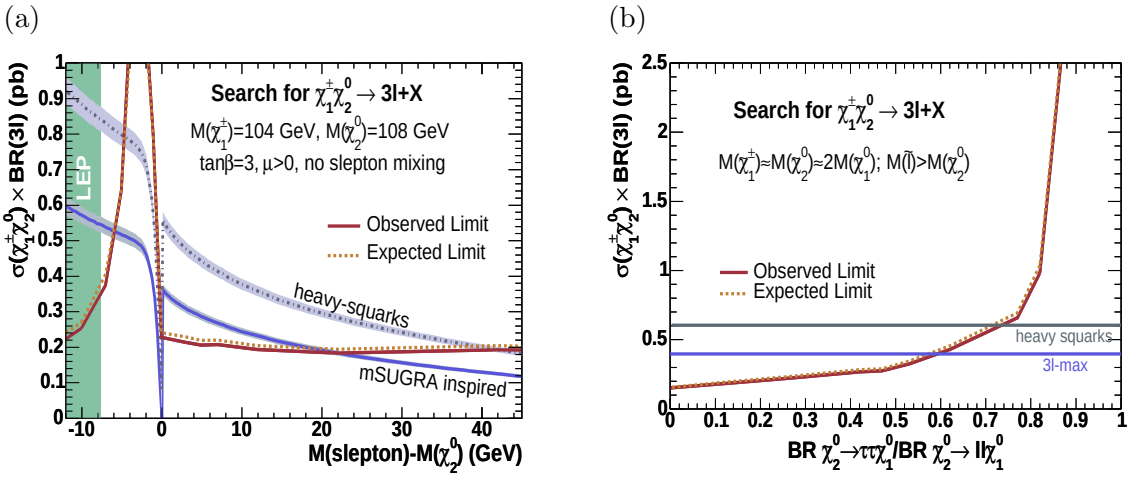

Figure 11.6: Observed (continuous line) and expected (dashed line) upper limits on the trilepton cross section $\sigma(\chi_2^0\chi_1^\pm) \times \mathrm{BR}(3\ell)$ set by the combined analysis for constraint SUSY models (a) without slepton mixing as a function of the mass difference between the second neutralino and the slepton and (b) for the 3-body domain as a function of the neutralino BR into τ-leptons for $m_{\chi^\pm} = 104\,\mathrm{GeV}$. The limits are compared with the predictions of two MSSM benchmark models, the mSUGRA-inspired and the heavy squarks model. Slepton masses < 100 GeV (with large mass differences to the LSP) are excluded by direct searches at LEP.

chargino and neutralino masses due to the decreasing cross section for associated production of charginos and neutralinos.

The cross section limits, derived in Fig 11.4 as a function of the branching ratio of the second neutralino into final states with τ-leptons are compared in Fig. 11.6b with the trilepton cross sections predicted by the 3l-max and the heavy-squarks benchmark scenario, assuming that the total leptonic branching ratio is not affected by the flavor composition of the final state. Chargino masses of 104 GeV are excluded in the 3l-max scenario up to a τ fraction of 59% within the leptonic neutralino decays. The larger cross section for heavy squarks, extends the exclusion power of the analysis up to a τ fraction of 73%.

Figure 11.7 compares the results of the chargino mass scan in the 3-body domain for the combined analysis (see Fig. 11.3b) with the model predictions for negligible $\tilde{\tau}$-mixing. This results in a lower limit on the chargino mass of

$$m_{\chi_1^\pm} > 117 \ \ \mathrm{GeV} \tag{11.1}$$

in the 3l-max scenario and

$$m_{\chi_1^\pm} > 132 \ \ \mathrm{GeV} \tag{11.2}$$

in the heavy-squarks scenario.

The combined analysis is sensitive to SUSY models with chargino and slepton masses beyond the limits from SUSY searches at LEP II and Tevatron Run I. The observed limit on the cross section results in the most stringent constraints on chargino and neutralino masses beyond the LEP II kinematic reach.

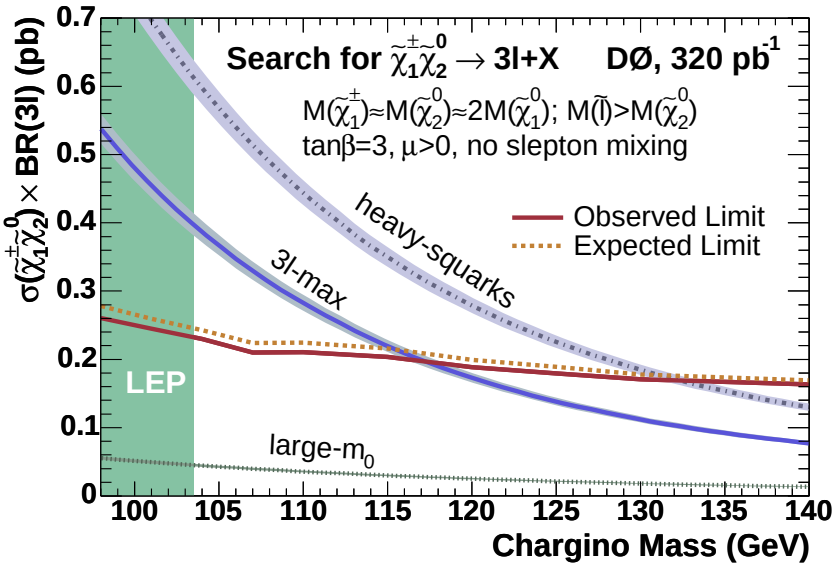

Figure 11.7: Observed (continuous line) and expected (dashed line) upper limits on the trilepton cross section $\sigma(\chi_2^0\chi_1^{\pm}) \times \mathrm{BR}(3\ell)$ set by the combined analysis for constraint SUSY models without slepton mixing as a function of the chargino mass in the 3-body domain. The limits are compared with the predictions of three MSSM benchmark models, the large-m_0 the 3l-max and the heavy squarks model. PDF-related errors on the cross section are shown as shaded bands. Chargino masses below 103.5 GeV are excluded by direct searches at LEP.

12 Outlook

Since the sensitivity of the DØ trilepton analyses is mainly limited by data statistics, the mass coverage of these analyses increases with the integrated luminosity in Run II. Improvements in understanding and simulating the detector are expected to increase the sensitivity of the SUSY searches further. The LHC experiments will continue the search beyond the Tevatron limits. In case SUSY is discovered at the Tevatron or at the LHC, the LHC expects to be able to measure the SUSY parameters and to determine which SUSY model is realized in nature.

12.1 Projections for SUSY searches in trilepton final states for Run II

By the end of Run II, Tevatron is expected to have delivered an integrated luminosity of 8 fb^{-1} per experiment. Studies have been performed within this thesis to estimate the exclusion and the discovery potential of the SUSY trilepton analyses with increasing luminosity of the Run II data set. The expected progress in the reconstruction and in the simulation of the detector has been taken into account as well as the inclusion of additional decay channels.

12.1.1 Trilepton final states with electrons and muons

The data set used for the analysis in this thesis corresponds to roughly 5% of the integrated luminosity expected per experiment for Tevatron Run II. Since the cross section for the production of charginos and neutralinos decreases with increasing masses, the mass reach of the analysis is mainly limited by the data statistics. This dependence is investigated in case of the no-mixing SUSY benchmark scenario with large slepton masses (see Section 11). Signal efficiencies and expected backgrounds of the four trilepton analyses are extrapolated towards higher integrated luminosities and the sensitivity for associated chargino-neutralino production with leptonic decays is recalculated.

The integrated luminosity can be doubled by a combination with the results of similar searches in CDF which are currently under development [117]. For the following studies, it is assumed that the CDF analyses reach the same sensitivity as the DØ analyses.

Figure 12.1a shows the upper limits on the total cross section for associated chargino-neutralino production with leptonic decays expected for different values of the total integrated luminosity per experiment in absence of a SUSY signal. The expected limit decreases with increasing chargino mass due to the increasing signal efficiency. For integrated luminosities of 1, 2 and 4 fb^{-1} per experiment chargino masses larger than 155, 170

(a) (b)

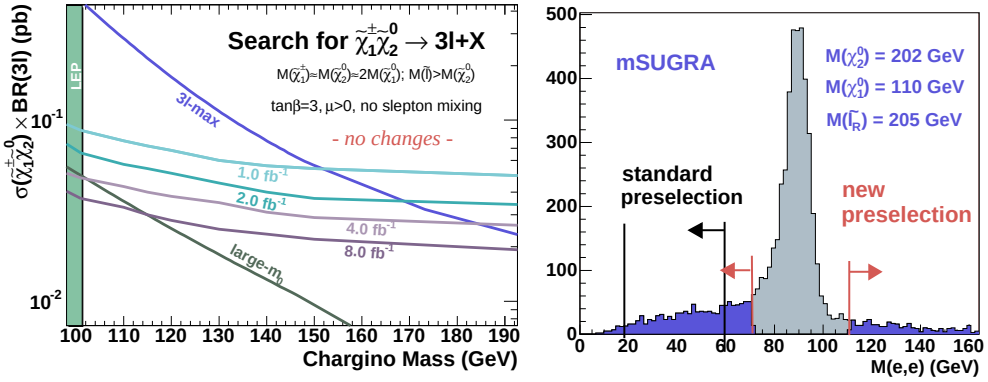

Figure 12.1: (a) Expected upper limits on the total cross section for associated chargino and neutralino production with leptonic final states in the absence of SUSY for various integrated luminosities per experiment as a function of the chargino mass in the 3-body domain within the no-mixing benchmark scenario. For further details see Fig. 11.7. (b) Invariant mass of the leading reconstructed electrons from associated chargino-neutralino production for a mSUGRA model where the second lightest neutralino decays predominantly into real Z-bosons ($m_{1/2} = 172\,\text{GeV}$, $m_0 = 286\,\text{GeV}$, $A_0 = 0$, $\tan\beta = 3$ and $\mu > 0$) and the position of the preselection cuts in the standard and in the optimized selection.

and 185 GeV are expected to be excluded in the SUSY scenario with enhanced leptonic branching ratio due to sfermion mediated 3-body decays (*3l-max* scenario, see Section 11). The *large-m0* scenario with large sfermion masses and gauge-boson mediated gaugino decays which would result in a low leptonic branching ratio is accessible beyond the LEP II limits for an integrated luminosity of 4 fb^{-1} per experiment. With the design luminosity of 8 fb^{-1} per experiment, SUSY models with large slepton masses can be probed for chargino masses up to 115 GeV.

Figure 12.1a shows extrapolations up to chargino masses of 200 GeV. For larger chargino masses, the final state changes considerably. As soon as the mass difference between the second neutralino and the LSP becomes larger than the Z mass, the second lightest neutralino decays dominantly into a real Z boson. This leads to a large fraction of events where the invariant mass of the leading two reconstructed electrons corresponds to the Z-mass such that they are rejected by the the Anti-Z cuts of the analysis in this thesis.

A first feasibility study shows, that the efficiency can be partly recovered for these points by a modified selection, where the upper cut on the di-electron mass is replaced by a small mass window around the Z-mass. The additional $Z \to ee$ background is suppressed by tighter requirements on $\not\!\!E_T$ and the momentum of the third track.

- $M(e,e) < 60\,\text{GeV} \longrightarrow 71\,\text{GeV} < \text{M(e,e)} < 91\,\text{GeV}$
- $\not\!\!E_T > 22\,\text{GeV} \longrightarrow \not\!\!E_T > 25\,\text{GeV}$
- $p_T(track) > 4\,\text{GeV} \longrightarrow p_T(track) > 6\,\text{GeV}$

(a) (b)

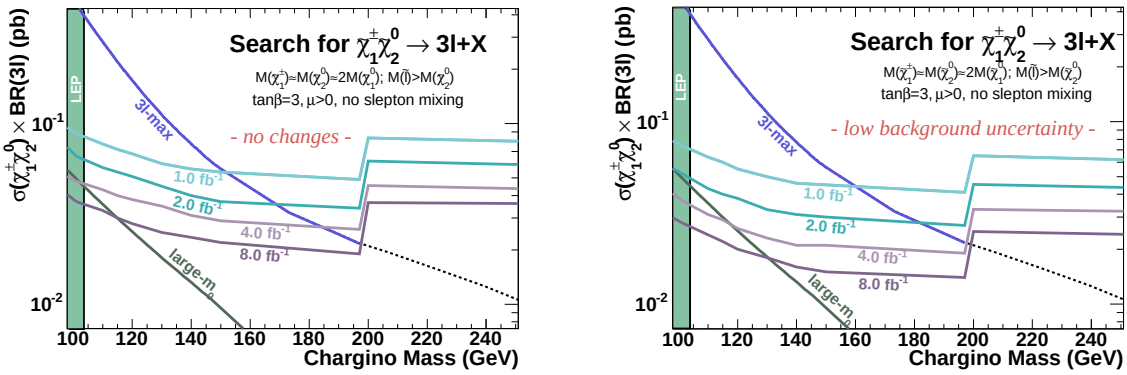

Figure 12.2: Expected upper limits on the total cross section for associated chargino and neutralino production with leptonic final states in the absence of SUSY for various integrated luminosities per experiment (a) in case no improvement of the analysis is achieved, (b) in case the errors of the background simulation are reduced. For further explanations see Fig. 11.7.

Figure 12.1b shows the invariant mass of the leading reconstructed electrons from associated chargino-neutralino production for a mSUGRA model point where the second lightest neutralino decays dominantly into a real Z-boson and the position of the preselection boundaries in the standard selection and in the modified selection. The efficiency of the modified analysis for leptonic final states is 1.5% for this model point, which corresponds to roughly 40% of the efficiency of the standard analysis for comparable scenarios with 3-body decays of the neutralino.

In the following, the sensitivity extrapolations for scenarios with dominant $\chi_2^0 \to \mathrm{Z} + \chi_1^0$ decays are performed using the signal efficiencies of the modified selection for the $\mathrm{e}+\mathrm{e}+\ell$ final state of this thesis. For simplicity, the same efficiency is assumed for the similar $\mu + \mu + \ell$ final state. The efficiencies of the two remaining analyses which rely on one lepton from the neutralino decay and one lepton from the chargino decay is assumed not to be affected by the invariant mass distribution of the two leptons from the neutralino decay. Figure 12.2a shows the expected upper limits on the total cross section depending on the chargino mass using the above assumptions for the extended gaugino mass range. The expected limit decreases with the chargino mass up to $m_{\chi^\pm} \approx 200\,\mathrm{GeV}$, where the neutralino starts to decay into a real Z boson and the expected upper limit jumps back to values derived for low chargino masses. Chargino masses up to 200 GeV are expected to be excluded with an integrated luminosity of 8 fb^{-1} per experiment.

The decays into real gauge bosons affect not only the sensitivity for leptonic final states but also the leptonic branching ratio of the charginos and neutralinos. If the second neutralino decays into a real Z boson and the nearly mass degenerated chargino decays into a real W boson, the leptonic branching ratio of the gauginos corresponds to the leptonic branching ratio of the Z boson and the W boson, which leads to a trilepton fraction of approximately 3%. As a consequence total cross sections in the range of the the *large-m_0* scenario are expected independent of the slepton mass, as long as the sleptons are heavier than the gauginos. Large leptonic branching ratios are possible, though, for slepton masses

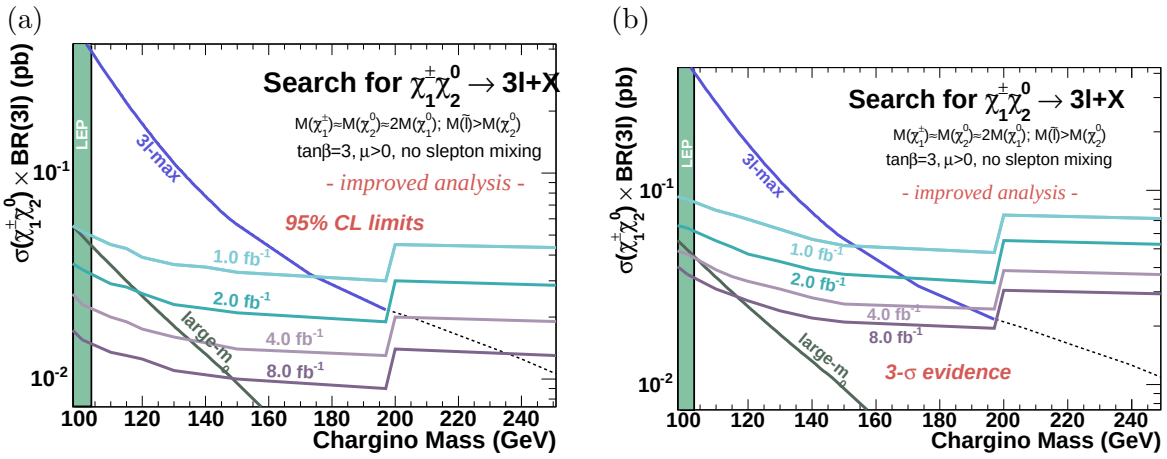

Figure 12.3: (a) Expected upper limits on the total cross section for associated chargino and neutralino production with leptonic final states in absence of SUSY for various integrated luminosities per experiment in case the background is reduced by a factor of two without net signal efficiency loss, and assuming the same efficiency and background for topology-related analyses. (b) Cross section with a probability of 50% for a 3-σ evidence for SUSY using the same assumptions as in (a). For further explanations see Fig. 11.7.

lower than the gaugino masses or neutralino and chargino field contents that disfavor the coupling to gauge bosons. The *3l-max* model line is therefore extrapolated as a reference line (dashed mode) beyond gaugino masses of 200 GeV.

The sensitivity of the analyses is, in addition, limited by insufficient understanding of various detector effects which decrease the ratio of signal and background efficiencies for the lepton identification and the topological cuts. Several ongoing studies [110], aiming at improving the understanding of the detector response and the readout, are expected to improve the performance of the analysis in the future.

A further source of sensitivity loss is the large uncertainty on the simulation of the background due to low MC statistics, problems in the detector simulation and insufficient modeling of higher order effects. With improved detector simulation, increasing computing resources and new MC generators being tested at the moment, the precision of the MC simulations is expected to increase.

The calculation of the expected sensitivity of the trilepton analyses, as presented in Fig. 12.2a, is therefore updated for the following two stages of assumptions:

- It is assumed, that the total error on the background prediction decreases from 25 % to 10 %.

- Since half of the expected background is due to misidentified leptons and mismeasured $\not{E}_T$, it is expected that (in addition to a reduced error) the background is reduced by a factor of two, with no net change in signal efficiency. In addition, the $\mu + \mu + \ell$ analysis and the $e + e + \ell$ analysis are assumed to have the same level of efficiency and background which are extrapolated from the $e + e + \ell$ analysis.

The first assumption leads to updated expected limits on the cross section which are shown in Fig. 12.2b. The combined trilepton analysis is expected to be sensitive for low-mixing models in the whole m_0 range up to chargino masses of 130 GeV.

The expected limits calculated with the more extensive set of assumptions are presented in Fig. 12.3a. The combined analysis is expected to be sensitive up to chargino masses of 150 GeV for any slepton mass.

The same set of assumptions has been used to calculate the discovery potential of the combined analysis for Run II. The *3-σ evidence* line with Poisson distributed background is defined for this study as the signal cross section for which $\mathrm{CL_B} < 0.0027$ (see Section 2.2.1), which corresponds to the probability for a 3-sigma deviation in a Gaussian distribution. The resulting 3-σ evidence ranges are shown in Fig. 12.3b. If SUSY is realized for chargino masses lower than 117 GeV, evidence for SUSY could be derived by the Tevatron even for large slepton masses. In case of lighter sleptons, evidence for SUSY is possible up to chargino masses of 200 GeV.

Additional SUSY scenarios with large leptonic branching ratios due to two-body decays of the gauginos into lighter sleptons (see Fig. 11.6) are not exploited in this study. For large enough mass differences between sleptons and gauginos, exclusion and discovery domains comparable or larger than in the *3l-max* scenario are expected.

12.1.2 Trilepton final states with τ-leptons

In parameter domains with large degree of stau mixing and comparably low slepton masses, the lightest chargino and the second-lightest neutralino decay dominantly into final states with τ-leptons (see Section 5.1.2). In this case, the selections that are based on final states with electrons and muons have a low efficiency. These domains are accessible to analyses which search for final states with τ-leptons, provided the events are triggered with a sufficient efficiency and the reconstruction and identification algorithms can separate τ-leptons with low p_{T} from the background. The efficiency of the identification at the trigger level and in the offline reconstruction stage for low-p_{T} τ-leptons is currently not sufficient to allow for a coverage of large-mixing domains. Both stages of the data processing are still under development and improvements are expected. For the time being, the selection of final states with τ-leptons can improve the sensitivity of the electron/muon based analyses for moderate stau-mixing [78, 79].

12.1.3 Search for Higgs bosons

Additional SUSY coverage is provided by the search for a Standard Model (SM) Higgs boson, reinterpreted as the search for a neutral Higgs boson in the MSSM (see Section 1.2.6). Figure 12.4 shows the DØ-CDF combined Higgs exclusion and discovery potential at Tevatron Run II [118]. The Tevatron expects to be able to provide evidence for a SM-like Higgs boson with a mass up to 130 GeV at 3 σ level.

SUSY models predict five Higgs bosons (see Section 1.2.3), two charged and three neutral ones, the lightest of which is expected to be not heavier than 140 GeV. In large domains of the parameter space, the final states expected from the production and decay of the light

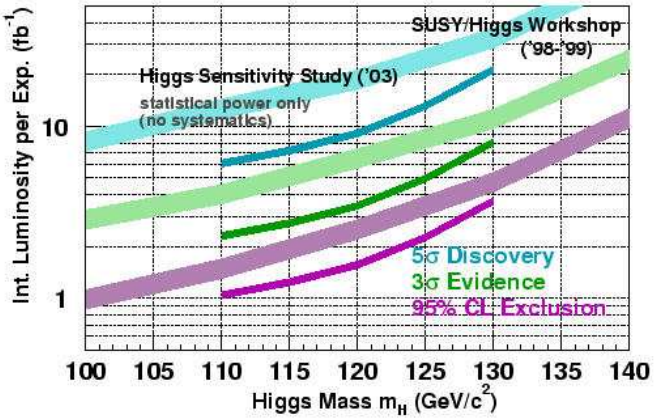

Figure 12.4: Discovery and exclusion potential for SM-like Higgs bosons at Tevatron Run II (from Ref. [118]).

neutral Higgs bosons are similar to those expected from a Standard Model Higgs boson. The predicted production rate can be suppressed or enhanced compared to the Standard Model case, depending on the value of $\tan\beta$. As a consequence, the results of searches for Higgs bosons can be translated into allowed domains for $\tan\beta$ as a function of the Higgs boson mass, which is usually parameterized by $M_{\mathrm{A}}$and $\tan\beta$.

Channels, where the production or decay rate in the MSSM can be considerably enhanced compared to the Standard Model case, are of particular interest. Figure 12.5a shows the expected exclusion potential of a DØ-CDF combined search for the associated production of a Higgs boson with two b-quarks in final states with four b-jets in the $\tan\beta$-M_{A} plane for various integrated luminosities per experiment [119]. The exclusion and the discovery potential for a CDF-DØ combined search for a light Higgs boson in final states with two τ-leptons [119] in the $\tan\beta$-M_{A} plane are shown in Figure 12.5b and c. The searches are expected to be sensitive for large $\tan\beta$ ranges down to $\tan\beta \approx 20$.

12.2 SUSY prospects at the LHC

Even with the full data set expected for Run II, the Tevatron experiments will only be sensitive to a limited SUSY mass range. The two LHC experiments ATLAS and CMS will be able to continue the search for SUSY beyond the Tevatron reach [120].

12.2.1 SUSY discovery potential

At the large center-of-mass energies of the LHC, the direct squark/gluino production is the dominant production channel for SUSY [121]. Subsequent cascade decays (see Figure 12.6a) of the primary SUSY particles lead to a variety of signatures with combinations of leptons, jets and $\not{E}_{\mathrm{T}}$. The direct production of chargino pairs and the associated chargino-neutralino production yield, in addition, final states with two or three leptons,

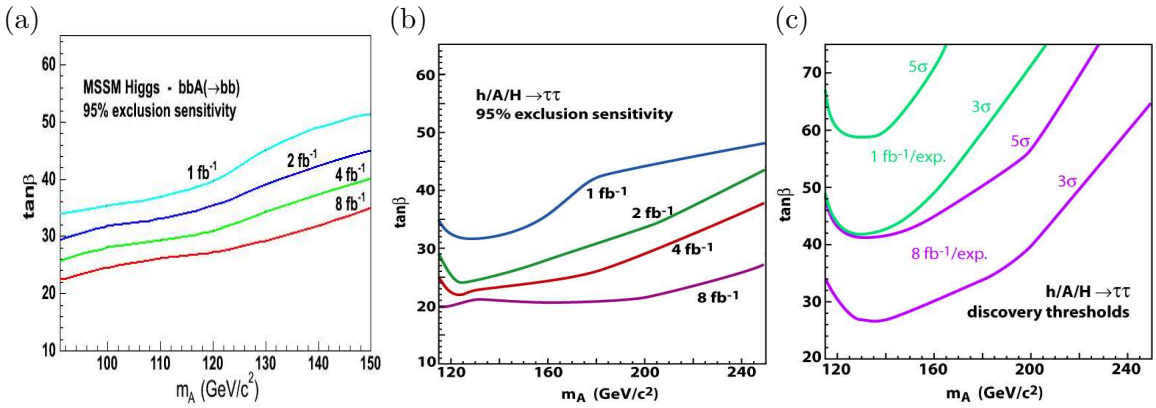

Figure 12.5: (a) Exclusion potential for a combined DØ-CDF search for the associated production of a Higgs boson with two b-quarks in final states with 4 b-jets and (b) exclusion potential and (c) discovery potential for a search of the Higgs boson in $\tau\tau$ final states in the $\tan\beta$-M_{A} plane for different luminosities per experiment at Tevatron Run II (from Ref. [119]).

large $\not\!\!E_{\mathrm{T}}$ and no jets. One of the quantities which can be used not only to discriminate between SUSY and background but also to estimate the mass scale of the SUSY particles is the *effective mass*, the scalar sum of the visible transverse energies of the final state particles and the $\not\!\!E_{\mathrm{T}}$. Figure 12.6b shows the distribution of this quantity for a selected SUSY point with masses at the TeV scale for background, modeled with NLO matrix elements, and the SUSY signal. The SUSY signal would be observed over the Standard Model background for large values of the effective mass. Studies of the discovery reach have been performed in both LHC experiments using mSUGRA as a reference model. Figure 12.7a shows the ATLAS discovery reach [122] for an integrated luminosity of 10 fb^{-1} for various SUSY signatures in the m_0-$m_{1/2}$ plane for $A_0 = 0$ and moderate values of $\tan\beta$. The covered domain corresponds to squark/gluino masses of up to ≈2 TeV. Similar studies have been performed by the CMS collaboration. Figure 12.7b shows the inclusive CMS discovery potential [124] in the m_0-$m_{1/2}$ plane for large $\tan\beta$ for various integrated luminosities. The domain preferred by cosmological results and electroweak precision measurements (see Section 1.2.6) is expected to be covered within a few weeks of data taking at low luminosity with a commissioned detector and the 1.5-2 TeV mass range for squarks and gluinos is expected to be accessible within one year of running at low luminosity. The final reach with the design luminosity of 300 fb^{-1} would allow for SUSY mass ranges up to 2.5 TeV to be excluded or discovered.

12.2.2 Determination of the SUSY-breaking parameters

In case evidence for SUSY is observed, the next task will be to measure masses, couplings and spins in order to check the compatibility with SUSY models and to determine the exact mechanism of SUSY breaking. Since in RPC SUSY models the decay products always contain invisible LSPs, masses cannot be measured directly but have to be extracted from measurements of mass differences, using endpoints of the distribution of the visible mass. An example is shown in Fig 12.8 for a mSUGRA point where the second lightest neutralino decays via a 2-body intermediate state into two opposite sign electrons or muons and

(a) (b)

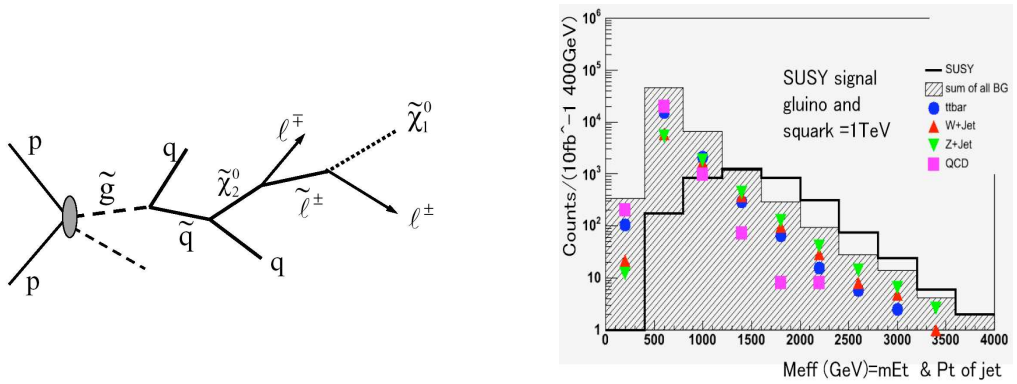

Figure 12.6: (a) Gluino production and decay at the LHC and (b) scalar sum of the visible transverse energy of the final state particles and the $\not\!\!E_T$ (*effective mass*) for background processes (histogram) and a mSUGRA point with $m_0 = 100$ GeV, $m_{1/2} = 300$ GeV, $A_0 = 300$, $\tan\beta = 2$ and $\mu > 0$ (empty histogram). The background includes $t\bar{t}$ (circles), W+jets (triangles), Z+jets (downward triangles) and QCD jets (squares) (from Ref. [122, 123]).

the LSP. Figure 12.8a shows the di-lepton mass distribution with Standard Model and SUSY background. The background with two independent decays into leptons can be estimated using events with a combination of an electron and a muon. The di-lepton mass distribution after subtracting this background (*flavor subtraction*) is shown in Fig. 12.8b. The position of the sharp upper edge of the mass distribution which can be determined with high precision is a function of the mass of the second lightest neutralino, the slepton and the LSP [122]. Typical precisions, expected for the measurement of gaugino and slepton masses are at the order of 5 GeV [125].

12.2.3 Search for Higgs bosons

As in the case of the Tevatron, Higgs searches yield additional sensitivity for SUSY [118, 126]. Figure 12.9 shows the luminosity per experiment which is needed for a 5σ discovery of a SM-like Higgs boson in an ATLAS-CMS combination. Different analyses contribute in different mass ranges. A Higgs discovery in the mass range beyond the LEP II lower limit and within the region preferred by electroweak precision measurements is expected after 1-2 years of running at low-luminosities (10-20 fb^{-1}). A SM-like Higgs boson heavier than two W or Z bosons is expected to be discovered with less than one year of data taking (see Section 1.2.3).

The prospects for the Higgs boson search can be translated into the parameter space of the MSSM Higgs sector. Figure 12.10a shows the combined ATLAS-CMS discovery potential in the $\tan\beta$-M_A plane. With an integrated luminosity of 30 fb^{-1}, corresponding to 3 years of data taking at low luminosity, the whole $\tan\beta$ domain which is allowed by LEP II measurements is expected to be covered.

The discovery of a Higgs boson could correspond to the Standard Model Higgs boson or to one of the neutral MSSM Higgs bosons. The observation of more than one type of Higgs

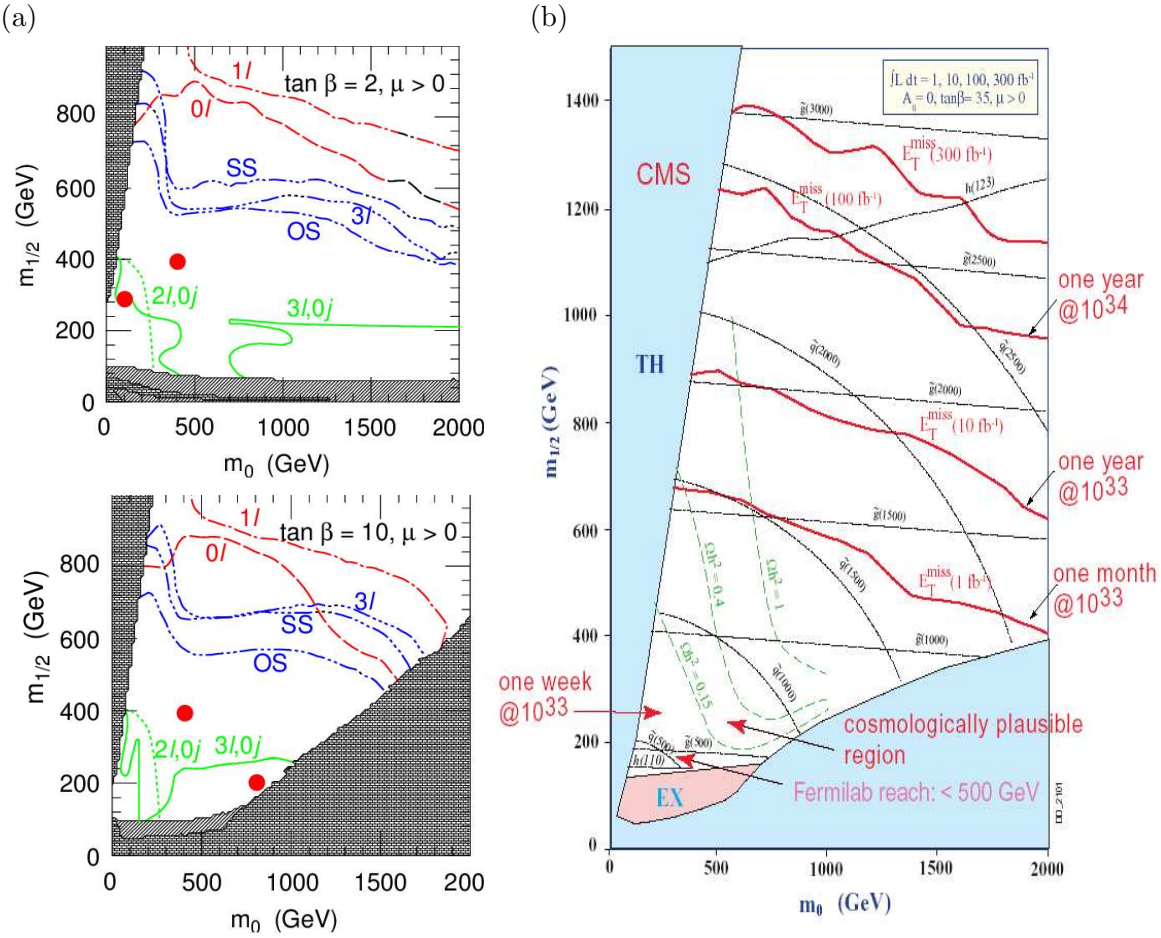

Figure 12.7: (a) ATLAS 5-σ discovery reach ($S/\sqrt{B} > 5$) with an integrated luminosity of 10 fb^{-1} (corresponding to one year of low luminosity) for various SUSY signatures in the m_0-$m_{1/2}$ plane for $A_0 = 0$ and for $\tan\beta$=2 (top) and $\tan\beta$=10 (down). SS: same-sign dileptons; OS: opposite-sign dileptons; 3l: trileptons; 0l: jets, $\not\!\!E_T$ and no leptons; 1l: jets, $\not\!\!E_T$ and 1 lepton; 3l,0j: trileptons with jet veto; 2l,0j: dileptons with jet veto. The dark shaded regions are excluded theoretically. The light shaded regions correspond to the indirect exclusion from the LEP II Higgs limits with the 1998 data set (from Ref. [122]). (b) Inclusive CMS 5σ discovery reach for mSUGRA scenarios for $A_0 = 0$, $\mu > 0$ and $\tan\beta = 35$ in the m_0- $m_{1/2}$ plane for various integrated luminosities. The continuous lines are isomass contours for squarks and gluinos. The dashed lines correspond to certain values of the dark matter density Ωh^2 (see Section1.2.6). Filled regions are excluded either theoretically or experimentally (from Ref. [124]).

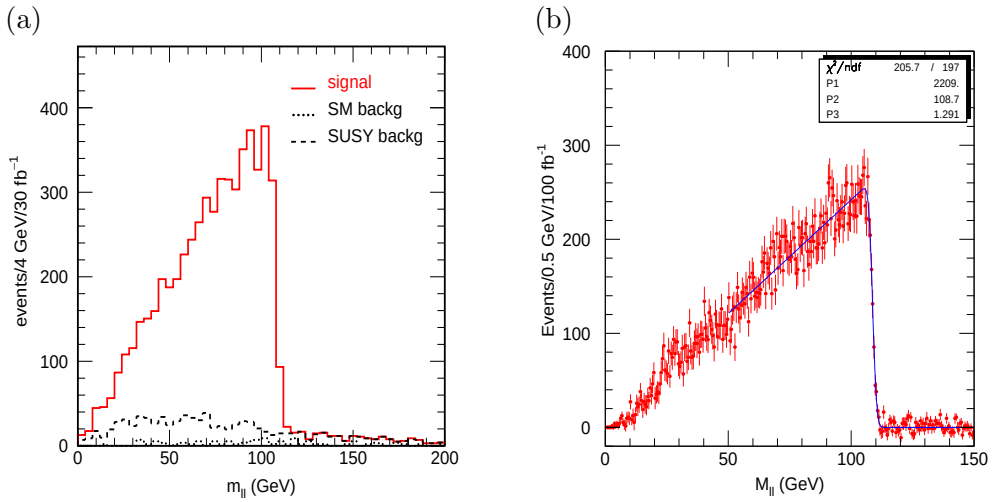

Figure 12.8: (a) dilepton mass distribution with Standard Model and SUSY background and (b) the minimum χ^2 fit of the flavor subtracted dilepton mass distribution for a mSUGRA point with a 2-body decay of the second lightest neutralino: $m_0 = 100$ GeV, $m_{1/2} = 300$ GeV, $A_0 = 300$, $\tan\beta = 2$ and $\mu > 0$ (from Ref. [122]).

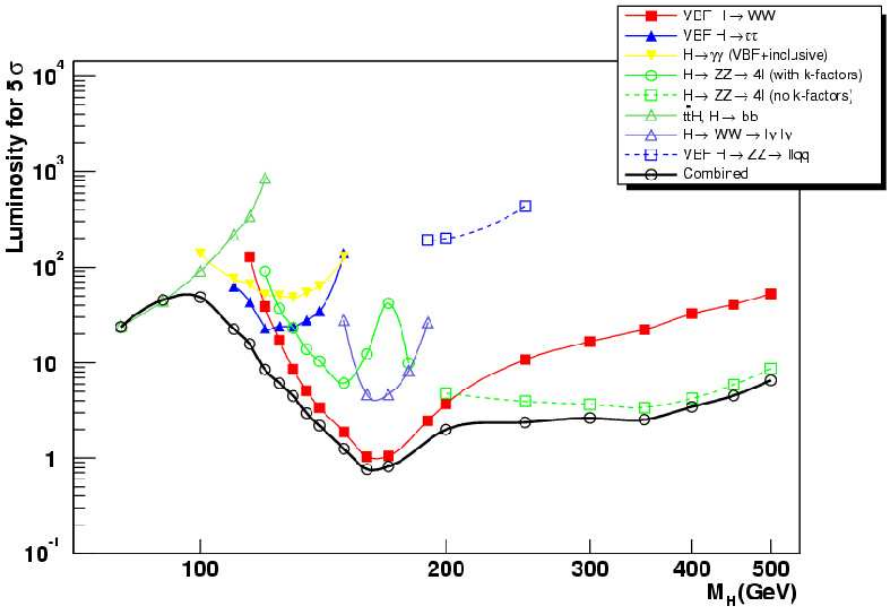

Figure 12.9: Combined ATLAS and CMS 5σ discovery potential for a Standard Model Higgs boson (from Ref. [118]).

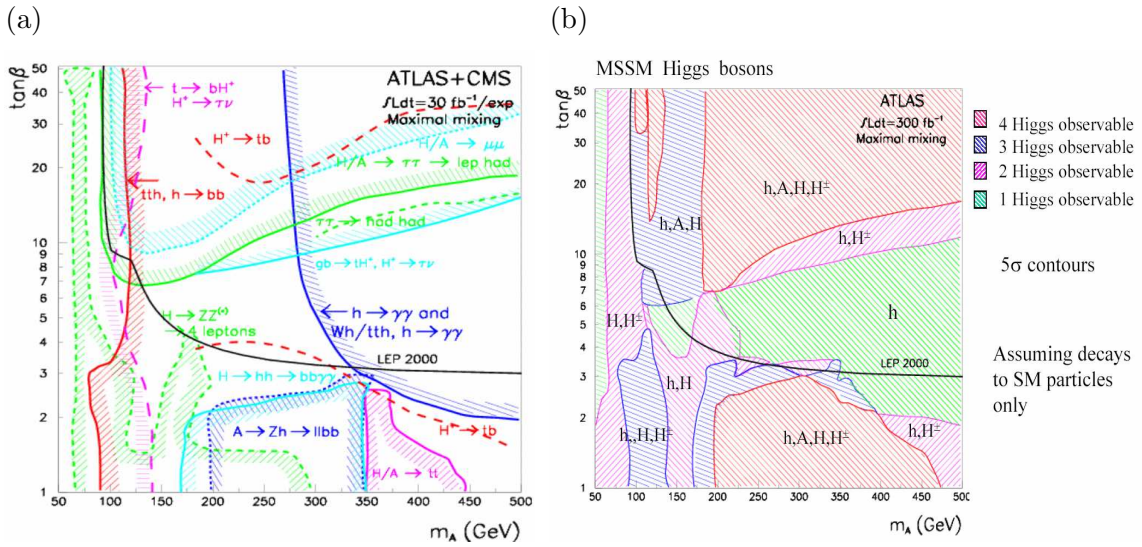

Figure 12.10: (a) 5σ discovery range for a MSSM Higgs boson in the $\tan\beta$-M_{A} plane for an integrated luminosity of 30 fb^{-1} and (b) the number of Higgs bosons that can be discovered with an integrated luminosity of 300 fb^{-1} in the ATLAS experiment (from Ref. [118, 126]).

bosons would, in addition to an excess of data in SUSY-like leptons+jets+$\not\!\!E_{\mathrm{T}}$ final states, strongly support the SUSY hypothesis. Figure 12.10b shows the number of Higgs bosons that could be discovered at ATLAS with the design luminosity of 300 fb^{-1}, corresponding to 3 years of high-luminosity data taking. In large domains of the $\tan\beta$-M_{A} space, in particular for sufficiently large values of $\tan\beta$, several Higgs bosons could be observed at the LHC.

Considering the results of all studies presented in this chapter, Tevatron has a chance to find evidence for SUSY in certain parameter regions or restrict the parameter space considerably. LCH has the capability to discover or exclude SUSY in mass ranges up to 2.5 TeV and to perform a first coarse measurement of the model parameters.

In case SUSY is realized in nature, a precise measurement of the SUSY parameters is expected from a future e^+e^- linear collider [125]. Depending on the parameter region, LHC and ILC will provide complementary information for SUSY parameter determination.

Summary

Supersymmetric (SUSY) particles with masses beyond the kinematic reach of the LEP II experiments may be produced at the Tevatron $p\bar{p}$ collider at Fermilab at a center-of-mass energy of 1.96 TeV. A promising source of SUSY particles at the Tevatron is expected to be the associated production of the lightest chargino $\chi_1^\pm$ and the second-lightest neutralino χ_2^0. Leptonic decay modes, $\chi_2^0 \to \chi_1^0 \ell\ell$ and $\chi_1^\pm \to \chi_1^0 \ell\nu$, lead to detector signatures with three leptons and large missing transverse momentum.

A search for this process has been performed in final states with two electrons and a third lepton in a dataset corresponding to an integrated luminosity of 320 pb^{-1}, collected with the DØ detector at the Tevatron from April 2002 to July 2004. No evidence for SUSY has been found and limits on the product of the cross section and the leptonic branching ratio, $\sigma(\chi_2^0\chi_1^\pm) \times \text{BR}(3\ell)$, have been set as a function of the mass of the lightest slepton, for different assumptions on the stau mixing and as a function of the chargino mass. For SUSY models with heavy, mass degenerated sleptons and chargino masses up to 200 GeV, values of $\sigma(\chi_2^0\chi_1^\pm) \times \text{BR}(3\ell) > 0.4$ pb are excluded.

These results have been combined with the results of three other analyses which have searched for the associated production of a chargino and a neutralino in final states with at least one muon. The combination results in improved upper limits on the product of the cross section and the branching ratio, $\sigma(\chi_2^0\chi_1^\pm) \times \text{BR}(3\ell) < 0.2$ pb.

The results have been interpreted within the framework of selected SUSY benchmark models in order to derive constraints on the sparticle masses. Of particular interest are models with comparable branching fractions for all lepton flavors due to a low degree of stau-mixing or due to very large slepton masses. For mSUGRA-inspired models with heavy sleptons and large leptonic branching ratios of charginos and neutralinos, a chargino lower mass limit of 117 GeV is derived at 95% confidence level. Chargino masses up to 132 GeV are excluded in related models with heavy squarks. These results constrain the SUSY parameter space beyond the existing limits.

Studies have been performed to estimate the sensitivity of the two Tevatron experiments for associated production of a chargino and a neutralino with the expected final Run II data set. Sensitivity for models with chargino masses up to ≈200 GeV is expected with a data set corresponding to an integrated luminosity of 8 fb^{-1} per experiment. The search for supersymmetric particles will be continued at the Large Hadron Collider (LHC) which is presently being constructed at CERN. The LHC experiments are expected to probe models with SUSY masses up to a mass range of 3 TeV and to answer the question of the existence of low-mass supersymmetry.

List of Tables

List of Figures

Bibliography

[1] A. Salam, in *Elementary Particle Theory*, (N. Svartholm, Hrsg.), Almquist and Wiksell, Stockholm (1968) 367-377;
S. L. Glashow, Nucl. Phys. **22** (1961) 579-588;
S. Weinberg, Phys. Rev. Lett. **19** (1967) 1264-1266;
P. W. Higgs, Phys. Rev. Lett. **13** (1964) 508-509;
D. J. Gross and F. Wilczek, Phys. Rev. **D 8** (1973) 3633;
H. D. Politzer, Phys. Rep. **14** (1974) 129.

[2] G. Altarelli, R. Barbieri and F. Caravaglios, *Electroweak Precision Tests: A Concise Review*, Int. J. Mod. Phys. **A 13** (1998) 1031-1058.

[3] Takaaki Kajita *et al.,* [Super-Kamiokande Collaboration and Kamiokande Collaborations] *Athmospheric Neutrino Results from Super-Kamiokande and Kamiokande: Evidence for Neutrino (μ) Oscillations*, Nucl. Phys. Proc. Suppl. **77** (1999) 123-132.

[4] P. Langacker, *Neutrino Physics (Theory)*, Invited talk at 32nd International Conference on High-Energy Physics (ICHEP 04), 2004.

[5] ALEPH, DELPHI, L3 and OPAL Collaborations, *Search for the Standard Model Higgs Boson at LEP*, Phys. Lett. **B 565** (2003) 61-75.

[6] LEP Electroweak Working Group (LEP EWWG),
`http://lepewwg.web.cern.ch/LEPEWWG/` (2005).

[7] C. Diaconu, *Electroweak measurements*, plenary talk at the Lepton-Photon conference, 2005, `http://lp2005.tsl.uu.se/` $\sim$ `lp2005/LP2005/programme/presentationer/morning/diaconu.pdf` .

[8] S. Eidelmann *et al.,* [Particle Data Group] Phys. Lett. **B 592**,283-288 (2004).

[9] R. N. Mohapatra, *Unification and Supersymmetry*,
Springer Verlag, New York, Berlin, Heidelberg (2003).

[10] W. de Boer and C. Sander *Global Electroweak Fits and Gauge Coupling Unification*, Phys. Lett. **B 585** (2004) 276-286.

[11] D. N. Spergel *et al., First Year Wilkinson Anisotropy Probe (WMAP) Observations: Determination of Cosmological Parameters*, Astrophys. J. Suppl. **148** (2003) 175.

[12] C. Froggatt *et al., Cosmological constant in SUGRA models and the multiple point principle*, Phys. Atom. Nucl. **67** (2004) 582-589.

[13] S. P. Martin, *A Supersymmetry Primer*, [arXiv:hep-ph/9709356] (1997).

[14] M. Drees, *An Introduction to Supersymmetrie*,
APCTP-5 KEK-TH-501, [arXiv:hep-ph/9611409] (1996).

[15] Y. A. Golfand and E. P. Likhtman, JETP Lett. **13** (1971) 452;
D. Volkov and V. P. Akulow, JETP Lett. **16** (1972) 438;
H. P. Nilles, Phys. Rep. **110** (1984) 1;
H. E. Haber and G.L. Kane, Phys. Rep. **117** (1985) 75;
J. Wess, B. Zumino, Phys. Lett. **B 49** (1974) 52.

[16] M. B. Green, J. H. Schwarz and E. Witten, *Superstring Theory*,
Cambridge Univerity Press, Cambridge (1987).

[17] C. Schwanenberger, *A review of searches for R-parity-violating SUSY*,
Eur. Phys. J. **C 33** (2004) 752-754.

[18] M. Carena *et al., Suggestions for Benchmark Scenarios for MSSM Higgs Boson Searches at Hadron Colliders*, Eur. Phys. J. **C 26** (2003) 601-607.

[19] A. Djouadi, J.-L. Kneur and G. Moultaka *SuSpect, a Fortran Code for the Supersymmetric and Higgs Particle Spectrum in the MSSM*, [arXiv:hep-ph/0211331] (2002).

[20] G. Bertone *et al., Particle Dark Matter: Evidence, Candidates and Constraints*, FERMILAB-Pub-04/017-A, [arXi:hep-ph/0404175] (2004).

[21] S. Abel *et al., Report of the SUGRA working group for Run II of the Tevatron*, [arXiv:hep-ph/0003154] (2000).

[22] E. Cremmer *et al.,* Phys. Lett **B 116** (1982) 231;
A. H. Chamseddine, R. Arnowitt and P. Nath, Phys. Rev. Lett. **29** (1082) 970;
J. Bagger and E. Witten, Phys. Lett. **B 118** (1982) 103.

[23] P. Horava and E. Witten, Nucl. Phys. **B 460** (1996) 506.

[24] LEPSUSYWG, ALEPH, DELPHI, L3 and OPAL experiments,
`http://lepsusy.web.cern.ch/lepsusy /Welcome.html` (2004).

[25] B. Abbott *et al.,* Phys. Rev. Lett. **80** (1998) 8.

[26] F. Abe *et al., Search for Chargino-Neutralino Associated Production at the Fermilab Tevatron Collider*, Phys. Rev. Lett. **80** (1998) 5275.

[27] LEPSUSYWG, ALEPH, DELPHI, L3 and OPAL experiments,
note LEPSUSYWG/04-01.1, `http : //lepsusy.web.cern.ch/lepsusy/Welcome.html` (2004).

[28] A. Heister *et al.* [ALEPH Collaboration], *Absolute Lower Limits on the Masses of Selectrons and Sneutrinos in the MSSM*, Phys. Lett., **B 544** (2002) 73-88.

[29] LEPSUSYWG, ALEPH, DELPHI, L3 and OPAL experiments,
note LEPSUSYWG/01-03.1, `http : //lepsusy.web.cern.ch/lepsusy/Welcome.html` (2001).

[30] ALEPH, DELPHI, L3 and OPAL Collaborations, *Search for Neutral MSSM Higgs Boson at LEP* , LHWG-Note 2004-01, contributed to the 2004 summer conferences.

[31] LEPSUSYWG, ALEPH, DELPHI, L3 and OPAL experiments, note LEPSUSYWG/02-06.1, `http://lepsusy.web.cern.ch/lepsusy/Welcome.html` (2002).

[32] LEPSUSYWG, ALEPH, DELPHI, L3 and OPAL experiments, note LEPSUSYWG/04-07.1, `http://lepsusy.web.cern.ch/lepsusy/Welcome.html` (2004).

[33] A. Heister *et al.* [ALEPH Collaboration], *Absolute mass lower limit for the lightest neutralino of the MSSM from e+e- data at sqrt(s) up to 209 GeV* ", Phys. Lett. **B 583** (2004) 247.

[34] K. Ackerstaff *et al.* [OPAL collaboration] *Search for chargino and neutralino production in* e^+e^- *collisions at* $\sqrt{s}$ *= 161 GeV*, Phys. Lett. **B 389** (1996) 616-630.

[35] S. Heynemeyer, D. Stoeckinger and G. Weiglein, *Electroweak and supersymmetric two-loop corrctions to* $(g-2)_\mu$, Nucl. Phys. **B 699** (2004) 103-123.

[36] P. Cushman, *Muon g-2 contraints to SUSY dark matter over the next decade*, [arXi:hep-ph/0501190] (2005).

[37] G. W. Bennet *et al.,* Phys. Rev. Lett **92** (2004) 161802.

[38] J. Ellis, S. Heinemeyer, K. A. Olive and G. Weiglein, *Indirect Sensitivities to the Scale of Supersymmetry*, JHEP 0502 (2005) 013.

[39] M. S. Alam *et al.* [CLEO Collaboration], Phys. Rev. Lett. **74** (1995) 2885.

[40] K. Abe *et al.* [Belle Collboration], Phys. Lett. **B 511** (2001) 151.

[41] R. Barate *et al.* [ALEPH Collaboration], Phys. Lett **B 429** (1998) 169.

[42] A. Buras, Phys. Lett. **B 566** (2003) 115.

[43] A. Dedes, H. K. Dreiner, U. Nierste and P. Richardson, Phys. Rev. Lett **87** (2001) 251804; A. Dedes *et al.,* [arXiv:hep-ph/0207026].

[44] V. M. Abazov *et al., A search for the Flavor-Changing Neutral Current Decay* $B_s^0 \to \mu^+\mu^-$ *in* $p\bar{p}$ *Collisions at* $\sqrt{s}$*=1.96 TeV with the DØ Detector*, Phys. Rev. Lett. **94** (2005) 071802.

[45] D. Acosta *et al.* [CDF collaboration], *Search for* $B_s^0 \to \mu^+\mu^-$ *and* $B_d^0 \to \mu^+\mu^-$ *Decays in* $p\bar{p}$ *Collisions at* $\sqrt{s}$ *= 1.96 TeV*, Phys. Rev. Lett. **93** (2004) 032001.

[46] J. Ellis, T. Falk, G. Ganis and K. Olive, *Supersymmetric Dark Matter in the Light of LEP and the Tevatron Collider*, Phys. Rev. **D 62** (2000) 075010.

[47] J. Ellis, K. A. Olive and Y. Santoso, *Constraining Supersymmetry*, New J. Phys. **4** (2002) 32.

[48] J. Ellis, K. Olive, Y. Santoso and V. C. Spanos, *Supersymmetric Dark Matter in Light of WMAP*, Phys. Lett. **B 565** (2003) 176-182.

[49] S. W. Barwick *et al.* [HEAT Collaboration], Astrophys. J. **482** (1997) L191.

[50] W. de Boer, M. Herold, C. Sander and V. Zhukov, *Excess of EGRET Galactic Gamma Ray Data interpreted as Dark matter Annihilation*, [arXiv:astro-ph/0408272] (2004).

[51] G.Cowan, *Statistical Data Analysis*, Oxford University Press, Oxford, New York (1998).

[52] R. J. Barlow, *Statistics, a guide to the use of statistical methods in the physical sciences*, John Wiley and Sons, New York (1997).

[53] V. Buescher *et al., Recommendation of the Ad-Hoc Committee on Limit-Setting Procedures to be Used by DØ in Run II*, DØ Note 4629 (2004); T. Junk, Nucl. Instr. and Meth., A**434** (1999) 435.

[54] Fermilab Beams division, *Run II Handbook*, `http://www-bd.fnal.gov/runII/index.html` (2003).

[55] `http://www.fnal.gov`.

[56] `http://lhc-new-homepage.web.cern.ch/lhc-new-homepage` (2005).

[57] `http://public.web.cern.ch/Public/Welcome.html`.

[58] `http://www-cdf.fnal.gov`.

[59] V. M. Abazov *et al., The upgraded DØ detector*, [arXiv:physics/0507191] (2005).

[60] Fermilab Beams division, *Fermilab Recycler Ring Technical Design Report*, Fermilab-TM-1991 (1997).

[61] `http://www-d0.fnal.gov/D0Code/source/d0reco`.

[62] CTEQ group *New Generation of Parton Distributions with Uncertainties from Global QCD Analysis (CTEQ6)*, JHEP 0207 (2002) 012.

[63] V. Buescher, J.-F. Grivaz, T. Nunnemann and M. Wobisch *Conclusions of Mini-Workshop on PDF uncertainties and related topics*, DØ Note 4618 (2004).

[64] F. Olness, *Drell-Yan Processes*, Lecture at the CTEQ summer school, 2003, `http://www.physics.smu.edu/~olness/cteq2003/olness_dy_all.pdf`.

[65] T. Sjostrand *et al.,* Comp. Phys. Commun. **135** (2001) 238.

[66] G. Altarelli and G. Parisi, Nucl. Phys. **B 126** (1977) 298.

[67] M. Seymour, *Introduction to event generators*, Lecture at the CTEQ summer school, 2003, http : //seymour.home.cern.ch/seymour/slides/cteq.html.

[68] S. Jadach *et al., The τ decay library TAUOLA, update with exact O(α) QED corrections in $\tau \to \mu(\mathrm{el})\nu\bar{\nu}$ decay mode*, Comput. Phys. Commun. **70** (1992) 69-76.

[69] M. L. Mangano, M. Moretti, F. Piccinini, R. Pittau and A. Polosa, *ALPGEN, a generator for hard multiparton processes in hadronic collisions*, JHEP 0307 (2003) 001.

[70] Y. Fisyak and J. Wormersley, *DØGSTAR, DØGEANT simulation of the Total Apparatus Response*, DØ Note 3191 (1997).

[71] http : //www − d0.fnal.gov/computing/MonteCarlo/simulation/d0sim.html.

[72] Application Software Group, CERN computing and Networks Division, *GEANT, Detector Description and Simulation Tool*, CERN Program Library Long Writeup W5013 (2003).

[73] W. Beenakker, R. Hopker, M. Spira and P. M. Zerwas, *Squark and Gluino Production at Hadron Colliders*, Nucl. Phys. **B 492** (1997) 51.

[74] W. Beenakker *et al., The production of Charginos/Neutralinos and Sleptons at Hadron Colliders*, Phys. Rev. Lett. **83** (1999) 3780-3783.

[75] M. Hohlfeld, *Search for Associated Production of Charginos and Neutralinos in the e$\mu + \ell$ Final State* , http : //www−clued0.fnal.gov/ ∼ hohlfeld/susy2005/susyupdate$_{\mathrm{v}}$04.pdf (2005).

[76] M. Binder, *Search for the Associated Chargino-Neutralino Production in the Final States with two Muons and additional Lepton*, DØ Note 4806 (2005).

[77] A. Yurkewicz, *Search for mSUGRA SUSY in the Like-Sign Dimuon Channel*, http : //www − d0.fnal.gov/d0pub/d0$_{\mathrm{p}}$rivate/4408/m$_4$408$_{\mathrm{m}}$sugrasearch$_3$.pdf (2005).

[78] DØ Collaboration, *Search for the Associated Production of Charginos and Neutralinos in the* e+ τ^{had} + ℓ *Final State*, DØ Note 4741-Conf (2005).

[79] DØ Collaboration, *Search for the Associated Production of Charginos and Neutralinos in the $\mu\tau$ + ℓ Final State*, DØ Note 4742-Conf (2005).

[80] C. Noeding, *Search for new physics in final states with electrons and taus*, PhD thesis in preparation at the Albert-Ludwigs-Universität, Freiburg.

[81] U. Blumenschein, *EM triggering at 60E30*, presentation on the ADM meeting, May 2nd, 2003, http : //www − d0.fnal.gov/atwork/adm/d0_private/2003 − 05 − 02/adm_etrig.ps; M.Verzocchi and T.Golling, private communication.

[82] A. Duperrin, U. Blumenschein, V. Buescher, J.-F. Grivaz, A. Patwa and R. Strohmer, *The v13 physics trigger list and New Phenomena triggers* , DØ Note 4641 (2004).

[83] F. Beaudette and J.-F. Grivaz *The Road Method (an algorithm for the identification of electrons in jets)* , DØ Note 3976 (2002).

[84] DØ collaboration, *Measurement of the Cross Section for W and Z Production to Electron Final States with the DØ Detector at* $\sqrt{s} = 1.96$ TeV,
DØ Note 4403-CONF (2004);
D. Chapin *et al., Measurement of* $Z \to ee$ *and* $W \to e\nu$ *production cross sections with* $|\eta| < 1.05$, `http://www-d0.fnal.gov/Run2Physics d0_private/eb/Run2EB_003/Run2EB_003.html`.

[85] `http://marwww.in2p3.fr/D0/files/ZandJPsiToeeEMscale-092004.pdf` (2004);
`http://www-d0.fnal.gov/D0Code/source/em_util/src/EMScale.cpp`.

[86] `http://www-d0.fnal.gov/computing/algorithms/calgo/calgo.html`.

[87] `http://www-d0.fnal.gov/phys_id/emid/d0_private/certification/welcome.html`;
`http://www-d0.fnal.gov/phys_id/emid/d0_private/EM_Particle_Documentation_EMID.html`.

[88] `http://www-d0.fnal.gov/D0Code/source/em_evt`.

[89] `http://www-d0.fnal.gov/cgi-bin/cvsweb.cgi/emreco`.

[90] `http://www-d0.fnal.gov/Run2Physics/cs/d0correct/d0correct.html`.

[91] J. Kozminski, R. Kehoe, H. Weerts, S. Park, A. Quadt, J. Gardner and Sh. Jabeen, *Electron Likelihood in p14*, DØ Note 4449.

[92] A. Abdesselam, *Comparison of H-Matrices for electron identification in DØ Run II*, DØ Note 3745 (2000).

[93] G. C. Blazey *et al., Run II Jet Physics*, DØ Note 3750 (2000).

[94] `http://www-d0.fnal.gov/phys_id/jes/d0_private/certified/certified_jes.html`;
S. Fatakia *et al., Jet Energy Scale and Resolution for p13 Data and MC*,
DØ Note 4115 (2003).

[95] `http://www-d0.fnal.gov/phys_id/jets/jetid.html`.

[96] `http://www-d0.fnal.gov/Run2Physics/cs/index.html`.

[97] M. Begel *et al., DØ luminosity in Run II: Triggered*, DØ Note 3970 (2002).

[98] `http://www-clued0.fnal.gov/~pverdier/d0_private/MetRunSel`.

[99] P. Verdier and S. Trincaz-Duvois, *Missing ET Status*,
presentation at the ADM meeting, octuber 10th, 2004,
`http://www-d0.hef.kun.nl///askArchive.php?base=agenda&categ=a041625&id=a041625s1t0/transparencies`.

[100] L. Duflot, V. Shary, R. Zitoun and I. Torchiani, *Cal_Event_Quality Package*,
DØ Note 4614 (2004).

[101] http : //www − d0.fnal.gov/computing/data_quality/dataqual.html.

[102] P. Kumar Mal, M. Begel, M. Verzocchi and H. Schellman, *D0 Luminosity in Run II: Reconstructed*, DØ Note 4438 (2004).

[103] M. Begel *et al., DØ luminosity in Run II: Delivered*, DØ Note 3970 (2002).

[104] M. Begel, *DØ luminosity in Run II: Recorded*, DØ Note 3972 (2002).

[105] T. Edwards, S. Yacoob, T. Andeen, M. Begel, B. C. Casey, R. Partridge, H. Schellman and A. Sznajder, *Determination of the Effective Inelastic* $p\bar{p}$ *Cross-Section for the DØ RunII Luminosity Measurement* , FERMILAB-TM-2278-E (2004).

[106] DØ New Phenomena MC webpage,
http : //www − clued0.fnal.gov/ ∼ nunne/cross − sections/
mcfm_cross − sections.html.

[107] T. Nunnemann, *NNLO Cross-Sections for Drell-Yan, Z and W Production using Modern Parton Distribution Functions*, DØ Note 4476 (2004).

[108] N. Kidonakis and R. Vogt, *Theoretical Status of the Top Quark Cross Section*, [arXiv:hep-ph/0410367] (2004).

[109] B. C. Allanach, *SOFTSUSY: a program for calculating supersymmetric spectra*, Comput. Phys. Commun. **143** (2002) 305-331.

[110] M. Verzocchi, *Status of Calorimeter Calibration*,
plenary talk at the DØ collaboration meeting, march 2005.

[111] B. Tiller and T. Nunnemann, *Measurement of the differential* Z^0*-boson Production Cross-Section as Function of Transverse Momentum*, DØ Note 4660 (2004).

[112] T. Golling, *Measurements of the Top Quark Pair Production Cross Section in Lepton+Jets Final States using a Topological Multivariate Technique as well as Lifetime B-Tagging in Proton-Antiproton Collisions at* $\sqrt{s} = 1.96\ TeV$ *with the DØ Detector at the Tevatron*, PhD thesis at the Bonn university, http : //www − d0.fnal.gov/results/publications_talks/thesis/golling/thesis.pdf (2005).

[113] A. Kumar, R. Kehoe, K. Ranjan and B. C. Choudhary, *Oversmearing of Missing Transverse Energy in Z→ee+X Monte Carlo Events*, DØ Note 4554 (2004).

[114] R. Stroehmer, *Common MC Smearing*, presentation available at:
http : //www − d0.hef.kun.nl///fullAgenda.php?ida = a042017 (2004).

[115] http : //www−d0.fnal.gov/ ∼ d0upgrad/d0_private/software/tauid/tauid.html.

[116] V. M. Abazov *et al.,* [DØCollaboration], *Search for Supersymmetry via Associated Production of Charginos and Neutralinos in Final States with Three Leptons*, [arXiv:hep-ex/0504032], FERMILAB-PUB-05/075-E,
accepted by Phys. Rev. Lett (2005).

[117] http : //www − cdf.fnal.gov/physics/exotic/r2a/20050310.trilepWebPage_hiptee (2005).

[118] V. Buescher and K. Jakobs, *Higgs Boson Searches at Hadron Colliders*, Int. J. Mod. Phys. **A 20** (2005) 2523-2602.

[119] `http://www-cdf.fnal.gov/physics/projections` (2005).

[120] F. Gianotti and M. Mangano, *LHC physics: the first one-two year(s)*, CERN-PH-TH/2005-072, [arXiv:hep-ph/0504221] (2005).

[121] W. Beenakker, R. Hoepker, M. Spira and P. M. Zerwas, *Squark and Gluino Production at Hadron Colliders*, Nucl. Phys. **B 492** (1997) 51-103.

[122] ATLAS collaboration, *ATLAS: Detector and Physics Performance Technical Design Report, Vol. II*, CERN-LHCC-99-15, `http://atlas.web.cern.ch/Atlas/GROUPS/PHYSICS/TDR/access.html` (1999).

[123] V. Buescher, *Physics Landscape Working Group Summary*, plenary talk at the third Tev4LHC meeting, CERN, 2005.

[124] S. Villa, *Discovery Potential for SUGRA/SUSY at CMS*, CMS CR-2003/033 — PRS PH-SUSY;
D. Denegri, *Summary of the CMS Discovery Potential for the MSSM SUSY Higgses*, [arXiv:hep-ph/0112045];
F. E. Paige, *SUSY signatures at LHC*, `http://www-library.desy.de/preparch/desy/proc/proc02-02/Proceedings/pl.1b/paige_pr.pdf`.

[125] G. Weiglein *et al.* [LHC/LC Study Group], *Physics Interplay of the LHC and the ILC*, [arXiv:hep-ph/0410364].

[126] K. Jakobs, *Higgs Boson Production*, presentation at the CTEQ summer school 2003, `http://www.phys.psu.edu/~cteq/schools/summer03/jakobs`;
A. Barr, *Mini-Review: Higgs and SUSY at the LHC*, Presentation at the 32th International Conference on High Energy Physics (ICHEP), 2004, `http://ichep04.ihep.ac.cn/12_bsm.htm`.

Acknowledgments

I would like to thank my supervisor Karl Jakobs for giving me the opportunity to work within the DØ collaboration at Fermilab, for the valuable advice and the inspiring and challenging discussions.

I am very thankful to Volker Büscher, who gave me the opportunity to gain experience in a large variety of topics and who supported me with useful advice and resourceful ideas, whenever necessary.

I would also like to thank Jean-Francois Grivaz for the fruitful discussions about numerous SUSY topics where I could profit from his vast experience. Many thanks to both Jean-Francois and Volker for convening the New-phenomena group in a challenging but also very exciting phase of the experiment. Special thanks to Terry Wyatt for his successful commitment for the L3-algorithm group and to Fritz Bartlett and Bill Lee for their support with the calorimeter slow-control.

I am deeply grateful to the collaborators who met the enormous challenges in the DØ experiment, working long hours to commission the detector and to provide acceptable data for the collaboration. Special thanks to the rest of the trilepton team, Marc Hohlfeld, Meta Binder and Adam Yurkewicz and Volker Büscher for all the hard work, often on short notice, and the fruitful discussions which made the publication possible.

Many thanks to many collaborators, who made my stay in Chicago a pleasurable experience, in particular to Sinjini Sengupta, Daniela Käfer and Meta Binder, to all my climbing partners for not letting me down and to the Eurotrash team for the great games, even if we lost them. Thanks to all people from Aachen, Bonn, Munich, Stockholm, Manchester, Amsterdam, Marseille, Paris and other places all over the world for the numerous undertakings in Chicago and in our suburban realm.

Special thanks to all my colleagues from Mainz and Freiburg, in particular Carsten Nöding and Andrea Dahlhoff, who where always there when I needed them, our M&M team Michael Heldmann and Michael Dührssen, Dietrich Schroff for his provocative viewpoints, Jens Konrath for the fruitful discussions, Henrik Nilsen for his contagious enthusiasm, Björn Penning for distracting us whenever we needed it, Olav Mundal for his Norwegian lessons, Uli Parzefal for the barbecues and the good fish, Maxim Titov for the support with Russian bureaucracy, Till Neunhöffer for numerous unbeatable physics discussions during the coffee breaks, David Meder-Marouelli and Marc Hohlfeld for the introduction into the DØ realm, Ingo Torchiani for the great company, Klaus Desch for the interesting discussions, Jürgen Thomas, Robindra Prabhu, Carmen Carpentieri, Didar Dobur, Harald Fox, Inga Ludwig, Frank Meisel and all the other collaborators and colleagues which I could not mention explicitely here and which have contributed to make the last few years an enjoyable experience.

Many thanks to Silvia Müller for achieving the impossible and to Elke Lützner for all the support in Freiburg.

I am very grateful to my administrators Dietrich Schroff, Till Neunhöffer, Slava Kulik, Michael Heldman and Michael Dührsen for valuable advice, even from abroad, in particular for helping me in setting up my notebook, for saving my disk with all my data and for not removing the localscratch on my desktop computer.

Many thanks to the german academic exchange service (DAAD) for the financial support of my stay at Fermilab.

I am very thankful to my family, who supported my career choice wholeheartedly. Special thanks to my parents for the financial and emotional support and the interesting discussions, to my sister who supported my choice to follow my true interests and my nephew for peppering me with all kinds of questions about the world of physics.